

Wavelength-Orthogonal Approaches Enabling Reprogrammable Gradient Materials

Zur Erlangung des akademischen Grades eines

DOKTORS DER NATURWISSENSCHAFTEN

(Dr. rer. nat.)

von der KIT-Fakultät für Chemie und Biowissenschaften

des Karlsruher Instituts für Technologie (KIT)

genehmigte

DISSERTATION

von

M. Sc. David Emmanuel Marschner

1. Referent: Prof. Dr. Christopher Barner-Kowollik

2. Referent: Priv.-Doz. Dr. Andreas-Neil Unterreiner

Tag der mündlichen Prüfung: 25. Juli 2019

Die vorliegende Arbeit wurde von Juli 2016 bis Juni 2019 im Rahmen eines DFG Projektes (Sachbeihilfe) zwischen dem Karlsruher Institut für Technologie (KIT) im Arbeitskreis von Prof. Dr. Christopher Barner-Kowollik angefertigt, in Zusammenarbeit mit Prof. Dr. Andreas Walther (Albert-Ludwigs-Universität Freiburg).

Erklärung

Ich erkläre hiermit, dass ich die vorliegende Arbeit im Rahmen der Betreuung durch Prof. Dr. Christopher Barner-Kowollik selbstständig verfasst und keine anderen als die angegebenen Quellen und Hilfsmittel verwendet habe. Wörtlich oder inhaltlich übernommenen Stellen sind als solche kenntlich gemacht und die Satzung des Karlsruher Instituts für Technologie (KIT) zur *Sicherung guter wissenschaftlicher Praxis* wurde beachtet.

Des Weiteren erkläre ich, dass ich mich derzeit in keinem weiteren laufenden Promotionsverfahren befinde und auch keine vorausgegangenen Promotionsversuche unternommen habe.

Ort, Datum

David Marschner

Abstract

The reversible and visible light induced cycloaddition of styrylpyrene has been investigated with regard to its formed isomeric photoproducts as well as its most efficient photochemical reaction conditions – *i.e.* trigger wavelength and number of photons required for maximum conversion – via a newly developed technique called Wavelength-dependent Photon Efficiency Analysis (WPEA). With wavelengths at 435 nm for the dimerisation and 330 nm for the dissociation, the investigated cycloaddition is among the mildest of its kind. The chromophore was further exploited in polymer studies, on the one hand towards wavelength-orthogonal reaction systems to alter material properties simply by using disparate colours of light, and on the other hand for reprogrammable gradient materials. In particular, styrylpyrene has been successfully employed in reversible block-copolymer formations over several dimerisation / dissociation cycles demonstrating the capability of styrylpyrene for reprogrammability. A further reversible visible light moiety based on a pyrenyl cinnamic acid derivate was combined with *o*-methyl benzaldehyde – which reacts in an irreversible cycloaddition under irradiation with UV light – in one molecule. The dichromophore was employed in wavelength-orthogonal studies with subsequent irradiation of distinct wavelengths to pathway-independently obtain the same product. Such a dichromophore can be further utilised as a cross-linking molecule for the generation of light responsive materials. Moreover, polymer strands with styrylpyrene or *o*-methyl benzaldehyde side groups were investigated in-depth for wavelength-orthogonal systems in small molecule, polymer and material studies including analysis via XPS and AFM. It is demonstrated that curing the latter with disparate colours of light induced different cross-linking reactions resulting in distinct material properties such as softness and adhesiveness. As a result, reversible visible light moieties such as styrylpyrene are suitable for reprogrammable gradient materials that can be combined with additional wavelength-orthogonal reactions to introduce further functionalisation.

Zusammenfassung

Die reversible und mit sichtbarem Licht induzierte Cycloaddition von Styrylpyrene wurde mit Augenmerk auf die durch sie geformten isomeren Photoprodukte sowie ihre effizientesten photochemischen Reaktionsparameter detailliert untersucht. Letztere wurden durch eine neu vorgestellte Methode mit dem Namen „Wellenlängenabhängige Photonen Effizienz Analyse“ bestimmt. Hierbei wird eine Reaktion auf ihre wirkvollste Startwellenlänge sowie die Anzahl der benötigten Photonen für den höchstmöglichen Umsatz untersucht. Im Falle von Styrylpyrene waren dies 435 nm für die Dimerisation und 330 nm für die Dissoziation, womit das untersuchte System zu den mildesten bekannten seiner Art gehört. Auf Basis dieser Eigenschaften wurde der Chromophore im Folgenden in Polymerstudien verwendet. Zum einen war das Ziel ein wellenlängen-orthogonales Reaktionssystem zu erhalten, um Materialeigenschaften rein basierend auf der Wahl der Bestrahlungswellenlänge zu ändern. Andererseits wurden Möglichkeiten erforscht wie durch photochemisch reversible Reaktionen reprogrammierbare Gradientenmaterialien erhalten werden können. In einem ersten Schritt wurde Styrylpyrene erfolgreich verwendet, um reversible Blockcopolymere zu bilden. Durch mehrfaches Durchführen des Dimerisations- und Dissoziationszyklus konnte bewiesen werden, dass sich Styrylpyrene sehr gut für reprogrammierbare Anwendungen eignet. In weiteren Studien wurde ein ähnliches, ebenfalls reversibles und mit sichtbarem Licht induziertes, System basierend auf einem Pyren-Zimtsäurederivat zusammen mit *o*-Methylbenzaldehyd untersucht. *o*-Methylbenzaldehyd ist in der Lage unter Bestrahlung mit UV Licht irreversible Cycloadditionen einzugehen. Durch Kombination der beiden licht-reaktiven Gruppen in einem Molekül wurde ein Dichromophor erhalten, dem ein wellenlängen-orthogonales Verhalten nachgewiesen werden konnte. Durch aufeinanderfolgende Bestrahlung mit zwei verschiedenen Wellenlängen wird unabhängig vom Reaktionsweg das gleiche Reaktionsprodukt erhalten. Ein solcher Dichromophor ist hervorragend geeignet, um als Vernetzer bei der Herstellung von licht-gesteuerten Materialien zu dienen. Zusätzlich wurden Polymere mit Styrylpyrene oder *o*-Methylbenzaldehyd als Seitengruppen detailliert auf ihre Eignung in wellenlängen-orthogonalen System untersucht. Neben Stu-

dien zur Reaktivität als kleine Moleküle und Polymere in Lösung, wurden ebenfalls Materialstudien unter Verwendung von XPS und AFM durchgeführt. Aushärten des Materials durch verschiedene Wellenlängen induzierte eine jeweils andersartige Vernetzungsreaktionen und führte damit zu deutlich unterschiedlichen Materialeigenschaften, beispielsweise in den Bereichen Weichheit und Haftfähigkeit. Basierend auf diesen Ergebnissen konnte gezeigt werden, dass sich reversible, mit sichtbarem Licht induzierte Systeme wie Styrylpyrene hervorragend eignen um reprogrammierbare Gradientenmaterialien herzustellen die weiterhin mit wellenlängen-orthogonalen Reaktionen kombiniert werden können um zusätzliche Funktionalisierung zu ermöglichen.

Table of Contents

Abstract	I
Zusammenfassung	III
Table of Contents	V
1 Introduction	1
2 Theoretical Background	5
2.1 Reprogrammable Gradient Materials	5
2.2 Polymer Chemistry	8
2.2.1 Free Radical Polymerisation.....	9
2.2.2 Reversible Addition Fragmentation Chain Transfer Polymerisation.....	11
2.3 Photochemistry.....	13
2.3.1 Beer-Lambert's Law	15
2.3.2 Franck-Condon Principle	17
2.3.3 Cycloadditions	18
2.3.3.1 Fundamentals.....	18
2.3.3.2 [2+2] Cycloadditions	20
2.3.3.3 Applications for Photochemical Cycloadditions	23
2.3.4 Bathochromic Shifts	27
2.3.5 Wavelength-Orthogonality	29
2.3.6 Photoenol Chemistry	33
2.4 Laser Systems	36
2.4.1 Tuneable Laser Systems	37
3 Styrylpyrene	39

3.1 History	41
3.2 Stereochemistry	42
3.3 Wavelength-dependent Photon Efficiency Analysis	47
3.4 Application and Outlook	53
4 Styrylpyrene meets <i>o</i>-Methyl Benzaldehyde	59
4.1 The Challenge of Wavelength-Orthogonality	59
4.2 Proving the Concept – Small Molecule Study.....	61
4.3 From Molecules to Materials.....	68
5 Polychromophores	73
5.1 Model Studies	76
5.2 Dichromophores	80
5.3 Preliminary Polymer Studies	85
6 Towards Reversible Gradient Nanocellulose Materials	89
7 Conclusion and Outlook	97
8 Experimental Part.....	101
8.1 Analytical Instrumentation and Methods.....	101
8.1.1 Nuclear Magnetic Resonance Spectroscopy (NMR).....	101
8.1.2 Size Exclusion Chromatography (SEC).....	102
8.1.3 Electrospray Ionisation - Mass Spectrometry (ESI-MS).....	103
8.1.4 Gas Chromatography-Mass Spectrometry (GC-MS).....	104
8.1.5 UV/Vis Spectroscopy	104
8.1.6 Mechanical Testing	105
8.2 Light Sources and Irradiation Setups.....	106
8.2.1 LED and UV Lamps.....	106
8.2.2 UV Light Photoreactor	107
8.2.3 Visible Light Photoreactor	108
8.2.4 Innolas Tuneable Laser System.....	109
8.3 Synthetic Protocols	116
8.3.1 Hydroxy-styrylpyrene (StyP, 1)	116

8.3.2 Carboxy-styrylpyrene (StyP-COOH)	117
8.3.3 mPEG-amine (mPEG-NH ₂).....	119
8.3.4 mPEG-styrylpyrene (mPEG-StyP, 3)	122
8.3.5 Methyl 4-((2-formyl-3-methylphenoxy)methyl)benzoate (<i>o</i> -MBA, 4)	124
8.3.6 Tetrathylene glycol difumarate (TGD, 5)	126
8.3.7 (<i>E</i>)-3-(pyren-1-yl)acrylic acid.....	127
8.3.8 Butyl (<i>E</i>)-3-(pyren-1-yl)acrylate (9).....	127
8.3.9 3-Hydroxypropyl (<i>E</i>)-3-(pyren-1-yl)acrylate via SOCl ₂ -mediated chlorination	128
8.3.10 (<i>E</i>)-3-((3-(pyren-1-yl)acryloyl)oxy)propyl 4- ((2-formyl-3-methylphenoxy)methyl)benzoate (7)	129
8.3.11 10-hydroxydecyl (<i>E</i>)-3-(pyren-1-yl)acrylate	129
8.3.12 (<i>E</i>)-10-((3-(pyren-1-yl)acryloyl)oxy)decyl 4- ((2-formyl-3-methylphenoxy)methyl)benzoate (8)	130
8.3.13 Styrylpyrene Monomer (StyP-O-MA, 10).....	131
8.3.14 Styrylpyrene-mTEGMA Copolymers.....	133
8.3.14.1 P3.....	133
8.3.14.2 P4.....	134
8.3.15 Boc Protected Styrylpyrene-amine (StyP-TOTA-Boc)	136
8.3.16 Decoration of TEMPO-oxidized cellulose nanofibrils (CNF) with tetrazole-NH ₂ in dispersion.....	137
Bibliography	139
Appendix.....	145
Styrylpyrene	145
Structures of Possible Photoproducts	146
Detailed NMR Analysis of the Photoproducts PP I – III.....	149
Styrylpyrene meets <i>o</i> -Methyl Benzaldehyde	174
Detailed NMR Analysis.....	174
Liquid Chromatography Mass Spectroscopy (LC-MS) Measurements.....	182
Polychromophores	193
Towards Reversible Nanocellulose Materials.....	202

Table of Contents

List of Investigated Chemical Compounds.....	203
List of Figures.....	205
List of Tables.....	213
Publications and Conferences.....	215
Acknowledgements	217

1

Introduction

The combination of materials science with photochemistry is a promising field in contemporary material science. Light can be employed in a spatially resolved fashion and is therefore uniquely suitable for manufacturing processes that require high precision. Furthermore, light sources can be instantly switched on and off, allowing to – on-demand – alter and tailor material properties. In comparison, conventional temperature triggered reactions can only be applied to modify spatially non-defined areas of a material, while also requiring control over heat distribution and dissipation. In addition, temperature for the initiation of reactions cannot be utilised on-demand, requiring heating and cooling periods. Thus, introducing photochemical reactions into the wide field of soft matter materials science enables highly interesting applications, *e.g.* 3D printing – from the macro- to nanoscale – as well as dental composites, optics, medicine, and many more.¹⁻³

Due to the unique features of light (*i.e.* spatial control, on-demand triggering), it can be employed with continuously changing parameters (*e.g.* light intensity, irradiation time, wavelength), while also varying which parts of a material are irradiated. Thus, one research field that can critically profit from photochemical reactions are gradient materials. In fact, light-induced cross-linking can stiffen and harden a material based on the light intensity or irradiation time and thus cross-linking density. Therefore, by varying one of these parameters throughout the irradiation of a material, gradient materials can be obtained. Traditionally, mostly homogeneous materials that are characterised by relatively uniform properties (composition, microstructure, etc.) are employed.⁴ However, modern applications usually feature heterogeneous modes of stress or strain. As a result, gradients critically enhance the performance of a material, *e.g.* for the utilisation in flexible electronics, medical implants, or aerospace projects.⁴

In-Depth Photochemical Investigations

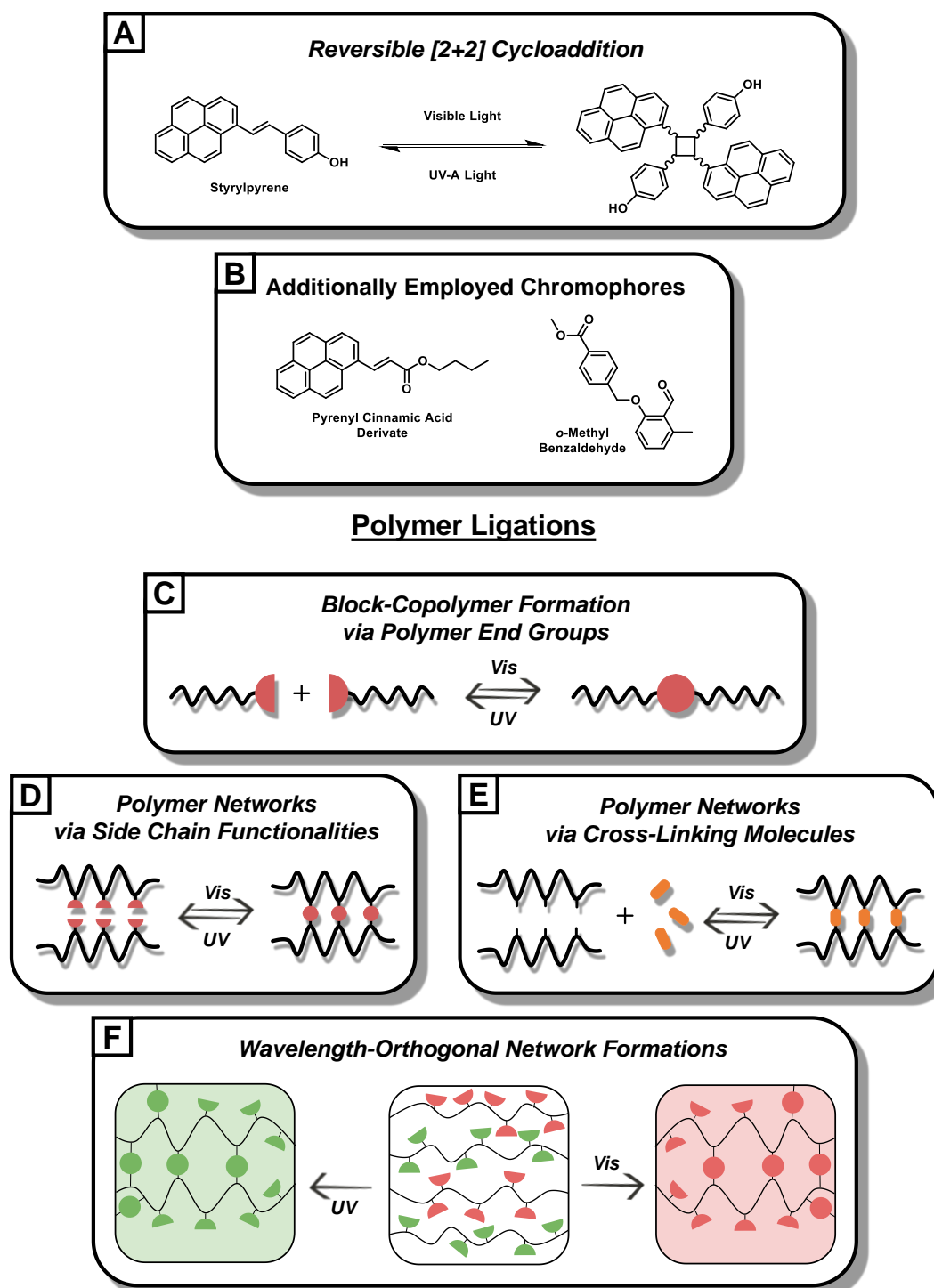


Figure 1. Schematic overview over the topics investigated in the present thesis: In-depth investigations of the reversible and visible light cycloaddition of (A) styrylpyrene (Chapter 3) for further utilisation alongside the chromophores (B) o-methyl benzaldehyde (Chapter 4 and 5) and a pyrenyl cinnamic acid derivate (Chapter 5). Polymer Ligations to form (C) block-copolymers (Chapter 3) as well as networks via (D) side chain functional polymer strands (Chapter 4) or (E) by employing cross-linking molecules (Chapter 5). (F) Wavelength-orthogonal network formations enabled by the incorporation of two different chromophores into one material (styrylpyrene and o-methyl benzaldehyde, Chapter 4).

Today, transitions between areas with different flexibility are mostly implemented via sandwich-type gradients.^{5,6} However, these are beset with disadvantages, including joints in between the different layers. Therefore, a gradual change in the degree of stiffness, toughness, ductility, and formability of a material is desired.⁴ By introducing photochemical cycloadditions, such linear gradients can be achieved via variations of the light-induced cross-linking density. Furthermore, photochemical cycloadditions have the interesting feature of reversibility.⁷ Thus, in addition to being spatially resolved and on-demand, this class of photoreactions allows for reprogrammability. As a result, gradients can be rewritten and altered to achieve the best attainable result for each application.

The photochemical system investigated in the current thesis is based on styrylpyrene (**Figure 1 A**). This specific molecule can undergo a [2+2] cycloaddition within the visible light range, with a cycloreversion that can be triggered with UV-A light. Both wavelengths are among the mildest known for their respective reaction type (*i.e.* [2+2] cycloaddition and cycloreversion) and thus greatly minimise the damage dealt to the surroundings of the reaction (*e.g.* solvent, organic tissue or polymeric material) in case harsh UV-B or -C light would be employed. As a result, the first goal of the presented thesis was to conduct a detailed analysis of the dimerisation and dissociation reaction of styrylpyrene (Chapter 3), with a focus on its most suitable photochemical reaction conditions (*i.e.* trigger-wavelength and amount of photons needed) that can be subsequently depicted in so called *action plots* (reaction yield vs. irradiation wavelength). These investigations were conducted using a unique tuneable laser system, featuring monochromatic irradiation and thus allowing to study the reactivity of styrylpyrene at any given wavelength. The insights obtained from the in-depth investigations of styrylpyrene are further applied in polymer ligation approaches to prove the suitability of styrylpyrene for the development of gradient materials. In detail, styrylpyrene was employed for reversible block-copolymer formations (**Figure 1 C**, refer to Chapter 3) and as a cross-linking moiety to obtain polymeric networks and films (**Figure 1 D and F**, refer to Chapter 4), including mechanical testing of the latter.

In addition to styrylpyrene, a second and similar reversible visible light responsive moiety – based on a cinnamic acid derivate functionalised with pyrene instead of the phenyl moiety (**Figure 1 B**, refer to Chapter 5) – as well as an irreversible chromophore, *i.e.* *o*-methyl benzaldehyde (**Figure 1 B**, refer to Chapter 4 and 5), were investigated

Generally, the implementation of photochemical moieties into soft matter can be accomplished with two different strategies: cross-linking of side-functional polymer strands (**Figure 1 D**, refer to Chapter 4) as well as the combination of polymers with a linking molecule (**Figure 1 E**,

refer to Chapter 5). Both approaches were investigated in the present thesis with a focus on wavelength orthogonality in which two disparate light-responsive moieties can be triggered independently from each other, while introducing unique properties into an irradiated material (**Figure 1 F**, refer to Chapter 4). In fact, such pathway independent irradiation systems can be obtained by combining the UV-responsive chromophore *o*-methyl benzaldehyde with one of the two investigated visible light chromophores, styrylpyrene (Chapter 4) or the pyrenyl cinnamic acid derivate (Chapter 5). The wavelength-orthogonal reaction systems were investigated as first steps towards gradient materials, in which both photochemical reactions would introduce a different set of properties into a material (*i.e.* stiffness, toughness, ductility, and formability). When irradiated with continuously changing parameters such as light intensity or irradiation time, a material can be obtained that features two independent lateral gradients.

Finally, styrylpyrene was introduced into water-soluble polymers to be combined with styrylpyrene-functional nanocellulose fibrils for mechanical testing and gradient studies (**Figure 2**, refer to Chapter 6). Nanocellulose was the material of choice for this approach since it is one of the stiffest natural materials, able to be cast into transparent films. Continuously changing irradiation (intensity or time) with visible light can cross-link the styrylpyrene moieties, leading to a gradient material with varying cross-link densities and, thus, a lateral change for example in stiffness or flexibility. In addition, employing light in the UV-A regime would lead to dissociation of the formed styrylpyrene dimers resulting in the starting material. Therefore, the combination of a reversible and visible light cycloaddition with nanocellulose is an attractive route to transparent reprogrammable gradient materials with vast opportunities in modern soft matter science technology.

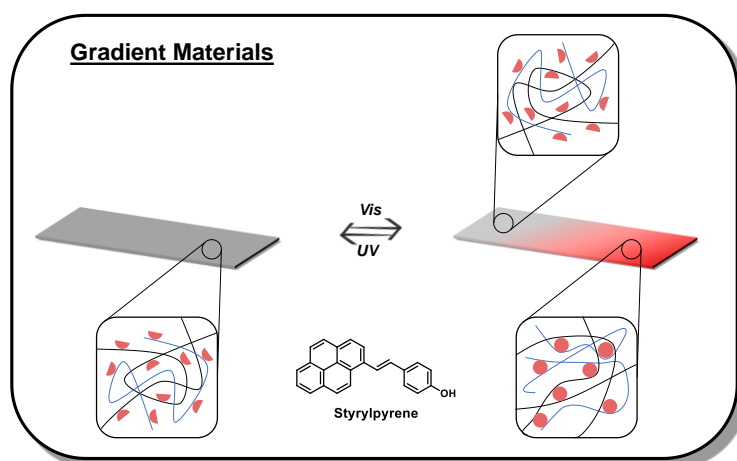


Figure 2. Gradually changing irradiation (intensity or time) of styrylpyrene-functional polymer strands (depicted as blue lines) and styrylpyrene-functional nanocellulose fibrils (depicted as black lines) with visible light, leads to different amounts of cross-linking and thus properties like toughness and stiffness. Irradiation with UV light reverts that process, resulting in a reprogrammable gradient material.

2

Theoretical Background

2.1 Reprogrammable Gradient Materials

Soft matter materials with adaptable properties are of high interest in modern research. Especially when it comes to materials that contain several different elasticities or connection points in between hard and soft material segments, it is important to consider the impact of stress and mechanical influences. By simply attaching a stiff to a more flexible material, the joint may face the disadvantage of a breaking point for the material that tends to fail if force is applied. Importantly, the bigger the difference in between the flexibility of the two materials, the sooner the joint will break. To prevent premature failure, inspired by nature itself (*e.g.* the attachment of ligaments to bones), gradient materials can be employed to gradually alter the degree of flexibility in a material.⁸ Despite the reduction of stress, gradient materials can be further optimised with regard to toughness, stiffness, resistance against abrasion, formability, and ductility.^{9,10} Further advantages of gradient materials include not only a remarkable ability to hinder crack propagation but also to resist contact deformation and damage.⁵ Mechanical failure of both materials and structures is a major problem for the economy and environment of modern society. Minimisation of these problems could include tougher structural materials or damage-reporting properties to avoid accidents or failure.

Alleviation of stress at interfaces can be achieved via gradually changing properties in materials. To-date, sandwich-type gradients are most common since they simply consist of layers

Unless stated otherwise, Chapter 2.1 is based on reviews by Walther *et al.*¹¹ and Ritchie *et al.*⁴

with different properties. Sandwich materials can be readily generated using classical engineering techniques such as stacking and fusing different materials or sequential photo cross-linking of subsequent layers.^{5,6,12} Strain can be effectively delocalised if layers with increasing stiffness are employed, but the materials still contain joints where the two different sandwich layers are fused, possibly acting as breaking points.

A possibility for avoiding any breaking points and mismatches in heterogeneous materials is the use of lateral gradients, although existing approaches to this solution are much scarcer than sandwich-type gradients. Lateral gradients are mostly achieved using irreversible cross-linking reactions, since changing the cross-linking density vastly influences the mechanical stiffness. One approach is to mix a prepolymer with a cross-linker via two syringes and gradually adjusting the mixing ratios.^{13,14} However, the result is highly specialised for a chosen application, and therefore, this approach is rather labour-intensive while not allowing for very steep gradients. Therefore, the goal is to obtain gradient materials that are not only more easily accessible but can also be erased and ultimately reprogrammed to be adaptable for complex operations on-demand.

Gradient materials have so far mostly been studied in 1D profiles due to the lack of adequate fabrication tools but also limitations in suitable analytical techniques. However, recent research has focussed on multidimensional and multimaterial approaches through the development of 3D printing platforms.¹⁵ Functional gradient materials open a wide spectrum of opportunities with possible application in thermal barrier coatings, biomedical implants, aerospace, and optoelectronics. All these fields require high-performance synthetic materials and illustrate the importance of high failure tolerances to ensure long lifetimes.

Recently, reprogrammable materials have been of high interest, for example due to their shape changing capabilities, enabling them to perform complex motions when triggered externally. These spontaneous changes, including folding or twisting, can be activated by various different stimuli such as humidity, temperature, light, or solvent and provide yet another dimension to the already mentioned reprogramming of a materials flexibility.¹⁶

As a conclusion, reprogrammable gradient materials are of high interest for modern technology, providing highly adjustable properties that can be tailored to each specific need, on-demand and only by applying an external trigger such as light. However, the combination of reprogrammable materials and gradient materials has not yet been achieved, and therefore the goal of this

thesis is to investigate fundamental principles such as reversible photochemistry in small molecules and polymer networks that can provide first insights towards reprogrammable gradient materials.

2.2 Polymer Chemistry

Improvements of functional gradients often rely on highly specialised materials that mimic natural and biological processes. For almost a century, researchers have been investigating materials and their respective science in the field of polymer chemistry.

The term *polymer* describes a molecule that is constructed from repeating units termed monomers and was mainly shaped by Staudinger in 1920. He postulated that polymers are in principle molecules of the same nature, covalently bonded together, acting as repeating units to form a long chain.¹⁷ A few years later, Staudinger also proposed the term *macromolecule*, describing molecules that consist of repeating units that are not necessarily equal to each other.¹⁸ Indeed, polymers can be categorised into natural and synthetic polymers, both playing an important role in our daily world.¹⁹ One of the most important natural polymers is the human DNA (deoxyribonucleic acid) which is constituted of nucleotides as the repeating units.²⁰ Nevertheless, synthetic polymers, likewise, are essential in our everyday life and modern technology. In fact, there are many different types of synthetic polymers, also incorporating additives to alter their properties (*e.g.* colour, stability) even further.^{21–23} As a matter of fact, all polymers can usually be characterised by their degree of polymerisation, their molecular weight, as well as their polydispersity.

Since a polymer sample can contain disparate chains with different lengths and therefore molecular weights, two different average terms have been introduced to distinguish them: the number average mass M_n and the weight average mass M_w . In addition, the degree of polymerisation DP_n expresses the number n of monomeric repeating units M_0 in a polymer chain:

$$DP_n = \frac{M_n}{M_0}$$

Furthermore, the polydispersity D implies molar mass distribution in a polymer sample, and hence its heterogeneity, by relating different average masses to each other:

$$D = \frac{M_w}{M_n}$$

Last but not least, polymer samples can be classified by their synthesis mechanism in chain-growth and step-growth polymerisation. In chain-growth polymerisations, an unsaturated monomer is required as well as an initiator. The latter is able to form a reactive centre that can react

Unless stated otherwise, Chapter 2.2 is based on books by Stevens,²⁴ Odian,²⁵ and Barner-Kowollik.²⁶

with one monomer transferring the reactive centre to the attached monomer which subsequently reacts with another unit, resulting in a growing chain. Possible reactive centres include radicals, ions (cations and anions) as well as coordinative systems. Step-growth polymerisation, in contrast, requires difunctional monomers which can undergo a reaction with each other. As a result, two monomers form dimers that can react to oligomers and eventually end in long polymer chains. Typical examples for this approach are polycondensation or polyaddition reactions.²⁷ Nevertheless, the latter polymerisation technique is beyond the scope of the current thesis, and thus will not be discussed in more detail.

2.2.1 Free Radical Polymerisation

The most used polymerisation technique in both industry and research is the free radical polymerisation (FRP).^{25,28} It usually features mild conditions while allowing a large range of different types of monomers to be polymerised.²⁹ Furthermore, FRP requires an initiator molecule that can be split into radicals when a trigger, such as heat or light, is applied (**Figure 3**).^{30,31} The initiator radical can subsequently attack a monomer transferring the radical to the latter. In the propagation step, the monomer reacts with the radical forming a growing chain, always containing the active centre at its end. A growing chain can be deactivated by two different pathways, either termination or chain transfer reactions. The termination reaction is diffusion controlled. For it to occur, two radically growing chains need to encounter each other,

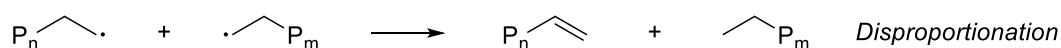
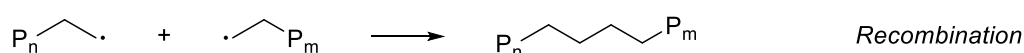
Initiation



Propagation



Termination



Transfer

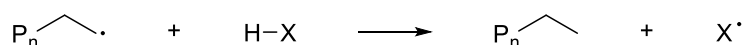


Figure 3. Overview of the FRP mechanism.

which is much slower than the reaction between two radicals itself. In addition, the rate of termination is also dependent on the monomer conversion, the chain length and the temperature. As a result, polymerisations often autoaccelerate at high conversions due to an increased viscosity, which is limiting chain movements and thus decreasing the possibility of a termination in comparison to the propagation step (Trommsdorff-Norrish effect).³² The termination reaction can be subdivided into recombination – the addition of two chains to form one chain with double the molecular weight – and disproportionation in which a hydrogen atom is transferred from one chain to the other leaving an unsaturated double bond behind.³³ The drawback of disproportionation is that the newly created double bond could again polymerise in the propagation step as a macromonomer.³⁴ Generally, random chain transfer reactions are mostly undesired side reactions since they can limit the maximum molecular weight of a polymer sample as well as the synthetic control.³⁵ In detail, a growing chain can transfer its radical to another chain's backbone by abstracting a hydrogen. Thus, the growing chain becomes inactive, while the attacked chain can now continue growth from its backbone. Chain transfer, however, can also occur within on chain, transferring the radical from the end of the chain towards its backbone, called 'back-biting'. Both chain transfer processes can lead to the formation of branched polymers due to the fact that the radical is not located at the end of the chain anymore.^{36,37} However, chain transfer agents can be deliberately added to a polymerisation mixture to take advantage of the transfer reaction and control the molecular weight.

Even though FRP is the most frequently used polymerisation technique, it features a few significant drawbacks that are associated with its mechanism. The end group fidelity of the obtained polymer chains as well as the dispersity of the molecular weight are rather hard to control. Polymer samples obtained via this technique often feature broad molar mass distributions, and the lack of control can be attributed to the termination and transfer steps.^{38,39} In fact, several different polymerisation techniques have been introduced to suppress both termination as well as undesired transfer reactions by temporarily deactivating the radical chains, and thus disabling their termination and transfer abilities. These reactions can be grouped under the name Reversible Deactivation Radical Polymerisation (RDRP)⁴⁰ and include Reversible Addition Fragmentation Chain Transfer (RAFT),⁴¹ Atom Transfer Radical Polymerisation (ATRP),³⁸ and Nitroxide Mediated Polymerisation (NMP).⁴² All these polymerisation techniques embody narrow polydispersities, predictable molecular weights and high end-group fidelities when compared to FRP.⁴³

2.2.2 Reversible Addition Fragmentation Chain Transfer

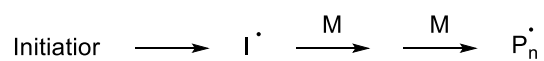
Polymerisation

RAFT was reported simultaneously but independently in Australia and France in 1989, although in France it was initially named macromolecular design by interchange of xanthates (MADIX).^{44,45} In detail, RAFT utilises a chain transfer agent (CTA or RAFT agent) to introduce an equilibrium of addition and fragmentation processes. Commonly employed CTAs are dithioester, dithiocarbamates and trithiocarbamates. The distinction of RAFT to any other RDRP technique is based on the fact that the concentration of radicals is actually not reduced but rather a new dormant radical is generated that exist in an equilibrium with the propagating chain. The advantage of not lowering the amount of radicals expresses itself in the comparable propagation rates for RAFT and FRP, while the rates for ATRP and NMP are drastically decreased.⁴⁶ Due to this, only RAFT was explored as a polymerisation technique in this thesis and will be explained in detail in this Chapter.

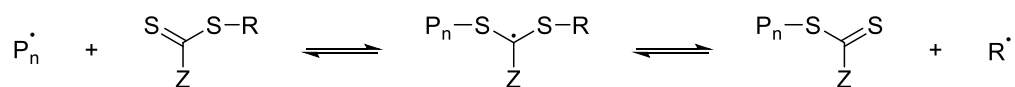
The mechanism for RAFT proceeds similarly to FRP, however after the initiation and propagation steps, the growing chain takes part in a reversible chain transfer, followed by reinitiation and a chain equilibrium before eventually undergoing termination. The key aspect of RAFT is the RAFT agent (*i.e.* CTA). By undergoing equilibrium reactions, the CTA provides control over the polymerisation leading to a narrow polydispersity. Tuning the ratio of the RAFT agent to the monomer can allow to determine the targeted molecular weight. However, the RAFT agent also exhibits challenges and drawbacks, since it needs to be specifically chosen and tailored for the desired monomers. In addition, RAFT agents are mostly coloured yellow or pink while introducing potential instability concerning the end group incorporated into the polymer chains. To overcome both drawbacks, the RAFT group often needs to be removed or altered via diverse post polymerisation functionalisation techniques.

Specifically, the RAFT mechanism (**Figure 4**) begins with an initiation step, in which a radical is generated that can attack a monomer and start a growing chain. Subsequently, the latter reacts with the CTA in an equilibrium reaction, creating a dormant species, which can eventually release its R-group as a new reactive radical to undergo reinitiation and subsequent propagation. The newly created growing chain again undergoes a chain equilibrium reaction suppressing undesired side and transfer reactions until ultimately the propagation is stopped by the termination process.

Initiation and Propagation



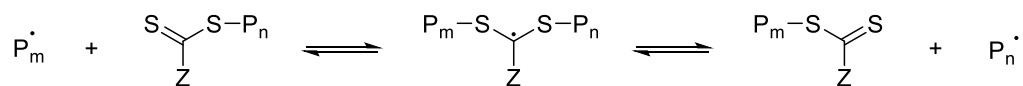
Reversible Chain Transfer



Reinitiation and Propagation



Chain equilibrium



Termination

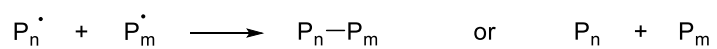


Figure 4. Overview of the RAFT mechanism.

2.3 Photochemistry

Photochemistry describes the alteration of molecules - including isomerisations, bond formations or physical changes such as fluorescence - under irradiation of light. Light is of high interest for both chemistry and materials science, since it offers reaction pathways that might not be thermally allowed, as well as a remote trigger for spatial control that can be switched on and off instantly. In addition, photochemical cycloadditions can be reversible, offering a wide range of possibilities for reprogrammable or self-healing properties within gradient materials.

In 1834, Trommsdorff published the first transformation introduced directly by light irradiation,⁴⁷ followed by the discovery of the photodimerisation of anthracene by Fritzsche.⁴⁸ More than thirty years later, Riiber observed that cinnamic acid is able to undergo a photocycloaddition as well,⁴⁹ which led to the publication of preliminary results by Ciamician and Silber in the early 19th century. This seminal work described the photodimerisation of several molecules including cinnamic acid, stilbene, and coumarin, both in solution and solid state, introducing the modern era of photochemistry.⁵⁰ At the same time, physicists like Planck and Einstein focused their attention on the theoretical background of photochemistry.^{51,52} Respectively, it was proven that light consists out of photons, which vary in their energy in dependence of their wavelength. Generally, light utilised for photochemical alterations is ranging from 200 nm (high energy) to 1000 nm (low energy), and divided into different sub-classes (**Table 1**):

Table 1. Classes and sub-classes of light suitable for photochemical reactions including their wavelength ranges.

Name	Sub-Class	Wavelength / nm
Ultraviolet (UV)	UV-C	200 - 280 nm
	UV-B	280 - 315 nm
	UV-A	315 - 380 nm
Visible Light (Vis)		380 - 750 nm
Infrared Light (IR)		750 - 10 ⁶ nm

In theory, a molecule can absorb light – in specific a photon of a suitable energy – which promotes that molecule from its ground state into an electronically excited state. Since excited

Unless stated otherwise, Chapter 2.3 is based on books and reviews by Atkins,⁵³ Balzani,⁷ Kaur *et al.*,¹ and Frisch *et al.*⁵⁴

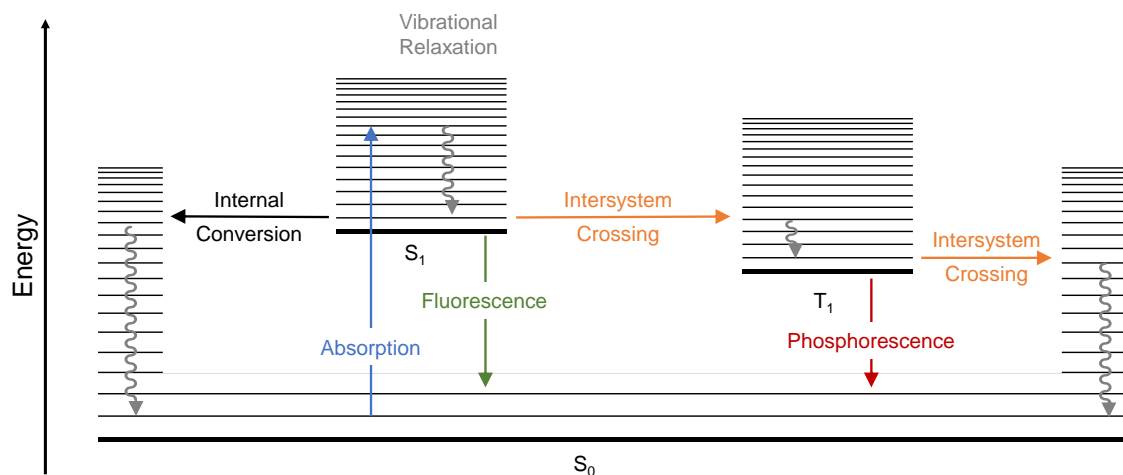


Figure 5. Jablonski diagram showing the possible deactivation pathways after a molecule is irradiated with light.

states are of a higher energy, the molecule subsequently undergoes a deactivation process to the more stable ground state, either by a photochemical or a photophysical pathway. Importantly, a molecule can undergo different reactions in the presence of light in comparison to heat as the trigger, due to the fact that a molecule's excited state reactivity is vastly different than the one of ground state.

In 1935, Jablonski published a schematic description illustrating the possible processes a molecule can undergo upon irradiation with light. A simplified version of the Jablonski diagram (**Figure 5**) depicts the ground (S_0) and both first excited states, singlet (S_1) and triplet (T_1), of a molecule including the respective vibrational states (thin horizontal lines). When a photon is absorbed, the molecule is usually excited from one vibrational state of its ground state S_0 to a vibrational state of its excited singlet state S_1 in a way that the energy difference of these two vibrational states matches the energy of the absorbed photon. Next, several different deactivation processes can take place, which are in competition with each other. After vibrational relaxation from a higher vibrational state to the lowest vibrational state took place, one of the following events can occur:

- Photophysical Deactivation
 - Non-Radiative Deactivation

During these processes no change in energy takes place and thus, no irradiation is emitted, usually followed by vibrational relaxation.

 - Internal Conversion (IC)

Radiationless transition from one vibrational level to another of a different electronic state but with the same multiplicity (e.g. $S_1 \rightarrow S_0$).

- Intersystem Crossing (ISC)
Radiationless transition from one vibrational level to another of a different electronic state and different multiplicity (*e.g.* $T_1 \rightarrow S_0$).⁵⁵ ISC is a spin-forbidden process and slower than IC, and thus only occurs when small energy gaps in between the singlet and triplet states are present.
- Radiative Deactivation (Luminescence)
 - Fluorescence
Deactivation from the S_1 to S_0 under emission of light. The transmission usually occurs within a radiative lifetime of 10^{-9} s.
 - Phosphorescence
After ISC from S_1 to T_1 , the molecule can undergo radiative deactivation from T_1 to S_0 , emitting light with a radiative lifetime which is longer than the one for fluorescence. Phosphorescence usually has a radiative lifetime of about 10^{-5} s but can be up to several hours because the transition is forbidden by quantum mechanics.⁵⁶
- Photochemical Deactivation
Photochemical processes are not shown in a Jablonski diagram and can range from isomerisations over bond forming processes such as cycloadditions and cyclisations to bond cleaving processes or decompositions (*e.g.* elimination reactions).

Nevertheless, in the presented thesis, most of the photochemical processes are being discussed with a focus on cycloadditions in addition to isomerisation reactions.

In general, the *trans*-isomer of a molecule is the thermodynamically more stable form. However, both *trans* \rightarrow *cis* and *cis* \rightarrow *trans* isomerisations can be achieved via irradiation with light. Therefore, a photochemical isomerisation system can result in an equilibrium of both isomers, named *photostationary state*, when the *trans*- as well as the *cis*-species absorb light in the same spectral region. Photoreactions can sometimes only arise from one of the isomers. However, due to the photostationary state, isomerisation can take place in advance to a photo-reaction making it possible to start with the unreactive isomer as well as isomer mixtures.⁵⁷

2.3.1 Beer-Lambert's Law

When light travels through a material or solution some of the light is absorbed, and thus its intensity decreases. In 1729, Bouguer discovered a concept which is fundamental to quantify the reduction of radiation intensity, however the break-through is attributed to Lambert who mentioned it in his book *Photometria* that was published close to 30 years later. The law was

finalised to its currently known version by Beer⁵⁸ in 1852, and relates a measured experimental absorbance A to the materials wavelength-dependent molar absorptivity coefficient ε_λ as well as the molar concentration c and the path length l (in cm) that the beam travels through the material solution:

$$A = \varepsilon_\lambda * c * l$$

In case the light beam needs to travel through several absorbing substances, their single terms can be co-added, resulting in the following equation:

$$A = (\varepsilon_1 * c_1 * l) + (\varepsilon_2 * c_2 * l) + \dots$$

The absorbance A of a molecule cannot simply be measured, however, it is logarithmically related to the transmission T which is the relation of the light intensity before (I_0) and after (I) it travelled through the absorbing material.

$$T = \frac{I}{I_0}$$

$$\Rightarrow A = -\log(T) = -\log\left(\frac{I}{I_0}\right)$$

As a conclusion, the intensity of light exponentially decreases with both, the concentration of the absorbing substance as well as the thickness of the materials as depicted in **Figure 6**:

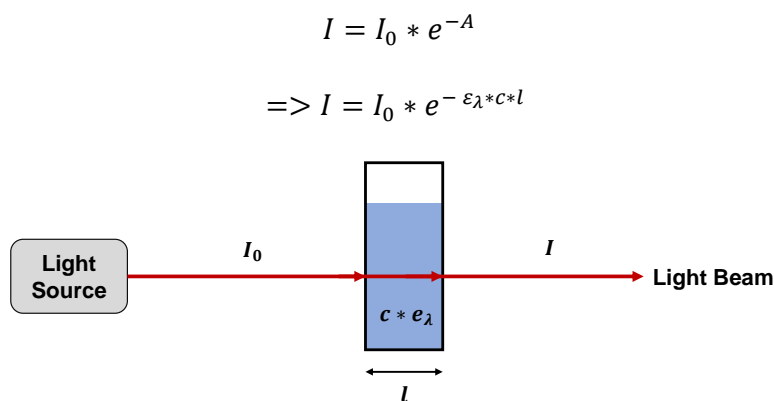


Figure 6. When light of the intensity I_0 passes through a material or solution with the path length l , concentration c , and molar absorption ε_λ , it is absorbed according to the Beer-Lambert law and thus reduced to the intensity I .

The Beer-Lambert law is an important principle for photochemical reaction because it states that often only the outer layers of a solution are irradiated with light due to its exponential decrease in intensity. This is of experimental importance since it limits the thickness an irradi-

ated material can possess. When working in solution, this can be overcome by stirring the solution or using photo flow systems in which under circulation only a small part of the solution is irradiated per time interval.

2.3.2 Franck-Condon Principle

As indicated by the Franck-Condon principle (depicted in **Figure 7**), electronic transitions are most likely to occur between states that possess similar nuclear configurations and vibrational behaviour.^{59,60} Since nuclei are much more massive than electrons, electronic transitions are much faster than nuclear motions. The nuclei can hardly respond in the respective time scale, and thus assumed to be at a fixed nuclear position. As a result, the vibrational level of an electron must be instantaneously compatible with the nuclei after excitation and, hence, the vibrational states of an electron before and after the transition need to overlap as much as possible (**Figure 7**).

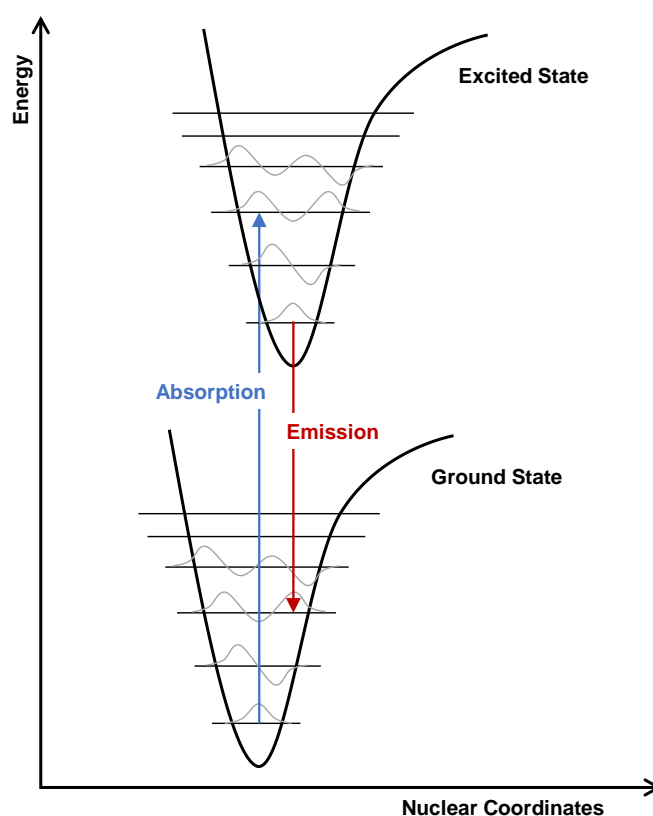


Figure 7. Franck Condon principle: Electronic transitions are more likely to occur in between vibrational states with high overlap.

2.3.3 Cycloadditions

2.3.3.1 Fundamentals

Concerted cycloaddition reactions utilise two or more double bonds, which upon reaction with each other form cyclic transition states through reorganisation of electrons. As a result, two double bonds are broken and reformed into two new σ -bonds, releasing a considerable high amount of energy to allow the formation of strained ring molecules. For example, two alkenes, which do not necessarily need to be of the same kind, can react with each other upon irradiation with light to form a cyclobutane-type structure. Cycloadditions have the advantage of high regio- and stereoselectivity providing a versatile tool in chemistry.^{61,62} Generally, they are characterised based on the number of π -electrons involved in the reaction (*e.g.* [2+2], [2+4], [4+4], etc.) and as depicted in **Figure 8** can be written as a continuous rearrangement of electrons.



Figure 8. Schematic overview of cycloadditions and their nomenclature.

The possibility for a cycloaddition to occur is often correlated either with the degree of strain a reaction introduces into the resulting structure or by entropic restrictions. However, a closer look at the linear combination of atomic orbitals (LCAO) for the two participating molecules can give further insight into which reactions are favourable or not. In particular, if the molecule orbitals are properly aligned and their symmetry matches each other, a reaction is likely to take place. A cycloaddition occurs between the frontier molecular orbitals (FMO) of two molecules: the highest occupied molecular orbital (HOMO) of one starting compound and the lowest unoccupied molecular orbital (LUMO) of the other. These two orbitals can react in two different ways to each other, *i.e.* *suprafacial* or *antarafacial* (**Figure 9**). Woodward and Hoffmann introduced a set of rules based on the number of π -electrons involved in a photocycloaddition that provide an easy overview, which of the thermal photoreactions are allowed (favourable) or forbidden (unfavourable) due to their orbital alignment (**Table 2**).^{62,63}

Table 2. Woodward-Hoffmann rules for thermal cycloadditions⁶³

π -electrons	supra / supra	supra / antara	antara / antara
$4n$	forbidden	allowed	forbidden
$4n+2$	allowed	forbidden	allowed

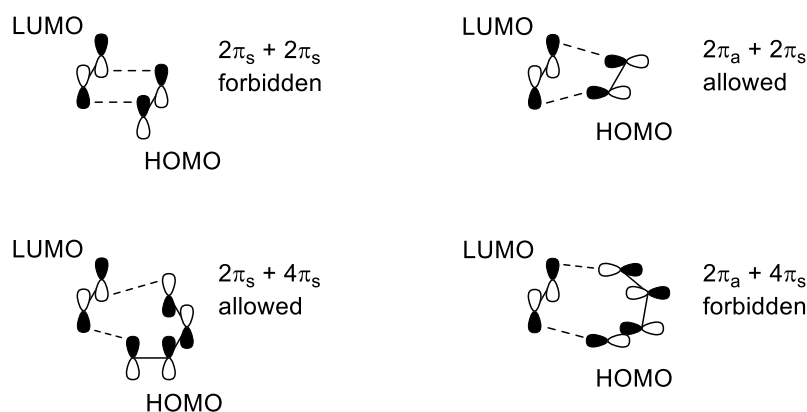


Figure 9. Pathways in which the orbitals of two molecules can partake in a cycloaddition.

According to the Woodward-Hoffman rules, suprafacial [2+2] cycloadditions are thermally forbidden and an antarafacial approach is very unlikely due to a high ring strain. Nonetheless, [2+2] cycloadditions can still occur photochemically since under irradiation with light an electron is excited from the ground state into an excited state, from the HOMO into the LUMO (**Figure 10**). Therefore, the orbital symmetry adjusts in a way that allows the [2+2] cycloaddition. Thus, the Woodward-Hoffmann rules that would apply for photochemical reactions are directly opposite to the thermal rules, allowing reactions that proceed under irradiation with light while they would not occur with heat.⁶⁴

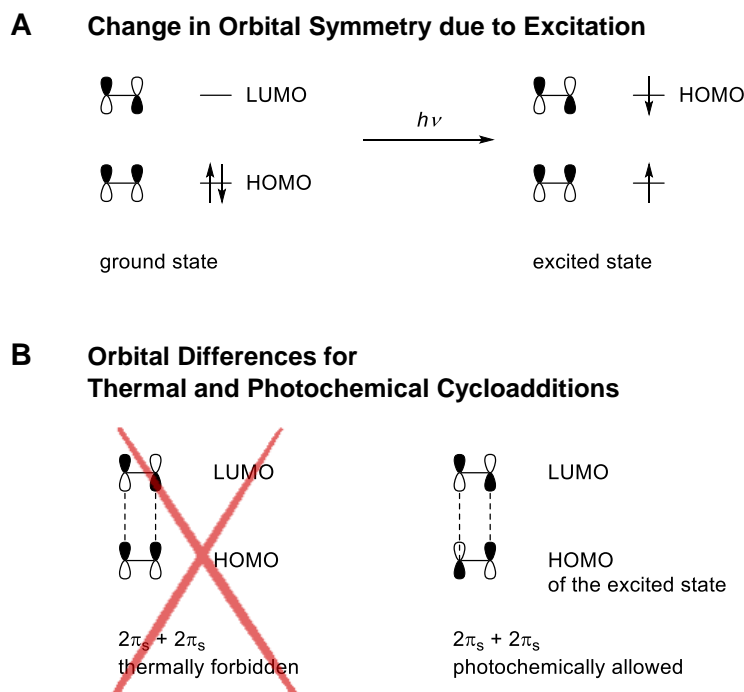


Figure 10. **A** Change in orbital symmetry after irradiation with light. **B** Orbital difference of thermal and photochemical cycloaddition.

2.3.3.2 [2+2] Cycloadditions

Upon irradiation with light, conjugated alkene derivatives can undergo excitation from the ground into the excited singlet state, and after subsequent ISC into the triplet state. As already mentioned in the beginning of Chapter 2.3, several different processes compete during the following deactivation process, including radiative and non-radiative decay, photoisomerisation, yet also photochemical reactions (compare Jablonski diagram, **Figure 5**). In addition to these competing processes, cycloaddition reactions are limited due to their bimolecular nature, particularly since a successful reaction requires that an excited alkene encounters a ground state species to react with. Forming a cyclobutane structure, the parent conjugation of the alkene is being destroyed, therefore introducing a shift in its absorption spectrum towards lower wavelengths. Indeed, the complexity of photochemical systems has been studied in detail for the photodimerisation of coumarin by the groups of Anet,⁶⁵ Hammond,⁶⁶ Schenk⁶⁷ and Morrison.^{68,69} In 1989, Lewis proposed that coumarin could undergo a cycloaddition from both the excited singlet and triplet state depending on the concentration and polarity of the solvent.⁷⁰ However, the latter has been questioned by more recent studies,⁷¹ suggesting that the reaction generally takes place from coumarin's excited triplet state enabling the enhancement of photochemical reactions and their yields through elongation of their singlet state lifetimes, and thus facilitation of ISC to achieve a higher population of the triplet state.^{70,72,73}

Due to their reversibility, cycloadditions are a highly interesting field with vast application opportunities in both synthetic chemistry as well as biology. Especially the ability of cycloaddition reactions to form and break bonds on-demand is advantageous for tailoring photo-responsive materials that can be applied in medicine, materials science, consumer goods, and many more. In addition, the reversibility can be exploited in the field of gradient materials to obtain rewriteable degrees of flexibility, which is the aim of this thesis. Light as a trigger for reactions carries many benefits, especially since it offers the ability to remotely trigger reactions in a spatially controlled manner. Due to their unique features, there was a peak of interest in cycloadditions in the 1960s, after the discovery that the reversibility of the pyrimidine dimerisation plays a key role in DNA damage.^{67,74,75} However, only about 20 years later, the focus of this research field has moved from the cycloaddition mechanism to its possible applications limiting the known photoreactive systems to only a few different reactions. The most prominent and at the same time single well studied [4+4] cycloaddition is the dimerisation of anthracene, while known examples for [2+2] reactions are coumarin, thymine, cinnamic acid, stilbene, and their derivatives (**Figure 11**). All these examples form a cyclic structure upon irradiation that can be reversed to the starting materials when light of a lower wavelength is applied. Although photodimerisations have already been employed in metal complexes,⁷⁶ metal

nanoparticles,⁷⁷ metal-organic frameworks,⁷⁸ and self-assembled structures of small molecules in biological application,⁷⁹ they are still far from being universally applicable or providing ready access to reversible and remotely triggered ligation techniques. In theory, cycloadditions fuse the abilities of forming and cleaving bonds simply by switching the colour of light, but most so far reported systems feature limited yields or need to be conducted in specifically tailored templates. To overcome these drawbacks, researcher were able to utilise triplet sensitizers, complexation molecules or Lewis acids.⁸⁰ However, these approaches complicate photoreactive systems and limit them to the very specific usage they were designed for. In addition, the reverse reaction of most known photo cycloadditions has attracted considerably less attention than its dimerisation counterpart. Often, monochromatic light with a wavelength of $\lambda = 254$ nm was applied without further in-depth investigation of different wavelength ranges that could be utilised.⁸¹ Light in these UV ranges is not only known to introduce photodamage, but the absorption bands of both the cycloaddition and cycloreversion can also overlap, resulting in the previously mentioned photostationary state. Without thorough investigation of both reaction pathways, the influence of the photostationary state can limit the yield of a reaction

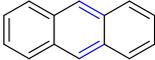
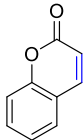
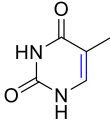
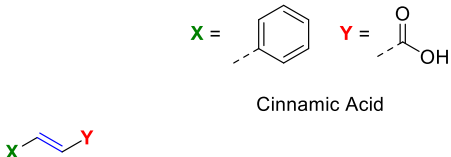
	Dimerisation $\lambda =$	Dissociation $\lambda =$
 Anthracene	> 350 nm	< 300 nm
 Coumarin	> 350 nm	< 260 nm
 Thymine	< 300 nm	< 260 nm
 Cinnamic Acid	> 300 nm	< 260 nm
 Stilbene	> 300 nm	< 260 nm

Figure 11. Overview over the different known reversible cycloadditions including their trigger wavelengths.

and thus its applicability. Investigation of 7-hydroxycoumarin, for example, demonstrated that variable degrees of cycloreversion can be achieved when applying different wavelengths.⁸² A possible limitation to the reversibility of a photo system is how the bonds of the photodimer are broken. This is especially important for systems that possess two orthogonal functional groups and are therefore unsymmetrical (*e.g.* cinnamic acid). If the photoreversion does not lead to the initial starting materials but rather symmetrical products, these might not be able to again undergo a cycloaddition, thus limiting the reversibility the system (refer to **Figure 12**).⁸³

To limit photodamage and ensure higher light penetration depths, the wavelengths applied for cycloadditions can be red-shifted. Unfortunately, a red-shifted absorption spectrum does not necessarily also provide a red-shifted reactivity. To-date, several strategies for bathochromic shifts have been developed and also successfully applied (compare Chapter 2.3.3.3). In 2008, the research group of Fujimoto was able to employ light at a wavelength of $\lambda = 366$ nm to cross-link trans-3-cyanovinylcarbazole with thymine within 1 s and a yield of 97 % (**Figure 13**).⁸⁴ Most importantly, the cycloreversion was red-shifted to $\lambda = 312$ nm, achieving a quantitative reaction in only 60 s. To that date, the trigger wavelength for the cycloreversion as well as the reaction times and yields were unique but could only be achieved in templating DNA, facilitating the reaction. So far, no studies have been published, proving a successful reaction between 3-cyanovinylcarbazole and thymine in solution, without the prearranging effect of DNA. An even further red-shifted example is provided in the work of Claus *et al.* who synthesised an anthracene molecule functionalised with triazole, achieving trigger wavelengths of $\lambda = 410$ nm for the cycloaddition and $\lambda = 360$ nm for the reversion (**Figure 13**).⁸⁵ In a similar range falls the reaction of styrylpyrene, undergoing the forward reaction at $\lambda = 455$ nm, while the backwards reaction was triggered with $\lambda = 340$ nm (**Figure 13**).⁸⁶ Although these three examples have been conducted in templated environments (*e.g.* DNA, surface chemistry), these are promising examples for cycloadditions that take place upon irradiation with visible light and can

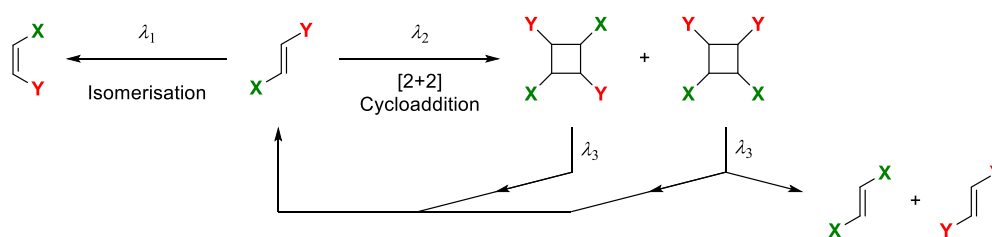


Figure 12. Reaction pathways after irradiation of asymmetric alkenes with light. Depending on the symmetry when the reverse reaction is triggered, the cyclobutane is either transferred back to its asymmetric starting material or symmetric analogues that can limit the reversibility of the reaction. λ_2 is higher than λ_3 , λ_1 can be higher, lower or the same than λ_2 and λ_3 .

serve as preliminary steps towards platform tools for forming and breaking bonds in a reversible fashion for applications in smart and responsive materials such as reprogrammable gradient materials.

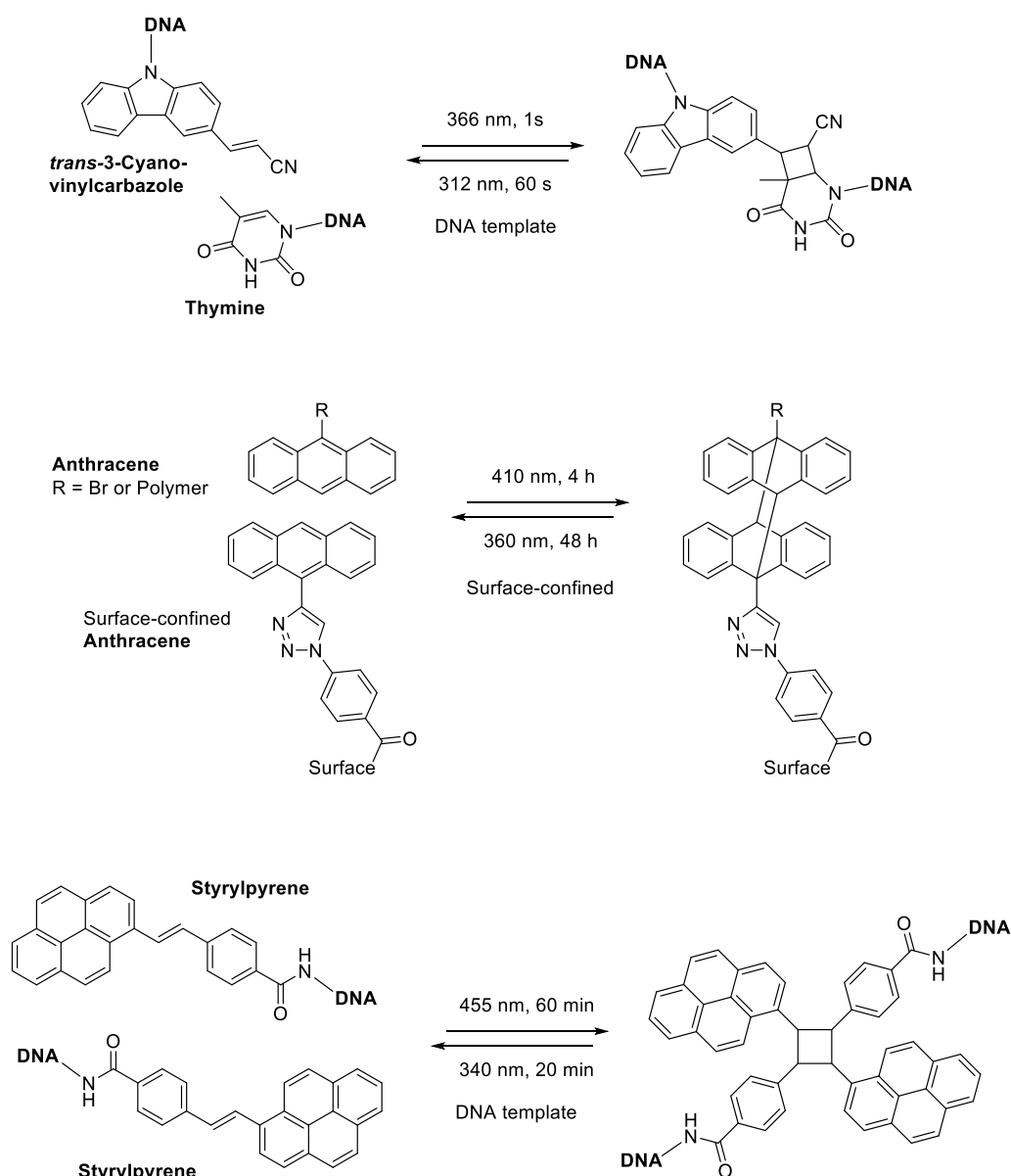


Figure 13. Examples for red-shifted [2+2] cycloadditions: *trans*-3-cyanovinylcarbazole, anthracene and styrylpyrene. All these examples use templating techniques (e.g. DNA, Surface Chemistry).

2.3.3.3 Applications for Photochemical Cycloadditions

In general, photochemical cycloadditions have a wide range of application. Particularly due to their reversibility, they are highly suitable for tailored smart materials for example in medicine, energy defence, computing, health care, information and communication, heavy industry, and consumer goods.^{87–92} Most uniquely, they can be employed in applications, in which high precision is requisite, since they offer high spatial control. The lack of heat, the ability to undergo

reactions in solid state, and the nature of photons have led researchers to consider light-driven reactions as green synthetic chemistry,⁹³ making photo-responsive as well as photo-reversible polymeric system highly attractive. In the sections below, a few examples for the successful application of light-triggered reactions will be discussed.

Light-driven cycloadditions in polymer networks have proven their applicability in photoresists via selective immobilisation of polymers, achieved through photo-cross-linking on various substrates. Generally, photoresists (**Figure 14**) have emerged for semiconductor technology in modern society. For instance, thymine can effectively be employed in polymer chains not only as reversible photoresists,^{94–97} but also in copolymers that Waner *et al.* exploited for water soluble photoresist coatings.^{98,99} By coating various substrates – including flexible plastics – with thymine functionalised copolymers, subsequent irradiation with UV light led to cross-linking and thus immobilisation for environmentally friendly ‘negative working’ photoresists.⁹⁹ In a similar fashion, Joy *et al.* have been investigating coumarin as an alternative compound for photoresists.¹⁰⁰ Incorporating coumarin into polyesters allowed for photo-cross-linking at the wavelength of $\lambda = 350$ nm. Moreover, irradiation at $\lambda = 254$ nm introduced chain de-cross-linking, unfortunately photodamage via chain scission.

In addition to photoresists, cycloadditions can be used to manufacture photoresponsive hydrogels. In detail, hydrogels consist of cross-linked polymer-networks that can absorb and retain large amounts of water. For the up-take of water, hydrophilic groups need to be introduced into the polymer network that can then hydrate in presence of an aqueous phase. As an example, by incorporating anthracene into polymer chains, Chujo *et al.* were able to transform the chains into a polymer network upon irradiation with light above 300 nm.¹⁰¹ Exposed to water, this network swelled up to 20 times the weight of the dry gel, while the degree of swelling was controlled via the irradiation time as well as the amount of photoresponsive anthracene groups per chain. Reversible hydrogels were studied by Yang *et al.* using thymine as the photoreactive moiety.¹⁰² Alternating irradiation with 365 and 240 nm could reversibly switch the hydrogel from solution to gel and back.

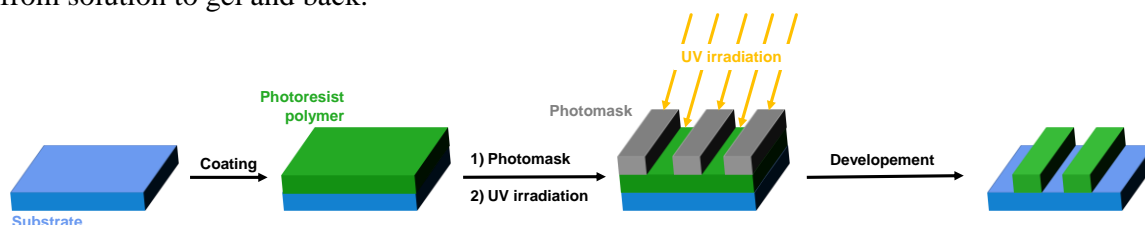


Figure 14. Schematic representation for the preparation of polymeric photoresist via selective photo-cross-linking and thus immobilisation for semiconductor technologies. Reprinted and adapted with permission of Royal Society of Chemistry, from: G. Kaur, P. Johnston, K. Saito, *Polym. Chem.*, 2014, 5, 2171–2186. Copyright 2019, permission conveyed through Copyright Clearance Center, Inc.

When exposing a material to stress, a formation and subsequent propagation of a crack or fracture can be induced. This process involves breaking chemical bonds that would need to be restored or replaced in a self-repairing process.¹⁰³ Thus far, the most exploited techniques for self-healing polymers are thermally reversible Diels-Alder reactions, although the application of heat is spatially not restrained.¹⁰⁴ Light offers the advantage to solely irradiate the damaged part of a material, reducing stress on the other parts. By introducing light-responsive moieties, self-curing can be induced via the formation of new chemical bonds. In fact, the polymer networks formed via dimerisation of photoreactive groups are most likely to break along the dynamic chemical bonds in between the photosensitive molecules, particularly due to the fact that they are weaker than normal covalent bonds. Therefore, the damaged area includes the monomeric form of the photoresponsive groups, facilitating the curing process. The healing process can be dramatically improved when the material is photochemically prepared. Prior to irradiation with light to start the repairing process, the material is locally irradiated with light of a shorter wavelength for further de-cross-linking the material, hence the mobility of the chains is increased yielding in a more efficient healing.¹⁰⁴ As an example, Zhang *et al.* tethered anthracene as a chromophore to polyurethane networks.¹⁰⁵ The material was fractured using either mechanical force or UV irradiation at $\lambda = 254$ nm. Afterwards, the material could be repaired not only by irradiation with 350 nm but also under exposure to sunlight (**Figure 15**).

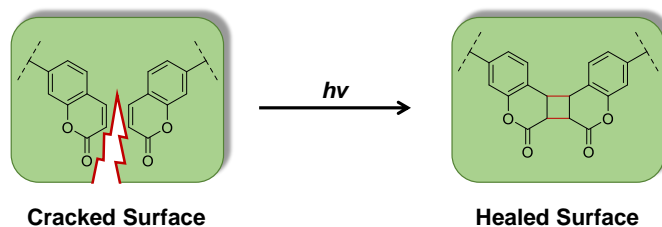


Figure 15. Upon irradiation with light, self-healable material through the usage of coumarin-functionalised polymer chain. Reprinted and adapted with permission of Royal Society of Chemistry, from: G. Kaur, P. Johnston, K. Saito, *Polym. Chem.*, 2014, 5, 2171–2186. Copyright 2019, permission conveyed through Copyright Clearance Center, Inc.

Photochemically reversible reactions can be used as nanocarriers and enable the instant release of a molecule or drug on-demand. Micelles can be formed due to hydrophilic and hydrophobic phase separations forming nanoscopic supramolecular core/shell structures. Photochemistry allows to stabilise these nanostructures and, compared to other methodologies, has the advantage to be non-toxic, economical and by-product as well as catalyst free. By integrating thymine into a block copolymer, Saito *et al.* were able to photochemically stabilise preformed micelles via light-triggered cross-linking.¹⁰⁶ Subsequent testing with two different drugs demonstrated that the rate for their release can be controlled by the degree of thymine dimerisation through light.

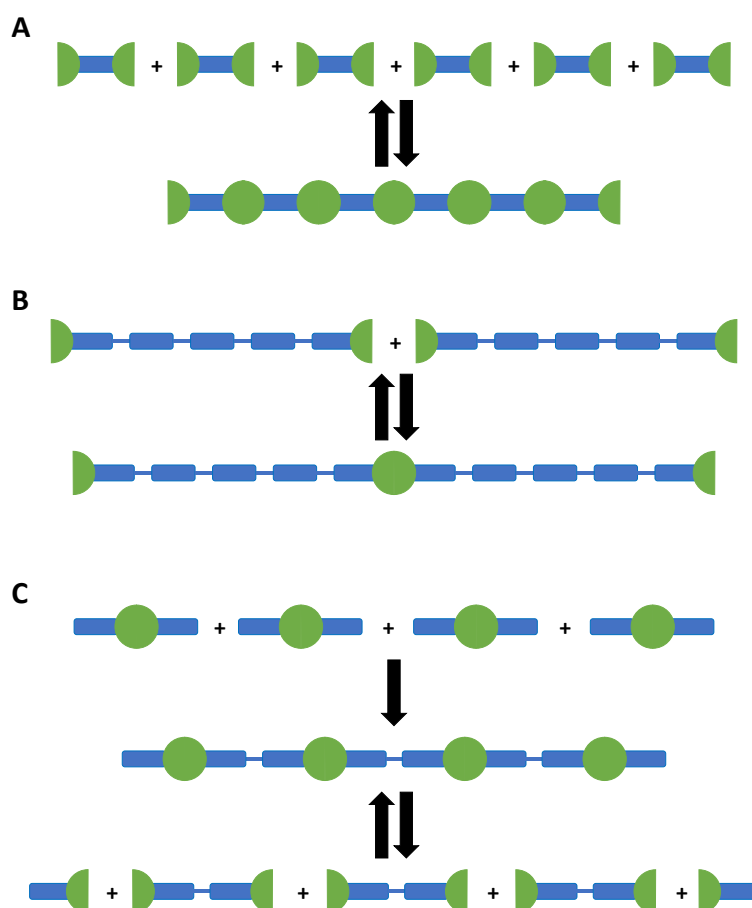


Figure 16. Photo-reversible linear polymers: **A** Photopolymerisation of difunctionalised monomers. **B** Photopolymerisation of difunctionalised macromonomers. **C** Polymerisation of monomer units containing already dimerised chromophores. Reprinted and adapted with permission of Royal Society of Chemistry, from: G. Kaur, P. Johnston, K. Saito, *Polym. Chem.*, 2014, 5, 2171–2186. Copyright 2019, permission conveyed through Copyright Clearance Center, Inc.

Another type of nanocarriers are nanogels that are constructed from cross-linked hydrogel nanoparticles.¹⁰⁷ Due to their internally cross-linked structure, they are highly dispersible in aqueous solutions and have attracted interest as materials that can fill the size gap between polymers and macroscopic hydrogels.^{108,109} The particular size of nanogels is of significance to researchers because it is comparable to viruses or common biomacromolecules such as proteins, while having advantageous properties like swellability, large cavities for encapsulation, or inclusion of various different responsive groups at once. Hence, nanogels are suitable for manifold biomedical applications including drug delivery, diagnostics, antivirals, or embolic therapies.¹¹⁰ Pioneers in the field of photoresponsive nanogels are Ji *et al.*, mainly focusing on coumarin as the chromophore.^{111,112}

A field that has not yet received much attention but could prove highly promising for the development of recyclable or light-degradable materials are linear reversible polymers. Possible synthesis routes in this field are either the polymerisation of difunctionalised monomers,

difunctionalised macromonomers (in detail, polymers with two chromophore end groups) or the synthesis of polymers that contain pre-formed cyclobutane structures in form of reversible dimerised photo-groups (**Figure 16**). However, these approaches proved to be challenging not only in terms of dimerisation yield, but also reversibility and molecular weight.^{113,114}

As shown in the current Chapter, photochemically triggered cycloadditions hold vast opportunities and manifold applications. Incorporation of chromophores into polymers opens interesting pathways to specifically tailored on-demand architectures and materials.

2.3.4 Bathochromic Shifts

Reactions that are stimulated by light most often occur in the wavelength regimes of UV light, which is a major disadvantage towards any application, particularly biomedical ones. The high energy irradiation is resulting in photodamage and many compounds, solvents, or biological systems are unstable when irradiated with short wavelengths.¹¹⁵ Furthermore, short wavelength irradiation is incompatible if high penetration depths into solid matter or solutions are required.¹¹⁶ To overcome drawbacks and limitations of UV light, current research efforts are directed to shifting photoreactive systems to higher wavelengths, so reactions can be triggered with visible light or possibly in the near infrared range. Different strategies exist to obtain systems that can be triggered with low energy light. For instance, catalysts can be added to promote photochemical reaction systems, including the important example of visible light photoredox catalysis, allowing for trigger wavelengths above 500 nm.^{117–120} Additive-free photoreactions are still far from being accessible in these wavelength regimes, nevertheless, catalysts can introduce further complications and limitations into photochemical system, especially if they cannot be removed from the produced material.^{121–123}

One additive-free approach is the utilisation of two photon absorption, which has been made possible by the development of high intensity laser systems. Due to the absorption of two photons and therefore energy portions, wavelengths far into the visible light and early IR regimes are accessible. In addition, experimental setups of two photon lasers allow for high spatial control since the reaction takes place in the laser focus (called *voxel*) only instead of in the complete light beam.^{124–127} However, the requirement of a specialised laser system with high intensities is rather limiting to the usability of two photon processes.

A more broadly applicable strategy is the additive-free process, enabled by a bathochromic shift in its absorption spectrum. Elevating the trigger to a higher wavelength is often referred to as ‘red-shifting’ a photochemical system. Strategies that to-date have been explored for this concept are the expansion of the aromatic system of the photoactive moiety, exchanging carbon

atoms with hetero atoms (*i.e.* oxygen, sulphur or nitrogen) as well as the introduction of further electron-drawing or -pushing substitutes.^{128,129} Most importantly, the absorption spectrum and photoreactivity of a molecule do not need to align, which requires precise evaluation of a photochemical system and its modification to gain information about achieved bathochromic shifts. The discrepancy of absorption and reactivity will be further discussed later in this Chapter as well as Chapter 3 of this thesis.

Extending the conjugated system of a molecule has proven to achieve acceptable results in red-shifting so far. Often, pyrene is utilised since it is a well-studied system featuring an absorption band with $\lambda_{max} = 340$ nm reaching up to a wavelength of 350 nm.¹³⁰ In addition, pyrene has been readily applied in photochemical system, shifting trigger wavelengths into the visible light range above 400 nm. Examples for successful red-shifts are shown in **Figure 17** and include tetrazoles, which are usually triggered at wavelengths from 300 – 320 nm.¹³¹ Via attachment of pyrene, the trigger wavelength is shifted by 100 nm, to 410 – 420 nm, allowing pyrene aryl tetrazole (PAT) to readily react with nucleophiles such as double bonds or carboxylic acids.¹³² Nevertheless, pyrene functionalisation is not the only known strategy to induce a bathochromic shift for tetrazole since functionalisation with oligothiophenes enabled a similar wavelength ($\lambda = 405$ nm).¹³³ Other molecules that could be red-shifted into the visible light range through attachment of pyrene are phenacyl sulfides (shift from $\lambda_{max} = 350$ nm to $\lambda = 410 - 420$ nm),¹³⁴ which can undergo a Norrish Type II rearrangement and subsequent reaction with different enes, and pyrenyl-2*H*-azirines (shift from $\lambda_{max} = 254$ nm to $\lambda = 410 - 420$ nm),¹²⁹ that enable reactions with electron deficient double bonds within minutes.

Another example, in which extension of the conjugated system can induce a red-shift, is anthracene. Usually reversibly undergoing [4+4] cycloadditions in the UV range (dimerisation: $\lambda > 300$ nm, typically 365 nm; dissociation: $\lambda < 300$ nm, typically 254 nm), anthracene can be functionalised with a benzyl triazole moiety yielding a photochemical molecule, that can react upon irradiation with broad emission visible light lamps (400 – 500 nm).¹³⁵

While there are readily available examples of red-shifted reaction system, the full potential of photoreactive systems towards visible light has not yet been exploited. Often chromophores are irradiated with broad band lamps that feature a maximum at the same wavelength that represents the highest absorption of the photocompound. As already discussed above in the current Chapter, the absorption and photoreactivity of a molecule are not necessarily congruent, therefore choosing a higher trigger wavelength (although it features a lower absorption maximum) could already be possible without changing the molecule itself. To assess optimal conditions

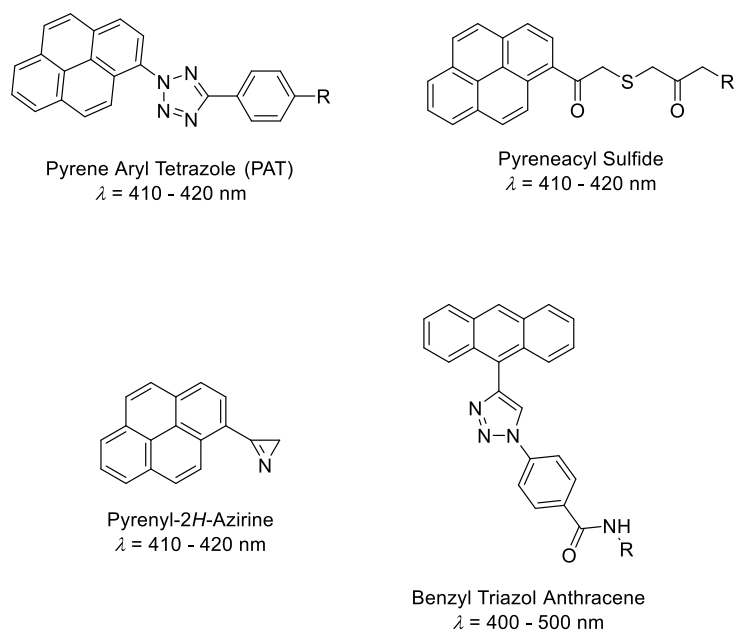


Figure 17. Examples for chromophores that were red-shifted via extension of the conjugated system.

for photo reactions, it is necessary to employ monochromatic light sources and irradiate a sample with the same number of photons at different wavelengths. Analysis of the photochemical yield with regard to the irradiation wavelength results in an action plot, allowing to optimise the efficiency for light triggered reactions in comparison to their UV/Vis spectra. Examples for the analysis of photochemical reactions via action plots are oxime based photoinitiators, *o*-quinodimethanes ('photoenol'), and tetrazoles.^{136,137} Irradiating the oxime based photo initiators with light leads to their fragmentation, allowing for a subsequent radical polymerisation. While the highest absorbance is around 330 nm, the highest conversion was detected at 405 nm, clearly showing the discrepancy of absorption spectra and reaction efficiencies. *o*-Methyl benzaldehydes proved to feature a similar but less pronounced feature, with significant tailing to longer wavelengths, while the amount of conversion for tetrazoles adhered closely to their absorbance with a second additional red-shifted conversion maximum. In conclusion, it is impossible to reliably predict photochemical conversion solely based on UV/Vis spectra, and each light-induced system needs to be closely evaluated with regard to its reactivity.

2.3.5 Wavelength-Orthogonality

In industry, photo-cured materials are already being widely employed in applications like coatings, displays or dentals materials.¹³⁸⁻¹⁴⁰ The advances that have already been achieved in red-shifting photochemical reactions have opened new pathways for the control of multi-responsive materials that had not yet been possible. The opportunity to alter material properties by simply switching the colour of light is highly promising and has fuelled recent research into the matter of wavelength-orthogonality (λ -orthogonality). For a system to be fully λ -orthogonal, a material

needs to incorporate two or more different reactive moieties that each respond to a specific different wavelength. This concept has proven to be very challenging since in the past most chromophores reacted at the same wavelengths in the UV-A regimes and only few orthogonal examples are known in literature to either selectively form¹⁴¹ or cleave¹⁴² specific covalent bonds by choice of the irradiation wavelength. Even though researchers have recently been able to push photochemical systems into the visible light range, it has still proven difficult to achieve complete λ -orthogonality. Due to the fact that most visible light responsive molecules still respond to light in the UV range, only a sequence-dependent reaction procedure can be established. Specifically, the red-shifted photoreaction must be completely triggered first before the next chromophore can react. Commencing the irradiation with the lower wavelength would at least partially trigger both chromophores without featuring orthogonality (**Figure 18**).

A possible approach to sequence independent λ -orthogonality is to further separate the absorption bands of the employed chromophores and thus reduce their spectral overlap (**Figure 18 A**). Aiming on improving photo switches, the group of Read de Alaniz was able to engineer various donor-acceptor Stenhouse products with sufficient separation of their absorption bands, allowing to alter films with regard to their colour through sequence-independent cyclisations.¹⁴³ Following a similar approach, Feringa and co-workers were able to combine a Stenhouse product with azobenzene.¹⁴⁴ The resulting overlap of the absorption bands was sufficiently small to allow for complete sequence independency unless shorter wavelengths were utilised, partially triggering both reactions. A drawback to the approach of Feringa is that covalently linking the two chromophoric moieties led to energy transfer in between them, completely disabling the previously achieved orthogonality.

An alternative strategy to the reduction of spectral overlap is the exploitation of reversible cycloadditions, which have been thoroughly explored in Chapter 2.3.3.2. Through irradiation in lower wavelength regimes, cycloreversion is induced (**Figure 18 C**). Generally, this can be used to split bonds that have been formed under irradiation of longer wavelengths. However, if the cycloaddition has not been triggered before, the molecule remains inactive with short wavelengths, not undergoing any reactions. Fusing this inactivity with another photoreactive group, can allow for a wavelength-orthogonal pathway. Thus, to achieve full λ -orthogonality, an irreversible photoreaction with a rather low trigger wavelength can be combined with a reversible cycloaddition. When irradiating such a mixture with the higher of two excitation wavelengths, only the reversible reaction forms new bonds, while the irreversible molecule does not absorb any light and stays inactive. Under irradiation with the lower wavelength, however, the irreversible reaction is induced exclusively since the reaction of the other system is suppressed

due to its reversibility and triggered cycloreversion. This idea has been an underpinning concept of this thesis and not yet been achieved when this research project began. However, in line with the concept of this thesis, there has recently been a surge in interest in the field of full λ -orthogonality. Based on the results presented in Chapter 3, Frisch *et al.* combined styrylpyrene with anthracene to achieve a wavelength-orthogonal system in which not only the reac-

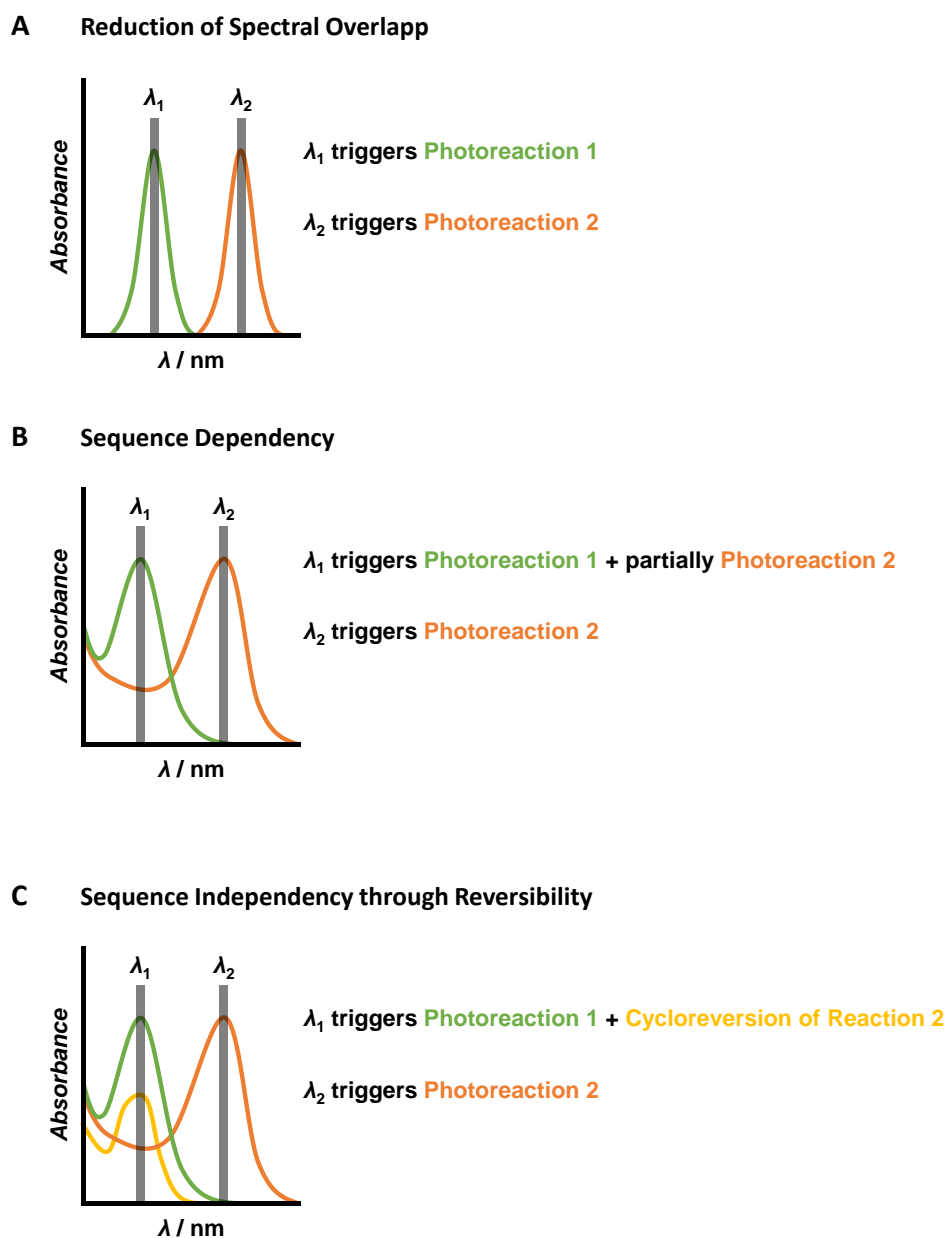


Figure 18. Different pathways and strategies to λ -orthogonality: **A** Minimal spectral overlap allows for independent triggering of two different photoreactive moieties. **B** Due to spectral overlap, the two reactions only feature sequence dependent orthogonality. **C** Reversible photochemical reactions allow for complete orthogonality since the cycloreversion of reaction 2 renders the photochemical group inactive when light of the wavelength λ_1 is used. Reprinted and adapted with permission of John Wiley and Sons, from: H. Frisch, D. E. Marschner, A. S. Goldmann, C. Barner-Kowollik, *Angew. Chem. Int. Ed.*, 2018, 57, 2036–2045. Copyright 2019, permission conveyed through Copyright Clearance Center, Inc.

tions can be triggered independently, but also subsequently without the limitation to one specific sequence.¹⁴⁵ Indeed, when irradiating the system with 455 nm, the dimerisation of styrylpyrene is triggered exclusively. When irradiating with 330 nm, the styrylpyrene is suppressed but anthracene dimerises. In addition, a third wavelength ($\lambda = 410$ nm) was introduced to trigger both cycloadditions. The third wavelength was necessary for a second subsequent ligation step. After dimerisation of styrylpyrene, it is not possible to use 330 nm for the second subsequent step since it would trigger both, the dimerisation of anthracene but also the dissociation of styrylpyrene. Whereas utilising 410 nm instead, the anthracene moiety can be triggered without influencing the styrylpyrene dimers.

Hitherto it has proven impossible to determine photochemical wavelength-dependent reactivities by simply investigating absorption spectra, considering they represent only the ground state of a molecule. Unfortunately, light triggered reactions are much more sophisticated since they involve excited states and it remains unknown how efficiently a reaction is triggered per photon until a photochemical system is specifically analysed in light of these parameters. Therefore, there are indeed a few examples of λ -orthogonal systems that could be triggered independently although they also feature a high spectral overlap. In the field of protection group chemistry, various different dimethylaminocoumarin-based labile moieties were used, which feature significantly different extinction coefficients.¹⁴⁶ In fact, the protection group with the smaller extinction coefficient proved to react much faster. The crucial factor making orthogonal reactions with a spectral overlap possible, is the quantum yield:

$$\text{Quantum yield} = \frac{\text{molecules reacted}}{\text{photons absorbed}}$$

In another attempt, two photon absorption was used to cleave photolabile groups selectively.¹⁴⁷ However, if a certain dose of photons was exceeded both reactions took place simultaneously, losing the selectivity of the system. As a result, it is important to not only examine the absorption spectrum of a compound but also its quantum yield or reactivity at a given wavelength.¹⁴⁸ Therefore, monochromatic light sources are necessary to explore specific single wavelengths and to obtain action plots for the photo reactivity of a molecule (compare Chapter 2.3.4). Such a tuneable laser system was used in this work and is further described in Chapter 2.4.1. Employing this laser, our group was able to screen photoreactions for their efficiency at given wavelengths, providing insights into the conversion of photoreactive groups in dependence of the utilised wavelength and number of photons a sample was irradiated with.¹³⁴ Such assessments showed that absorption spectra indeed do not necessarily correlate with the reaction efficiency at a specific wavelength.¹³⁷ Thus, to achieve perfect photochemical control it is not

only necessary to be able to control spectral overlaps and triggering wavelengths but to thoroughly investigate photochemical system with regard to their action plots.

2.3.6 Photoenol Chemistry

Since [4 + 2] cycloadditions are favourable in the suprafacial mode with respect to their orbitals symmetry and because they result in six-membered rings that do not have the disadvantage of ring strain, they are the most common concerted pericyclic reactions. In 1928, [4 + 2] cycloadditions have been discovered and described in detail by Diels and Alder and are therefore referred to as Diels-Alder reactions.^{62,149}

One particular example for [4+2] cycloadditions is the reaction of photochemically activated *o*-methyl benzaldehydes (*o*-MBA), which was pioneered by Tchir and Porter.¹⁵⁰ The cycloaddition is a photoinduced reaction, although [4+2] cycloadditions with light are forbidden according to Woodward and Hoffmann. However, under excitation with light, *o*-MBA itself is not undergoing the cycloaddition, but rather an enolization product, which can be readily trapped by electron poor dienophiles (refer to **Figure 19**). Due to the light induced enolisation process, the molecule is often referred to as ‘photoenol’ allowing photochemically triggered access to [4+2] cycloadditions, without the need for elevated temperatures.^{150,151}

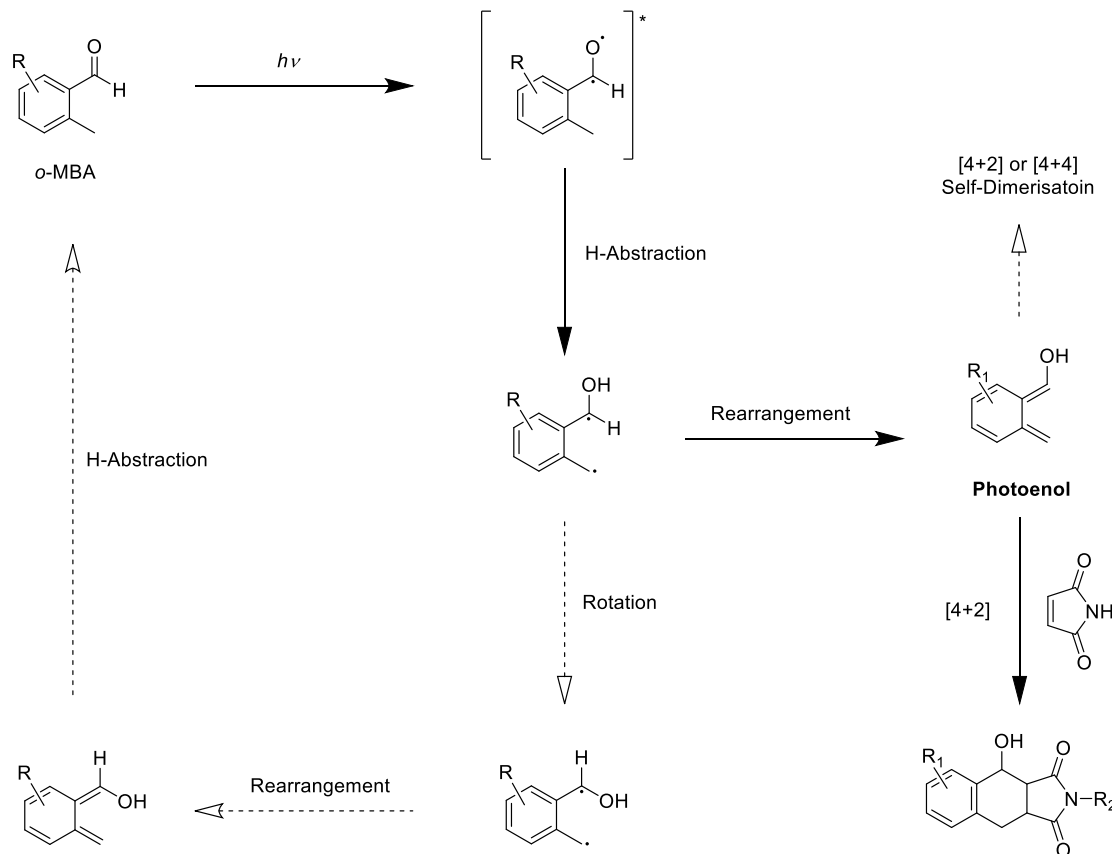


Figure 19. Mechanism of the photoenol cycloaddition.¹⁵¹

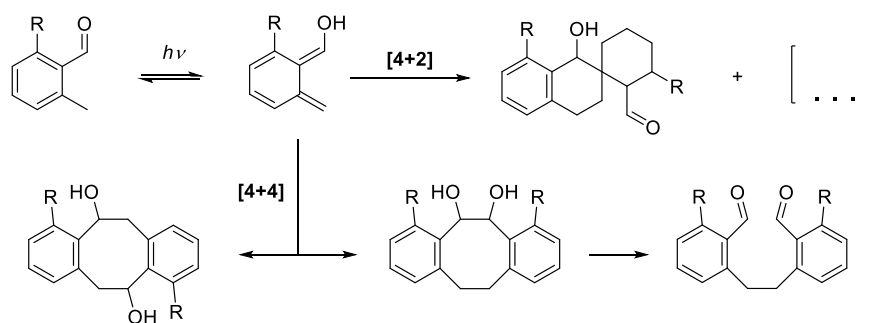


Figure 20. Possible Pathways for the photoenol self-dimerisation. The reaction can proceed either via [4+4] or [4+2] cycloaddition. The former can only yield in two different isomers, either head-to-head or head-to-tail, while the latter can form eight different structure depending on which double bond in the photoenol is taking the reaction part of the dienophile (refer to **Figure 21**).¹⁵³

In detail, under irradiation with light, *o*-MBA is excited and subsequently proceeds in an H-abstraction. The thus obtained intermediate can either undergo a rearrangement or a rotation step. In case the rotation takes place, the molecule quickly reverts back to the initial *o*-MBA molecule. However, when rearrangement takes place, the activated photoenol structure is obtained that can proceed in two different reactions. In the case that two photoenol structures encounter each other, self-dimerisation takes places (refer to **Figure 20**). In presence of dienophiles such as fumarates or maleimides, the more dominant reaction pathway is a Diels-Alder reaction between the two different species (activated photoenol and dienophile). However, the lifetime of the activated structure is highly dependent on the reaction temperature, enabling control over the different reaction pathways. Especially in absence of other dienophiles, the fact that the activated photoenol is more stable at the lower temperature ranges is facilitating the dimerisation reaction. The latter can proceed as both, a [4+2] and a [4+4] cycloaddition leading to a complicated mixture of several photoproducts (for details and structures refer to **Figure 20** and **Figure 21**).^{152,153} Due to the versatility of the photoenol reaction and its trigger wavelength in the UV-C regime, it was chosen for the wavelength-orthogonal approaches in this thesis. Both, the reaction with dienophiles as well as the additive-free self-dimerisation were utilised towards cross-linked networks applicable in gradient materials.

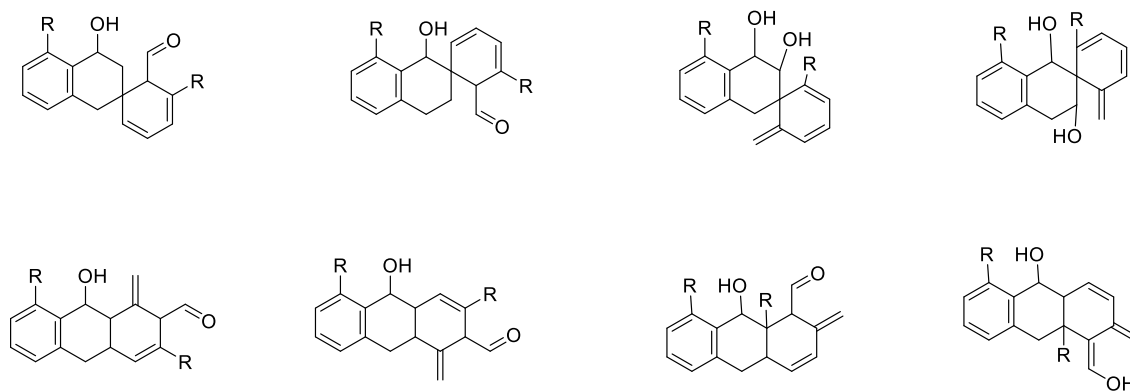


Figure 21. Isomers formed during the light induced [4+2] self-dimerisation of photoenol.¹⁵³

2.4 Laser Systems

The word *LASER* describes both a physical effect as well a device able to generate laser beams and is an acronym for *Light Amplification by Stimulated Emission of Radiation*. The first experimental laser device was demonstrated by Maiman in 1960 and is based on a microwave amplifier – *maser* - that was developed by Townes.^{154,155} The basic concept of stimulated emission was indeed already described by Einstein in 1905, who used it to explain Planck's law. In contrast to common light sources, laser beams are highly directional, monochromatic, coherent and polarised.¹⁵⁶

Stimulated emission can occur for atoms that possess an electron in an excited state. When this atom encounters a photon, the excited state can be stimulated to revert back to the ground state via emission of a photon of the same wavelength. Overall, one photon is introduced into the system and two identical photons are obtained in this process called *gain* in laser physics. Both of these photons can anew trigger stimulated emission. Thus, the more photons are present in a system, the more likely this process, which is the fundamental principle for a laser to work. However, to allow stimulated emission, the population of metastable excited states needs to be higher than the one of the ground states which is usually not the case. Therefore, a *population inversion* is required, e.g. by employing intense flashes of light to achieve excitation into the metastable state in a process called *pumping*.⁵³

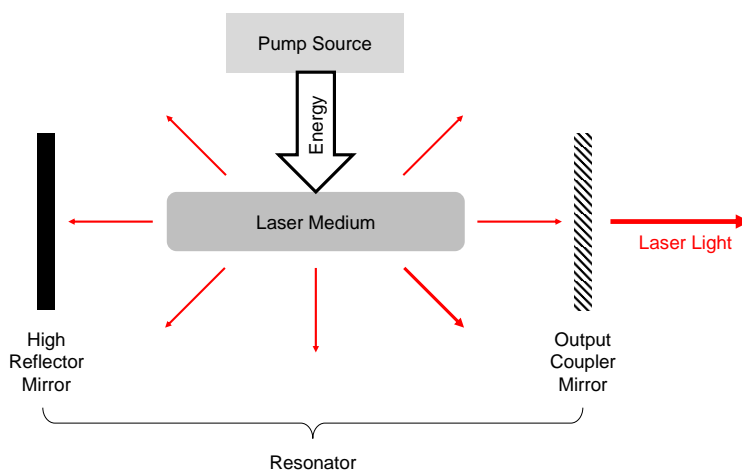


Figure 22. Schematic diagram of a laser device.

A laser utilises the stimulated emission to combine emitted light of several atoms and achieve a planar light wave. Another advantage of lasers over common light sources is that they can produce light pulses that can be very short or feature a high energy output. Generally, a laser is

Unless stated otherwise, Chapter 2.4 is based on books by Atkins,⁵³ and Eichler.¹⁵⁶

built of three main components, *i.e.* pump source, laser medium and optical resonator (**Figure 22**).¹⁵⁶

The pump source can be either optical, electrical or chemical and supplies energy to the laser medium in which the light amplification is occurring. The optical resonator consists out of two parallel mirrors that reflect the photons back and forth through the laser medium, in which the light is amplified each time. One of these mirrors is a high reflector mirror that reflects 100 % of the light, and the other mirror is an output coupler that is transparent to allow a small amount of light – the laser beam – to exit the laser medium.¹⁵⁶

2.4.1 Tuneable Laser Systems

In general, laser devices have a fixed wavelength. However, specific construction of the laser setup allows for tuneable laser systems in which the output wavelength is adjustable. Tuneable systems can be achieved from both, a single laser source or the combination of two sources and they are mostly based on dye lasers or optical parametric oscillators (OPO).^{157,158} The difference is that dye lasers are primary lasers that can be continuously pumped, while OPOs are secondary lasers that require a coherent pump source. To achieve tuneability over a wide range of wavelengths, OPOs base the optical gain on parametric amplification via oscillation pump-pulses in a non-linear crystal utilising three photon processes. In the latter, a pump photon is converted into two photons with different energies: a ‘signal’ photon and an ‘idler’ photon ($E_{\text{signal}} > E_{\text{idler}}$). The conversion depends on phase-matching conditions, while the energy needs to be conserved:

$$E_{\text{pump}} = E_{\text{signal}} + E_{\text{idler}}$$

In the tuneable system employed in the current thesis (**Figure 23**), a Nd:YAG laser was combined with an OPO. As a result, the laser is tuneable from 270 – 670 nm providing a monochromatic light source not only in the visible light but also the UV light range.

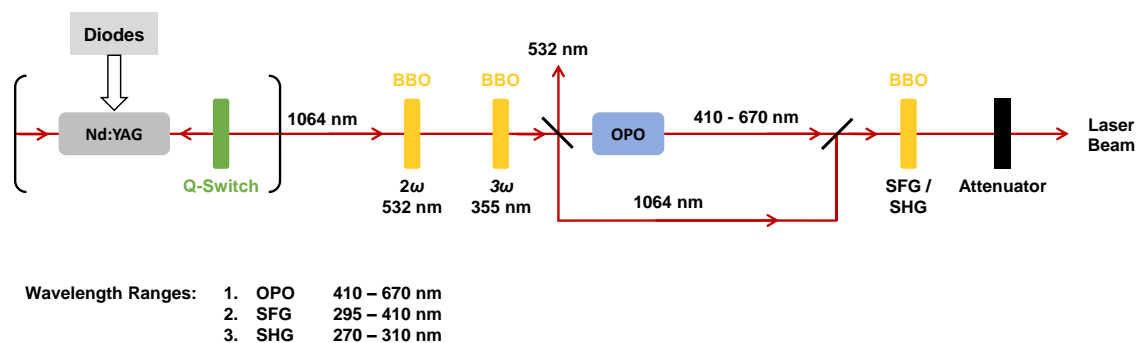


Figure 23. Schematic setup of the employed tuneable laser device.

The laser medium in the employed laser is based on a transparent yttrium aluminium garnet crystal (YAG, $\text{Y}_3\text{Al}_5\text{O}_{12}$) that contains neodymium³⁺ ions (Nd). Coherent pumping of the Nd:YAG laser with diodes produces pulses that are delayed and shortened by a Q-switch enabling an extremely high peak power. The emitted laser beam features a wavelength of 1064 nm at a frequency of 100 Hz and a pulse-length from 5 to 7 ns. To achieve tuneability, the laser beam is frequency doubled (2ω , $\lambda = 532$ nm) and subsequently frequency-tripled (3ω , $\lambda = 355$ nm) using non-linear β -barium-borate (BBO) crystals. Since the OPO is pumped with the 3ω wavelength, the other two wavelengths are reflected and thus blocked out of the laser beam using mirrors. The OPO has an output range from 410 – 670 nm and, due to non-linear processes, cannot be tuned into the UV range. This wavelength regime is obtained via an additional non-linear BBO crystal that allows either frequency-doubling (second harmonic generation, SHG) or -mixing (sum frequency generation, SFG) processes. For the frequency mixing, the previously reflected 1064 nm laser beam is reintroduced into the system. The last part of the laser setup is an attenuator which amplifies the laser beam while also separating the two regions (UV and Vis light) from each other.

3

Styrylpyrene

Photochemistry offers vast opportunities in modern technology. Features such as unprecedented temporal and spatial control have inspired researchers for decades to investigate light induced reactions and their possible applications. From medicine to highly specialised materials, photochemical reactions provide an attractive toolbox that has already shown its utility without having yet reached its full potential. An especially interesting feature of light induced reactions is their control over chemical selectivity via wavelength and intensity. Smart materials in particular can benefit from light induced alterations, due to their precision and even more appealing, reversibility. Using light to create and break bonds on-demand provides access to reprogrammable features by simply choosing disparate colours of light. Material scientists are often inspired by nature with its unprecedented levels of precision and control. An important topic in the field of materials science are gradient materials since they allow to greatly enhance the performance of a material with regard to flexibility, ductility or strength by connecting different material areas to each other via a gradual change instead of fusing two vastly different materials, introducing a breaking point with high materials strain or stress. However, especially in gradient materials, modern technology is still far from the ideals of perfect precision and control mainly due to technical limitations in synthesis and analytics. Most often, sandwich-type structures are employed even though they can still contain undesired breaking points. A more promising approach for stress reduction is the use of lateral gradient materials, especially if they feature reversibility and hence reprogrammability. Understanding the basic principles

The results and graphs in Chapter 3 are reprinted and adapted with permission from:

D. E. Marschner, H. Frisch, J. T. Offenloch, B. T. Tuten, C. R. Becer, A. Walther, A. S. Goldmann, P. Tzvetkova, C. Barner-Kowollik, *Macromolecules*, 2018, **51**, 3802–3807. Copyright 2018 American Chemical Society

underpinning photochemical systems is critical to achieve perfect control and, therefore, a main motivation of the current thesis. Particularly, photochemical cycloadditions hold significant potential to be employed in reversible systems. However, most known photochemical systems are triggered with UV light, which can damage the surrounding material, solvent or even the chromophore itself, making molecules that can react upon visible light highly attractive. One of the few examples for visible light chromophores is styrylpyrene with its reversible photochemical [2+2] cycloaddition, which possesses unique wavelengths to initiate bond forming and cleaving processes but had not been thoroughly investigated in the past. Thus, the present Chapter will provide an in-depth analysis of styrylpyrene and its applicability in polymer and materials science.

3.1 History

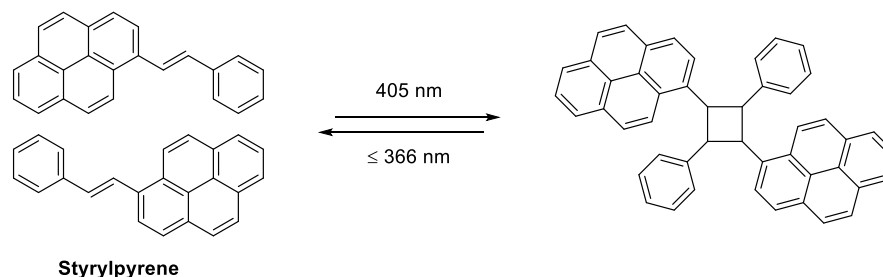


Figure 24. Dimerisation ($\lambda = 405 \text{ nm}$) and dissociation ($\lambda \leq 366 \text{ nm}$) of styrylpyrene as described by Kovalenko *et al.* in 1980.

The [2+2] cycloaddition of styrylpyrene with visible light (**Figure 24**) was first incidentally observed by Kovalenko *et al.* in 1980, who investigated its isomerisation behaviour.^{159,160} Surprisingly, and despite its unique features, the dimerisation reaction was no topic of further research until its rediscovery by Doi *et al.* more than 30 years later.⁸⁶ Via the exchange of one phenyl ring with pyrene, the conjugated system of styrylpyrene is extended and the trigger wavelengths for both, the cycloaddition and cycloreversion significantly red-shifted in comparison to stilbene. In their study, Doi *et al.* incorporated styrylpyrene into DNA strands as cross-linking sites, allowing dimerisation in the presence of visible light at $\lambda = 455 \text{ nm}$ (stilbene: $> 300 \text{ nm}$) and subsequent dissociation upon irradiation with 340 nm (stilbene: $< 260 \text{ nm}$). Especially the cycloreversion wavelength is of interest since it allows to break bonds with UV-A light instead of the common UV-C light at $\lambda = 254 \text{ nm}$, which is employed for most other reversible systems. The red-shift of close to 100 nm enables access to reprogrammable materials without the high amount of damage that is introduced to biological tissue, materials, solvents and chromophores when using short wavelengths. However, currently, such drastic changes in trigger wavelengths have only been possible through templating environments including DNA, while in free solution, these reactions are often suppressed. Most importantly, investigations into the possible isomeric structures produced during the photoreaction, or the most suitable irradiation conditions, have not been conducted. Therefore, fundamental reactivity studies of styrylpyrene are subject of the current Chapter, possibly paving the way to new reprogrammable gradient materials.

3.2 Stereochemistry

Prior to the detailed wavelength-dependent investigations of *trans*-(*p*-hydroxy)styrylpyrene (StyP, **1**), it was necessary to establish which photoproducts are formed during irradiation of **1**. Therefore, a solution of StyP in acetonitrile was irradiated with an LED lamp ($\lambda_{max} = 444$ nm, a complete emission spectrum can be found in **Figure 65**) under inert atmosphere and thoroughly investigated via $^1\text{H-NMR}$ spectroscopy. Careful separation of the photoproducts via preparative thin layer chromatography (TLC) led to five distinguishable species. Further characterisation revealed that only three of these are derived from photoproducts, while one species represents the starting materials *trans*-StyP, and the last belongs to its *cis*-isomer. The *cis*-structure is obtained via photodimerisation that can be triggered over a wide range of wavelengths, however, utilisation of irradiation at $\lambda = 254$ nm only introduces the isomerisation reaction without the formation of the three photo dimers (**Figure 25**). Characterisation of *cis*-**1** via $^1\text{H-NMR}$ reveals distinct new resonances that can be associated with the olefin proton of styrylpyrene ($\delta = 7.20$ ppm).

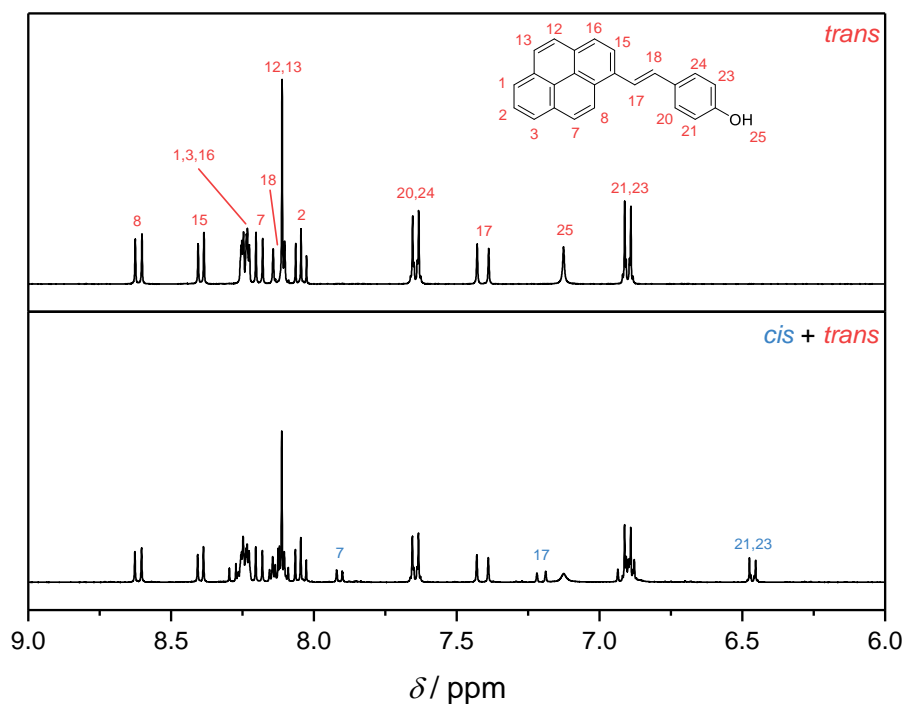


Figure 25. Enlarged $^1\text{H-NMR}$ (400 MHz, CD_3CN) spectra showing the isomerisation of StyP **1** under irradiation with UV-C light ($\lambda_{max} = 254$ nm; solvent: deuterated acetonitrile) showing distinct new resonances for the *cis*-isomer of **1** including one representing a proton of the double bond (resonance 17, 7.20 ppm, $J = 12.1$ Hz). For a complete spectrum refer to Appendix **Figure 94**. Copyright 2018 American Chemical Society.

The NMR analysis for the different photoproducts described in Chapter 3.2 was conducted in cooperation with Dr. P. Tzvetkova from the group of Prof. Dr. B. Luy at the KIT.

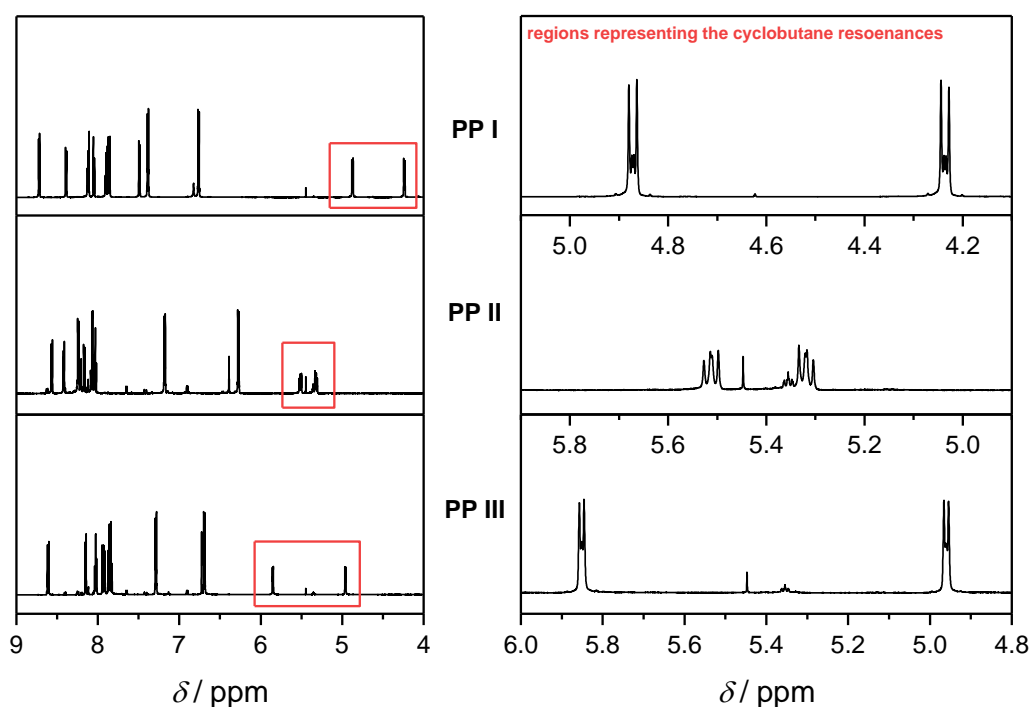


Figure 26. Enlarged $^1\text{H-NMR}$ (600 MHz, CD_3CN) spectra showing the three different and separated photo-products (**PP I - III**) that are obtained under irradiation of **1** ($\lambda_{\text{max}} = 444$ nm, in deuterated acetonitrile), including enlarged spectra showing the distinct peak pattern for the cyclobutane resonances (red boxes). For complete spectra refer to Appendix Section **Styrylpyrene**. Copyright 2018 American Chemical Society.

After the assignment of two photoproduct species to *trans*- and *cis*-StyP, three spectra (**Figure 26**) needed to be further analysed and related to their respective dimer structures. However, from a theoretical standpoint, there are twelve different pathways for the dimerisation of **1** according to which isomer the reaction proceeds from as well as constitutional isomerism. Two of these twelve isomers are stereochemically the same, resulting in eleven possible cyclobutane configurations (**Figure 27**). Thus, for the assignment of the obtained three products, all theoretically possible structures (**2a – 1**, **Table 7** on page 146) were systematically listed and named according to:

1. Stereoisomerism (*trans* / *cis*)
 - a. of the excited molecule that is attacking
 - b. the molecule in the ground state.
2. Constitutional isomerism (head-to-tail (ht) or head-to-head (hh))
3. The position of the functional group of the ground state molecule in relation to the pyrenyl group of the excited molecule after addition (*anti* / *syn*).

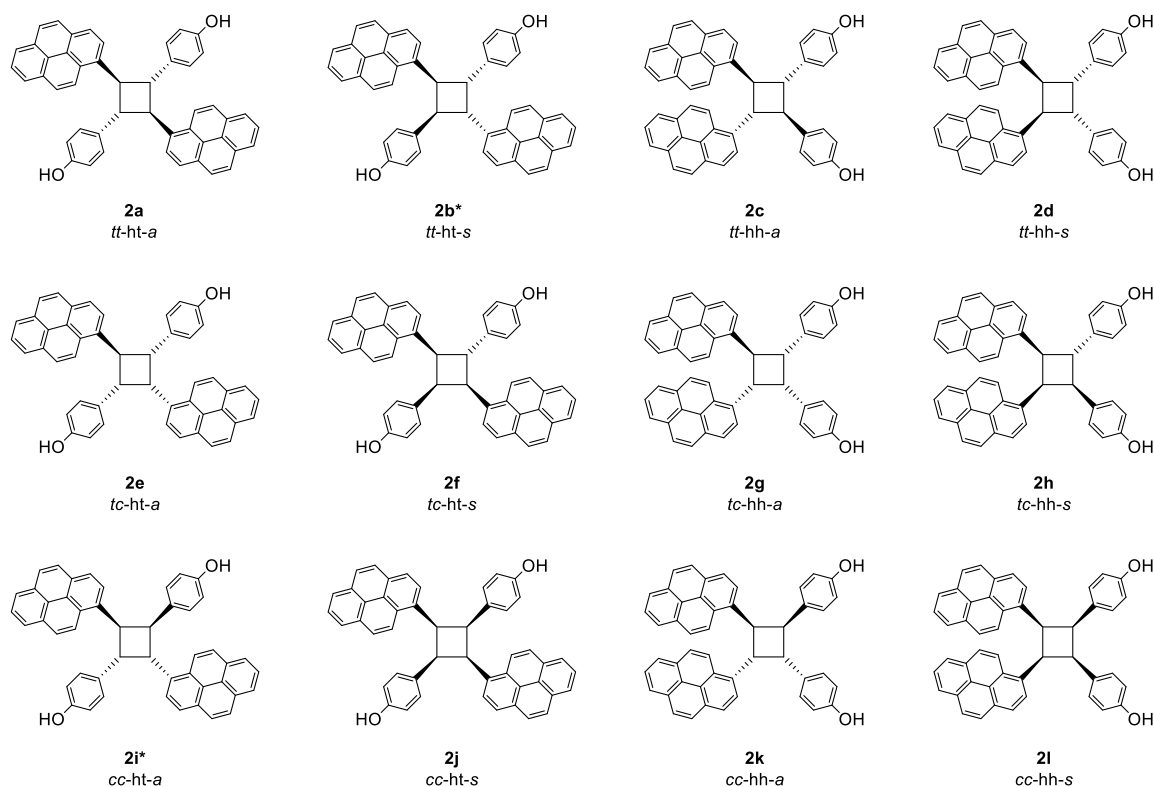


Figure 27. Theoretically possible products obtained via the cycloaddition of styrylpyrene **1** (a more detailed description can be found in **Table 7** on page 146, *stereochemically identical but possible via different dimerisation approaches). Copyright 2018 American Chemical Society.

Close examination of the $^1\text{H-NMR}$ spectra for the three unknown photoproducts (**PP I – III**) reveals two distinct coupling patterns for the cyclobutane ring protons (**Figure 26**). These are derived from different spatial orientations of the proton atoms along the ring and the influence of the phenyl and the pyrene substituents on them. The distinct coupling patterns are either an unresolved second order multiplet structure (**PP I** and **PP III**) or a doublet of doublets (dd, $J = 10.2$ Hz and 7.5 Hz, **PP II**). Due to the similarity of the eleven different photo dimers, all of the model structures needed to be evaluated including an energy optimisation step (molecular mechanics force field MMFF94⁶ from the software package Avogadro). The following structures feature the lowest energies and are most likely to occur (a complete lists can be found in **Table 7**):

1. *tt-ht-a* **2a** (692.69 kJ mol⁻¹)
2. *tt-hh-s* **2d** ($+2.5$ kJ mol⁻¹ difference)
3. *tt-hh-a* **2c** ($+19.6$ kJ mol⁻¹)
4. *tc-ht-s* **2f** ($+26.3$ kJ mol⁻¹)
5. *tc-hh-s* **2h** ($+49.2$ kJ mol⁻¹)
6. *tt-ht-s* **2b** ($+55.5$ kJ mol⁻¹)

Due to their symmetry, the cycloadducts can be categorised into four main groups: First, two fully symmetric photoproducts with alternating top and down orientation of the cyclobutane protons (*tt*-*ht*-*a* **2a** and *tt*-*hh*-*a* **2c**), which are both among the lowest energy products. In addition, such an alternating pattern causes a doublet peak pattern as observed in **PP II**. Next, products obtained via *cis*-*cis* dimerisation with all protons being above the cyclobutane ring (*cc*-*ht*-*s* **2j** and *cc*-*hh*-*s* **2l**). However, structures **2j** and **2l** do not fit any of the observed peak patterns and are energetically unfavoured. In addition, structures that are characterised by three protons pointing to one plane of the ring (*tc*-*ht*-*a* **2e**, *tc*-*ht*-*s* **2f**, *tc*-*hh*-*a* **2g**, and *tc*-*hh*-*s* **2h**), which, however, also do not fit the recorded peak patterns although their energies are more favourable. Last, two neighbouring protons – one next to a pyrene group, the other to a phenyl group – both pointing into the same direction (*tt*-*ht*-*s* **2b***, *tt*-*hh*-*s* **2d**, *cc*-*ht*-*a* **2i***, and *cc*-*hh*-*a* **2k**; ***2b** and **2i** are stereochemically identical). Such a constellation, in which a phenyl neighbored proton has two pyrene protons on both sides but facing to different orientations (*syn* and *anti*), leads to multiplet patterns that inherit strong second order artefacts due to coupling constants that have high values yet different orientations, observable for **PP I** and **PP II**.

As a result, symmetrical considerations narrow the possible dimerisation products to two possibilities (**2a** and **2c**) for **PP II** in addition to three remaining structures (**2b**, **2d**, and **2k**) for **PP I** and **PP III**. Further differentiation can only be derived via in-depth analysis of ¹H- and ¹³C-NMR spectra, detailed resonance assignments as well as elaborate evaluation of proton proximities via the nuclear Overhauser effect (NOE). Important are the presence of shielding and deshielding effects on the chemical shift values for ¹H and ¹³C measurements of the photoproducts when compared to the starting materials *trans*-styrylpyrene (refer to Appendix Section **Styrylpyrene**). Due to influences of the ring currents of the phenyl and pyrenyl group, the chemical shifts in the ¹³C spectra vary in the range from + 6.76 to – 6.87 ppm. The deshielding and shielding effects of the pyrenyl and phenyl carbon chemical shift values in combination with their 3D arrangement in geometry optimised structures allows for the final product assignments. The presence of a NOE in between H-15 and H-18 (refer to Appendix Section **Styrylpyrene**) can only occur for the structure *tt*-*ht*-*a* **2a**, which can therefore be assigned to **PP II**. Although the structures for **PP I** and **III** (**2b**, **2d**, and **2k**) feature different constellations for the bulky pyrene substituents, ¹³C chemical shifts and peak pattern are virtually the same, not allowing an unambiguous assignment. However, investigation of the proton proximities that can be observed via NOE signals provide the missing details resulting in the final correlation: the observed NOE signals (H-18 and H-15, H-8 and H-15, H-8 and H-20/H-24, refer to Appendix Section **Styrylpyrene**) cannot derive from *cc*-*hh*-*a* **2k**. As a result, two structures remain (**2b**, **2d**) that are characterised by different arrangement of the pyrene rings to each other. If the latter

are substituent to neighbouring carbon atoms, NOE in between H-8 and H-18 cannot be present, while H-8 and H-15 occurs (refer to Appendix Section **Styrylpyrene**). Thus, **PP I** can readily be assigned to *tt*-*hh*-*s* **2d** and consequently **PP II** to *tt*-*ht*-*s* **2b**. In addition, final in-depth comparison with the calculated energy models and all observed NOE proximities verify the assignments. Most interestingly, all resulting structures favour *trans-trans* cycloadditions, aligned with findings by Fujimoto *et al.* for the photochemical reaction in between 3-cyanovinylcarbazol and thymine, noting that cycloadditions occur from *trans*-isomers, while their *cis*-counterparts remains inactive.⁵⁷

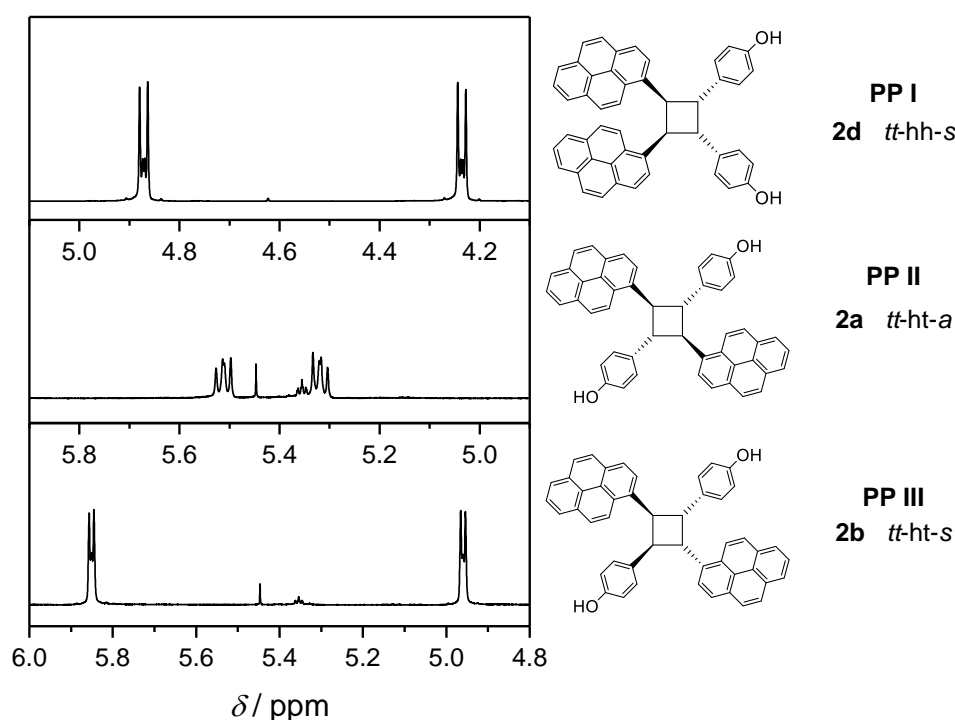


Figure 28. Enlarged ¹H-NMR spectrum (600 MHz, CD₃CN) of the cyclobutane resonances for the photo-products **PP I**, **PP II**, and **PP III** as well as their assigned structures. Copyright 2018 American Chemical Society.

3.3 Wavelength-dependent Photon Efficiency

Analysis

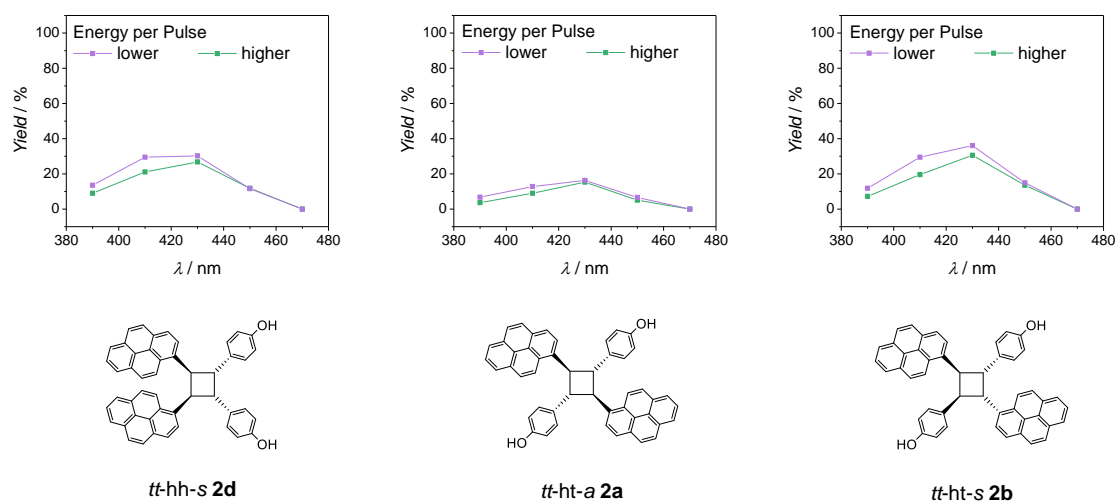
After having successfully determined which photoproducts are generated during irradiation of styrylpyrene **1**, comprehensive analyses of the photochemical reaction in relation to wavelength and efficiency were conducted. Quantitative investigations for both the cycloaddition and cycloreversion as well as the overlap of both reaction channels are necessary to utilise the light induced reaction for further applications. Obtaining detailed information about the most suitable wavelengths for photochemical reactions requires monochromatic light sources such as a tuneable laser system (refer to Chapters 2.4.1 and 8.2.4). As a result, action plots of detailed wavelength screenings can be acquired as has been pioneered in our group for irreversible reaction systems (*i.e.* tetrazole and *o*-methyl benzaldehydes,¹³⁶ pyreneacyl sulfides,¹³⁴ or photoinitiators¹³⁷). In the current thesis, the wavelength screenings were further developed into a novel concept named *Wavelength-dependent Photon Efficiency Analysis* (WPEA) in which the photoreactivity of styrylpyrene in solution was mapped to identify its optimal reaction conditions. Most importantly, WPEA does not only include a detailed *wavelength screening* action plot but is combined with *photon kinetics*, analysing the number of photons necessary to obtain maximum conversion.

In specific, for the *wavelength screening*, styrylpyrene is irradiated at different wavelengths, however, with a constant photon count. The reaction conversion of each photoexperiment, determined via ¹H-NMR analysis, is plotted in an action plot in relation to the reaction wavelength, resulting in a graph that clearly depicts the most effective wavelength for irradiation and allows for comparison with the absorption spectrum of the chromophore. The ideal reaction wavelength is subsequently used to obtain *photon kinetics*, irradiating samples with varying numbers of photons. By plotting the reaction conversion vs. the number of photons, an action plot is obtained, indicating the number of photons necessary to obtain the highest possible conversion. Combining wavelength screening and photon kinetics in our novel analysis concept WPEA allows to determine the ideal parameters for a photo reaction that can subsequently be employed in polymer chemistry or materials science.

In addition to the wavelength screening, the reaction of **1** was investigated for its reactivity with and without the presence of oxygen as well as effects from the laser settings on the samples. The present thesis utilised a tuneable laser setup, operating in a pulsed mode with adjustable intensities in order to calculate how many photons reach the samples at a specific wavelength

per laser pulse (refer to Chapter 8.2.4). As a result, every single irradiation experiment can be designed in multiple ways with regard to the ratio of intensity and number of pulses shot at a sample. Yet, the overall number of photons deposited into the sample remains identical. Hence, when increasing the number of pulses, the energy per pulse needs to be decreased to keep the number of photons constant. To rule out that the energy per pulse has an impact on the reactivity of styrylpyrene, a set of different experiments was conducted featuring different pulse energies but the same number of photons. The dimerisation conversions were plotted, compared to each other (**Figure 29 A**) and are within experimental error identical. Therefore, the energy per pulse can be neglected. Kovalenko *et al.* stated in their study that the dimerisation of StyP can be conducted under both, inert as well as atmospheric conditions.¹⁵⁹ Consequently, in two sets of experiments, styrylpyrene samples were irradiated with identical parameters and conditions but one sample under argon atmosphere and the other in presence of oxygen (**Figure 29 B**). The results showed that it is indeed possible to dimerise styrylpyrene under atmospheric conditions.

A Energy per Pulse



B Influence of Oxygen

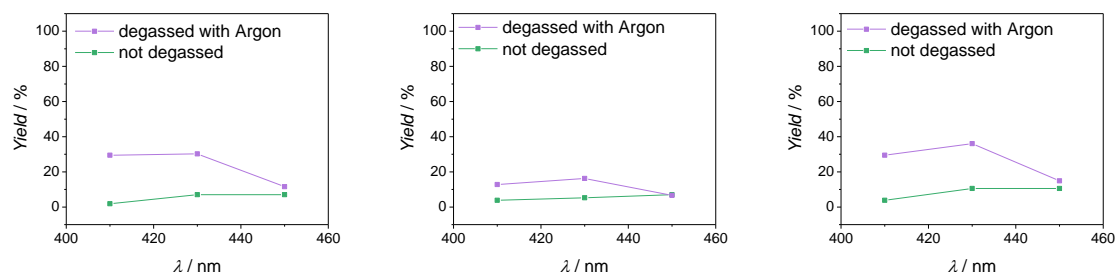


Figure 29. Investigation of the dimerisation of styrylpyrene **1** (10 mM, deuterated acetonitrile, 242 μmol photons) in relation to **A** the energy per pulse (purple: 120 000 pulses, green: 360 000 pulses) and **B** the impact of oxygen in the reaction mixture (purple: argon, green: oxygen) as determined via $^1\text{H-NMR}$ analysis. Copyright 2018 American Chemical Society.

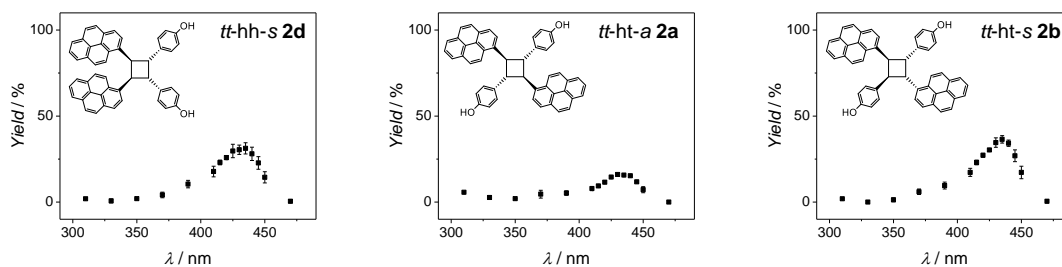


Figure 30. Wavelength screening for the conversion of **1** (10 mM, deuterated acetonitrile) into the three different photoproducts (**2a**, **2b**, **2d**) upon irradiation with 242 μmol as determined via $^1\text{H-NMR}$ analysis. Copyright 2018 American Chemical Society.

However, the reaction proceeds considerably slower when oxygen is present in the reaction mixture during irradiation.

Having investigated its stereochemistry and surrounding parameters (*i.e.* pulse energy and atmosphere), **1** was irradiated in deuterated acetonitrile (concentration = 10 mM) at a constant number of photons (242 μmol) with a monochromatic laser at wavelengths from 310 - 470 nm. Each sample was subsequently analysed via NMR to quantify the amount of the five assigned species that are present after irradiation. Next, the yield of each photoproduct (**2a**, **2b** and **2d**) was plotted against the respective irradiation wavelength (**Figure 30**). The thereby obtained three action plots feature traces of similar shapes, however, the amount of **2a** was half of **2b** and **2d** for each measured data point. Nevertheless, the similar overall reaction behaviour could be due to the fact that all photochemical products are formed from the same *trans*-styrylpyrene **1**, while the differences in amount might be associated with sterical considerations.

For further insights, and to obtain the final action plot, the individual graphs were combined into one trace depicting the overall reaction yield by irradiation wavelength. As shown in **Figure 31 A** (squares), the most suitable wavelength to induce the dimerisation of StyP **1** is at $\lambda = 435$ nm, for which the highest yield (83 %) at 242 μmol photons is achieved. Comparing the wavelength screening with the UV/Vis spectrum of styrylpyrene confirmed that both traces are not necessarily congruent to each other. Thus, assuming the photoreactivity of a molecule is near impossible (refer to Chapter 2.3.4). Indeed, the highest reactivity for **1** has been observed at a red-shift of close to 60 nm when compared to the point of highest absorbance at $\lambda_{\text{max}} = 375$ nm. In addition, the absorbance of styrylpyrene at its most effective trigger wavelength is rather low ($\epsilon = 388$ L mol $^{-1}$ cm $^{-1}$). Likely explanations for this wavelength shift are on the one hand, the penetration depth of photons, which can travel a longer pathways at lower extinctions, hence exciting more molecules (Chapter 2.3.1 Beer-Lambert's Law) and on the other hand – as the UV/Vis spectra only represent molecules in their ground state – the maximum absorption does not necessarily represent the most effective transitions. Another reason

for the red-shifted reactivity may be due to the reversible nature of StyP. Both excitation ranges for the cycloaddition and cycloreversion are likely to overlap to some extent, and hence the reactions compete, eventually leading to photostationary states. Since the reverse photochemical reaction proceeds at shorter wavelengths, the overlap should decrease towards longer wavelengths, allowing the dimerisation reaction to proceed more efficiently. However, independently of the fact if the discrepancy in between absorption and reactivity is caused by a combination of the above mentioned reasons (*i.e.* penetration depth, nature of absorbance spectra, competing reactions) or just one, the result is that the most suitable conditions of a photochemical reaction are impossible to predict without an elaborate analysis as conducted herein.

After the successful wavelength screening for styrylpyrene **1**, the maximum conversion needed to be determined. Therefore, photon kinetics via irradiation of StyP at the same conditions as the previous set of samples (solvent: deuterated acetonitrile, concentration: 10 mM) yet with the fixed wavelength of $\lambda = 435$ nm at varying numbers of photons were conducted. The photon kinetics were carried out with close to 2000 μmol photons to determine from which point on the reaction reaches a plateau or complete conversion (**Figure 31 B**). As a result, the dimerisation of **1** can proceed to a yield of around 95 % (for **2a**, **2b**, and **2d** combined), while the remaining 5 % consist of a mixture of the *cis*- and *trans*-isomer of StyP **1**.

With the dimerisation reaction fully examined, the dissociation reaction was investigated following the same analytical concept. First, the samples were irradiated with 483 μmol of photons at a wavelength of 435 nm to achieve maximum dimerisation and subsequently submitted to photochemical dissociation experiments, either a wavelength screening or the subsequent photon kinetics (**Figure 32**). The former was performed at the same conditions as previously

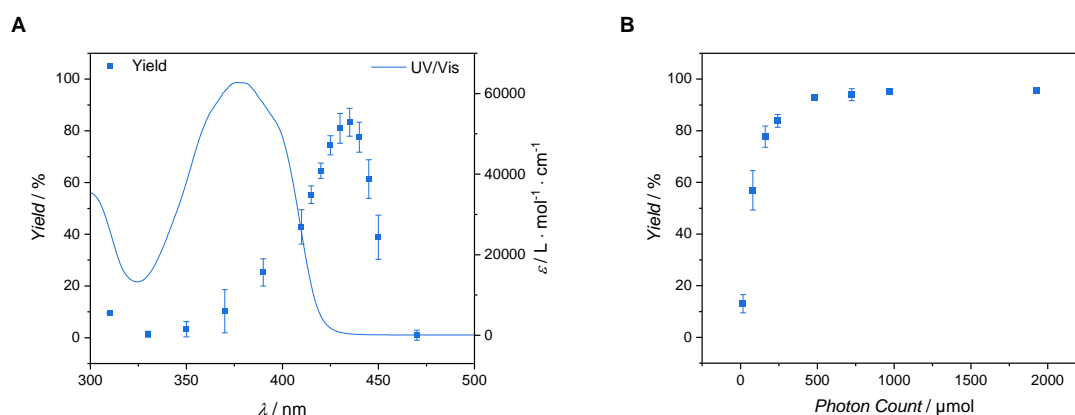


Figure 31. WPEA for the photochemical reaction of styrylpyrene **1** (1 mM, deuterated acetonitrile) consisting of (A) the wavelength screening of the dimerisation yield (squares) at a constant number of photons (242 μmol) in comparison with the absorbance of **1** (solid line) and (B) photon kinetics at the most efficient wavelength of $\lambda = 435$ nm. Yields are resulting from $^1\text{H-NMR}$ analysis subsequent to irradiation. Copyright 2018 American Chemical Society.

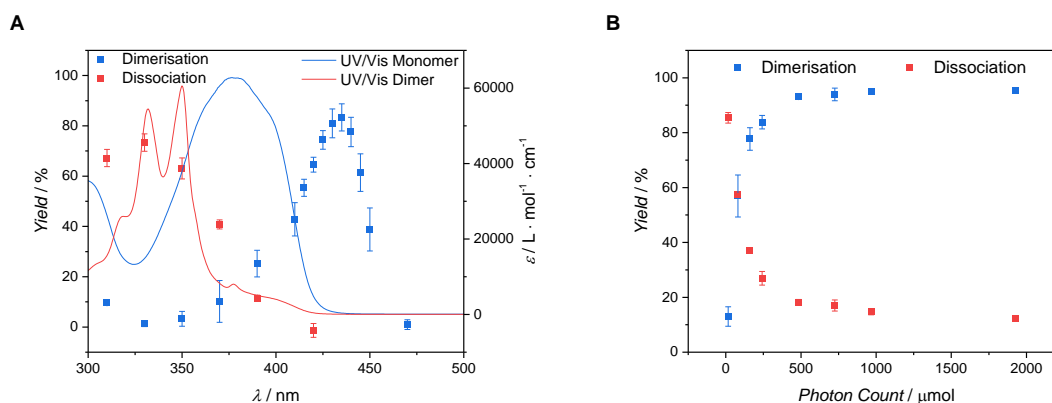


Figure 32. WPEA for the dimerisation (blue) and dissociation (red) of styrylpyrene **1** (1 mM, deuterated acetonitrile) consisting of (A) the wavelength screening of the dimerisation/dissociation yield (squares) at a constant number of photons (242 μmol) in comparison with the absorbance of **1** (blue solid line) and the photoproduct mixture (red solid line), and (B) photon kinetics at the most efficient wavelengths of $\lambda = 435 \text{ nm}$ (blue squares) and $\lambda = 330 \text{ nm}$ (red squares). Yields are resulting from $^1\text{H-NMR}$ analysis subsequent to irradiation. Copyright 2018 American Chemical Society.

for the dimerisation with regard to solvent, concentration and number of photons (242 μmol), yet at wavelengths below $\lambda = 435 \text{ nm}$ (420 – 310 nm). Intriguingly, the dissociation reaction does not compete with the dimerisation at wavelengths above 400 nm, which – as mentioned above – can be one of the reasons why the cycloaddition is most effective at $\lambda = 435 \text{ nm}$. The cycloreversion is triggered starting from around 390 nm with 11 % conversion to the monomeric forms while it proceeds most efficient at $\lambda = 330 \text{ nm}$ (**Figure 32 A**). Comparing the dimerisation and dissociation reactions, it is notable that both reactions have their maximum conversion at a wavelength which does not trigger the opposite reaction, providing excellent wavelength orthogonality between both processes. At the time these results were published, the conditions for the styrylpyrene system were the mildest in literature, providing excellent opportunities to reversibly alter material properties.

Having established the most efficient cycloreversion wavelength, photon kinetics were carried out to investigate the extent of the reversibility of styrylpyrene. As shown in **Figure 32 B**, the dissociation reaction (of **2a**, **2b** and **2d**) seems to possess approximately the same speed as the dimerisation reaction, leading to a photostationary state with a maximum dissociation yield of 85 % under irradiation with close to 500 μmol of photons.

In conclusion, styrylpyrene was thoroughly examined as a model molecule applying the novel analysis concept WPEA to determine its most suitable reaction conditions. While the dimerisation reaction proceeds most efficiently at $\lambda = 435 \text{ nm}$ with around 500 μmol of photons, the dissociation reaction should be triggered at a wavelength of 330 nm using approximately the same number of photons. Furthermore, inert conditions are the most suitable for the reaction of

styrylpyrene **1**, whereas the reaction can also proceed under atmospheric conditions, albeit at a slower rate.

3.4 Application and Outlook

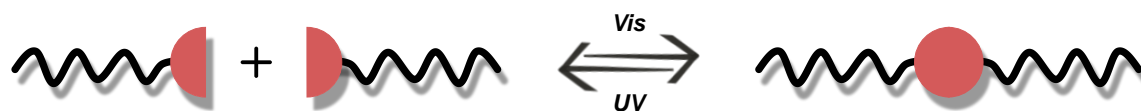


Figure 33. Concept of block-copolymer formation via reversible photochemical ligation.

Having successfully conducted the WPEA for styrylpyrene as a model molecule in solution, the optimal reaction conditions were applied to a photochemical and reversible polymer ligation system (**Figure 33**). For first polymer-based tests, a polymer with styrylpyrene as an end group was chosen in order to allow for in-depth analysis in a well-defined system. In detail, PEG-amine was coupled with StyP **1** in an amidation reaction to yield **3** and subsequently irradiated with visible and UV light in an alternating fashion to reversibly achieve a covalent block-copolymer ligation (**Figure 34**). The irradiation parameters were based on the previously determined conditions, *i.e.* irradiation at $\lambda = 435$ nm (visible) or $\lambda = 330$ nm (UV) with $483 \mu\text{mol}$ of photons (polymer concentration: 10 mM). The results of the polymer ligation were in excellent agreement with the previously studied model molecule and limited by a photostationary state with a minimal amount (ca. 6 %) of non-ligated polymer **3** remaining. In addition, small traces of non-ligated PEG-amine could have been present as it has been reported in literature for other polymer studies.¹⁶¹ In addition, similar to **1** in solution, the dissociation of the thus formed block-copolymer could not be reverted back completely. Overall, three consecutive cycles of subsequent dimerisation and dissociation were conducted and only small amounts of photodamage could be detected, possibly because of asymmetric cleavage, unreactive amounts

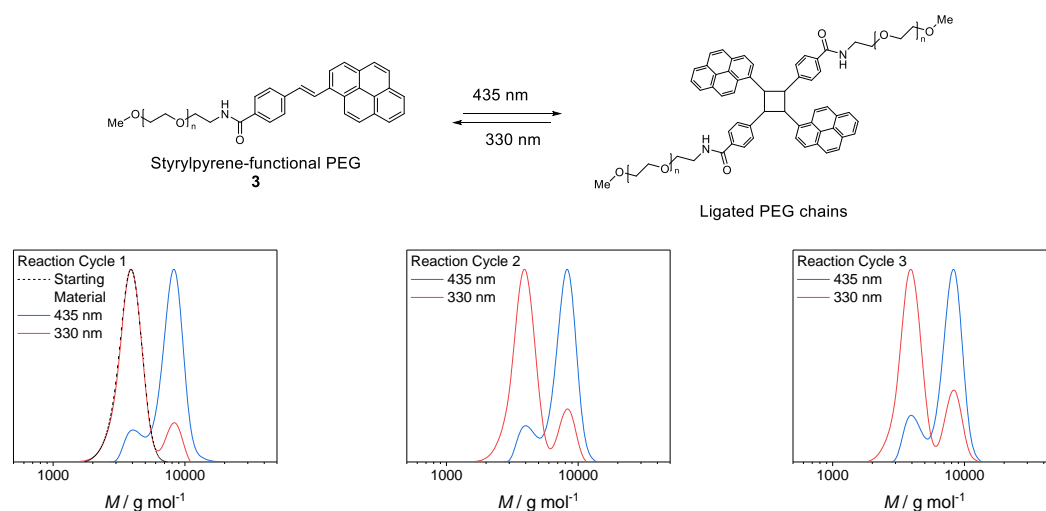


Figure 34. Reversible polymer ligation via alternating irradiation of styrylpyrene-functional PEG (10 mM) with visible light ($\lambda = 435$ nm, $483 \mu\text{mol}$ photons) and UV light ($\lambda = 330$ nm, $483 \mu\text{mol}$ photons) as well as subsequent analysis via PSS THF SEC (RI detector). Copyright 2018 American Chemical Society.

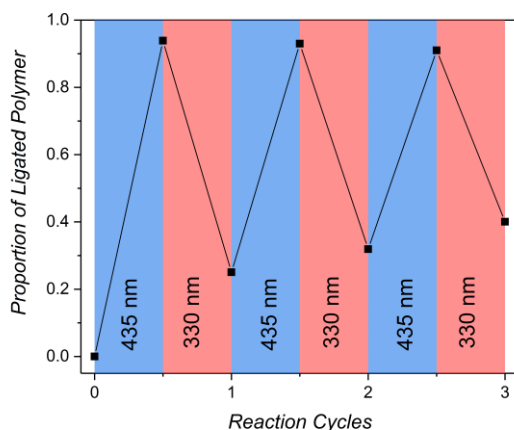


Figure 35. Reaction cycles conducted for the reversible photochemical polymer ligation of **3**. Copyright 2018 American Chemical Society.

of the *cis*-isomer of styrylpyrene or intramolecular rearrangements (**Figure 35**). The latter would occur as a cyclisation reaction from the *cis*-isomer to form a larger conjugated system as is known in literature for the similar structure motive stilbene.¹⁶² Since the employment and availability of tuneable monochromatic light systems, such as the current tuneable laser system, is limited to few research groups, the polymer ligation was also tested with commonly available light sources ($\lambda_{max} = 313 \text{ nm} / 441 \text{ nm}$) emitting at wavelengths close to the ideal WPEA parameters. As shown in **Figure 36**, the results for irradiation with broad band lamps are in excellent agreement with the ligation under laser irradiation.

In conclusion, in-depth investigations of styrylpyrene **1** have been conducted giving detailed insights into its photochemical behaviour and most efficient light-induced reaction conditions. The results have been successfully applied to a polymer ligation system including the use of readily available light sources proving the versatility of styrylpyrene as a reversible platform

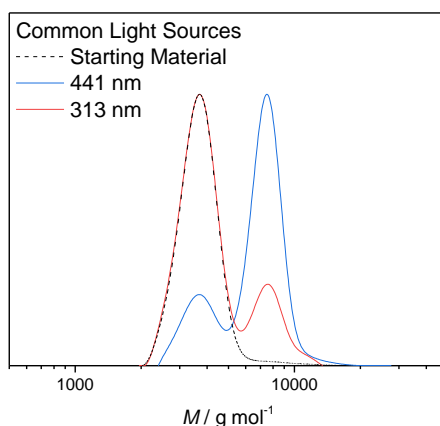


Figure 36. Irradiation of styrylpyrene-functional PEG (11.3 mg in 0.5 mL DMAc) with common light sources: The dimerisation was conducted at $\lambda_{max} = 441 \text{ nm}$ (11 h) and the dissociation at $\lambda_{max} = 313 \text{ nm}$ (11 h), as evidenced via DMAc SEC (RI detector). Copyright 2018 American Chemical Society.

with potential for applications in the fields of molecular biology, self-healing or reprogrammable materials, as well as orthogonal photoresists.

In fact, in parallel to the work published with the results of the current Chapter as well as using these findings as a base for further investigations, several different studies have been published so far and will be shortly described in the following paragraphs to highlight the versatility of styrylpyrene.

Simultaneously – but independently – to the investigations of Chapter 3, the group of Forsythe investigated the suitability of styrylpyrene for reversible and cytocompatible hydrogels.¹⁶¹ Tethering styrylpyrene to a PEG-amine, they achieved reversible block-copolymer formation under irradiation ($\lambda = 340 \text{ nm} / 400\text{-}500 \text{ nm}$) in water for six irradiation cycles with minimal photobleaching or photochemical oxidation. By exchanging the linear PEG with a 4-arm PEG, they were able to synthesise photolabile hydrogels that proved to be fully soluble in water and could be cross-linked before being analysed via rheology. As expected, the gelation of the styrylpyrene films can be tuned by simply changing the intensity of the light used for irradiation. In a first attempt, they used the reversibility of the styrylpyrene system to irradiate a fractured hydrogel with UV and subsequently visible light, allowing for self-healing of the damaged material. However, irradiation with only UV or visible light did not induce healing, suggesting that the material needs to be further de-cross-linked to achieve better mobility for the styrylpyrene groups before self-healing can be conducted. In addition, styrylpyrene materials proved to be nontoxic and suitable for cell loading in materials engineering.

In another study from our group conducted by Frisch *et al.*, styrylpyrene was employed for the formation of single chain nanoparticles.¹⁶³ Coupling **1** to a methacrylate to obtain a monomer that could be copolymerised with methyl methacrylate *via* RAFT, the resulting polymers could be intramolecularly folded not only upon irradiation with visible ($\lambda = 445 \text{ nm}$), but also ambient light. Overall, the reactivity of StyP was significantly enhanced in comparison to the small molecule study presented in the current thesis. The improvements in reaction rate and wavelengths can be attributed to the macromolecular confinement and preorganisation, hence, the high local concentrations and proximities of styrylpyrene molecules.

In addition, Frisch *et al.* further utilised the reversible dimerisation reaction of styrylpyrene in combination with the [4+4] cycloaddition of anthracenes to obtain a wavelength-orthogonal system simply by irradiation with three different wavelengths ($\lambda = 330 \text{ nm} / 410 \text{ nm} / 455 \text{ nm}$).¹⁶⁴ Furthermore, styrylpyrene can be triggered not only by employing light sources such as LEDs and lasers but also through chemiluminescence as shown in a recent study from Kockler *et al.* by employing the same reaction mixture that is used in common glow sticks to emit light and act as a trigger for the dimerisation of **1**.¹⁶⁵

Due to the versatility of styrylpyrene and its unique trigger wavelengths for the dimerisation as well as dissociation reaction, and having established that **1** can react in materials as well, StyP was part of further investigations that were conducted in the course of this thesis. Overall, the system was investigated as a platform technology towards reprogrammable gradient materials that can be triggered in a wavelength-orthogonal fashion. The dimerisation reaction of styrylpyrene for network formations can be exploited to cross-link samples using two main approaches (**Figure 37**):

1. Side-functional polymer chains

By introducing styrylpyrene as a side group in polymer chains, these can be cross-linked upon irradiation with light. While this approach has the advantage of only requiring one type of polymer without the addition of other moieties, it may be difficult to introduce the styrylpyrene as a polymer side-group.

2. Multifunctional cross-linking molecules

Styrylpyrene can be employed as a cross-linker molecule that photochemically reacts with functional polymer chains. To achieve such a system, it is necessary to have a mixture of polymer and cross-linker, however, this strategy allows for simpler polymer synthesis in combination with the possibility to readily alter the cross-linking molecule, for example by going from a linear di-functional chain to star-shaped molecules. In addition, the small molecule can contain more than one chromophore to introduce further functionalities.

Importantly, both approaches allow for ready access to alter the cross-linking density of the synthesised materials simply by changing the irradiation time or intensity as well as the density of functional groups. In the course of this thesis both strategies have been investigated within Chapter 4 focusing on approach 1, while Chapter 5 further exploits the applicability of pathway 2.

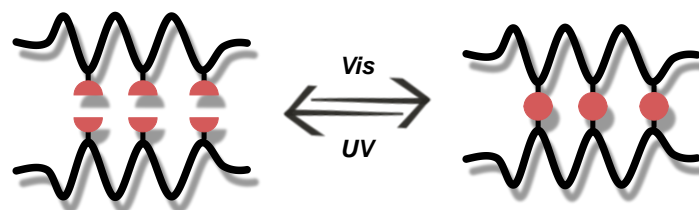
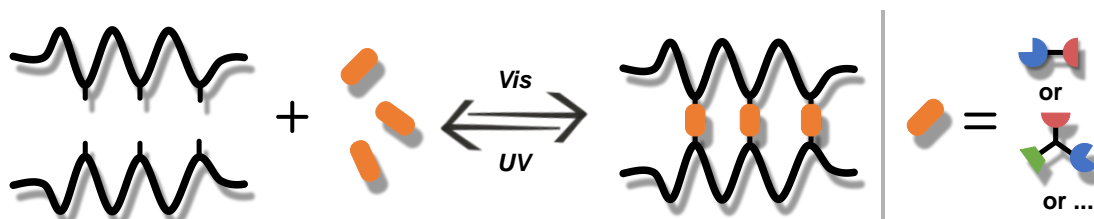
Approach 1 – Side-functional Polymer Chains**Approach 2 – Multifunctional Cross-linking Molecules**

Figure 37. Overview over the two approaches that allow for reversible network formation.

4

Styrylpyrene meets *o*-Methyl Benzaldehyde

4.1 The Challenge of Wavelength-Orthogonality

In materials science, curing processes initiated by light come with vast benefits, such as high spatial precision (*e.g.* for 3D printing) or the ability to instantly start and stop processes, simply by turning the light source on or off. Indeed, in modern technology, photocuring is a fundamental part for applications including automotive coatings, high-performance dental materials, or display technologies.^{138–140} However, most known photoreactions require trigger wavelengths in the UV light regime, possibly introducing degradation and damage into the irradiated material (refer to Chapter 2.3). Thus, bathochromic shifts have been thoroughly investigated to push the required activation wavelengths into the realm of visible light and potentially towards IR irradiation. Such red-shifts have already been successfully applied for example for photoinitiators,¹⁶⁶ with styrylpyrene representing a reversible photochemical reaction system that employs irradiation in the mildest known wavelength regimes. However, for the generation of light-adaptive materials it is necessary to thoroughly investigate and understand photochemical

The investigations in Chapter 4 have been conducted in a cooperation between D. E. Marschner (small molecule study and photochemical investigations), S. Bialas (QUT, resist design and cross-linking) and L. Michalek (QUT, AFM / XPS measurements). For completeness, selected data produced by Bialas and Michalek are included here. More detailed information can be found in their respective theses. The results and graphs in Chapter 4 are reprinted and adapted with permission from:

D. E. Marschner,[#] S. Bialas,[#] L. Michalek,[#] T. Krappitz, M. Wegener, J. Blinco, E. Blasco, H. Frisch, C. Barner-Kowollik, *Adv. Mater.*, 2019, 1807288. Copyright 2019 John Wiley and Sons

[#] These authors contributed equally.

systems. As demonstrated in the previous Chapter, the UV/Vis spectrum of a chromophore does not need to be congruent with its photo reactivity, hence, styrylpyrene has been thoroughly investigated due to its most ideal reaction parameters. Furthermore, materials that can respond independently to two different colours of light have recently been of particular interest, since they allow for two different processes to occur, *e.g.* separate network formation and functionalisation steps. As discussed in Chapter 2.3.5, it is highly challenging to achieve such photo-responsive systems, due to the absorption overlap of most known chromophores. As a result, in a mixture that features two different chromophores, irradiation with high-energy light will induce both reactions, preventing the material to be fully λ -orthogonal. To achieve completely separate bond forming processes, a new concept introduced by our group was proposed, combining an irreversible photochemical reaction in the regime of UV light with a reversible and red-shifted cycloaddition.⁵⁴ Consequently, the two chromophores can be triggered independently from each other. Under irradiation with visible light, only the cycloaddition will be active. However, upon high-energy light, the latter is suppressed, since the cycloreversion is triggered, and only the irreversible reaction proceeds. Such an approach was adopted in the context of the current thesis, since it allows to employ the thoroughly investigated styrylpyrene system and benefit from its mild reaction conditions. In addition, the in Chapter 4 discussed network formations represent the next steps towards reprogrammable gradients materials via the use of side-functional polymers (Approach 1, refer to **Figure 37**). Particularly the reversible ligation of block-copolymers via styrylpyrene end-groups has already successfully been proven, making StyP highly interesting for materials science (refer to Chapter 3.4).

In order to investigate the concept of λ -orthogonality in a dual photoresist, two different chromophores were combined. In specific, *o*-methyl benzaldehyde (*o*-MBA) on the one hand, as a UV-triggered species and styrylpyrene on the other – featuring a dimerisation in the visible light range – while remaining inactive at high-energy irradiation. The orthogonality of the two moieties to each other was investigated as model molecules and polymers in solution, as well as spin-coated films, including in-depth analysis via NMR, LC-MS, XPS and AFM.

4.2 Proving the Concept – Small Molecule Study

Based on the WPEA conducted in Chapter 3.3, the most effective trigger wavelengths of styrylpyrene are at 435 nm (dimerisation) and 330 nm (dissociation). Hence, combination with another chromophore that undergoes a reaction at the shorter wavelength only, results in a dual photo resist featuring complete λ -orthogonality. Indeed, the photoenol precursor species methyl 4-((2-formyl-3-methylphenoxy)methyl)benzoate (*o*-MBA, **4**) represents a highly suitable counterpart to StyP **1**. Investigation of its action plot, previously recorded by our group,¹³⁶ confirmed that **4** is most effectively reacting at 330 nm – the wavelength regime that renders **1** inactive – while featuring no reactivity at 435 nm – which represents ideal dimerisation parameters for styrylpyrene (**Figure 38**). Nonetheless, it is required to study the reactivities of both chromophores, **1** and **4**, together to eliminate the possibility that the presence of one chromophore affects the other.

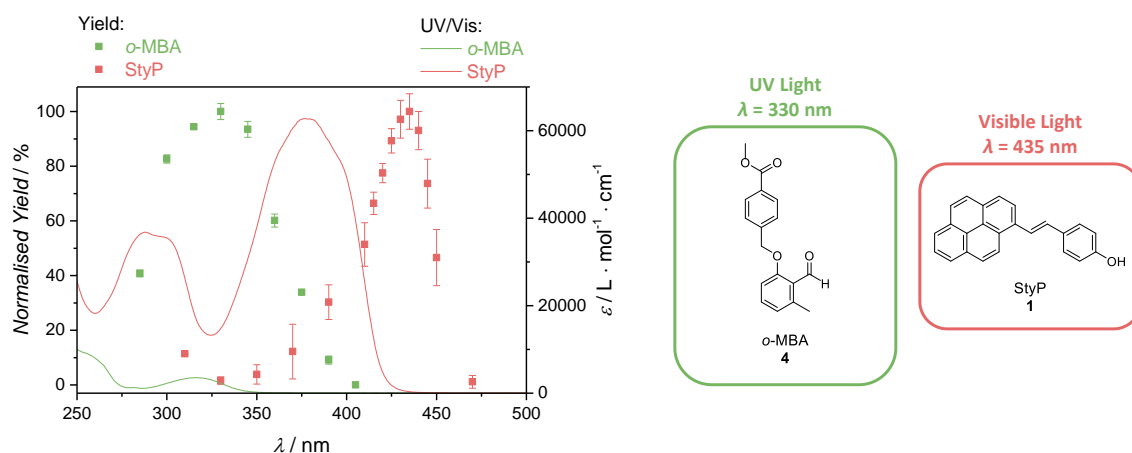


Figure 38. Action plots for *o*-MBA **4** and StyP **1** showing their normalised conversion for their dimerisation vs. the irradiation wavelength (squares) as well as their UV/Vis spectra (solid lines). The most efficient wavelength to trigger the UV light reaction of **4** is 330 nm, while the dimerisation of **1** proceeds best under irradiation with visible light at 435 nm. Copyright 2019 John Wiley and Sons.

Initially, the reaction of *o*-MBA was anticipated to proceed with tetraethylene glycol difumarate (TGD, **5**, **Figure 39**) since photoenol species are known to readily undergo cycloaddition reactions with dienes such as fumarates and maleimides (for further details on the photoenol reactivity refer to Chapter 2.3.6). However, the addition of TGD introduces another type of double bond into the reaction mixture, and it was unclear if cross-reactions in between the three molecules (StyP **1**, *o*-MBA **4**, TGD **5**) might occur. Therefore, the reactivity of the photochemically reactive moieties in one pot was investigated. First of all, the dimerisation behaviour of styrylpyrene in presence of the double bonds of **5** was assessed (**Appendix Figure 130**).

Under irradiation with light at 435 nm, in excellent agreement with the results of Chapter 3, **1** dimerised into the three expected photoproducts (**2a**, **2b**, **2d**) in addition to isomerisation to its *cis*-structure. Most importantly, no cross-reactivity with **5**, which proved to be completely unreactive, was detected.

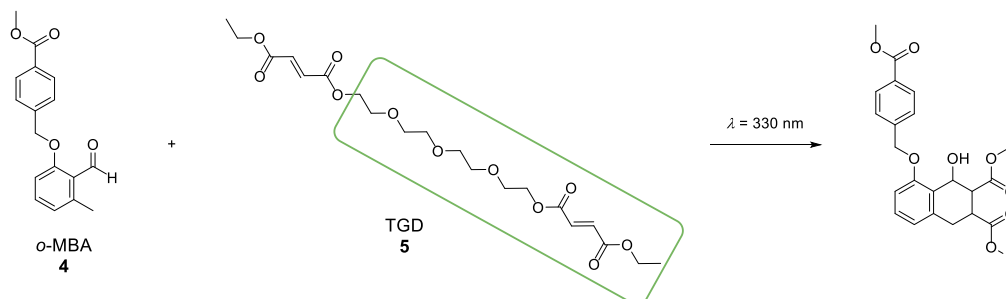


Figure 39. Photochemical reaction of *o*-MBA **4** with TGD **5** when irradiated with light in the UV-A range.

Although no cross-reaction should be expected when a mixture of StyP and TGD is irradiated in the UV range, a test reaction was conducted with light at $\lambda = 330$ nm. On one hand, the styrylpyrene dimerisation should be suppressed, on the other hand, TGD is not known to undergo any cyclisation reactions on its own. As a result, only the isomerisation of **1** was detectable when analysed via NMR, which confirmed these assumptions (Appendix **Figure 131**).

Furthermore, to achieve an orthogonal system, it is important to ensure that the only chromophore active at visible light irradiation is styrylpyrene **1**. As described in the beginning of the current Chapter, separate analysis of the photochemical reactions of **1** and **4** in actions plots revealed that *o*-MBA **4** has entirely no absorptivity at wavelengths above $\lambda = 410$ nm (**Figure 38**). However, a short irradiation experiment of a mixture of **4** and **5** was conducted to experimentally prove and support the respective findings. Due to the lack of absorptivity at 435 nm, irradiation of the two chromophores *o*-MBA and TGD at this wavelength induced no change in the measured $^1\text{H-NMR}$ spectra, proving both compounds to be unreactive in the visible light regime (Appendix **Figure 132**).

The reaction of *o*-MBA with fumarates has been previously reported in the literature, which was in agreement with conducted irradiation tests of a mixture of **4** and **5** at $\lambda = 330$ nm.^{152,167} Analysis via NMR reveals that a highly complex mixture of several different photoproducts between *o*-MBA and TGD was formed, while complete conversion was achieved when employing 483 μmol of photons. The latter is indicated by the disappearance of the resonances that are derived from the methyl and aldehyde groups of *o*-MBA (resonance **1** and **2** in **Figure 40**) in the respective NMR spectra. In addition, a small excess of TGD that was left in the

mixture underwent photoisomerisation from its *trans*- to the *cis*-isomer (resonance **4** and **5** in **Figure 40**).

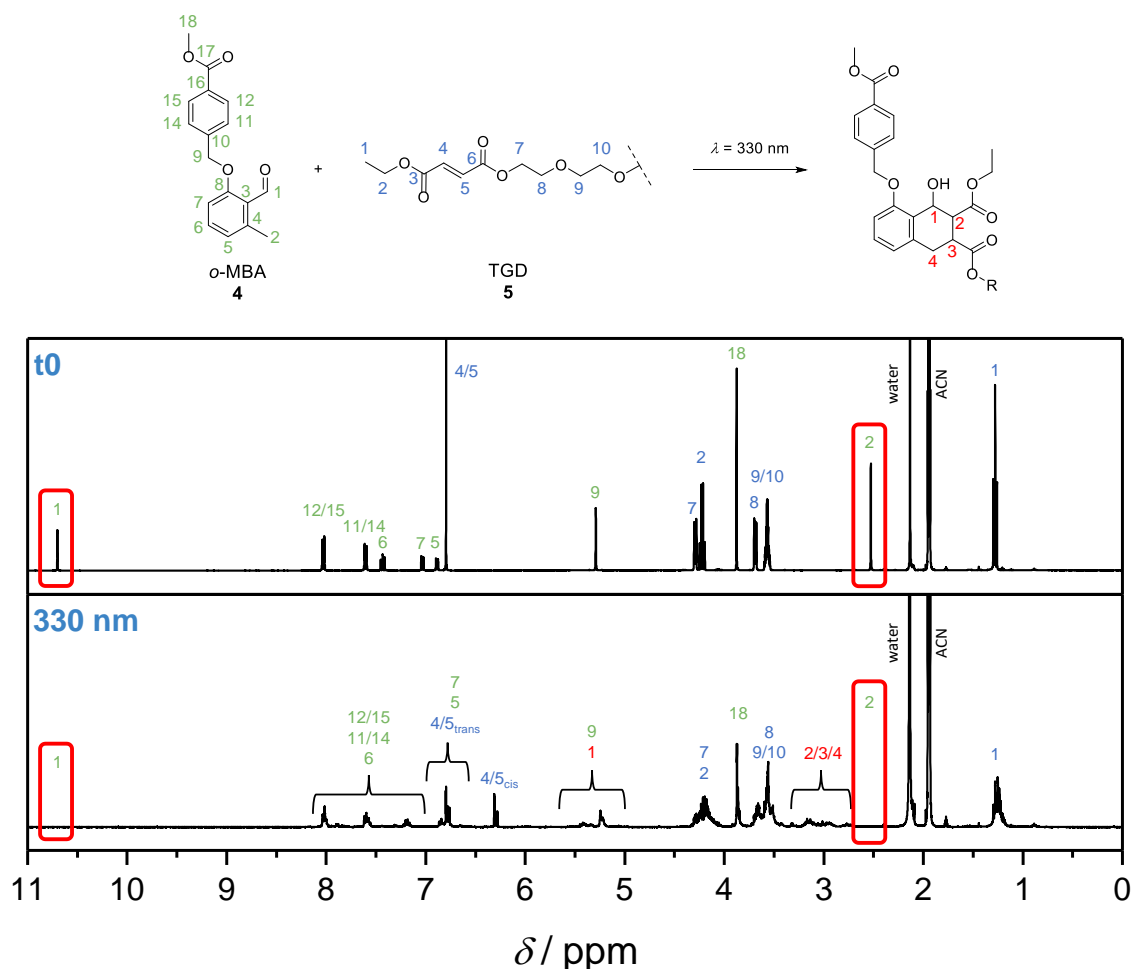


Figure 40. Reaction of *o*-MBA with TGD when irradiated in deuterated acetonitrile with a wavelength at 330 nm with 483 μmol of photons. Analysis via $^1\text{H-NMR}$ (400 MHz, CD_3CN). The disappearance of the resonances **1** (aldehyde) and **2** (methyl) of the *o*-MBA species **4** proved its complete conversion.

Having established that no cross-reactions take place in between StyP **1** and TGD **5**, as well as the inactivity of the cycloaddition of *o*-MBA **4** with TGD **5** in the visible light range, the complete wavelength-orthogonal system (**1**, **4**, and **5**) was subsequently investigated. Upon visible light ($\lambda = 435$ nm), **1** underwent dimerisation revealing new resonances (in between 4 and 6 ppm) in the $^1\text{H-NMR}$ spectra (Appendix **Figure 132** and **Figure 134**) featuring the same peak pattern already described in the stereochemical investigation for styrylpyrene in solution (refer to Chapter 3.2). However, irradiation within the UV light range ($\lambda_{\text{max}} = 330$ nm) did not lead to the expected results (Appendix **Figure 135**). Due to the absence of the respective cyclobutane peak pattern (**2a**, **2b**, **2d**), styrylpyrene did not undergo dimerisation. However, the magnetic resonances of TGD remained as well, while *o*-MBA was completely consumed, proven by the

absence of the magnetic resonances for the aldehyde and methyl group of *o*-MBA in the NMR spectrum (Appendix **Figure 135**). Hence, **4** underwent a cycloaddition with itself instead of reacting with **5**. While both reactions have been reported in literature, previous studies revealed that the self-dimerisation of **4** is suppressed in the presence of a dienes such as **5**.^{152,153,167} The inactivity of TDG in the irradiated reaction mixture appears to be derived from the presence of styrylpyrene, however, no similar findings have been reported by other groups and the reason remained unknown.

Nevertheless, the mixture was considered as wavelength-orthogonal, since visible light only triggered the styrylpyrene cycloaddition, while *o*-MBA completely dimerised with itself upon irradiation with UV-A without the need for TGD. Indeed, the removal of **5** from the reaction mixture could be of benefit for materials science, particularly due to the fact that the employed polymers only need to include two functional groups instead of three, vastly facilitating their synthesis. Thus, reaction mixtures of **1** and **4** were thoroughly studied next. To efficiently prove

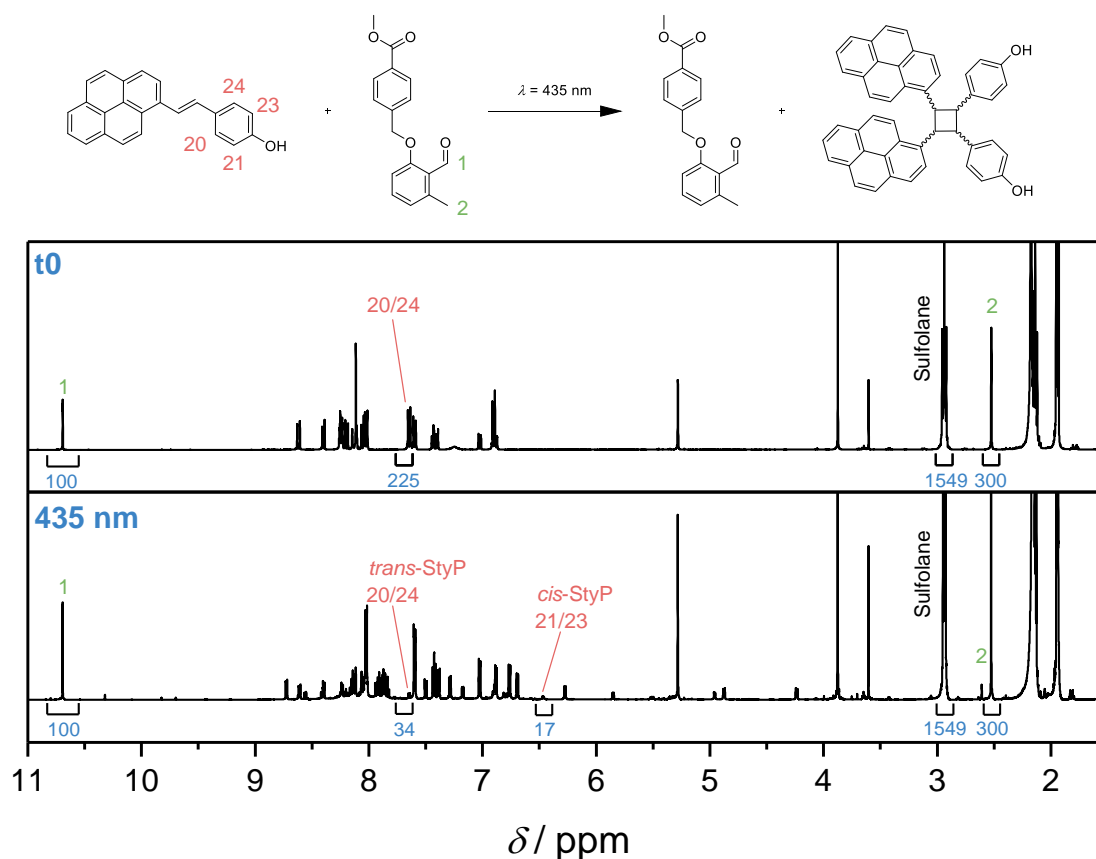


Figure 41. Irradiation of a mixture of StyP **1** and *o*-MBA **4** with visible light (435 nm, 1.93 mmol of photons). The magnetic resonances in the ¹H-NMR spectra (400 MHz, CD₃CN) were integrated in comparison to sulfolane as a reference. Since the peaks 20/24 of *cis*-StyP are overlaying with other resonances, protons 21/23 were chosen since they feature the same value than *cis*-20/24. For fully assigned spectra referred to Appendix **Figure 136**. Copyright 2019 John Wiley and Sons.

the λ -orthogonality of the latter, sulfolane was added to the samples since it can act as a reference during NMR analysis. Irradiation of **1** (1.13 eq.) and **4** (1.00 eq.) in an approximately equimolar ratio (in 0.4 mL CD₃CN; ca. 5.00 mM each) with light at the wavelength of 435 nm (1.93 mmol photons) led to the dimerisation of StyP. In agreement with the previously conducted studies (Chapter 0), ¹H-NMR measurements (**Figure 41**) confirmed the formation of the three photoproducts **2a**, **2b** and **2d** as well as *cis*-StyP, while leaving only 15 % of the starting material behind (integrals in comparison to the reference sulfolane: before irradiation: 225, after irradiation: 34 (*trans*-**1**) and 17 (*cis*-**1**)). In addition, *o*-MBA remained inactive when compared to the amount of the reference sulfolane (**Figure 41**, resonances **1** and **2**)

Irradiating a similar sample (1.00 eq. **1**, 1.00 eq. **4**, 0.4 mL CD₃CN, ca. 5.00 mM each, with sulfolane as a reference) with UV-A light at a wavelength of 330 nm (0.97 mmol of photons), the self-dimerisation behaviour of *o*-MBA was explored (**Figure 42**). While the latter results in a highly complex mixture that was thoroughly characterised by Krappitz *et al.* (for more details refer to Chapter 2.3.6),¹⁵³ analysis via ¹H-NMR showed almost complete consumption (98 %) of **4**. The conversion of **4** was determined via comparison of the methyl (**2**) and aldehyde

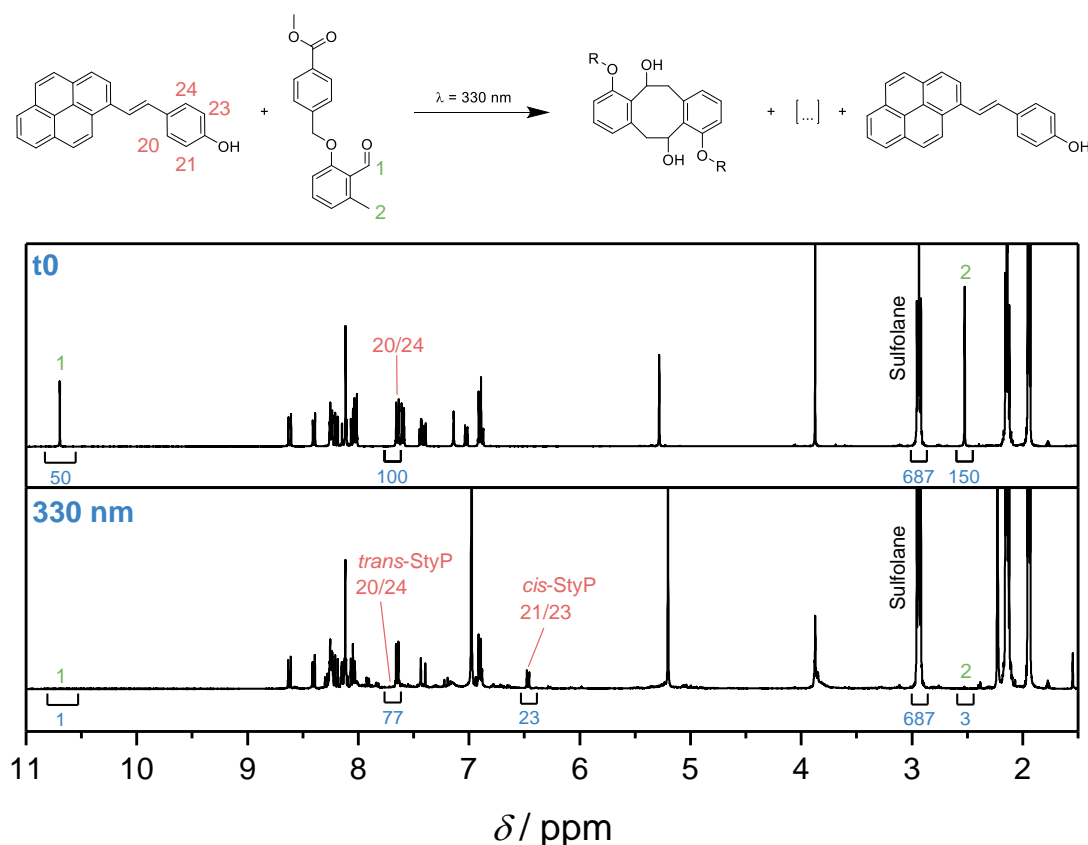


Figure 42. Irradiation of a mixture of StyP **1** and *o*-MBA **4** with UV light (330 nm, 0.97 mmol of photons). The magnetic resonances in the ¹H-NMR spectra (400 MHz, CD₃CN) were integrated in comparison to sulfolane as a reference. Since the peaks 20/24 of *cis*-StyP are overlaying with other resonances, protons 21/23 were chosen since they feature the same value than *cis*-20/24. Copyright 2019 John Wiley and Sons.

(1) resonances when integrated against the reference sulfolane before irradiation (aldehyde **1**: 50; methyl **2**: 150) and after irradiation (**1**: 1, **2**: 3). In contrast, **1** underwent isomerisation only, with the integral of both structures, *trans*- and *cis*-**1** combined, representing the same value after irradiation (*trans*: 77, *cis*: 23) as before (starting material *trans*-**1**: 100). Thus, no dimerisation of StyP took place, successfully proving the wavelength-orthogonality of the employed two chromophores.

The main photoproduct produced during irradiation of **1** and **4** with 330 nm was isolated and is formed in a [4+4] cycloaddition of two light-activated *o*-MBA species (for the structure refer to **Figure 42**, a detailed NMR spectrum can be found in the Appendix **Figure 137**). Unfortunately, the product mixture obtained during irradiation with UV-A light proved to be extremely complex, with structures too similar to each other to be separated and quantities smaller than

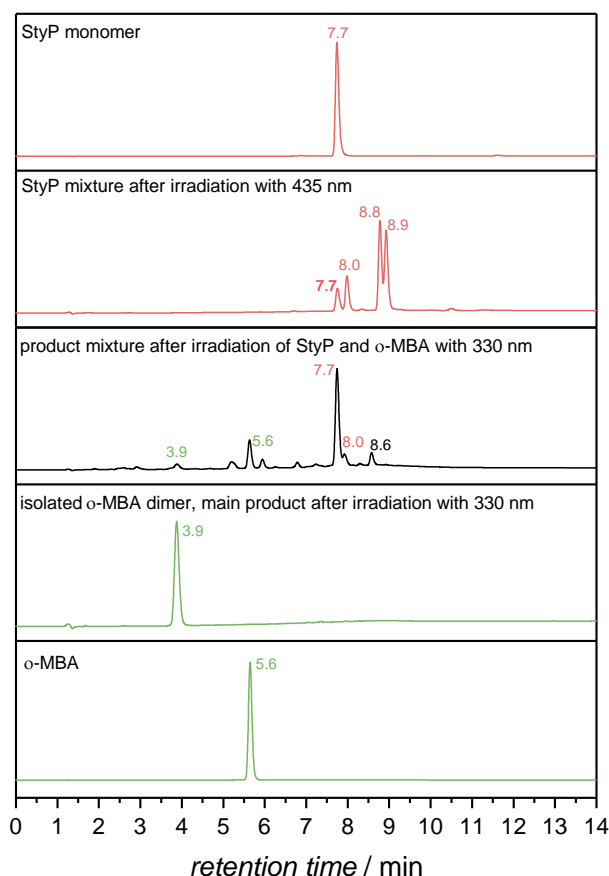


Figure 43. Comparison of the LC traces (detector wavelength 254 nm) for StyP **1**, the mixture of StyP **1** and its photoproducts after irradiation with 435 nm, the mixture of *o*-MBA and StyP after irradiation with 330 nm, the main *o*-MBA dimer formed after irradiation with 330 nm, and *o*-MBA. Copyright 2019 John Wiley and Sons.

the amount necessary for analysis via NMR spectroscopy. Therefore, additional characterisation techniques were carried out to further proof the wavelength selectivity of the different cycloadditions. The at 330 nm irradiated samples were subjected to LC-MS measurements and investigated to prove that no cross-reaction in between StyP and *o*-MBA occurred (**Figure 43**). Therefore, the LC traces of the irradiation mixture were compared to LC traces of untreated samples containing only StyP or *o*-MBA respectively, as well as samples of StyP after irradiation with 435 nm, and the isolated *o*-MBA dimer after irradiation with 330 nm. The LC of **1** and **4** after irradiation with 330 nm showed no peaks at the retention time for the StyP dimers (8.8 and 8.9 min) but small amounts of *cis*-**1** (8.0 min) and the remaining starting material *trans*-**1** (7.7 min). In addition, peaks representing the [4+4]-dimer (3.9 min) and the monomeric form (5.6 min) of *o*-MBA could be detected. For the remaining unassigned peaks, a closer look into the respective mass spectra indicated that no peaks were present that can be associated with a cross-reaction product of **1** and **4** (refer to Appendix).

In conclusion, detailed NMR and LC-MS studies revealed the complete wavelength orthogonality of StyP **1** and *o*-MBA **4** to each other, under irradiation in the visible and UV-A light ranges. Without a heterogenous dimerisation reaction taking place, the chromophore mixture proved highly suitable for altering and adapting the properties of a material, simply by choosing in between two different colours of light. To further establish the concept and investigate the vast possibilities enabled by such a λ -orthogonal approach, polymer as well as material studies were carried out as described in the following Chapter.

4.3 From Molecules to Materials

Utilising light in materials science, especially for photocuring of polymer strands in photoresists, has already been successfully applied since decades. However only after the macromolecular hypothesis from Hermann Staudinger in the 1920s that macromolecules are constituted out of covalently bonded monomer units and the further understanding of linear macromolecular chain structures, further insights into the complex network forming processes were made possible.^{17,168} To-date, photocuring is used for advanced coatings, display technologies or high-performance dental materials and, thus represent an industrial standard process.^{138–140} Light has the advantage of being spatially controlled, while it can be switched on and off on-demand. However, most known photochemical systems feature low trigger wavelengths, hence, high energy light, which can introduce damage to the irradiated material. As a result, researchers have focused much attention to the field of red-shifted photochemical reaction system, since they not only reduce damage dealt to a material but also allow for greater penetration depths. Combining such red-shifted systems with a wavelength-orthogonal approach allows to fabricate two different sets of properties (*e.g.* stiffness, cross-link density, swell-ability) into one material simply by changing the colour of light. Such a use of two different wavelengths to independently access disparate materials is pioneered within this thesis, employing the already

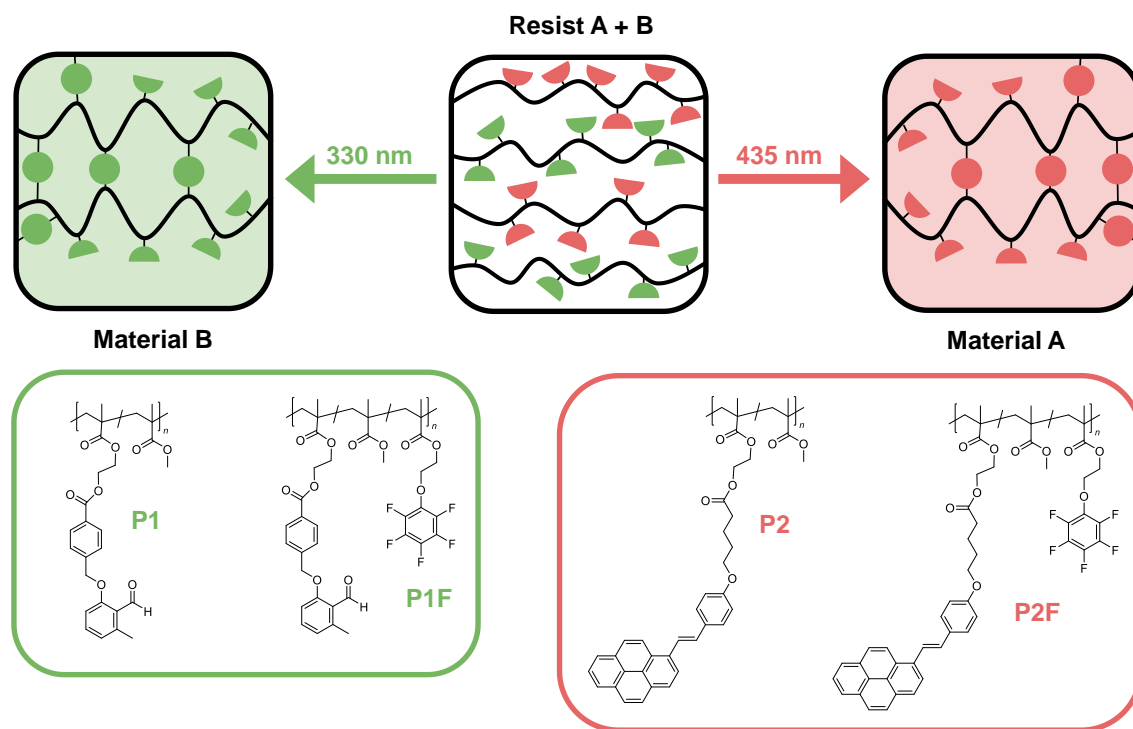


Figure 44. Concept of a wavelength-orthogonal system by implementing to different chromophores that can be cured under irradiation with disparate colours of light and result in two different materials. Below, the structures of the investigated polymer strands are shown. Copyright 2019 John Wiley and Sons.

investigated system of styrylpyrene **1** and *o*-MBA **4**, as they have been proven highly suitable for wavelength-orthogonal approaches (refer to Chapter 4.2). Therefore, the moieties **1** and **4** have been incorporated into polymer strands in order to, first, investigate their ability to cross-link in solution, and second, cast them into a resist, irradiate them with disparate colours of light leading to different properties, and as a result obtain a λ -orthogonal multimaterial resist (**Figure 44**).

For the polymer cross-linking studies, *o*-MBA and StyP were tethered as side groups onto the polymeric backbone of poly(methyl methacrylate) (PMMA, refer to **Figure 44**). As a result, two different polymer samples were synthesised: PMMA containing approximately 23 mol% *o*-MBA units (**P1**) as well as PMMA with a close to identical amount of StyP (21 mol%, **P2**). To thoroughly investigate the reactivity of both polymers and support the results presented in Chapter 4.2, the polymers should not only be investigated with regard of material properties but also to enforce that no cross-reactivity is taking place. Hence, respective fluorine tagged counterparts to **P1** and **P2**, *i.e.* **P1F** and **P2F** were synthesised (**Figure 44**). This approach

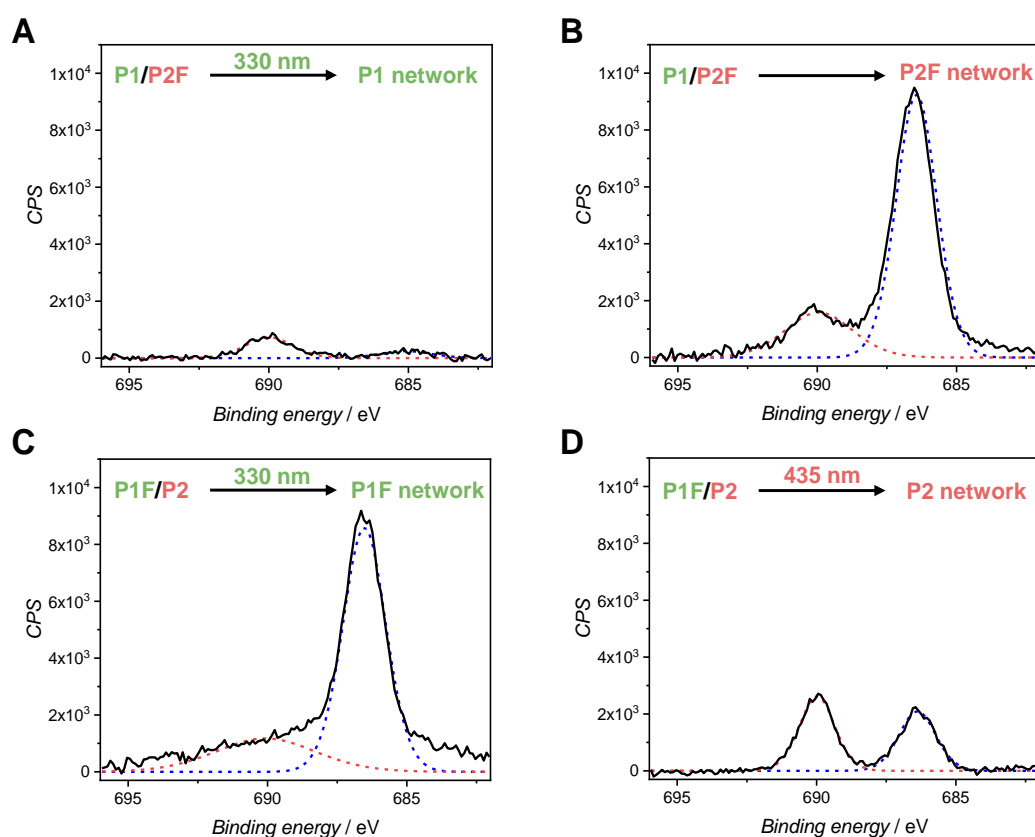


Figure 45. XPS $F 1s$ measurements of **P1** + **P2F** irradiated with **A** 330 nm or **B** 435 nm and **P1F** + **P2** irradiated at **C** 330 nm or **D** 435 nm. The blue dashed line represents a fitted function corresponding to the fluorine signals from the tagged-polymer present in the sample (**P1F** or **P2F**). The red dashed line matches the fluorine signal of the vial caps used during the irradiation experiments (PTFE). Copyright 2019 John Wiley and Sons.

allows for the analysis of cured photoresists via X-ray photoelectron spectrometric (XPS) analysis to illustrate which samples contain fluorine after being irradiated and thoroughly washed with chloroform (CH_3Cl). In total, four irradiation experiments in solution (DMF) were carried out under irradiation with visible (435 nm) or UV (330 nm) light to obtain either the respective fluorine-tagged or fluorine-free photoresists, subsequently followed by analysis via XPS (**Figure 45**).

The XPS analysis demonstrated that under irradiation with UV-A light (330 nm), only the *o*-MBA moiety undergoes cycloaddition, resulting in a fluorine signal in case **P1F** (**Figure 45 C**) is being used, while no peaks are visible for **P1** (**Figure 45 A**). Similar results could be achieved when visible light (435 nm) was employed to trigger the dimerisation of StyP. Irradiating a mixture of **P1** and **P2F** (**Figure 45 B**) led to a distinct fluorine peak in addition to the signal that was present in all spectra (fitted function with the red dotted line, **Figure 45**) and could be assigned to the vial caps used during irradiation (PTFE¹⁶⁹). However, for the sample containing **P1F** and **P2** (**Figure 45 D**), a small fluorine signal appeared although it has been proven already in the model study (refer to Chapter 4.2) that *o*-MBA is completely inactive under irradiation with visible light. Therefore, the fluorine signal is representing the P1F that could not be removed completely from the irradiated samples due to its entanglement in the formed StyP network. In conclusion, the polymer strands could be successfully cured in a wavelength-orthogonal fashion using two colours of light. The combination of *o*-MBA **4** and StyP

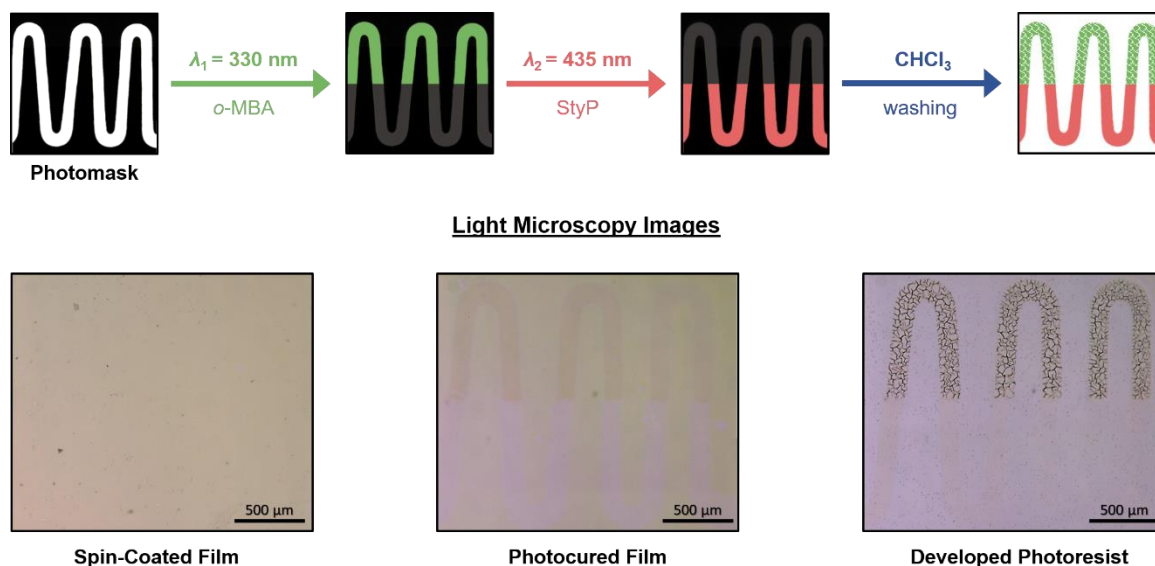


Figure 46. Schematic representation of the spatially resolved photocuring process resulting in two different distinct areas. Half of the photomask was blocked for each irradiation procedure (illustrated by the grey areas in the photomask). Subsequently, the film was post cured via washing with CHCl_3 . Below, light microscopy images are showing the spin-coated film before and after irradiation as well as post-curing, clearly highlighting the differences between the irradiated areas (wrinkled areas: *o*-MBA **4**, smooth areas: StyP **1**). Copyright 2019 John Wiley and Sons.

1 as a platform technology can enable the selective spatially resolved photocuring of disparate materials that inherit different properties from one single photoresist, as depicted in the following paragraphs.

In order to obtain resists of **P1** and **P2**, binary mixtures of the two polymers were spin-coated into films of close to 700 nm thickness. Irradiation of these took place from the bottom with a circular monochromatic laser beam (diameter: ca. 6 mm) using either 330 or 435 nm as the curing wavelength. Applying a shadow mask, the films were employed in a spatially resolved fashion. To compare the properties of the irradiated materials, one resist was cured with both wavelengths, while blocking one half of the photomask for each wavelength (**Figure 46**). Already light microscopy images visually revealed that two different materials were obtained via treatment with light while postcuring via washing with chloroform made these differences even more obvious (**Figure 46**, a supplementing movie of the photocuring can be found online[§]). As a result, the network that was based on the dimerisation of StyP **1** upon irradiation with visible light formed a smooth homogenous layer, while the *o*-MBA based material developed wrinkles that were also noticeable via atomic force microscopy (AFM). AFM topographical images showed distinct step profiles with sharp edges (ca. 10 μm in size) in between irradiated and

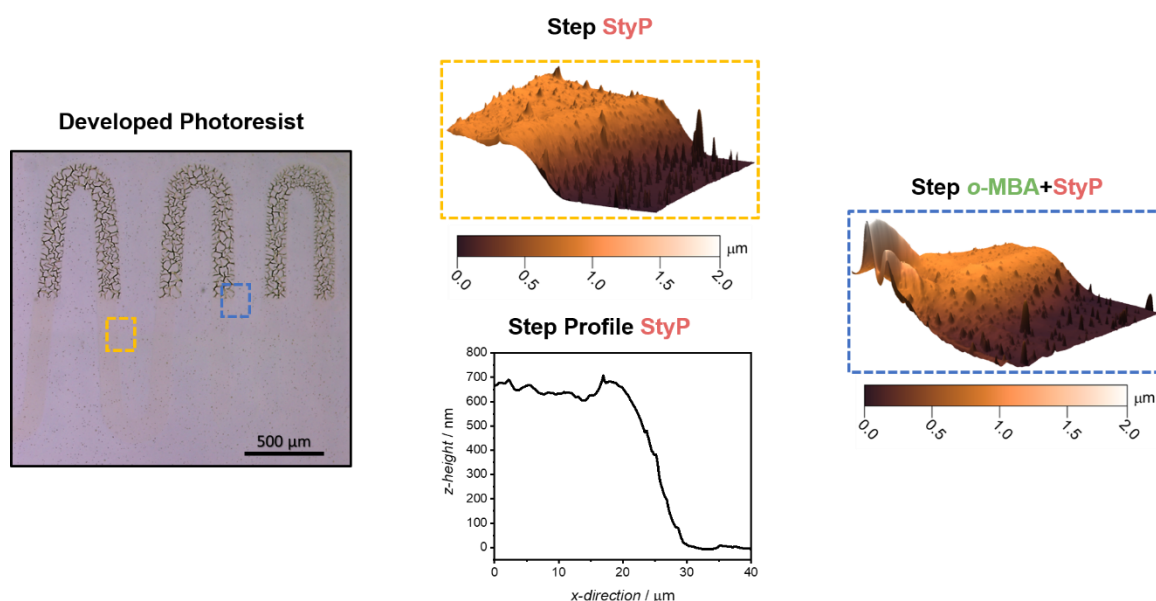


Figure 47. AFM topographical images of the step profile and border in between the substrate and photoresists, including a microscopy image of the developed photoresist to highlight the location where the respective AFM measurements were conducted. Copyright 2019 John Wiley and Sons.

§ A timelapse video of the postcuring process can be found in the following publication with *Advanced Materials*:
D. E. Marschner,[#] S. Bialas,[#] L. Michalek,[#] T. Krappitz, M. Wegener, J. Blinco, E. Blasco, H. Frisch and C. Barner-Kowollik, *Adv. Mater.*, 2019, 1807288. Copyright 2019 John Wiley and Sons

[#] These authors contributed equally.

non-irradiated areas (**Figure 47**), demonstrating the spatial resolved curing ability of the material. Furthermore, the mechanical properties of both the photocured resists were investigated with regard of their Young's moduli and adhesion energies (AFM, PinPoint Nanomechanical Mode). The results showed that the polymer with *o*-MBA ($E = 0.77 \pm 0.07$ GPa and $W_{\text{adh}} = 58.2 \pm 9.4$ aJ), cured in the UV-A range, led to a softer and less adhesive material than its StyP (visible light) containing counterpart ($E = 2.20 \pm 0.42$ GPa and $W_{\text{adh}} = 99.2 \pm 11.6$ aJ), further explaining the wrinkles in the remaining films.

In conclusion, by combining StyP **1** and *o*-MBA **4** into a PMMA film, a multimaterial resist was obtained. Wavelength-orthogonal photocuring with two different colours of light led to different materials with disparate properties in a spatially resolved fashion. The presented results are highly interesting for the further processing of gradient materials while the incorporation of **1** can also allow for reprogrammability. Thus, in further studies, the reversibility of StyP in such a multimaterial resist needs to be investigated via subsequent irradiation with visible and UV light over several different lifecycles. In addition, the photoresists should be cured employing light gradients, however monochromatic irradiation with a continuously changing intensity has not yet been possible with the herein employed tuneable laser setup. Regardless, the wavelength orthogonal photocuring already proved to be successful paving the way to disparate material properties and thus allowing to alter materials properties in a spatially resolved fashion.

5

Polychromophores

For the realisation of materials, which can be altered by light, utilising more than one chromophore enables vast possibilities to induce different changes (*e.g.* in flexibility, solubility, etc.) or reactions (*i.e.* cross-linking, de-cross-linking, folding, etc.) simply by using disparate wavelength regimes. To introduce these chromophores into one system, various strategies are available (compare Chapter 3.4 and **Figure 37**). For instance, the chromophores can be introduced into the polymer chains as side groups, either via pre- or post-functionalisation (**Figure 37**, Approach 1). However, both of these functionalisation strategies entail distinct disadvantages and advantages. Monomers that are functionalised prior to the polymerisation step can not only be synthetically challenging to access, but their comonomers as well as initiators also need to be carefully selected to ensure a polymerisation that leads to samples with controlled molecular weights and weight distributions. For post-functionalisation, the polymerisation needs to be conducted including a monomer with a functional group that can actively take place in subsequent reactions, while not affecting the polymer formation. Most importantly, it is analytically difficult to determine the amount of post-functionalised groups and thus the amount of the chromophore. As a result, in both approaches, the reaction conditions and polymers require to be specifically selected and tested for every introduced chromophore instead of providing a readily accessible platform tool. In contrast, by introducing the chromophores with a cross-linking molecule instead of polymer chain side groups, aforementioned disadvantages can be

The results presented in Chapter 5 were obtained in a cooperation between C. O. Franck (Master Student, synthesis) and D. E. Marschner (in-depth photochemical investigations). The results and graphs in Chapter 5 are reprinted and adapted with permission from:

D. E. Marschner,[#] C. O. Franck,[#] D. Abt, H. Mutlu, C. Barner-Kowollik, *Chem. Commun.*, 2019, **55**, 9877-9890. Published by The Royal Society of Chemistry.

[#] These authors contributed equally.

overcome (**Figure 37**, Approach 2). In addition, these small molecules can be designed in manifold ways, enabling the possibility to introduce various different chromophores at once, for example by employing star-shaped molecules with distinctive light-responsive moieties at each chain end. The approach of cross-linking molecules as additives was tested in the following Chapters in a model study and preliminary polymer tests that provide highly promising results. To allow for comprehensive investigations of a molecule combining several different light-responsive moieties, a di-functional molecule was chosen, since it allows to perform in-depth analytical characterisation, as well as the demonstration of the underlying concept of a dichromophoric molecule that can proceed in two site-specific and wavelength-orthogonal cycloadditions. In further research, the di-linker can be expanded to a molecule featuring multiple different light-responsive groups, *e.g.* by utilising a star-shaped linker, yielding a polychromophore able to respond to several different light-regimes.

In the di-linker approach that was investigated in the current thesis, *o*-MBA **4** was selected as one of the chromophores since it can undergo a cycloaddition in the UV-A regime to react with electron-deficient double bonds (*e.g.* maleimides, fumarates). Further, **4** is known to self-dimerise, however, in the presence of maleimides it has proven to preferably react with the diene.^{152,170} Furthermore, *o*-MBA ($\lambda = 310 - 350$ nm) already proved its suitability for λ -orthogonal reactions, for example in combination with tetrazoles¹⁷⁰ ($\lambda = 270-310$ nm, sequence-dependent) or styrylpyrene **1** (compare Chapter 4, sequence-independent). The *o*-MBA was combined with a cinnamic acid derivate able to undergo reversible cycloaddition. However, to achieve sufficient separation of the absorption bands, the phenyl ring of cinnamic acid was substituted with pyrene (pyrenyl cinnamic acid, PCA **6**, refer to **Figure 48**), to achieve a red-shift into the visible light range (compare Chapter 2.3.4). Finally, **4** and **6** were combined into one molecule using a linear linking molecule (molecules **7** and **8**, **Figure 48**), resulting in a dichromophore. The latter was investigated regarding its reactivity upon irradiation with visible and UV light. Most importantly, a reaction cycle should be possible with subsequent irradiation in both light regimes leading to the same final product, regardless in which sequence the different irradiation wavelengths have been used (**Figure 48**).

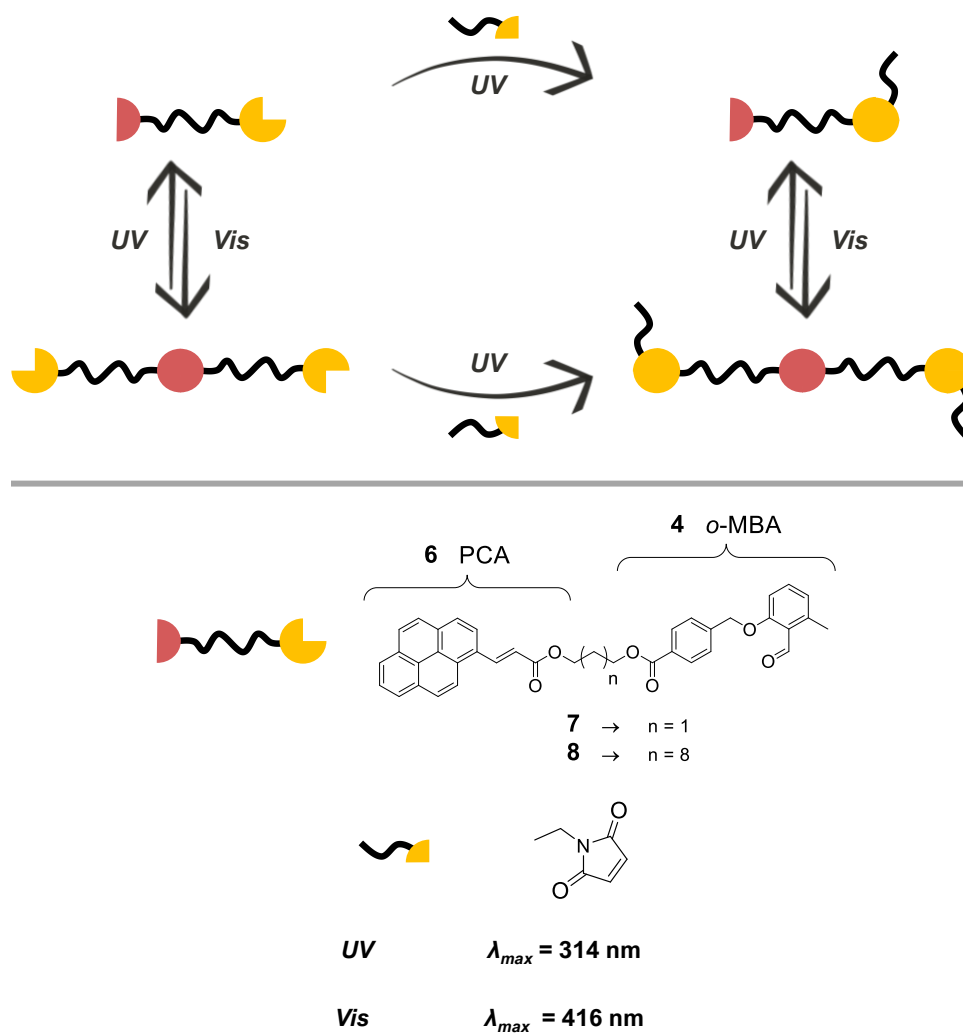


Figure 48. Reaction overview for the wavelength-orthogonal reaction cycle of a dichromophore (7 or 8) featuring two different light-responsive moieties (o-MBA 4 and PCA 6), which can take part in site specific cycloaddition reactions. Published in 2019 by The Royal Society of Chemistry.

5.1 Model Studies

To achieve a reversible and visible light triggered dimerisation system, a cinnamic acid derivate was functionalised with pyrene. In order to determine the reactivity of the double bond in proximity of a pyrene and an ester group, a model compound end-capped with a butanol chain (**9**) was synthesised allowing to explore the reactivity of the alkene moiety – especially in the UV range – without the effect of the *o*-MBA group **4** that will be part of the final dichromophore (**7** / **8**). Pyrene functionalisation of the cinnamic acid led to a shift in absorbance of close to 100 nm, from $\lambda_{max} = 272$ nm (cinnamic acid) to $\lambda_{max} = 370$ nm (**9**, compare **Figure 49**). Thus, **9** (10 mM in DCM-*d*₂) was irradiated with visible light ($\lambda_{max} = 416$ nm, 1 h) to trigger the dimerisation of the double bond and subsequently with UV light ($\lambda_{max} = 314$ nm, 1 h) to revert the formed dimers back to the starting material. Following the light treatment, the samples were analysed via NMR as well as UV/Vis spectroscopy to confirm successful reactions. The NMR spectrum after visible light irradiation (**Figure 50 t1**) clearly indicates the formation of magnetic resonances for the cycloadducts in the range between 3.5 and 6.0 ppm (red box), thus confirming that **9** is able to undergo cycloaddition in the visible light range (79 % conversion, according to ¹H-NMR). Similarly to styrylpyrene, several different stereoisomers are being formed, resulting in different chemical resonances (for the detailed resonance assignments refer to Appendix **Figure 149**). Along dimerisation – analogue to styrylpyrene – isomerisation of the starting *trans*-**9** to its respective *cis*-structure took place ($\delta = 6.36$ ppm). Upon subsequent irradiation with UV light (**Figure 50 t2**), the cycloadducts dissociated to their monomer form

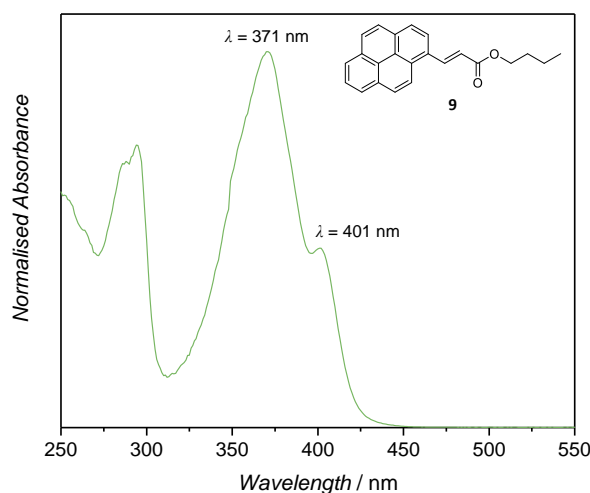


Figure 49. UV/Vis spectrum of **9** (in DCM). Published in 2019 by The Royal Society of Chemistry.

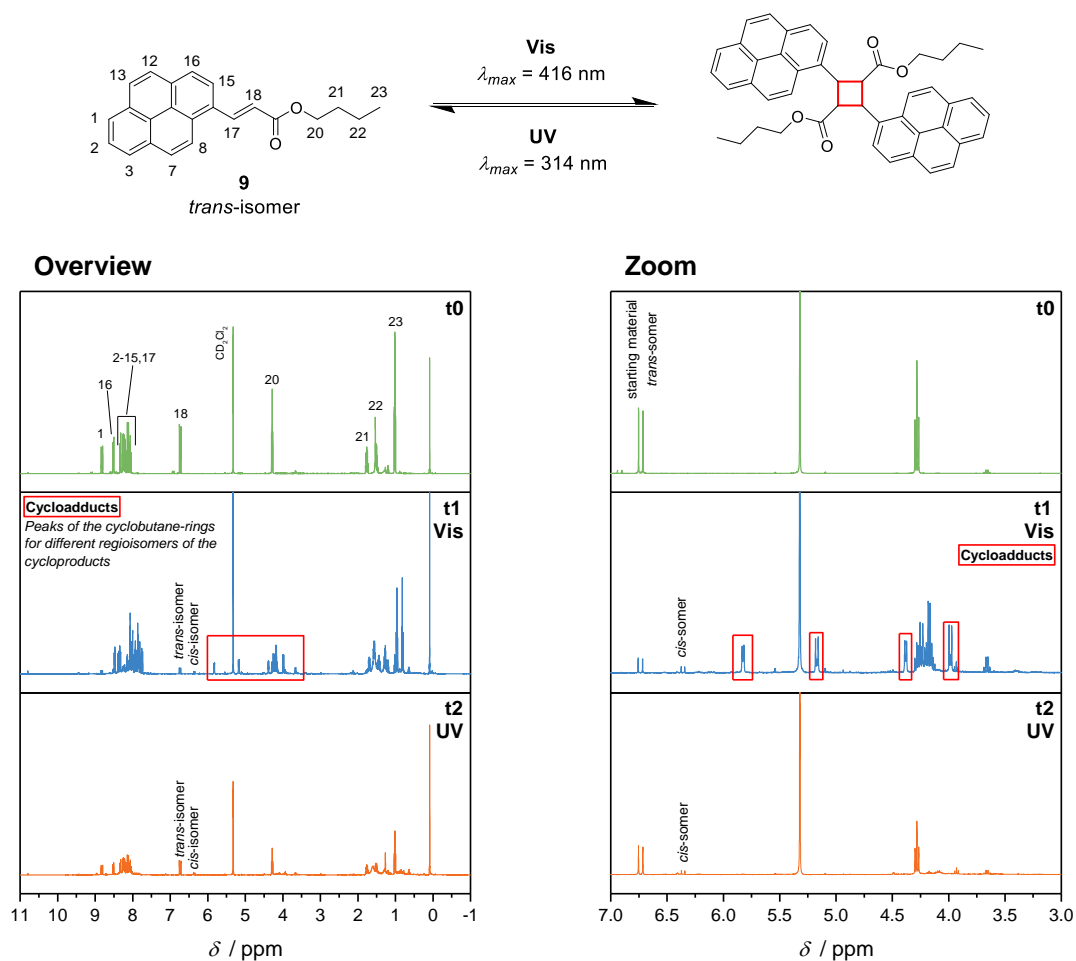


Figure 50. Proton NMR (400 MHz, DCM-d_2) of **9** before irradiation (t0, green line), after irradiation with visible light ($\lambda_{max} = 416$ nm, t1, blue line), and subsequent UV light irradiation ($\lambda_{max} = 314$ nm, t2, orange line) including an enlarged version which is highlighting the crucial magnetic resonances representing the cycloproducts. Published in 2019 by The Royal Society of Chemistry.

9, yielding a mixture of both *cis*- and *trans*-isomer, while leaving only traces of dimer behind (3 %, according to $^1\text{H-NMR}$).

When analysing the visible light dimerisation of **9** via UV/Vis spectroscopy, the absorption bands at 370 and 410 nm decrease, while new absorption bands at 333 and 348 nm arise (**Figure 51**). Such observations are in agreement with published studies (e.g. for styrylpyrene¹⁶⁰) since the fully conjugated and planar system of **9** – consisting of the double bond, the pyrene, and the ester bond – that is responsible for the red-shifted absorption is removed during the cycloaddition. Thus, the absorption of the dimer molecules is shifted to lower wavelengths. Subsequent irradiation of the cycloadducts with UV light ($\lambda_{max} = 314$ nm), however, did not result in the expected absorbance spectrum (**Figure 51** t2). According to the previous NMR studies, the cycloadducts almost completely disappeared under irradiation with UV light. Therefore, the spectrum t1 in **Figure 51** was expected to revert back to a spectrum similar in shape to t0. The measurements after UV irradiation (t2, **Figure 51**) displayed a new unknown

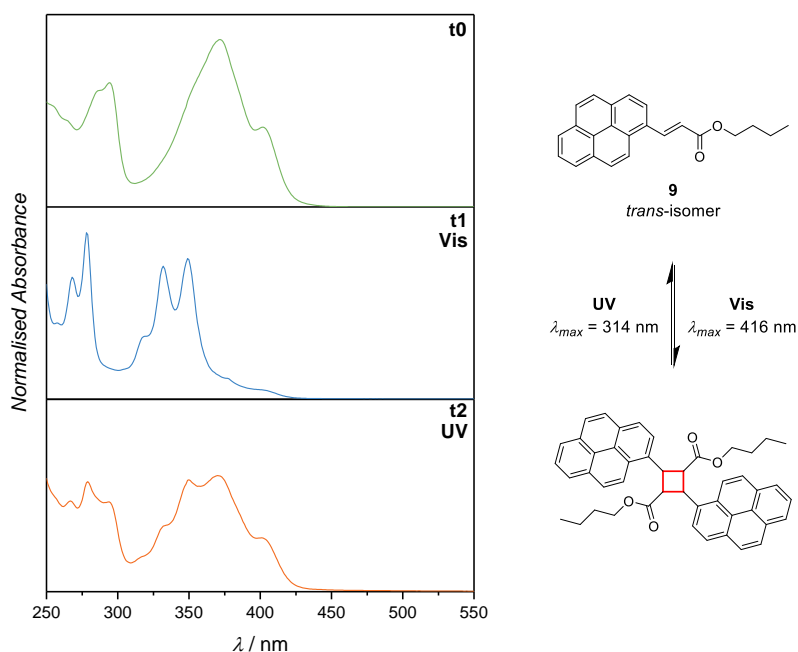


Figure 51. UV/Vis spectrum (DCM-d₂) of **9** before irradiation (t₀, green line), after irradiation with visible light ($\lambda_{max} = 416$ nm, t₁, blue line), and subsequent UV light irradiation ($\lambda_{max} = 314$ nm, t₂, orange line). Published in 2019 by The Royal Society of Chemistry.

absorbance spectrum, featuring absorbance bands at $\lambda_{max} = 333, 349, 370$ and 401 nm. Thus, in addition to NMR and UV/Vis spectroscopy, samples of **9** before irradiation (t₀), after irradiation with visible light (t₁), as well as after irradiation with visible and subsequently UV light (t₂) were investigated via GC-MS to detect mass fragments that are smaller than the mass of **9** (refer to Appendix **Figure 150 - Figure 152**). Such fragments may hint to photodamage to the sample during irradiation. However, no smaller mass values were observed, hence, the samples are not prone to light-induced damage.

To further investigate the absorption pattern of t₂ (**Figure 51**), experiments with different irradiation times were carried out and analysed via UV/Vis spectroscopy to observe the change of the traces from the starting material to the point of maximum conversion. **Figure 52** shows that the latter is reached after approximately 1 h for each, visible light and subsequent UV light irradiation. Especially when analysing the dissociation reaction (**Figure 52 B**), it is apparent that the t₂ absorption pattern (**Figure 51**) is most likely not derived from a new species present in the solution but rather a mixture of monomer and dimer. This is supported by the fact that the absorption maxima are at similar wavelengths in all measured spectra (refer to **Figure 51** and **Figure 52**). Thus, adding the absorption traces of monomer and dimer together would result in the pattern observed in t₂ (**Figure 51**). In literature, conversion of photoreactions is often

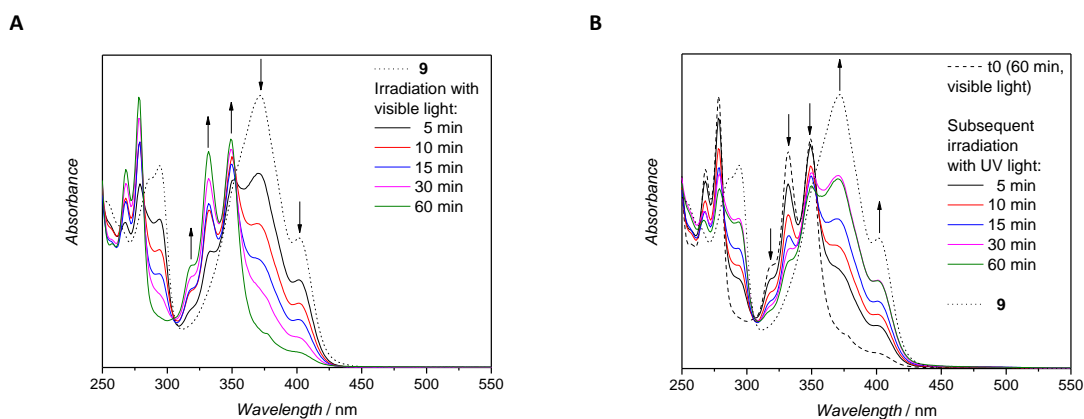


Figure 52. UV/Vis spectra of **9** (dotted line) and light treatment of **9** with different irradiation times: (A) irradiation with visible light (416 nm) as well as (B) irradiation with visible light (416 nm) for 60 min (dashed line) and subsequent treatment with UV light (314 nm). Published by The Royal Society of Chemistry.

determined via UV/Vis spectra by following the absorbance at one given maximum.¹⁷¹ Irradiation of **9** with visible light for 1 h, led to a conversion of 86 %. Subsequent irradiation with UV light led to dissociation to *trans*- and *cis*-**9** (70 % conversion), while leaving approximately 30 % of the dimer structures behind (determined with the absorption band at $\lambda_{\text{max}} = 372$ nm). However, in the present case, determination of the conversion from UV/Vis spectra is highly challenging due to the fact that all absorbance bands are overlaying and thus contain not only one species. Especially the calculation of the conversion after irradiation with UV light is inaccurate since the absorption traces of the dimer structures are too close to the monomer absorption bands and thus overlay. In addition, the absorption spectrum of the *cis*-structure remains completely unknown and thus cannot be factored in. Therefore, to fully understand the detected pattern, all structures present after irradiation would need to be separated (*e.g.* via quantitative thin layer chromatography) and characterised. However, separation has proven challenging and has not yet been accomplished. It is also critical to ensure that the samples are not exposed to light before analysis can be conducted. In conclusion, the absorption pattern observed in **Figure 51** t2 is most likely derived from small amounts of dimers left after irradiation with UV light, while the actual percentages can only be determined via ¹H-NMR spectra (approximately 3 % of dimer) and not UV/Vis spectroscopy.

Overall, the reactivity of **9** is comparable to the already investigated styrylpyrene (refer to Chapter 3) with a dimerisation reaction that takes place in the visible light range and a dissociation reaction under irradiation with UV light. Therefore, PCA is highly suitable to be combined with other light-responsive moieties into polychromophores, as will be explored in the following chapters.

5.2 Dichromophores

With the alkene reactivity of PCA **6** upon irradiation fully explored, it was combined in a dichromophore with *o*-MBA **4** via the linear 1,3-propanediol to yield **7**. Despite thorough investigation of the *o*-MBA moiety with different lamps and irradiation times, a quantitative [4+2] cycloaddition with *N*-ethyl maleimide (Et-Mal) could not be achieved, although the reaction is known to undergo complete conversion in short reaction times.¹⁷² The inability to reach full conversion strongly suggests inhibiting effects due to the close proximity of the two reactive sites, likely caused by steric hindrance (especially considering the bulky pyrene unit) or prohibitive electronic effects (e.g. FRET effect or depletion processes).^{173–175} Therefore, 1,10-decandiol was introduced as a spacer in between the PCA and the *o*-MBA moieties resulting in compound **8**. In contrast to **7**, irradiation of **8** with UV light ($\lambda_{\max} = 314$ nm) in the presence of Et-Mal and subsequent analysis via NMR showed complete conversion of the *o*-MBA functionality (**Figure 53**), indicated by the disappearance of the aldehyde (**43**, 10.7 ppm) and methyl resonances (**44**, 2.6 ppm).

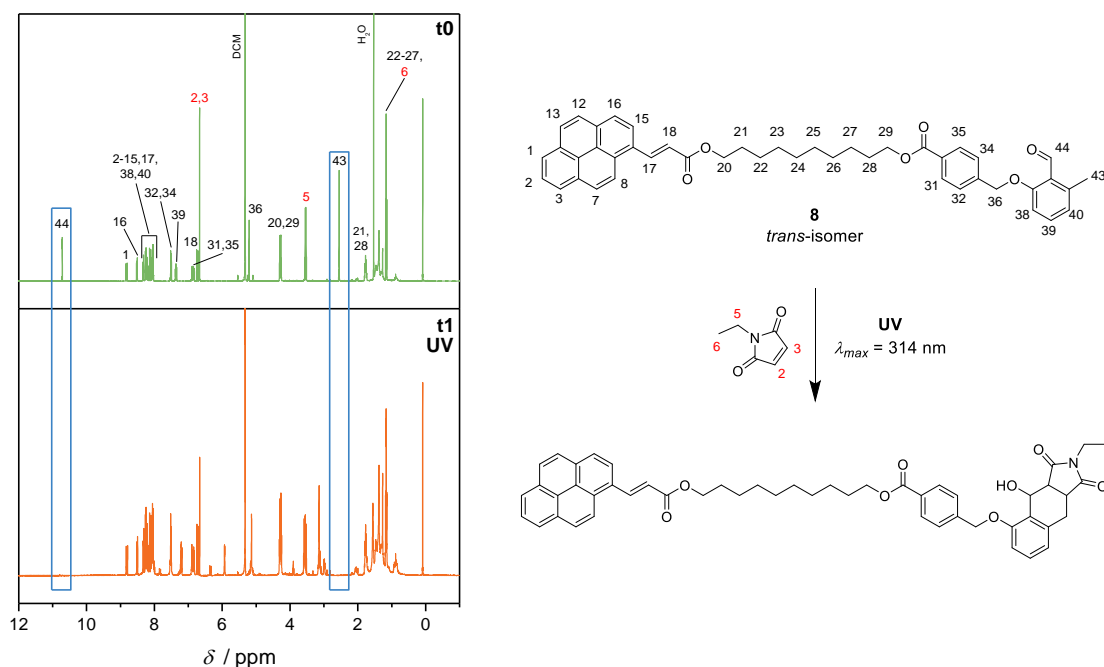


Figure 53. ¹H-NMR (400 MHz, deuterated DCM) spectra of **8** (10 mM) in the presence of Et-Mal (10 mM) before and after irradiation (in DCM-d₂) with UV light ($\lambda_{\max} = 314$ nm, 3 h). Disappearance of the methyl (**43**) and aldehyde (**44**) resonances suggests full conversion of *o*-MBA moiety. Published in 2019 by The Royal Society of Chemistry.

Next, PCA **6** was irradiated with visible ($\lambda_{max} = 416$ nm) and UV light ($\lambda_{max} = 314$ nm) to investigate if its reversible dimerisation, when incorporated into **8**, resembles that of the *o*-MBA-free **9**. Upon exposure to light at $\lambda_{max} = 416$ nm, **8** dimerised, which could be proven via the formation of distinct cyclobutane resonances (**Figure 54**) in the respective NMR measurements as well as via UV/Vis spectroscopy in which the absorption bands at 371 and 402 nm, representing the fully conjugated PCA system, disappeared (**Figure 54**). In addition to dimerisation, *trans*- to *cis*-isomerisation took place (**Figure 54**). Subsequent treatment of the photoproducts with light in the UV range ($\lambda_{max} = 314$ nm) could prove the reversibility of the cycloadducts,

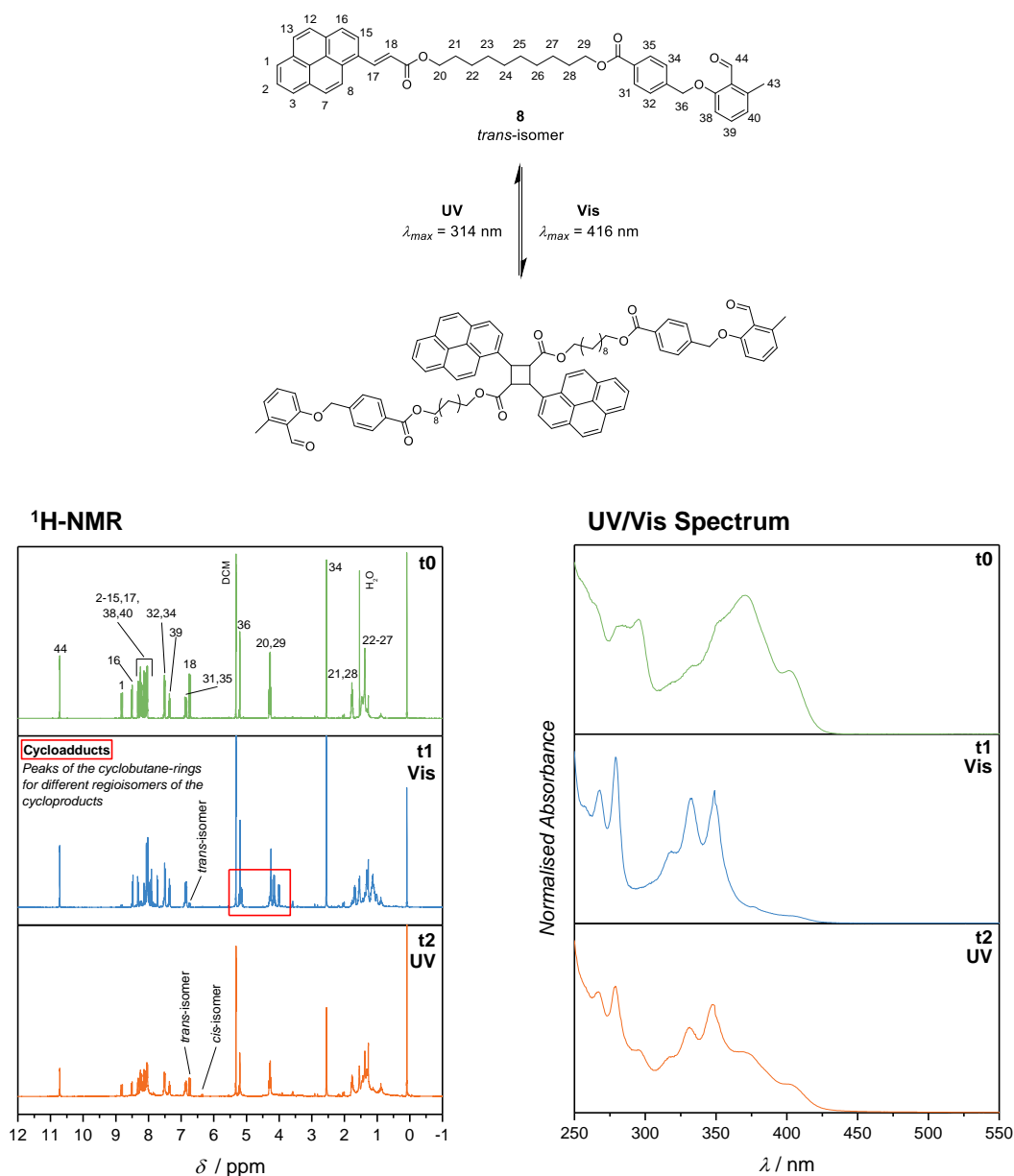


Figure 54. $^1\text{H-NMR}$ (400 MHz, deuterated DCM) and UV/Vis spectrum of **8** (10 mM, DCM- d_2) before irradiation (t_0), after irradiation with visible light (t_1 , $\lambda_{max} = 416$ nm, 5 h), and subsequent irradiation with UV light (t_2 , $\lambda_{max} = 314$ nm, 3 h). Published in 2019 by The Royal Society of Chemistry.

indicated by the disappearance of their magnetic resonances when analysed via NMR (**Figure 54**) as well as the reappearance of the UV/Vis absorption bands representing **8**.

Since both light-responsive moieties (**4** and **6**) and their reactions ([4+2] and [2+2] cycloaddition) had been proven suitable for a wavelength orthogonal dichromophore, both pathways of the complete and sequence-independent reaction cycle (compare **Figure 48** on page 75) of **8** – in presence of Et-Mal – with subsequent irradiation in both wavelength regimes were investigated. Ideally, the photochemical cycloadditions should lead to the same product, independently if a sample is irradiated with UV followed by visible light or in an inverse succession.

As shown in **Figure 55**, UV/Vis spectroscopy of **8** and Et-Mal (10 mM each, DCM-*d*₂) showed similar results to the previous model studies and test experiments. Initial irradiation with UV light ($\lambda_{max} = 314$ nm, 3 h) led to the complete reaction of *o*-MBA with Et-Mal (proven by ¹H-NMR, Appendix **Figure 153**). However, small amounts of the already discussed absorption pattern, which might be derived from a mixture of both monomer and dimer structures, with bands at $\lambda = 333, 349, 370$ and 401 nm were observed (**Figure 55**). The generation of small amounts of dimer might be due to the broad emission spectrum of the employed lamp, reaching into wavelength ranges up to almost 400 nm. To avoid such behaviour, narrowly distributed

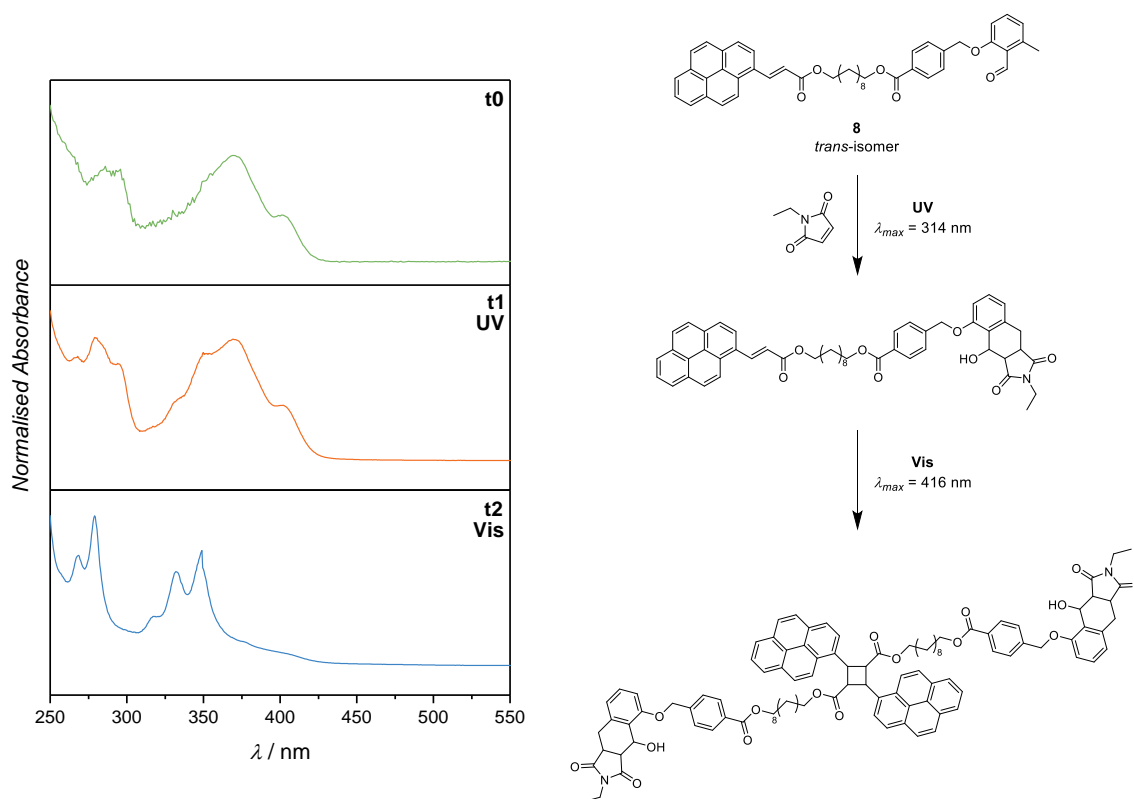


Figure 55. UV/Vis spectrum of **8** in the presence of Et-Mal (10 mM each, DCM-*d*₂) before irradiation (*t*₀), after irradiation with UV light (*t*₁, $\lambda_{max} = 314$ nm, 3 h), and subsequent irradiation with visible light (*t*₂, $\lambda_{max} = 416$ nm, 5 h). Published in 2019 by The Royal Society of Chemistry.

light sources (such as LEDs) should be employed in future studies. Subsequent irradiation in the visible light regime ($\lambda_{max} = 416$ nm) induced dimerisation of the double bond, indicated by the decrease of the absorbance bands at $\lambda = 370$ and 410 nm (as well as $^1\text{H-NMR}$, Appendix **Figure 154**).

As expected, Et-Mal did not interfere with the reaction of **8** upon visible light irradiation ($\lambda_{max} = 416$ nm, 5 h). Both UV/Vis (**Figure 56**) and NMR (Appendix **Figure 155**) measurements showed the successful formation of the PCA cycloadducts. However, subsequent irradiation with UV light ($\lambda_{max} = 314$ nm, 3 h) did not only induce the [4+2] cycloaddition of *o*-MBA, but also the cycloreversion of the previously formed photoproducts. Both absorbance spectra (**Figure 56**) and $^1\text{H-NMR}$ analysis (Appendix **Figure 155**) proved that the two reactions proceed, and while the UV/Vis spectrum featured the newly observed pattern with four major absorption bands, NMR spectroscopy revealed that the transition from the cyclobutane-like structures towards the double bond occurred with almost full conversion. While this was not the anticipated reaction route, it does not interfere with the orthogonal nature of the system

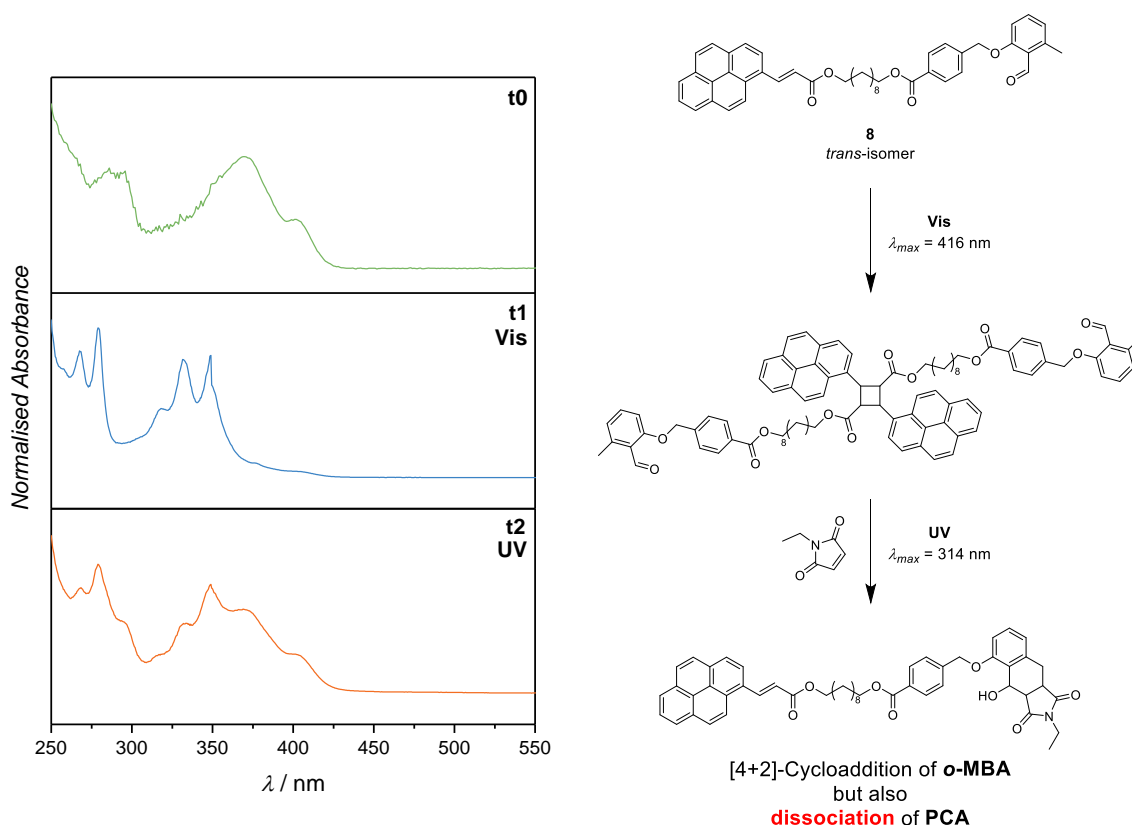


Figure 56. UV/Vis spectrum of **8** in the presence of Et-Mal (10 mM each, DCM- d_2) before irradiation (t0), after irradiation with visible light (t1, $\lambda_{max} = 416$ nm, 5 h), and subsequent irradiation with UV light (t2, $\lambda_{max} = 314$ nm, 3 h). Upon irradiation with UV light, not only the [4+2] cycloaddition of the *o*-MBA moiety took place, but also dissociation of the previously via the double bond of PCA formed photodimers. Published in 2019 by The Royal Society of Chemistry.

since an additional irradiation step in the visible light regime could again trigger the dimerisation reaction of PCA (compare **Figure 57**). As a result, both chromophores can undergo a photochemical cycloaddition through subsequent irradiation steps allowing **8** to act as a dichromophore towards a linking molecule in materials science. The successful conversion of both light-responsive moieties was established by NMR as well as UV/Vis spectroscopy with the model molecule Et-Mal. In additional studies, the latter can be substituted by more complex polymer chains, feature the diene either as a functional side or end group. To further establish the concept of polychromophores, preliminary polymer tests with **8** in presence of a commercially available PEG, which featured maleimide as an end group, were conducted and will be discussed in the following Chapter.

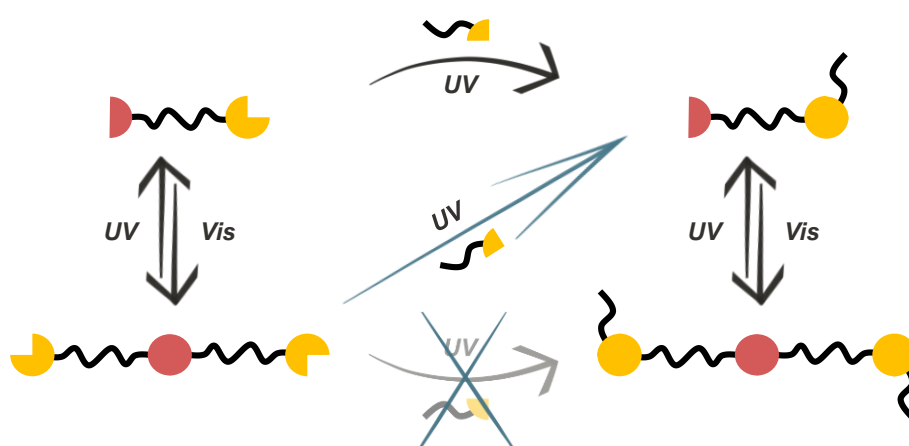


Figure 57. Complete reaction cycle of **8** when irradiated with two disparate wavelengths, visible and UV light, in a subsequent fashion. The reaction pathways were proven via $^1\text{H-NMR}$ as well as UV/Vis spectroscopy. The fact, that UV irradiation did trigger both, the cycloaddition of one functionality (yellow) as well as the dissociation of the other moiety (red) does not introduce a disadvantage for the proposed system, since – due to the reversibility of the visible light system (red) – an additional step results can again trigger the dimerisation to obtain the final product.

5.3 Preliminary Polymer Studies

Due to the fact that the dichromophore studies, described in the previous Chapter, had been successful, the employed Et-Mal was substituted with an end-functional polymer to explore first steps towards network formations. Specifically, the reactivity of **8** was tested in the presence of PEG with maleimide as an end group (mPEG-Mal). Experiments were conducted in a similar fashion than with Et-Mal to investigate the occurring reactions in both wavelength regimes (visible and UV light). Analysis via UV/Vis spectroscopy (**Figure 58**) depicted similar results, as already discussed in Chapter 5.2, with the *o*-MBA moiety completely undergoing a [4+2] cycloaddition under irradiation with UV light ($\lambda_{max} = 314$ nm, **Figure 58 B t1**), while subsequent utilisation of visible light ($\lambda_{max} = 416$ nm, **Figure 58 B t2**) led to the dimerisation of the PCA double bond. When irradiating **8** in the presence of mPEG-Mal with light in reverse order ($\lambda_{max} = 416$ nm and subsequent $\lambda_{max} = 314$ nm), first the dimerisation of the PCA functionality was triggered and subsequently its dissociation alongside the cycloaddition of the *o*-MBA side (**Figure 58 A**). In both cases, UV irradiation led to similar absorption patterns, encountered with the model compounds. In addition to UV/Vis spectroscopy, the samples were analysed via SEC. However, while the SEC traces depicted the anticipated changes (**Figure**

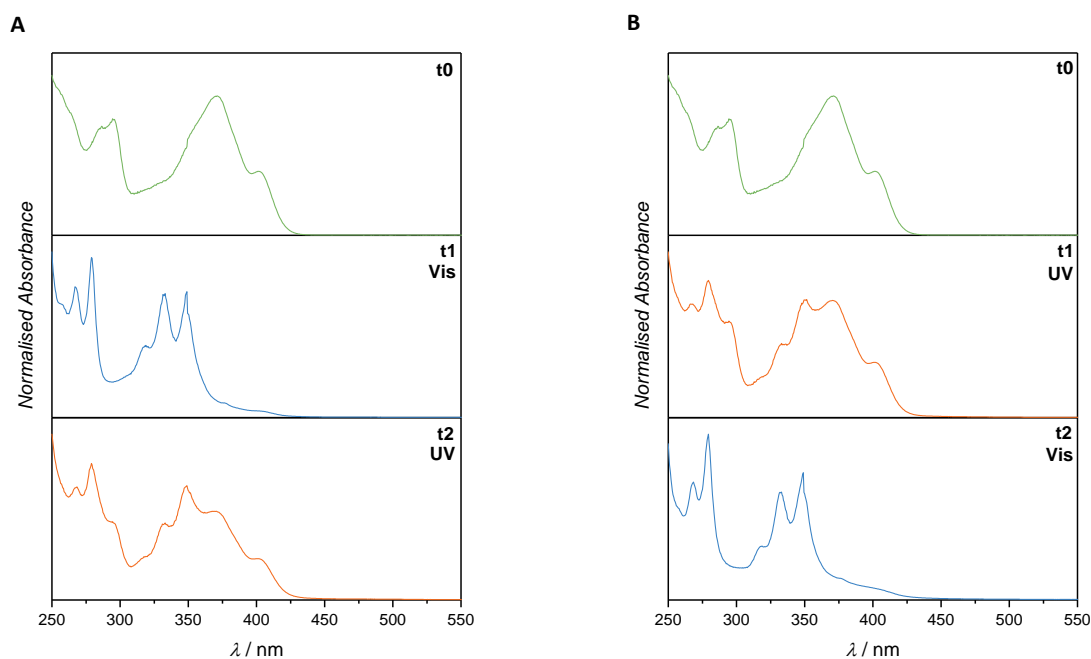


Figure 58. UV/Vis spectra of **8** in presence of mPEG-Mal: (A) before irradiation (t_0), after irradiation with visible light (t_1 , $\lambda_{max} = 416$ nm, 5 h), and subsequent irradiation with UV light (t_2 , $\lambda_{max} = 314$ nm, 3 h). (B) before irradiation (t_0), after irradiation with UV light (t_1 , $\lambda_{max} = 314$ nm, 3 h), and subsequent irradiation with visible light (t_2 , $\lambda_{max} = 416$ nm, 5 h). Published in 2019 by The Royal Society of Chemistry.

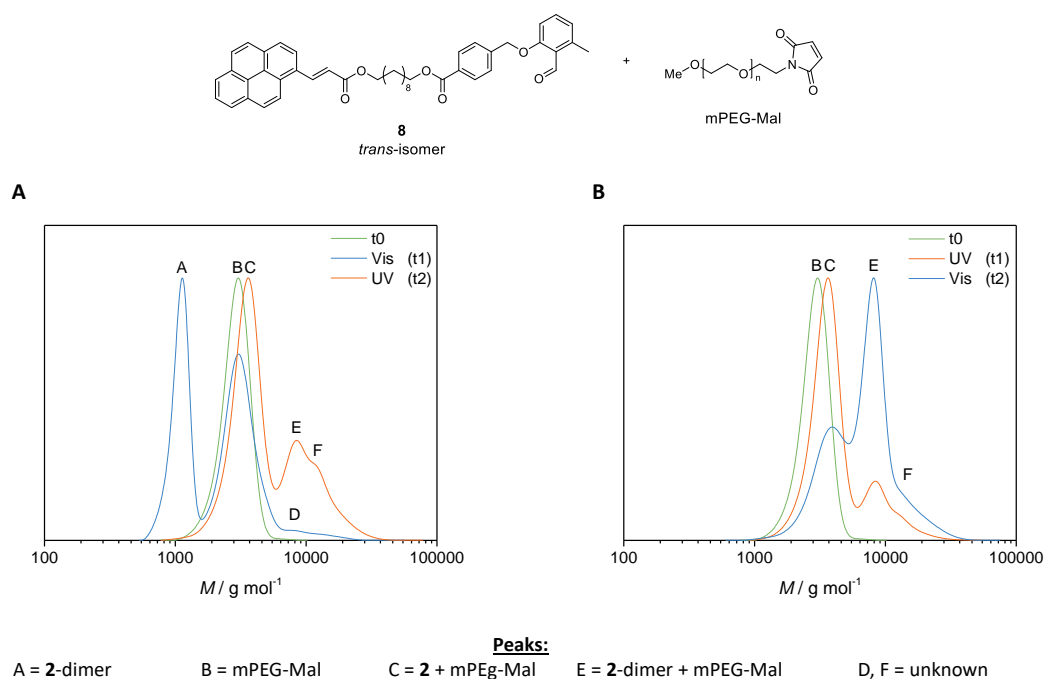


Figure 59. THF-SEC measurements of **8** in the presence of mPEG-Mal: (A) before irradiation (t_0), after irradiation with visible light (t_1 , $\lambda_{\max} = 416$ nm, 5 h), and subsequent irradiation with UV light (t_2 , $\lambda_{\max} = 314$ nm, 3 h). (B) before irradiation (t_0), after irradiation with UV light (t_1 , $\lambda_{\max} = 314$ nm, 3 h), and subsequent irradiation with visible light (t_2 , $\lambda_{\max} = 416$ nm, 5 h). Published in 2019 by The Royal Society of Chemistry.

59), they also featured unknown shoulders to higher molecular weights. In detail, irradiation with visible light (blue trace, **Figure 59 A**) introduced dimerisation of **8** with a new peak arising at around 1100 g mol^{-1} (A). In addition, there is a small shoulder towards higher molecular weights (D) that remained unknown. Subsequent irradiation with UV light (orange trace) led to a small shift of the starting material mPEG-Mal (B) to peak C caused by the reaction of the polymer with **8**. Such findings confirm that the cycloreversion is taking place alongside the [4+2] cycloaddition of the *o*-MBA unit. However, in these preliminary studies, no full conversion was reached, due to presence of peak E that represents the adduct of mPEG-Mal with the **8**-dimer. An additional shoulder could be found at even higher molecular weights (F) including some tailing that could not be explained within the time frame of the current thesis.

Irradiating **8** in presence of mPEG-Mal in reverse order (UV and subsequently visible light), similar results were obtained (**Figure 59 B**). The starting material B slightly shifted to peak C under treatment with $\lambda_{\max} = 314$ nm, while also undergoing the [2+2] cycloaddition of the dimerisation of the PCA unit. Subsequent utilisation of visible light significantly increased the amount of peak E, successfully indicating the dimerisation reaction. However, upon irradiation with both wavelengths a high molecular weight shoulder (F) was formed.

To further investigate the shoulders and tailing observed in the SEC traces, all photochemical experiments conducted in Chapter 5.1 and 5.2 were submitted to SEC analysis and thoroughly

investigated. The unknown shoulder towards higher molecular weights was present in all measured spectra. Since similar results were found when irradiation **8** with Et-Mal (Appendix **Figure 156**), the mPEG-Mal could not be responsible for the unexpected behaviour. Furthermore, the unidentified peaks were also present in SEC chromatograms of previously irradiated **8** in absence of Et-Mal (Appendix **Figure 157**) as well as photochemical experiments with **9** (Appendix **Figure 158**), which did not feature a *o*-MBA moiety. Hence, both functional groups, Et-Mal and *o*-MBA, cannot be the reason for the unexpected behaviour during SEC measurements. For further clarification, only pyrene without any functional groups was irradiated with both wavelengths ($\lambda_{max} = 314$ and $\lambda_{max} = 416$ nm) and analysed via NMR and SEC. Unfortunately, the molecules **9** and especially pyrene feature low molecular weights that were overlapping with the SEC systems peaks, making the analysis challenging. Nonetheless, irradiated pyrene samples show unknown shoulders and tailing in SEC chromatograms (red boxes, Appendix **Figure 159**), while there are no visible changes in the NMR spectra (Appendix **Figure 160**). As a result, the shoulders observed in all SEC measurements are very likely due to the pyrene moiety present in the molecules **8** and **9** and possibly caused by pyrene-pyrene stacking. However, there is no literature available clarifying the effect of stacking on SEC measurements and thus, these assumptions would need to be confirmed in further studies.

Nonetheless, it could be shown that the shoulder is not arising from side reactions that could interfere with the presented wavelength-orthogonal system presented in this study. The preliminary polymer studies could already show promising results for further investigations not only with maleimide as a polymer end group but in a further step towards wavelength-orthogonal materials with maleimide side functionalities along a polymer backbone.

Overall, the wavelength-orthogonality was proven for the first irradiation step for the dichromophore presented in the current thesis. An additional second step might not be orthogonal anymore, however, due to the reversibility of the PCA moiety, subsequent irradiation leads to the same final product and, thus does not pose any challenge to the dichromophore. Therefore, PCA and *o*-MBA could be readily employed in studies towards cross-linking molecules in networks. In future studies, the end-functional mPEG-Mal can be exchanged with side-functional polymer strands to be cast into films and cured upon irradiation with light. Further expanding the concept, the linear alkyl-chain used a linker in between PCA and *o*-MBA can be exchanged with different molecules, *e.g.* star-shaped structures to obtain multifunctional polychromophores, while investigating photochemically reactive functional groups that can be employed alongside the PCA and *o*-MBA. Such polychromophores would allow to generate materials

that can be cured in a wavelength-orthogonal fashion, to obtain disparate materials simply by choice of the employed wavelength.

6

Towards Reversible Gradient Nanocellulose Materials

Gradient materials are a highly interesting class of materials, since they enable stress delocalisation, while concomitantly their mechanical properties such as stiffness or toughness can be finely adjusted. In addition, such materials can provide more resistant joints in a material that features regions of high elasticity and high stiffness. If gradients would feature reversibility, it would allow the material to be reprogrammable and therefore perform complex operations on-demand. As described in Chapter 2.1, the most common type of gradients are sandwich type gradients. However, these feature disadvantages such as breaking points in between each layer type. A more favourable gradient type are lateral gradients that continuously change from stiff to flexible. Photochemistry holds vast promise towards rewriteable lateral gradient materials. On the one hand, due to its reversible cycloadditions and on the other hand, due to its spatially resolved nature, allowing to control which parts of a material should be cross-linked to a further extent and thus, feature a higher stiffness. Especially styrylpyrene could pave the way towards reprogrammable gradients since its trigger wavelengths are among the mildest known, allowing its reversibility to be used without introducing damage to the material itself or its surroundings (*e.g.* solvent, non-functionalised material, human tissue). In the previous Chapters, styrylpyrene has already been investigated with regard to reversibility and its applicability in materials. The reversible chromophore can not only be triggered over several lifetimes (Chapter 3.4) but

also be incorporated into synthetic polymer strands and cross-linked in a spatially resolved and wavelength-orthogonal fashion (Chapter 4.3).

While synthetic polymer strands can be used in many different industry fields such as automotive coatings, dental applications, or in computer science, they are often rather limited in more biologically oriented areas. To achieve compatibility with the latter, nanopapers and nanocomposites formed with sustainable cellulose nanofibrils (CNF) can be used. CNFs are typically isolated from wood and are well-defined bionanoparticles.^{103,176} Featuring a highly crystalline character, the nanofibrils are also a desirable material, since cellulose is one of the stiffest natural materials. As a result, CNFs open promising pathways towards sustainable and high-performance soft matter materials.

Combining CNFs with the reversible photochemistry of styrylpyrene allows to introduce not only spatially resolved lateral gradients but also reprogrammability. Hence, to achieve such properties, the expertise of the group of Prof. Andreas Walther (Albert-Ludwigs-University Freiburg) – and his PhD student Daniel Hönders – on the topic of nanocellulose was combined with our expertise in photochemistry, in particular styrylpyrene, obtained throughout the current thesis.

The overall strategy followed in this cooperation was to cast modified CNFs together with functionalised polymers into films that can subsequently be irradiated to achieve cross-linking

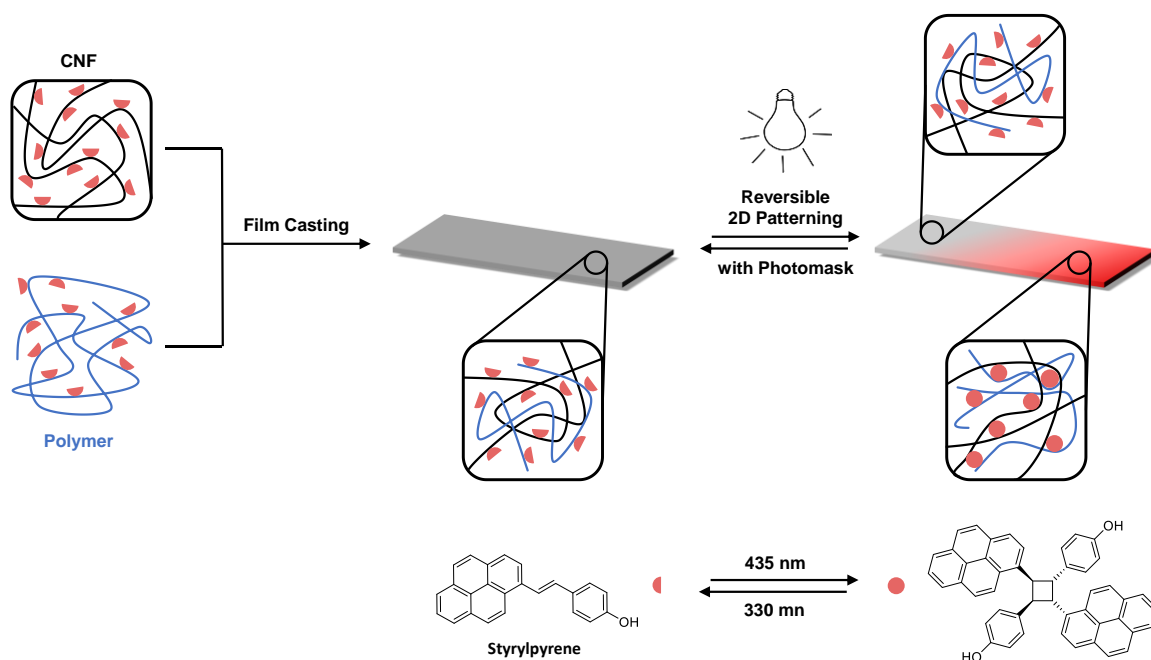


Figure 60. After casting CNF and a water-soluble polymer, both functionalised with styrylpyrene **1**, into a film, the latter can be employed in a reversible 2D patterning step to obtain a material with a lateral gradient. The cross-link density, and therefore stiffness of the material, is dependent on the light intensity and time the film is irradiated with.

(**Figure 60**). The latter was achieved via styrylpyrene groups incorporated into both, CNF and polymer, to allow for a light-induced cycloaddition for gradient materials or patterned films. Due to the reversible nature of the chromophore, the obtained materials could be rewritten simply through irradiation with different wavelengths.

Cellulose is usually handled in water and, thus, the in Chapter 4.3 employed polymer samples were unsuitable for this project. To obtain water-solubility, a StyP-Monomer (StyP-O-MA, **10**), synthesised from StyP **1**, hydroxyethylmethacrylate (HEMA), and 5-bromovaleric acid, was copolymerised with triethylene glycol methyl ether methacrylate (mTEGMA) since the latter is known to feature a good solubility in water (**Figure 61**). Due to its versatility and control over the resulting dispersity and molecular weight, RAFT was chosen as the polymerisation technique (refer to Chapter 2.2.2). The reaction was conducted in toluene with 2-cyano-2-propyl dodecyl trithiocarbonate (CPDT) as CTA and azobisisobutyronitrile (AIBN) as the initiator. To conduct mechanical testing and compare the effect of the amount of StyP per chain, two different samples should be synthesised: a polymer with a low molecular weight and a low amount of the chromophore vs. a high-molecular weight sample with a higher amount of styrylpyrene. In addition, sufficient amounts of approximately 3 g per sample were required to be able to perform all cross-linking experiments with one polymer batch.

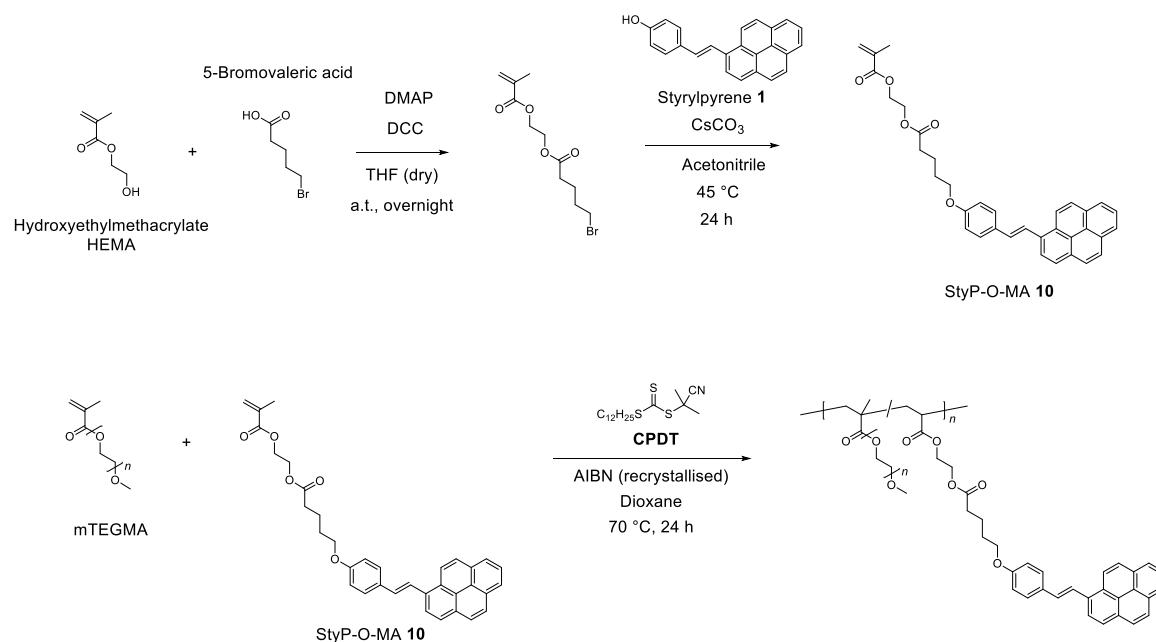


Figure 61. Synthesis of the styrylpyrene monomer StyP-O-MA **10**, and its copolymerisation with mTEGMA to yield the polymers **P3** and **P4**.

Small-scale polymerisation tests revealed that the polymerisation of both monomers was feasible at 70 °C for 24 h, with a targeted amount of 6.9 mol-% styrylpyrene (68.3 eq. mTEGMA : 5.00 eq. StyP-O-MA). Scale-up with a factor of 10 resulted in 2.73 g of a polymer

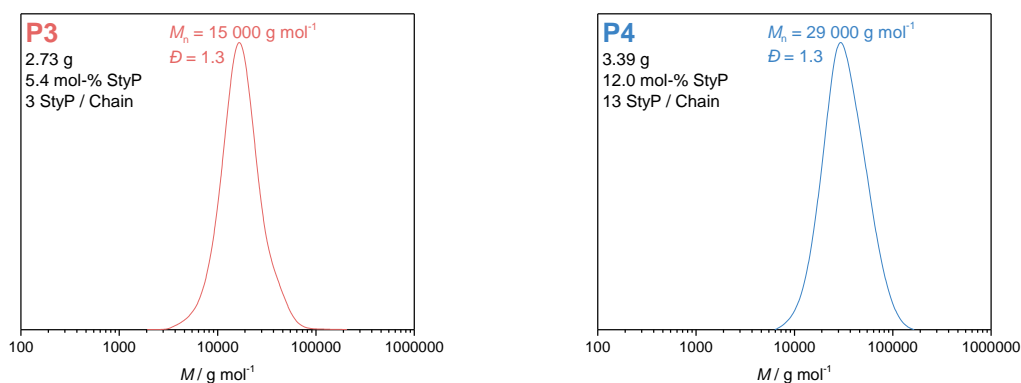


Figure 62. THF-SEC measurements (RI detector) of the polymers **P3** and **P4**.

P3 with a molecular weight of $15\,000\text{ g mol}^{-1}$ ($\bar{D} = 1.3$) and around 5.4 mol-% of styrylpyrene, which represents approximately three light-responsive units per chain (**Figure 62**).

To synthesise a sample that not only features a higher molecular weight but also more chromophore molecules per chain, the amount of mTEGMA was doubled (136 eq) while styrylpyrene was multiplied by four (20 eq.). The obtained polymer (**P4**, 3.39 g) featured a molecular weight of $29\,000\text{ g mol}^{-1}$ ($\bar{D} = 1.3$) with approximately 12.0 mol-% of styrylpyrene and thus, 13 units per polymer strand (**Figure 62**).

Both polymers (**P3** and **P4**) were soluble in water up to at least 2 wt-%, while short irradiation experiments of **P3** could visually reveal that the sample cross-links into a film when utilising visible light (Appendix **Figure 161**). However, **P3** and **P4** were very sticky and viscous samples, which made their handling rather difficult. Due to the limited amount of the samples, no further irradiation experiments were conducted before sending the samples to Daniel Hönders in Freiburg.

In accordance with the project plan in **Figure 60**, the styrylpyrene-containing polymers should be cast into films together with nanocellulose fibrils carrying the same chromophore **1**. Specifically, nanocellulose is oxidised using TEMPO, transforming its hydroxy into carboxyl groups. Subsequently, the carboxy-functional nanocellulose can react with amines to form amide bonds. Therefore, styrylpyrene was functionalised with Boc-TOTA using *N*-hydroxysuccinimid to form an active ester as an intermediate (**Figure 63**). The successful formation of the product was evidenced via $^1\text{H-NMR}$ (**Figure 63**). A diamine TEG derivate was selected to not only improve the water-solubility when compared to a comparable alkyl derivate but also to avoid ester bonds in the final molecule since they are prone to degradation in aqueous basic conditions, which are necessary for the nanocellulose functionalisation. Since one of the two amine groups of TOTA is protected with a Boc group, difunctionalisation with StyP can be

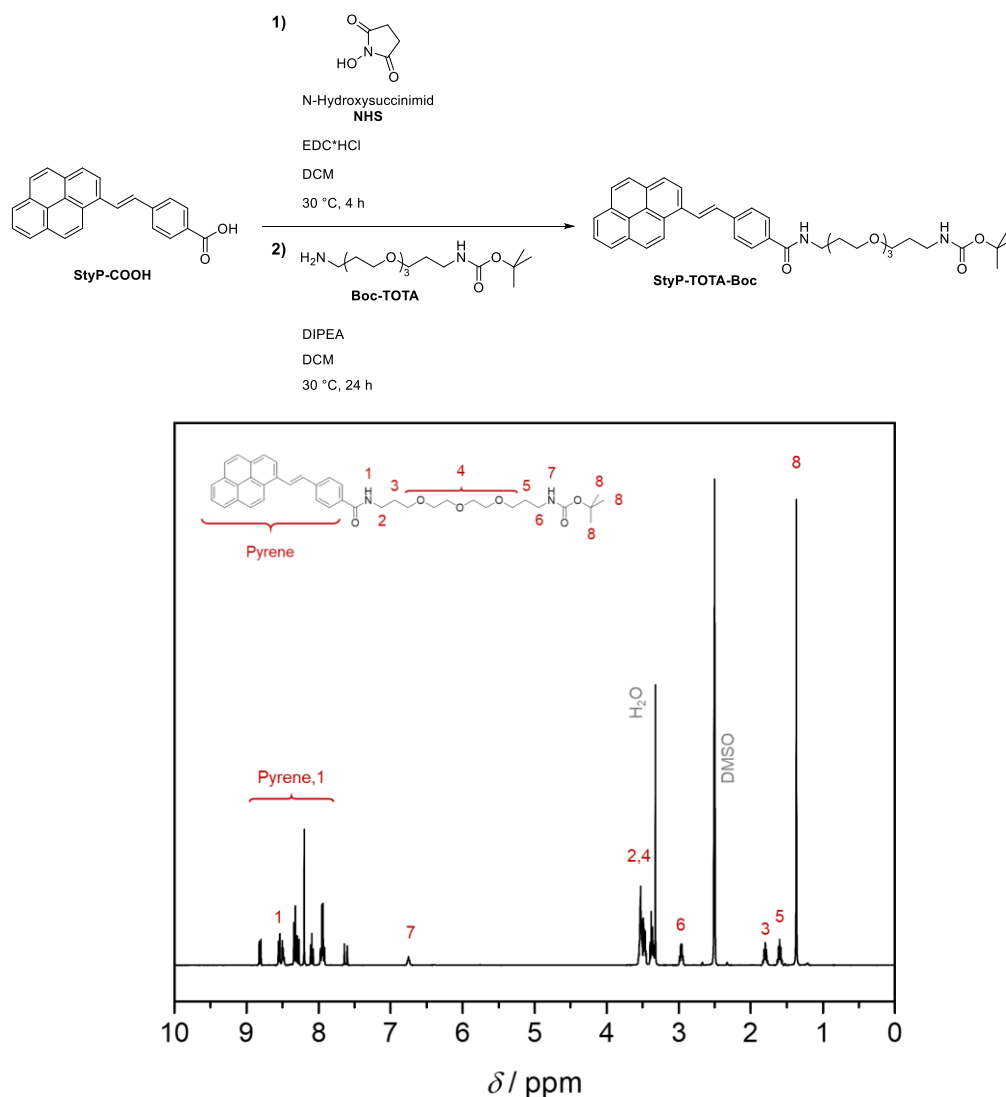


Figure 63. Synthesis and $^1\text{H-NMR}$ spectrum (DMSO-d_6) of the styrylpyrene-functional amine.

avoided and purification via column chromatography is facilitated when comparing the Boc protected amine to a free amine group. In addition, the Boc protection group can be readily removed via acidic treatment. Functionalisation of the nanocellulose fibrils was successfully conducted by Daniel Hönders and further results as well as experimental descriptions can be found in his thesis, with a short overview given in the following section.

The obtained styrylpyrene-CNF (COOH / StyP / DMTMM = 1 / 3 / 3, refer to Chapter 8 ‘Experimental Part’) were too hydrophobic and could not be employed in a stable dispersion. Thus, the respective films were brittle, prone to breakage upon handling and visibly inhomogeneous. A possible solution to this problem is to reduce the degree of styrylpyrene functionalisation (*e.g.* COOH / StyP / DMTMM = 1 / 1 / 1) or possibly substituting the styrylpyrene in a second position to attach an additional hydrophilic group. However, on the one hand, altering the electronic system of styrylpyrene via attachment of another functional group would possibly also

alter the photochemical reactivity of styrylpyrene, rendering it impossible to predict if the light-induced cycloaddition would still proceed upon irradiation with visible light. On the other hand, reducing the amount of styrylpyrene per CNF by the factor of three might decrease the cross-linking performance of the CNFs.

Overall, the styrylpyrene-functional polymer strands as well as the final styrylpyrene-containing nanocellulose fibrils should be cast into films and subsequently investigated in photochemical experiments. Irradiation with visible light introduces intramolecular cross-linking of the styrylpyrene units to form a network between polymer and nanocellulose fibrils. The films will be characterised via mechanical tests to observe the changes introduced during irradiation. In addition, treatment with UV light results in dissociation of the styrylpyrene dimers and thus, to de-cross-linking of the previous films. The cross- and de-cross-linking should be conducted in various subsequent experiments to observe the behaviour of the material over several lifecycles and towards reprogrammability. In addition, irradiation with variation of the irradiation intensities, for example by employing a photomask that is gradually changing from transparent to opaque, introduces different cross-linking densities. The resulting materials should be gradually changing from flexible to stiff and thus inherit a lateral linear gradient, which should be confirmed via mechanical testing, *e.g.* digital image correlation (DIC) or atomic force microscopy (AFM).

Due to the fact that no stable styrylpyrene-CNF dispersion for film casting could be achieved yet, irradiation and mechanical tests were conducted on films consisting of styrylpyrene-functional polymers with unfunctionalised CNFs (50 / 50 wt-%). The films with a thickness of close to 20 μm have been irradiated with 430 nm for 30 minutes. Mechanical testing (*i.e.* tensile tests) could reveal changes before (solid line) and after irradiation (dotted line), with the latter being stiffer, proving the successful cross-linking of the films via the dimerisation of styrylpyrene (**Figure 64 A**). In addition, the fluorescence of the films visibly changed during the irradiation procedure (**Figure 64 B**), which is caused by the cycloaddition of StyP **1** and has been described in literature already.⁸⁶ For comparison, the polymer samples were cast into films of close to 20 μm thickness without CNFs. However, due to the high viscosity and stickiness of the polymer samples, the films stuck to the glass surfaces they were cast onto and could not be removed. Therefore, a petri dish made from PET was designed and is currently being manufactured. In addition, UV irradiation tests have not yet been conducted with the irradiated polymer / CNF films.

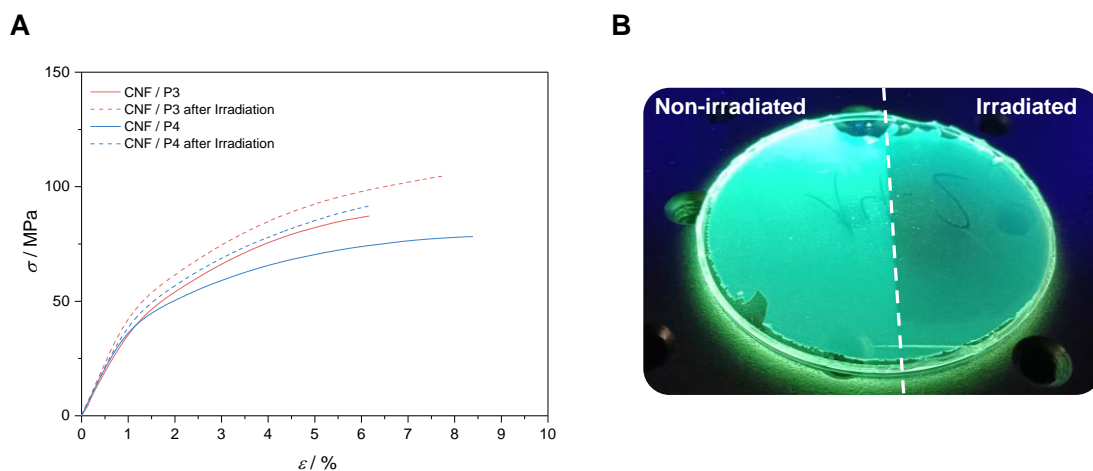


Figure 64. (A) Mechanical testing and (B) macroscopically observed fluorescence of films containing CNF and styrylpyrene-functional polymers (**P3**, **P4**) before and after irradiation with $\lambda_{\text{max}} = 430 \text{ nm}$ for 30 min.

In conclusion, several styrylpyrene-functional polymers as well as a styrylpyrene-amine molecule were synthesised. Functionalisation of nanocelluloses acid groups with the styrylpyrene-amine results in light responsive fibrils that – combined with the styrylpyrene-functional polymers – will be subjected to irradiation experiments and mechanical tests towards reprogrammable gradient materials. However, the so far obtained styrylpyrene-CNFs did not yield any stable dispersions suitable for film casting yet. Several different approaches – such as reducing the amount of styrylpyrene per CNF – are available to overcome these problems. As described in Chapters 3 and 4, styrylpyrene has already been shown to not only form and break bonds on-demand once but also over several dimerisation / dissociation cycles. Thus, **1** is highly suitable for application in reprogrammable materials. In addition, polymer ligations to form either block-copolymers or networks were successfully conducted, and first mechanical tests showed improved performance for irradiated films of styrylpyrene-polymers mixed with CNF. With these first successful steps already taken, styrylpyrene is highly promising for gradient materials that can be reprogrammed on demand. The next steps for the investigation of reprogrammable gradient materials with styrylpyrene-functional polymers and CNFs are optimising the functionalisation of the CNFs with **1** to obtain a stable dispersion suitable for film casting, as well as casting films of polymers **P3** and **P4** utilising the newly design PET petri dish to compare the obtained films with the already obtained results presented in **Figure 64**. Finally, the styrylpyrene polymers and styrylpyrene CNFs will be cast into films and mechanically tested, before irradiation and after irradiation with visible light, expecting the films to feature a higher stiffness and strength when treated with visible light. Mechanical testing can be conducted via tensile tests, subjecting a sample to controlled tension until failure, or dynamic mechanical tests (DMA), in which a sinusoidal stress is applied to a material while measuring the introduced

strain. Subsequently to curing with visible light, the films will be irradiated with UV light to obtain the starting material that should be more flexible due to a lower cross-link density. Overall, several different irradiation cycles will be conducted to prove the reversibility of the styrylpyrene-containing material and, thus, its suitability for reprogrammable materials. Most importantly, films will be irradiated while employing 2D patterning photomasks to obtain materials that feature lateral linear gradients in flexibility and strength towards reprogrammable gradient materials.

7

Conclusion and Outlook

In the present thesis, reversible photochemical cycloadditions were explored to obtain fundamental insights into the precise wavelengths required to trigger their reactions and develop strategies for their implementation in potential reprogrammable gradient materials. In particular, the cycloaddition and -reversion of the red-shifted chromophore styrylpyrene (StyP) were investigated. Detailed analysis of the dimerisation reaction of StyP upon irradiation with visible light above 400 nm revealed that – starting from the *trans*-structure of StyP – isomerisation as well as dimerisation takes place. The light-induced [2+2] cycloaddition generates three isomeric cyclobutane structures that are all derived from two *trans*-molecules that react with each other and lead to final photoproducts with different orientations for the pyrene and phenyl systems.

Based on the structural assignments with $^1\text{H-NMR}$ spectroscopy, detailed photochemical investigations via a newly developed procedure, i.e. Wavelength-dependent Photon Efficiency Analysis (WPEA), were conducted. Specifically, irradiating a sample with different wavelengths, but constant parameters such as concentration and number of photons, yields an action plot depicting the conversion of a chromophore per wavelength. Based on this action plot, the efficiency of the light-induced reaction can be compared to the absorbance spectrum of the molecule, while also revealing information about the most suitable wavelength to trigger the cycloaddition. In a following step, a further action plot is obtained at the latter wavelength while varying the number of photons the sample is irradiated with. As a result, the reaction conversion can be plotted *vs.* the number of photons required to obtain maximum conversion.

In the current thesis, StyP was explored via WPEA revealing that the most suitable conditions for its dimerisation and dissociation are $\lambda = 435$ nm and $\lambda = 330$ nm respectively, while maximum conversion is obtained at approximately 500 μmol photons. In comparison to its absorbance spectrum, the most suitable trigger wavelength of StyP is shifted by approximately 60 nm to higher wavelengths, allowing the visible light cycloaddition to be triggered with wavelengths that are among the mildest known for reversible cycloadditions.

Moreover, the reaction of StyP was successfully employed in a block copolymer ligation. Irradiation with visible light induced the cycloaddition, forming a block copolymer from two styrylpyrene end-capped polymer strands. The cycloreversion back to the starting materials was achieved by irradiation with UV light. Several dimerisation / dissociation cycles were conducted successfully proving the suitability of the chromophore for reprogrammable materials.

Next, to generate reprogrammable gradient materials, it is essential to introduce the reversible photo responsive moieties into polymeric networks, which can be achieved by several routes, such as the implementation of the chromophores as side groups into polymer chains or as cross-linking additives that can react with the polymer strands to form the network. Both strategies were investigated in the process of the current thesis, while a second chromophore was added to achieve a wavelength-orthogonal system. The advantages of such a system are that one material can be cured with disparate wavelengths to obtain two distinct sets of properties (*e.g.* with regard to stiffness or strength), and that two different reactions can be induced subsequently to each other (*e.g.* network formation and subsequent network functionalisation).

In the studies towards networks via cross-linking molecules, a visible light responsive, reversible pyrenyl cinnamic acid (PCA) derivative was linked to an *o*-methyl benzaldehyde (*o*-MBA) moiety that can undergo an irreversible cycloaddition with maleimides when irradiated with UV light. The resulting dichromophore was tested with regard to its dimerisation in the visible light range as well as the cross-reaction of PCA with Et-Mal when irradiated with UV-light. Both reactions were conducted successfully and independently from each other without any cross-reactions between the two different chromophores. In addition, both reactions can be triggered subsequently to each other and sequence-independent to finally obtain the same product in which both light-responsive moieties underwent their respective light-triggered cycloaddition. Indeed, preliminary polymer studies with a maleimide functional PEG already indicated the high suitability of the investigated dichromophore towards reprogrammable and gradient materials.

Furthermore, the second approach towards reprogrammable gradient materials was investigated, in which side chain-functional polymers can form a network. Therefore, polymer chains were decorated with StyP or *o*-MBA as the side chain functionality. The combination of the two chromophores was tested with regard to cross-reactions via both, small molecules and polymers in solution and it was successfully proven that no reaction takes place and thus, the combination of StyP and *o*-MBA is uniquely suitable for wavelength-orthogonal systems. To further investigate the latter, polymers functionalised with StyP or *o*-MBA were cast into films and irradiated with disparate wavelengths. As a result, two different distinctive materials were obtained that were already visually different after irradiation. Post developing introduced wrinkles into the material cross-linked via *o*-MBA (cured with UV-A light), while areas that were cross-linked utilising the dimerisation of StyP (cured with visible light) remained smooth. In addition, mechanical testing via AFM showed that the material cured with visible light is stiffer and more adhesive than the material cured with UV-A light.

In conclusion, the investigations showed that StyP as a reversible visible light chromophore can be combined with the UV-light triggered *o*-MBA dimerisation to obtain a fully wavelength-orthogonal material. Combined with the reversibility of StyP – investigated in the previous polymer ligation studies – StyP proved to be highly suitable towards reprogrammable material design.

In additional studies, StyP was introduced into water-soluble polymer strands (via copolymerisation with a TEG monomer) to be combined with StyP-functional nanocellulose fibrils. Mechanical testing of the StyP polymers revealed that irradiation with visible light led to a stiffer material. In on-going studies – conducted by Daniel Hönders, the cooperation partner of this project at the University of Freiburg – the polymers are currently investigated towards their reversibility under irradiation with UV-A light. In addition, the polymers will be combined with the nanocellulose fibrils and cast into films to compare the differences in mechanical properties to the pure polymer films. Subsequently, the materials will be investigated in studies towards gradient materials that – due to the reversibility of StyP – will inherit reprogrammable properties as well. In conclusion, the already obtained results throughout the current thesis show the high suitability of StyP for such reprogrammable gradient materials.

To finally obtain reprogrammable gradient materials, the polymer films that have been employed in the current thesis need to be investigated separately for both, reprogrammability as well as properties such as toughness and flexibility with gradients. Therefore, styrylpyrene films need to be cured in a spatially resolved fashion (by employing shadow masks) with visible light to trigger the cycloaddition. After analysis of these cross-linked areas – for example via

AFM – the film needs to be irradiated with UV-A light to achieve de-cross-linking. These two irradiation procedures should be repeated several times, on the one hand employing the same shadow mask to rule out that photodamage is introduced to the material through repeated light-treatment, and on the other hand with different photomasks to prove that the material can be reprogrammed to specific distinct patterns. In addition, the styrylpyrene materials need to be irradiated employing light gradients. To achieve such an irradiation procedure either photo masks can be used that gradually change from transparent to opaque or the irradiation source can be moved while either changing the light intensity or irradiation time. The thus obtained materials need to be mechanically tested for differences, *e.g.* in flexibility / stiffness or adhesiveness. After having successfully proved the suitability of styrylpyrene for both, reprogrammable and gradient materials, the two features need to be combined. In specific, styrylpyrene gradient materials should be generated and subsequent to curing de-cross-linked to obtain the starting material, while repeating these curing / de-cross-linking processes over several irradiation cycles. Combining such a reprogrammable gradient material with a second wavelength-orthogonal reaction, would lead to a highly light-responsive material.

8

Experimental Part

8.1 Analytical Instrumentation and Methods

8.1.1 Nuclear Magnetic Resonance Spectroscopy (NMR)

NMR spectra were recorded using one of the following setups. Measurements were conducted in deuterated solvents and the δ -scale was normalized relative to the respective solvent signals for ^1H spectra and ^{13}C spectra. The annotation of the signals is based on HSQC and COSY experiments. Abbreviations for the multiplicity of the respective signals are: singlet (s), doublet (d), doublet of the doublet (dd), triplet (t), quartet (q), quintet (qu), multiplet (m).

400 MHz NMR Spectrometer at KIT

NMR spectra were recorded on a Bruker Ascend 400 instrument, performing at 400 MHz and a temperature of 298 K.

600 MHz NMR Spectrometer at KIT

The NMR data analysed for the detailed structure assignments in Chapter 3 was obtained with the following parameters:

The NMR spectra were recorded on Bruker Avance III 600 MHz spectrometer with a 5 mm CPTCI inversely detected ^1H , ^{13}C , ^{15}N triple resonance cryogenically cooled probe head with an actively shielded z-gradient. The spectrometer frequencies are 599.70 MHz for proton and 150.79 MHz carbon. The temperature is controlled with the Bruker VT-unit and set to 27° C. The following standard Bruker library experiments are used: proton 1D experiment (zg), COSY

(cosygpmf), TOSY (dipsi2etgpsi), NOESY (noesygpshz), decoupled HSQC (hsqcedetgpsisp2.2) and HMBC (hmbcetgpl2nd). The 1D ^{13}C experiments are recorded with a modified pulse sequence with broadband excitation pulse¹⁷⁷ and spin state selective version of HSQC-TOCSY experiment is performed.¹⁷⁸ The 1D experiments are recorded with 32k (^1H) and 132k (^{13}C) points in the full spectral widths of 14 ppm and 230 ppm. The homonuclear 2D experiments are recorded with 8k or 16k points in the direct dimension leading to spectral resolution of 1 Hz or 0.5 Hz; and 512 increments in the indirect dimension and 16 Hz resolution. The decoupled HSQC experiments are recorded with 2k direct points and 4 Hz resolution, while all other heteronuclear experiments contain 16k direct points and 0.5 Hz resolution; and 640 increments in the indirect dimension leading to resolution of 38 Hz. All 2D matrices are twice zero filled and linear prediction in the indirect dimension is performed.

600 MHz NMR spectrometer at QUT

NMR spectra were recorded on a Bruker System 600 Ascend LH, equipped with an ONP-Probe (5 mm) with z-gradient (^1H : 600 MHz, ^{13}C : 151 MHz,) at a temperature of 298 K.

8.1.2 Size Exclusion Chromatography (SEC)

If not specified otherwise SEC measurements were performed using the Agilent SEC setup.

Agilent SEC at KIT

SEC was performed on an Agilent 1200 system, consisting of an autosampler, a Plgel 5 μm bead-size guard column (50 \times 7.5 mm), one Plgel 5 μm Mixed E column (300 \times 7.5 mm), three Plgel 5 μm Mixed C columns (300 \times 7.5 mm), a differential refractive index detector and a UV detector, using THF as eluent at 35 $^\circ\text{C}$ with a flow rate of 1 mL min^{-1} . The SEC system was calibrated using linear poly(styrene) standards ranging from 370 to 2.5×10^6 g mol^{-1} or poly(methyl methacrylate) standards ranging from 800 to 2.2×10^6 g mol^{-1} . Typically, 100 μL of a 2.0 mg mL^{-1} polymer solution was injected into the columns.

Tosoh SEC at KIT (Soft Matter Synthesis Laboratory)

SEC was performed on a TOSOH Eco-SEC HLC-8320 SEC System, consisting of an autosampler, a SDV 5 μm bead-size guard column (50 \times 8 mm, PSS) followed by three SDV 5 μm columns (300 \times 7.5 mm, subsequently 100 \AA , 1000 \AA and 105 \AA pore size, PSS), and a Waters 2487 dual wavelength absorbance detector (analysis at 254 nm) in series with a refractive index detector using tetrahydrofuran (THF) as the eluent at 30 $^\circ\text{C}$ with a flow rate of 1 mL min^{-1} . The SEC system was calibrated using linear polystyrene standards ranging from 266 to 2.52×10^6 g mol^{-1} .

PSS SEC at QUT

SEC was performed on a *PSS SECurity*² system consisting of a *PSS SECurity* Degasser, *PSS SECurity* TCC6000 Column Oven (60 °C), *PSS GRAM* Column Set (8x 150 mm 10 µm Pre-column, 8 x 300 mm 10 µm Analytical Columns, 1000 Å, 1000 Å and 30 Å) and an Agilent 1260 Infinity Isocratic Pump, Agilent 1260 Infinity Standard Autosampler, Agilent 1260 Infinity Diode Array and Multiple Wavelength Detector (A: 254 nm, B: 360 nm), Agilent 1260 Infinity Refractive Index Detector (35 °C). HPLC grade DMAc, 0.01 M LiBr, is used as eluent at a flow rate of 1 mL min⁻¹. Narrow disperse linear poly(styrene) ($M_n = 266 \text{ g mol}^{-1}$ to $2.52 \times 10^6 \text{ g mol}^{-1}$) and poly(methyl methacrylate) ($M_n = 202 \text{ g mol}^{-1}$ to $2.2 \times 10^6 \text{ g mol}^{-1}$) standards (*PSS ReadyCal*) were used as calibrants. All samples were passed over 0.22 µm PTFE membrane filters. Molecular weight and dispersity analysis were performed in *PSS WinGPC UniChrom* software (version 8.2).

DMAc SEC at QUT

The SEC measurements were conducted on a *PSS SECurity*² system consisting of a *PSS SECurity* Degasser, *PSS SECurity* TCC6000 Column Oven (60 °C), *PSS GRAM* Column Set (8x150 mm 10 µm Pre-column, 8x300 mm 10 µm Analytical Columns, 1000 Å, 1000 Å and 30 Å) and an *Agilent* 1260 Infinity Isocratic Pump, *Agilent* 1260 Infinity Standard Autosampler, *Agilent* 1260 Infinity Diode Array and Multiple Wavelength Detector (A: 254 nm, B: 360 nm), *Agilent* 1260 Infinity Refractive Index Detector (35 °C). HPLC grade DMAc, 0.01 M LiBr, is used as eluent at a flow rate of 1 mL·min⁻¹. Narrow disperse linear poly(styrene) ($M_n: 266 \text{ g} \cdot \text{mol}^{-1}$ to $2.52 \times 10^6 \text{ g} \cdot \text{mol}^{-1}$) and poly(methyl methacrylate) ($M_n: 202 \text{ g} \cdot \text{mol}^{-1}$ to $2.2 \times 10^6 \text{ g} \cdot \text{mol}^{-1}$) standards (*PSS ReadyCal*) were used as calibrants. All samples were passed over 0.22 µm PTFE membrane filters. Molecular weight and dispersity analysis were performed in *PSS WinGPC UniChrom* software (version 8.2).

8.1.3 Electrospray Ionisation - Mass Spectrometry (ESI-MS)

ESI-MS at KIT

Mass spectra were recorded on a Q Exactive (Orbitrap) mass spectrometer (*Thermo Fisher Scientific*, San Jose, CA, USA) equipped with an HESI II probe. The instrument was calibrated in the m/z range 74 - 1822 using premixed calibration solutions (*Thermo Scientific*). A constant spray voltage of 4.7 kV and a dimensionless sheath gas of 5 were applied. The capillary temperature and the S-lens RF level were set to 320 °C and 62.0, respectively. The samples

were dissolved with a concentration of 0.05 mg mL^{-1} in a mixture of THF and MeOH (3:2) containing $100 \text{ }\mu\text{mol}$ of sodium trifluoroacetate and infused with a flow of $5 \text{ }\mu\text{L min}^{-1}$.

ESI-MS at QUT

Spectra were recorded on a Q Exactive Plus (Orbitrap) mass spectrometer (*Thermo Fisher Scientific*, San Jose, CA, USA) equipped with an HESI II probe. The instrument was calibrated in the m/z range 74 - 1822 using premixed calibration solutions (*Thermo Scientific*) and for the high mass mode in the m/z range of 600 - 8000 using ammonium hexafluorophosphate solution. A constant spray voltage of 3.5 kV, a dimensionless sheath gas and a dimensionless auxiliary gas flow rate of 5 and 3 were applied, respectively. The capillary temperature was set to $320 \text{ }^\circ\text{C}$, the S-lens RF level was set to 62, and the aux gas heater temperature was set to $50 \text{ }^\circ\text{C}$. The sample was injected using a syringe pump with a constant flow rate of $5 \text{ }\mu\text{L min}^{-1}$.

8.1.4 Gas Chromatography-Mass Spectroscopy (GC-MS)

GC-MS (EI) chromatograms were recorded by using a Varian 431-GC instrument with a capillary column FactorFour™ VF-5ms ($30 \text{ m} \times 0.25 \text{ mm} \times 0.25 \text{ }\mu\text{m}$), and a Varian 210-MS detector. Scans were performed from 40 to 650 m/z at rate of 1.0 scans s^{-1} . Measurements were performed in the split-split mode (split ratio 50:1) using helium as carrier gas (flow rate $1.0 \text{ mL} \times \text{min}^{-1}$). The oven temperature program was: initial temperature $95 \text{ }^\circ\text{C}$, hold for 1 min, ramp at $15 \text{ }^\circ\text{C min}^{-1}$ to $200 \text{ }^\circ\text{C}$, hold for 2 min, ramp at $15 \text{ }^\circ\text{C min}^{-1}$ to $325 \text{ }^\circ\text{C}$, hold for 5 min. The injector's transfer line temperature was set to $250 \text{ }^\circ\text{C}$.

8.1.5 UV/Vis Spectroscopy

UV/Vis Spectrometer at KIT

UV/Vis spectra were recorded on a Cary 100 UV-Visible Spectrophotometer (Agilent Technologies, USA) equipped with a tungsten halogen light source (190 to 900 nm, accuracy $\pm 2 \text{ nm}$) and a R928 PMT detector. The samples were measured in Starna GmbH quartz high precision cell cuvettes at ambient temperature and baseline corrected with respect to pure solvent. Spectra can be collected between 200 and 800 nm.

UV/Vis Spectrometer at QUT

UV/Vis spectra were recorded on a Shimadzu UV-2700 spectrophotometer equipped with a CPS-100 electronic temperature control cell positioner. The samples were measured in Hellma Analytics quartz high precision cell cuvettes at ambient temperature and baseline corrected with respect to pure solvent. Spectra can be collected between 200 and 800 nm.

8.1.6 Mechanical Testing

Tensile tests: Tensile mechanical properties of the materials were characterised using a Deben Minitester equipped with a 20 N load cell. The tensile test was performed at a controlled relative humidity of 50 % at 23 °C. Rectangular specimen strips of 12.5 mm in length, 2 mm in width, and a thickness in the range of 20-30 μm were tested at a strain rate of 0.1 mm min^{-1} and a gauge length of 10 mm. 7 specimens were tested for each sample.

8.2 Light Sources and Irradiation Setups

8.2.1 LED and UV Lamps

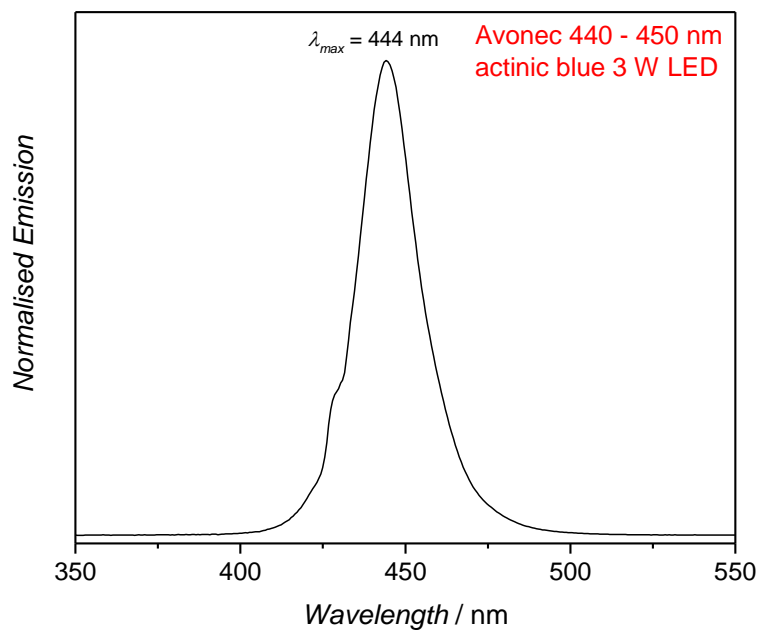


Figure 65. Emission spectrum of the Avonec actinic blue 3 W LED setup for irradiation with $\lambda_{max} = 444 \text{ nm}$.

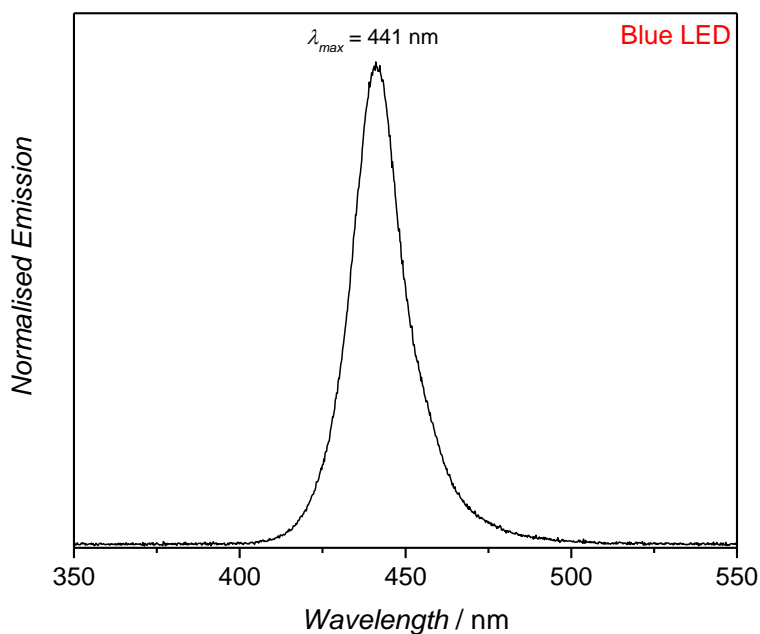


Figure 66. Emission spectrum of the Luzchem LZC-LBL LED for irradiation with $\lambda_{max} = 441 \text{ nm}$.

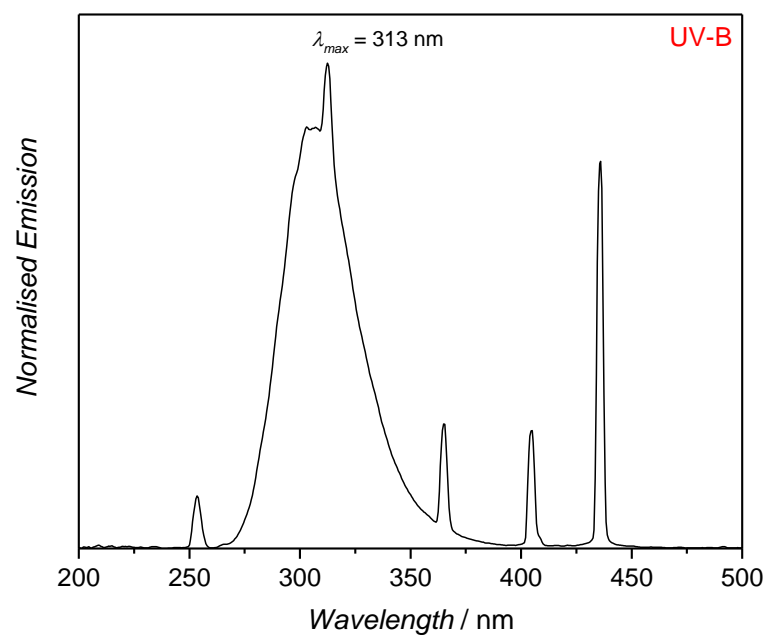


Figure 67. Emission spectrum of the Luzchem LZC-UVB lamp for irradiation with $\lambda_{max} = 313 \text{ nm}$.

8.2.2 UV Light Photoreactor

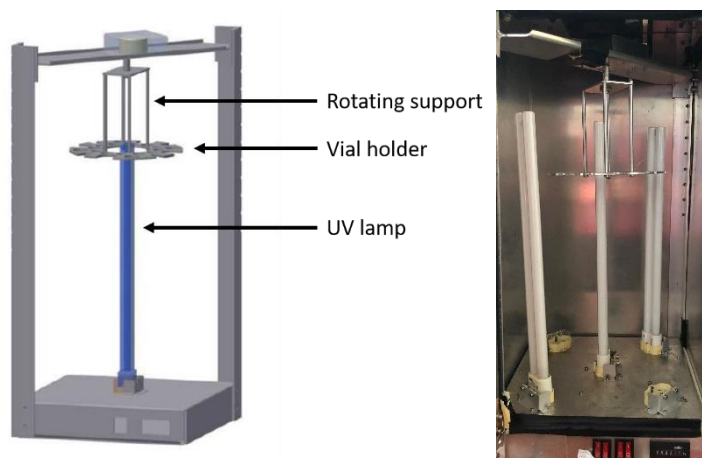


Figure 68. Photoreactor used for irradiation with broad band UV lights. The setup can be equipped with up to five lamps and features a rotating support for the vial holder.

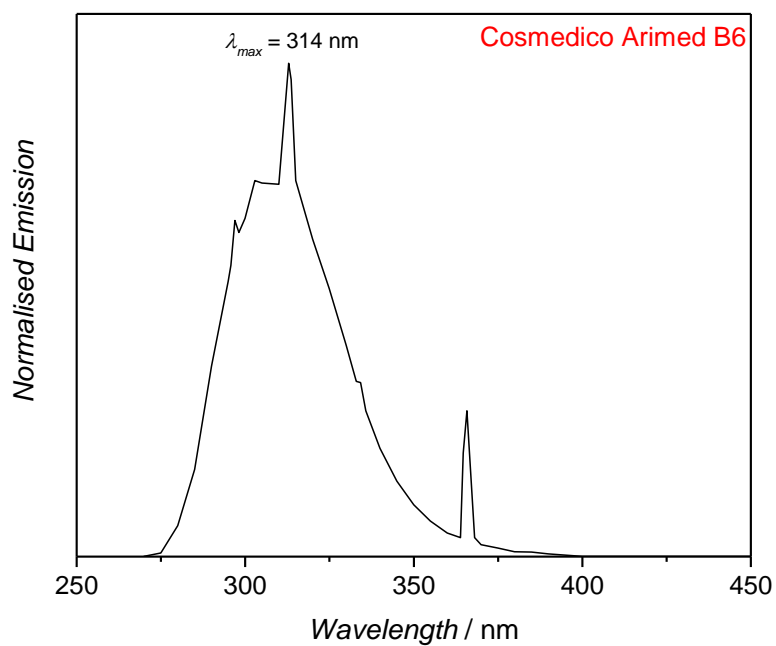


Figure 69. Emission spectrum for the Cosmedico Arimed B6 that can be used with the UV photoreactor for irradiation with $\lambda_{max} = 314$ nm.

8.2.3 Visible Light Photoreactor



Figure 70. Photoreactor used for irradiation with LEDs in the visible light range.

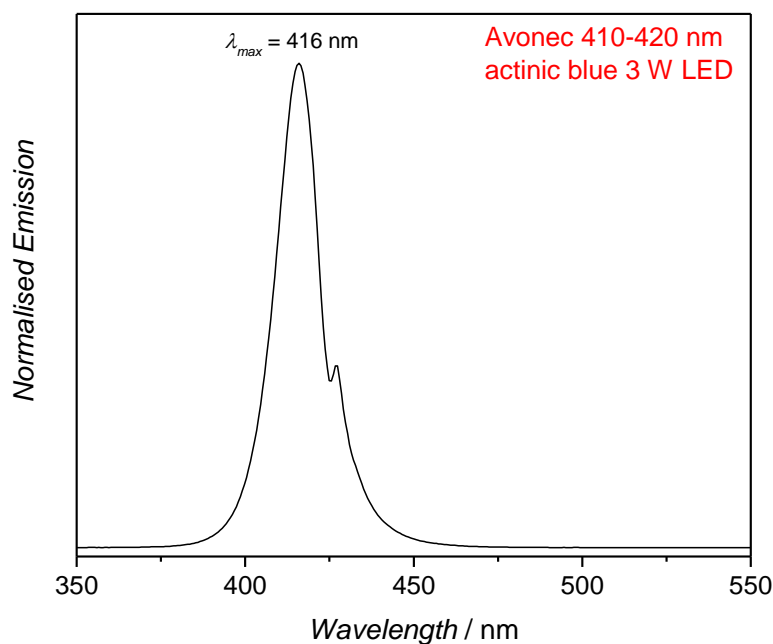


Figure 71. Emission spectrum of the Avonec actinic blue 3 W LED used with the visible light photoreactor for irradiation with $\lambda_{max} = 416$ nm.

8.2.4 Innolas Tuneable Laser System

An Innolas Tuneable Laser System SpitLight 600 OPO was applied as a light source. An optical parametric oscillator (OPO) was pumped with a diode pumped Nd:YAG laser (repetition rate 100 Hz). The energy of the laser pulses was downregulated by an attenuator (polarizer). The beam is redirected into the vertical cylindrical hole of a custom-made sample holder, which contains the samples during the experiments (**Figure 72**). These glass vials are crimped 0.7 mL vials by LLG Labware, Lab Logistic Group GmbH (Art. Nr. 4-008202). The energy of the incident laser pulses was measured by an Energy Max PC power meter (Coherent) directly above the sample holder. Prism and sample holder are positioned in a way that the complete diameter of the hole of the sample holder is covered by the incident laser beam.

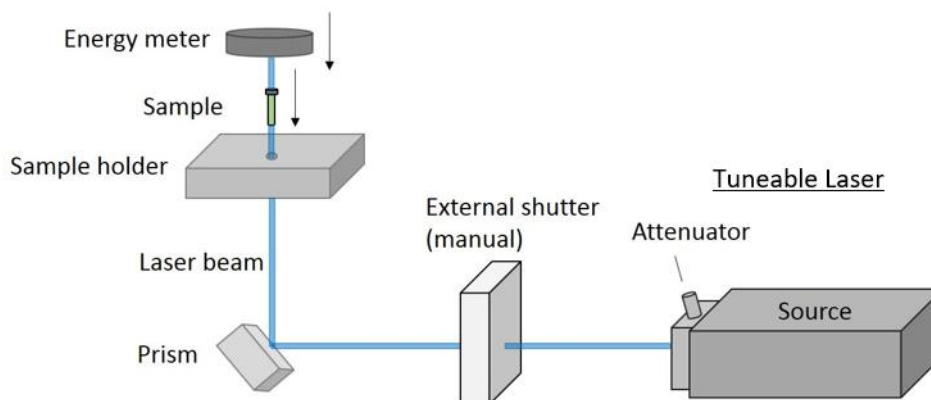


Figure 72. Experimental setup for the tuneable laser experiments. The energy output is regulated with the attenuator and controlled with the energy meter (setup without sample). Measurement of energy and irradiation of samples cannot be carried out simultaneously. An individual setting of the attenuator is necessary before each irradiation experiment.

Control over the Incident Number of Photons in a Tuneable Laser Experiment

The number of photons n_p ($[n_p] = \text{mol}$) that a monochromatic laser pulse contains can be calculated by application of the Planck-Einstein relation from the energy of the pulse E_{pulse} , the incident wavelength λ , Planck's constant h and the speed of light c .

$$n_p = \frac{E_{\text{pulse}} \lambda}{h c N_A}$$

If the absorption of the glass vial and the extent of reflection and scattering at the vial at the respectively relevant wavelength is known, a target energy value can be calculated that must be reached during the above described measurement to guarantee that the desired number of photons penetrates the sample solution during the subsequent irradiation. The wavelength dependent transmittance of the glass vials was determined experimentally using the above setup. Three glass vials were randomly selected as calibration vials. For varying wavelengths and in each case at a constant power output of the laser the energy was measured both with and without the calibration vials fitted into the sample holder. The top parts of these vials were cut off to minimize errors in the procedure, since only the bottom and sides of the glass vials would contribute significantly to the reduction of the photon flux that enters the solution.

The measured energy per pulse without a calibration vial in the sample holder is denoted as E_0 and the measured energy per pulse with a calibration vial in the sample holder as E_n . The transmittance was calculated as the ratio of E_n to E_0 . The average transmittance over the measurements of the three vials (T_λ) was plotted together with the respective error (compare **Figure 74** and **Figure 75**).

$$T_{\lambda} = \frac{E_n}{E_0}$$

The target energy per pulse E_0 can be calculated directly from the wavelength λ , the number of pulses k , the transmittance of the glass vial at the respective wavelength T_{λ} and the desired total photon count n_p .

$$E_0 = \frac{n_p N_A h c}{k T_{\lambda} \lambda}$$

By controlling the target E_0 at the respective wavelength, the number of photons that penetrate each sample solution of one set of experiments as described in the following subsections was guaranteed to be identical despite irradiation at different wavelengths.

Procedure for the Transmittance of the Glass Vials

The transmittance of the glass vials that were used for photoreactions with the tuneable laser system was determined as follows. Measurement of the energy of laser pulses at a constant energy output was carried out directly above the sample holder first without a glass vial in the sample holder and subsequently with an empty glass vial in the sample holder. The headspace section of the glass vials was removed for these measurements to detect only the absorbance of the bottom of the vial (**Figure 73**). The described procedure was performed for three individual glass vials to account for variabilities between the vials. The obtained averaged values are listed in **Table 3** (KIT) and **Table 4** (QUT).



Figure 73. Left: uncrimped vial; right: vial after removal of the headspace section.

Data for the Transmittance of the Glass Vials at KIT*Table 3. Transmittance of the glass vials used for the laser experiments. These values were measured with the tuneable laser setup and vials at KIT.*

KIT Setup		
λ / nm	T_λ / %	Mean Deviation / %
285	13.2	0.2
295	19.7	0.6
305	30.3	0.5
315	37.7	1
325	45.6	0.5
335	47.5	1
345	51.1	0.6
355	56.3	1.2
365	58.9	0.8
375	61	0.9
385	62.9	0.9
395	60.4	0.9
405	64.5	1.6
415	60.4	1.1
425	62.1	0.9
435	65.1	0.3
445	65.9	1.2
455	66.3	1.2
465	67.7	3.1
475	68.8	3.0
485	65.6	3.2
495	65.9	4.0

The data was subsequently fitted to obtain values for the wavelengths that have not been measured during the calibration process (compare **Figure 74**).

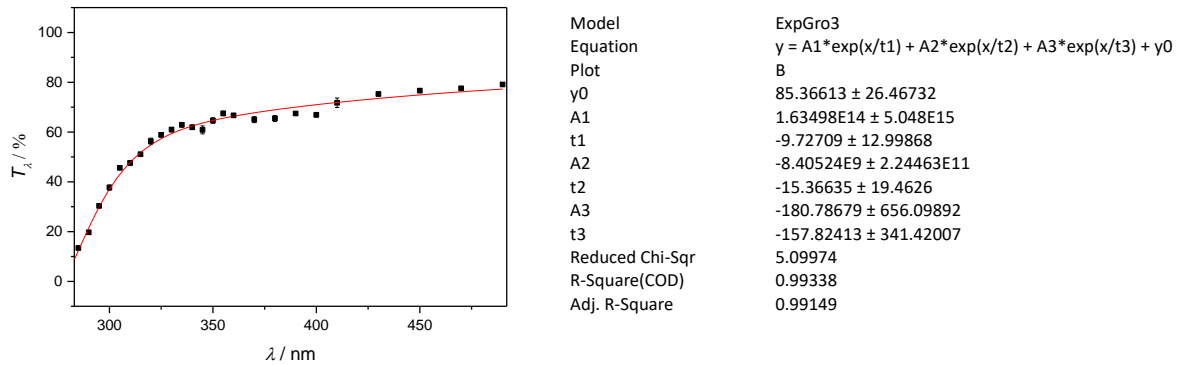


Figure 74. Calibration of the glass vial transmittance including a fit to obtain the values that were not determined experimentally. This calibration was done for the laser setup and Glass vials at KIT.

Data for the Transmittance of the Glass Vials at QUT

Table 4. Transmittance of the glass vials used for the laser experiments. These values were measured with the tuneable laser setup and vials at QUT.

QUT Setup		
λ / nm	$T_\lambda / \%$	Mean Deviation / %
285	13.3	1.3
295	28.2	2.6
305	33.0	3.2
315	43.9	4.3
325	49.1	2.7
335	55.1	3.5
345	55.7	2.4
355	57.5	3.3
365	60.3	4.3
375	61.0	3.6
385	61.1	3.2
395	62.8	3.6
405	62.4	4.6

415	64.8	1.9
425	65.0	2.6
435	67.5	2.0
445	65.9	3.0
455	64.5	2.4
465	67.7	3.1
475	68.8	3.0
485	65.6	3.2
495	65.9	4.0

The data was subsequently fitted to obtain values for the wavelengths that have not been measured during the calibration process (compare **Figure 75**).

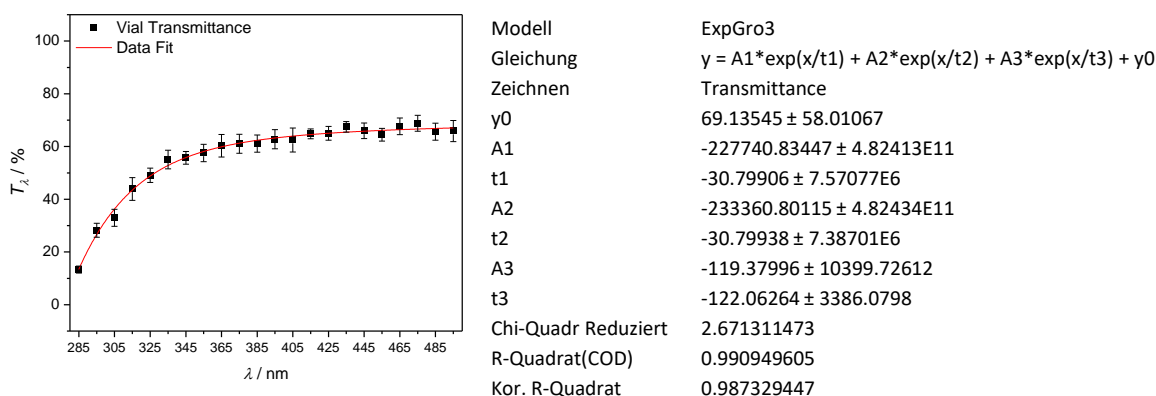


Figure 75. Calibration of the glass vial transmittance including a fit to obtain the values that were not determined experimentally. This calibration was done for the laser setup and Glass vials at QUT.

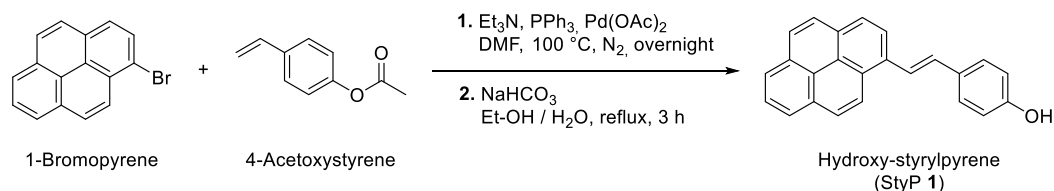
Irradiation Procedure with Control over the Photon Count

Prior to each irradiation, the respective solution was deoxygenated by purging with a stream of nitrogen for five minutes. The tuneable laser, including the pump source, was started and the internal shutter was opened several minutes before irradiation to allow the energy output of the laser to stabilize. The direction of the beam was controlled by adjusting the orientation of the prism. The entire cross-sectional area of the sample is irradiated by the laser beam. The inten-

sity of the beam was monitored and adjusted with the built-in polarizer (attenuator). A calculated target energy value was set, which enables the irradiation with the desired number of photons during the irradiation time.

8.3 Synthetic Protocols

8.3.1 Hydroxy-styrylpyrene (StyP, 1)

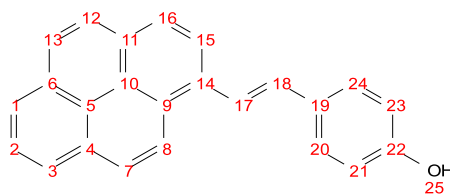


Hydroxy-styrylpyrene was synthesized following a similar reaction procedure published previously in the literature.⁸⁶

4-Acetoxystryrene (0.54 mL, 0.58 g, 3.56 mmol, 1.00 eq.), 1-bromopyrene (1.00 g, 3.56 mmol, 1.00 eq.), palladium(II) acetate (8.00 mg, 35.6 μmol , 0.01 eq.), triphenylphosphine (18.7 mg, 71.1 μmol , 0.02 eq.) and triethylamine (0.73 mL, 1.00 g, 9.88 mmol, 2.78 eq.) were dissolved in DMF (19.8 mL), degassed with nitrogen for 20 minutes and heated to 100 $^\circ\text{C}$. After stirring for 1 day, the solvents were removed under reduced pressure. The obtained solid was dissolved in ethyl acetate (ca. 100 mL), subsequently washed with water (3 x 50 mL) and brine (50 mL), dried over MgSO_4 , filtered and evaporated under reduced pressure.

To obtain the final hydroxy-structure the crude product was deprotected via suspension with NaHCO_3 (0.79 g, 9.44 mmol, 3.00 eq.) in a mixture of ethanol (100 mL) and water (25 mL) under reflux for 3 hours. The mixture was precipitated into a mixture of 1M HCl (100 mL) and ice water (300 mL), filtered, washed with water and purified using a flash chromatography system (cyclohexane / ethyl acetate from 9 : 1 to 8 : 2) to obtain 0.50 g of the product (yield 41 %) as a yellow powder.

$^1\text{H-NMR}$ (400 MHz, Acetonitrile- d_3) δ / ppm = 8.60 (d, J = 9.3 Hz, 1H, 8), 8.38 (d, J = 8.1 Hz, 1H, 15), 8.25 - 8.20 (m, 3H, 1,3,16), 8.17 (d, J = 9.3 Hz, 1H, 7), 8.11 (d, J = 16.1 Hz, 1H, 18), 8.10 (s, 2H, 12,13), 8.03 (t, J = 7.7 Hz, 1H, 2), 7.66 - 7.62 (m, 2H, 20,24), 7.39 (d, J = 16.1 Hz, 1H, 17), 7.1 - 7.2 (bs, 1H, 25), 6.93 - 6.88 (m, 2H, 21,23).



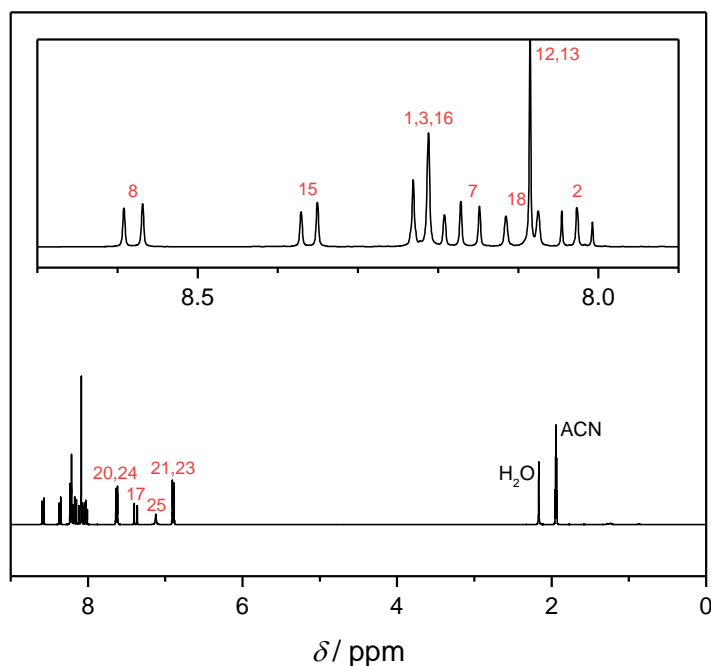
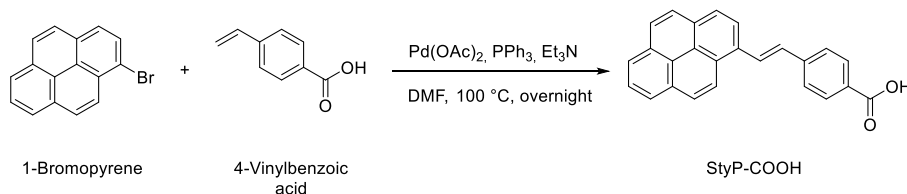


Figure 76. $^1\text{H-NMR}$ (400 MHz, deuterated acetonitrile) of hydroxy-styrylpyrene (StyP 1).

8.3.2 Carboxy-styrylpyrene (StyP-COOH)



Carboxy-styrylpyrene was synthesized following a reaction procedure published previously in the literature.⁸⁶

After dissolving 1-bromopyrene (2.91 g, 9.99 mmol, 1.00 eq.), 4-vinylbenzoic acid (14.0 mL, 1.48 g, 9.99 mmol, 1.00 eq.), triphenylphosphine (52.4 mg, 0.20 mmol, 0.20 eq.) and triethylamine (15 mL, 10.9 g, 108 mmol, 10.8 eq.) in dry DMF (30 mL), the solution was degassed with argon for 30 minutes and next, palladium(II) acetate (22.4 mg, 99.9 μmol , 0.01 eq.) was added. The mixture was heated to 100 $^\circ\text{C}$ and stirred overnight. After the reaction mixture was cooled to ambient temperature, the solvents were removed using a rotary evaporator (60 $^\circ\text{C}$) and the remaining yellow/brown solid suspended in ethyl acetate for 1 h. Subsequently, the solid was filtered off, washed with a small quantity of ethyl acetate and that procedure was repeated twice. Afterwards, the solid was dissolved in little dimethylformamide, precipitated

into water and after filtering freeze-dried. The desired product carboxy-styrylpyrene was obtained as a yellow powder (2.95 g, 82 % yield).

$^1\text{H-NMR}$ (600 MHz, $\text{DMSO-}d_6$): δ / ppm = 8.80 (d, $J = 9.3$ Hz, 1H, 8), 8.57 - 8.52 (m, 2H, 15,18), 8.34 - 8.26 (m, 4H, 1,3,7,16), 8.19 (s, 2H, 12,13), 8.09 (t, $J = 7.6$ Hz, 1H, 2), 8.04 - 7.97 (m, 4H, 20,12,23,24), 7.63 (d, $J = 16.1$ Hz, 1H, 17).

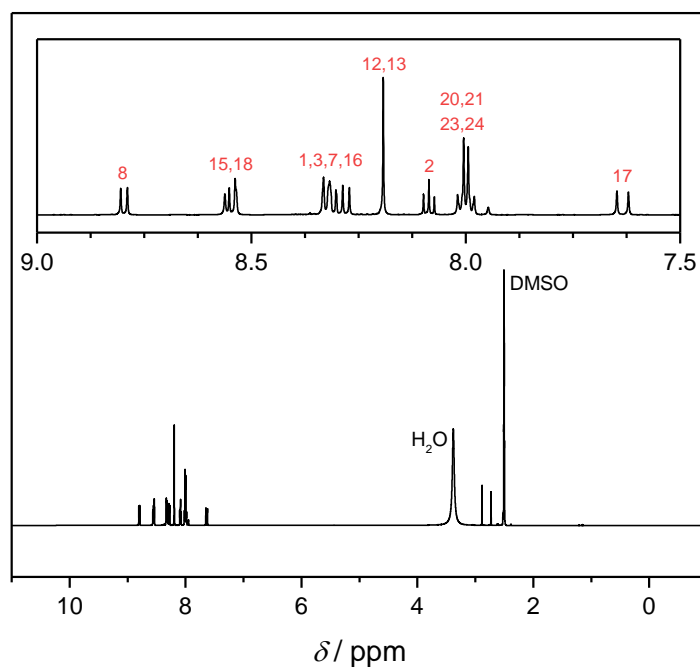
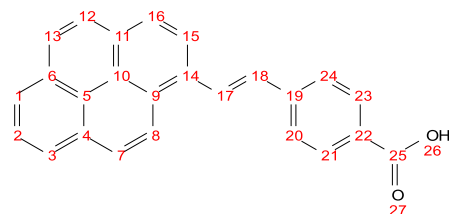
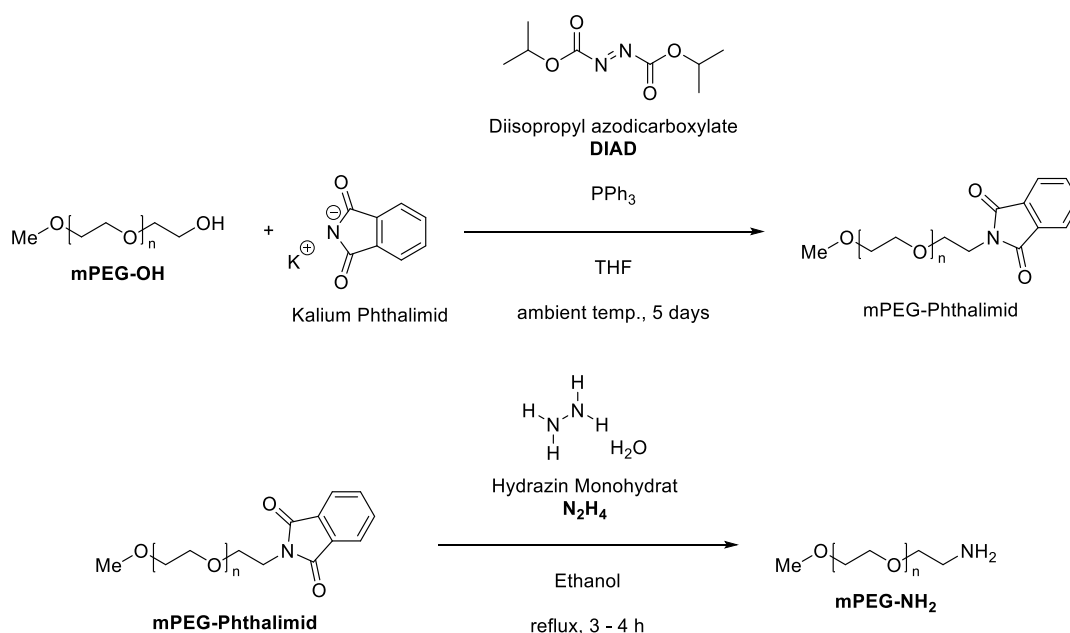


Figure 77. $^1\text{H-NMR}$ (600 MHz, deuterated DMSO) of carboxy-styrylpyrene (StyP-COOH).

8.3.3 mPEG-amine (mPEG-NH₂)



mPEG amine was synthesized from hydroxy-PEG monomethyl ether (mPEG-OH) according to a two-step literature procedure.¹⁷⁹

The experimental procedure described for the preparation of 2-octylamine¹⁸⁰ was adapted to polymers. Diisopropyl azodicarboxylate (DIAD; 2.95 mL, 3.03 g, 0.015 mol, 3.00 eq.) was added dropwise to a solution of mPEG-OH (average $M_n = 1900 \text{ g mol}^{-1}$, 10 g, 0.005 mol, 1.00 eq.), phthalimide (2.21 g, 0.015 mol, 3.00 eq.) and triphenylphosphine (3.93 g, 0.015 mol, 3.00 eq.) in tetrahydrofuran (17 mL) at ambient temperature. The solution was stirred at ambient temperature for 5 days. The solvent was removed under reduced pressure. Afterwards, the product was dissolved in water. The solid was removed by filtration and the aqueous solution was washed with diethyl ether. Water was removed under reduced pressure and the oily product was dried at 40 °C under high vacuum. The yields were quantitative.

Phthalimido-PEG (10.0 g, 0.005 mol, 1.00 eq.) in ethanol (100 mL) were treated with an aqueous solution of hydrazine monohydrate (65%; 2.5 g, 0.05 mol, 10.0 eq.) under reflux for 3 - 4 h. Concentrated hydrochloric acid was added to the cold solution up to pH 2 - 3 and afterwards the solvents removed until only little amounts were left that could be precipitated into cold diethyl ether. The obtained product was then analysed via NMR, ESI-MS and SEC (DMAc).

¹H-NMR (600 MHz, DMSO-*d*₆): δ / ppm = 3.51 (m, b), 3.24 (s, 3H, a), 2.77 (t, $J = 5.6 \text{ Hz}$, 2H, c).

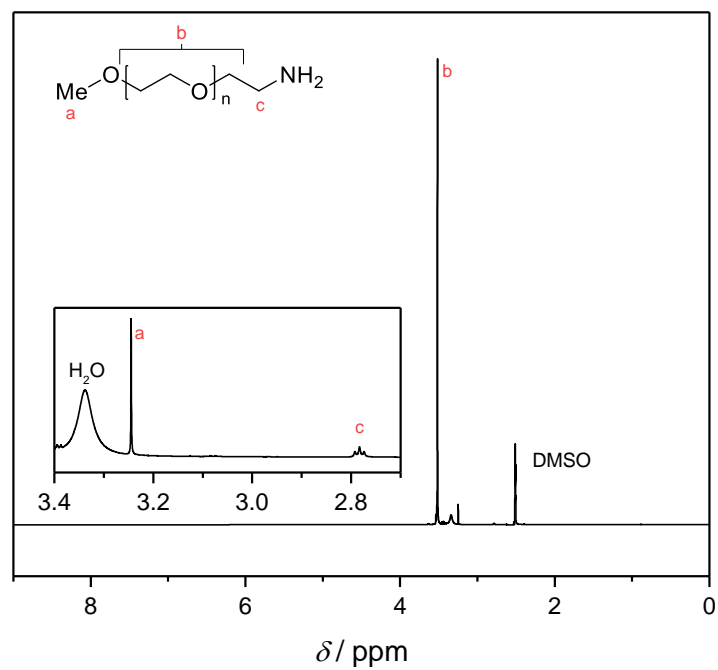


Figure 78. ¹H-NMR (600 MHz, deuterated DMSO) of mPEG-NH₂.

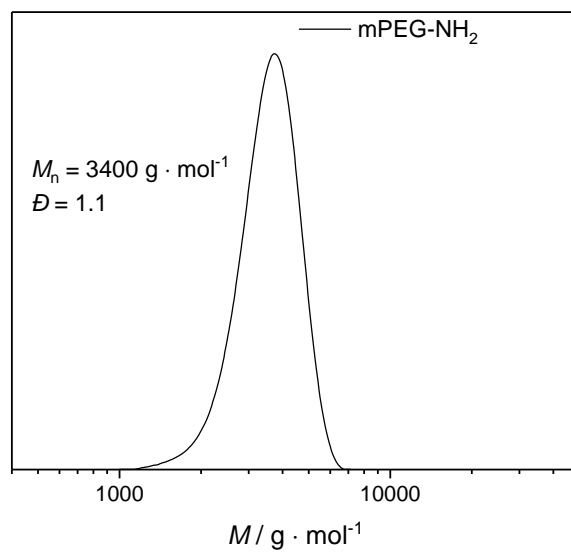


Figure 79. DMAc SEC (RI detector) measurement of mPEG-NH₂.

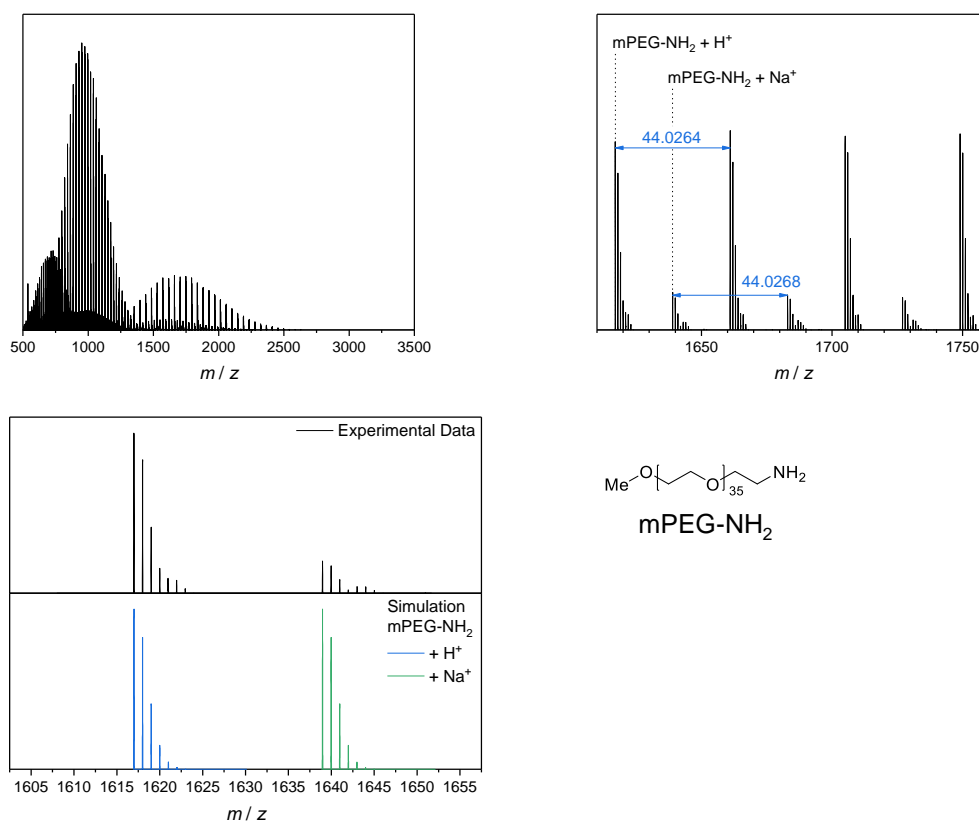
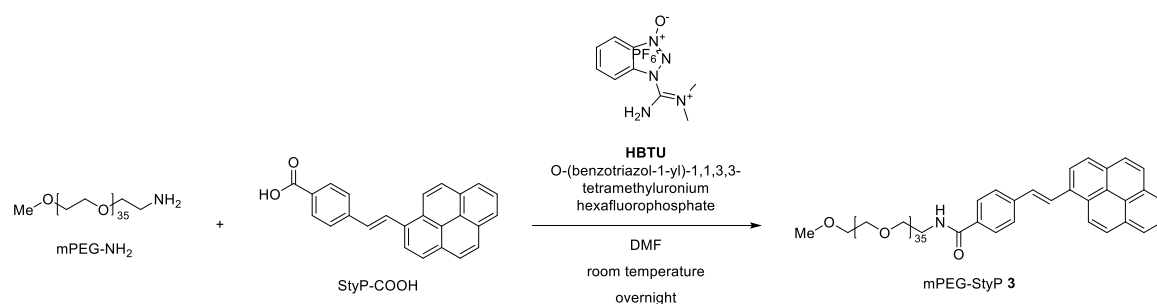


Figure 80. ESI-MS measurement of mPEG-NH₂.

Table 5. Peak assignment of the ESI-MS data of the synthesized mPEG-NH₂ showing the structures assigned in **Figure 80**, the experimental as well as theoretical m/z values and the resolution.

Structure	Resolution	m/z (exp)	m/z (theo)	$\Delta m/z$
mPEG-NH ₂ + H ⁺	54806	1616.9924	1616.9932	0.0008
mPEG-NH ₂ + Na ⁺	51606	1638.9733	1638.9752	0.0019

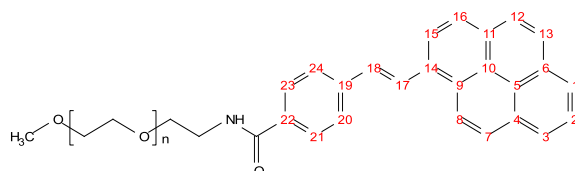
8.3.4 mPEG-styrylpyrene (mPEG-StyP, 3)



To a solution of carboxy-styrylpyrene (0.11 g, 316 μmol , 3.00 eq.), mPEG-amine (average $M_n = 1900 \text{ g mol}^{-1}$, 0.20 g, 105 μmol , 1.00 eq.) and triethylamine (63.9 mg, 632 μmol , 6.00 eq.) in dry DMF, HBTU (0.24 g, 632 μmol , 6 eq.) was added and the mixture stirred at ambient temperature for 20 hours. Afterwards the solvents were removed under reduced pressure (60 $^{\circ}\text{C}$), the remainder suspended in ethyl acetate for 1 h and the non-dissolvable solid filtered off. After removing ethyl acetate, the remaining solid was suspended in water, the remaining solid filtered off and after adding saturated aqueous sodium chloride solution, the water containing layer extracted with dichloromethane until the organic layer stayed clear instead of changing its colour to yellow. The combined organic layers were dried over magnesium sulfate, filtered, the mixture concentrated until only little dichloromethane was left and precipitated into cold diethyl ether.

The pure polymer was obtained as a yellowish powder (99.5 mg, 42 % yield) and analysed via NMR, ESI-MS and SEC (DMAc).

$^1\text{H-NMR}$ (600 MHz, $\text{DMSO-}d_6$): $\delta / \text{ppm} = 8.82$ (d, $J = 9.4 \text{ Hz}$, 1H, 8), 8.59 - 8.49 (m, 2H, 15,18), 8.36 - 8.26 (m, 4H, 1,3,7,16), 8.20 (s, 2H, 12,13), 8.09 (t, $J = 7.6 \text{ Hz}$, 1H, 2), 7.99 - 7.92 (m, 4H, 20,21,23,24), 7.62 (d, $J = 16.0 \text{ Hz}$, 1H, 17), 3.60 - 3.40 (m, polymer backbone), 3.23 (s, 3H, -OMe), 3.11 - 3.03 (m, 4H, $-(\text{CH}_2)_2\text{-NH-}$).



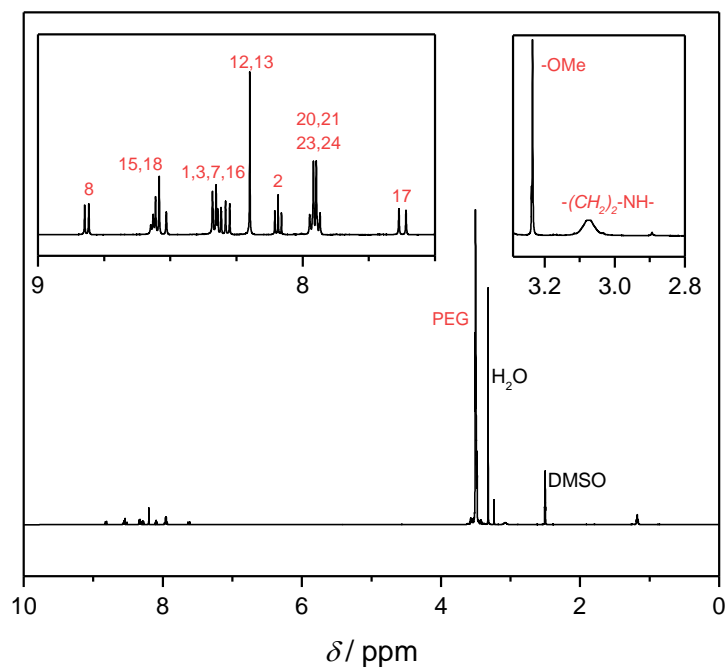


Figure 81. $^1\text{H-NMR}$ (600 MHz, deuterated DMSO) of *mPEG-StyP 3*.

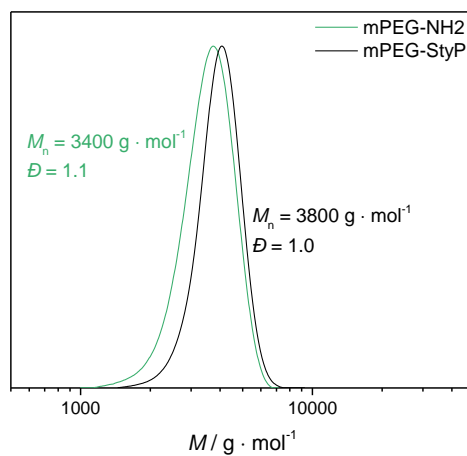


Figure 82. DMAC SEC (RI detector) measurement of *mPEG-StyP*.

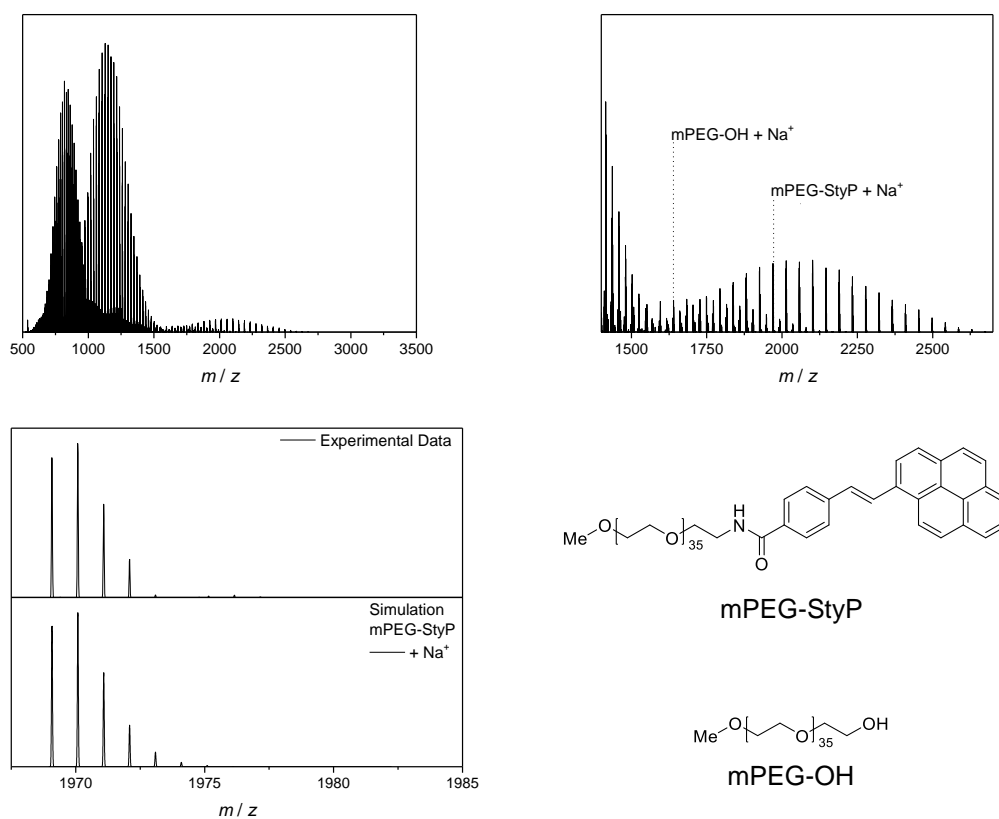
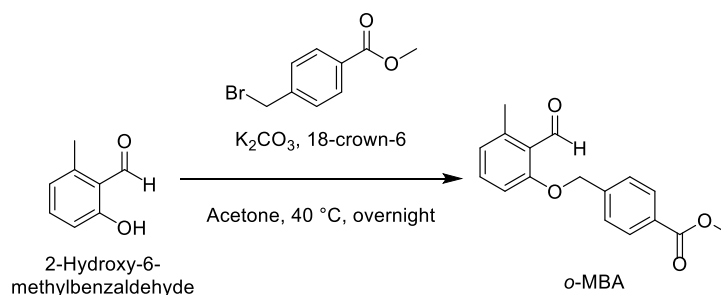


Figure 83. ESI-MS measurement of *mPEG-StyP*.

Table 6. Peak assignment of the ESI-MS data of the synthesized *mPEG-NH₂* showing the structures assigned in **Figure 83**, the experimental as well as theoretical *m/z* values and the resolution.

Structure	Resolution	<i>m/z</i> (exp)	<i>m/z</i> (theo)	$\Delta m/z$
<i>mPEG-OH</i> + Na ⁺	52603	1639.959	1639.9592	0.0002
<i>mPEG-NH-CO-StyP</i> + Na ⁺	47506	1969.07823	1969.0796	0.0014

8.3.5 Methyl 4-((2-formyl-3-methylphenoxy)methyl)benzoate (*o*-MBA, 4)



2-Hydroxy-6-methylbenzaldehyde was synthesised in a two-step procedure according to literature^{181–183}.

The synthesis of methyl 4-((2-formyl-3-methylphenoxy)methyl)benzoate was slightly adapted from a previously published reaction procedure:¹⁸³

In a round bottom flask 2-hydroxy-6-methylbenzaldehyde (0.25 g, 1.83 mmol, 1.00 eq.) and methyl 4-(bromomethyl) benzoate (0.46 g, 2.02 mmol, 1.10 eq.) were dissolved in acetone (12 mL). K_2CO_3 (0.38 g, 2.75 mmol, 1.50 eq.) and 18-crown-6 (9.70 mg, 36.7 μ mol, 0.02 eq.) were added to the solution. The resulting dark brown suspension was stirred overnight at 40°C. The undissolved K_2CO_3 was filtered off and the solvent was evaporated. The residue was dissolved in DCM / H_2O (400 mL, 1 : 1), the phases were separated, and the aqueous layer was extracted with DCM (2 x 40 mL). The combined organic layers were dried over $MgSO_4$ and the solvent was removed under reduced pressure. The product was purified by recrystallization from cyclohexane / ethyl acetate (7 : 1) to obtain 0.40 g (yield: 63.6%) of the white product.

1H -NMR (400 MHz, Acetonitrile- d_3) δ / ppm = 10.69 (s, 1H, 2), 8.02 (d, J = 8.4 Hz, 2H, 12,13), 7.59 (d, J = 8.7 Hz, 2H, 11,14), 7.42 (t, J = 8.2 Hz, 1H, 6), 7.02 (d, J = 8.4 Hz, 1H, 7), 6.88 (d, J = 7.6 Hz, 1H, 5), 5.28 (s, 2H, 9), 3.87 (s, 3H, 18), 2.52 (s, 3H, 1).

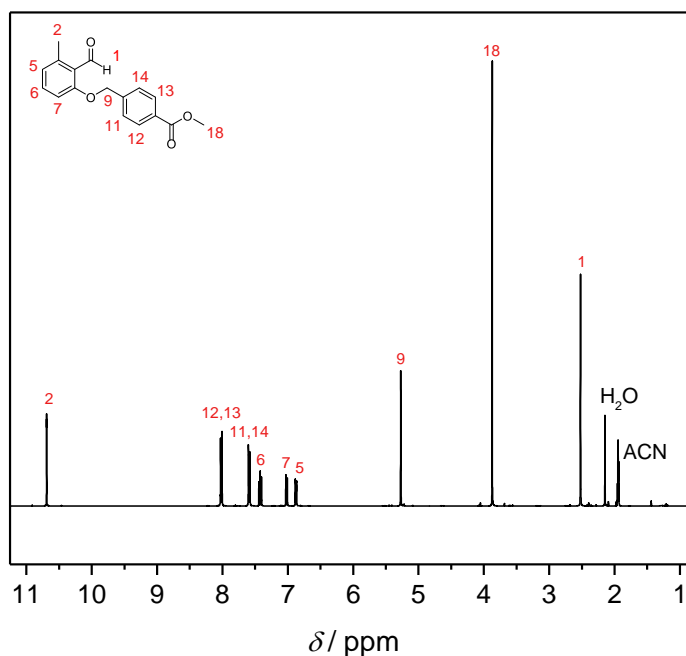
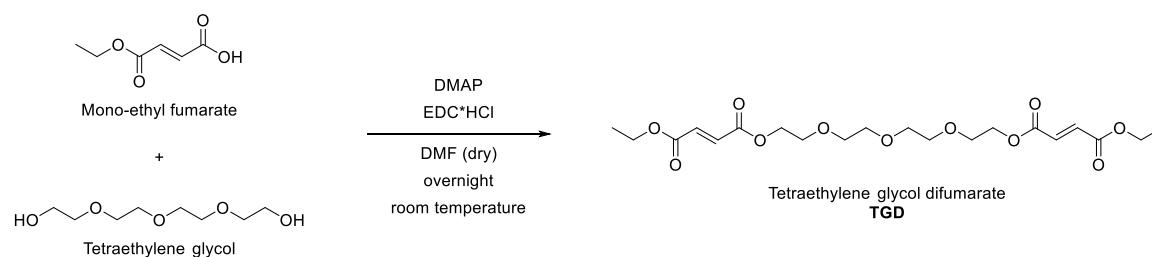


Figure 84. 1H -NMR (400 MHz, deuterated acetonitrile) of o-MBA 4.

8.3.6 Tetraethylene glycol difumarate (TGD, 5)



Tetraethylene glycol (2.63 g, 13.5 mmol, 1.00 eq.), mono-ethyl fumarate (4.48 g, 31.1 mmol, 2.30 eq.), 4-dimethylaminopyridine (DMAP, 0.50 g, 4.06 mmol, 0.30 eq.), and EDC·HCl (7.77 g, 40.6 mmol, 3.00 eq.) were dissolved in dry DMF. Next, water (ca. 100 mL) and DCM (ca. 100 mL) were added to the reaction mixture. The layers were separated, the organic layer washed with water (2 x 100 mL), dried over MgSO₄, filter and the solvents removed under reduced pressure. The crude product was purified via flash chromatography (cyclohexane / ethyl acetate) to obtain 3.16 g of TGD (yield: 52.4 %).

¹H-NMR (400 MHz, Acetonitrile-*d*₃) δ / ppm = 6.79 (s, 4H, 3), 4.31 - 4.27 (m, 4H, 4), 4.22 (q, *J* = 7.1 Hz, 4H, 2), 3.71 - 3.66 (m, 2H, 5), 3.60 - 3.53 (m, 8H, 6), 1.27 (t, *J* = 7.1 Hz, 6H, 1).

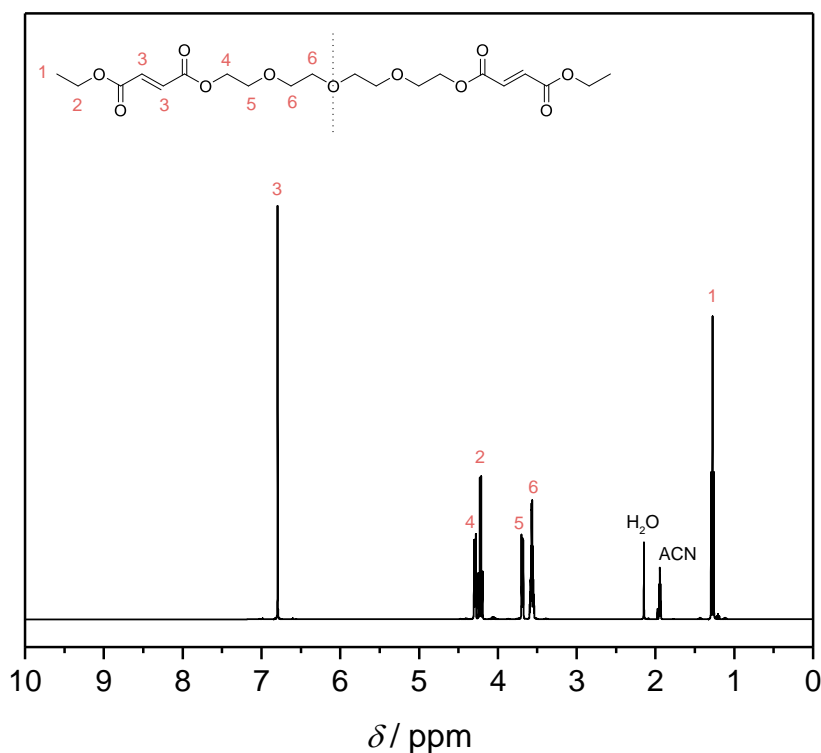
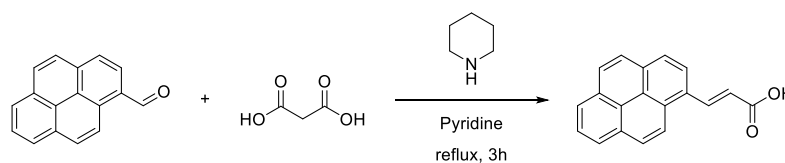


Figure 85. ¹H-NMR (400 MHz, deuterated acetonitrile) spectrum of TGD, 5).

8.3.7 (*E*)-3-(pyren-1-yl)acrylic acid

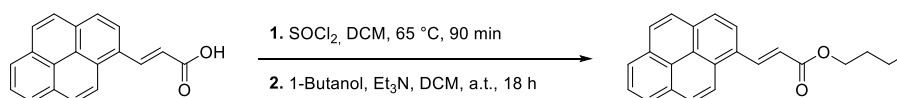


(*E*)-3-(pyren-1-yl)acrylic acid was synthesized according to a literature procedure (949 mg, 3.49 mmol, 73.0 % yield).¹⁸⁴

¹H-NMR (400 MHz, DMSO-*d*₆) δ / ppm = 12.61 (s, 1H), 8.71 (d, *J* = 15.7 Hz, 1H), 8.56 - 8.08 (m, 9H), 6.84 (d, *J* = 15.7 Hz, 1H).

¹³C-NMR (101 MHz, DMSO-*d*₆) δ / ppm = 167.81, 141.16 - 120.39 (m).

8.3.8 Butyl (*E*)-3-(pyren-1-yl)acrylate (9)



500 mg (*E*)-3-(pyren-1-yl)acrylic acid (1.84 mmol, 1.00 eq.) was suspended in anhydrous DCM (15 mL) in a flame-dried flask equipped with a reflux condenser. 1.33 mL SOCl₂ (2.18 g, 18.4 mmol, 10.0 eq.) were added to the suspension and the mixture was heated to 65 °C for 90 min. Excess SOCl₂ and the solvent were evaporated under reduced pressure. The remaining solid was dissolved in anhydrous DCM (15 mL) and 255 μ L NEt₃ (185.8 mg, 1.84 mmol, 1.00 eq.) were added. A solution of 185 μ L 1-butanol (149.7 mg, 2.02 mmol, 1.10 eq.) in 10 mL anhydrous DCM was added dropwise to the stirred mixture at ambient temperature. After stirring for 18 h, the reaction was quenched by carefully adding ice-cold water. DCM (100 mL) was added and the phases were separated. The aqueous phase was extracted with DCM (3 \times 50 mL) and the combined organic phases were dried over Na₂SO₄. The solvents were evaporated, and the crude product was recrystallised in EtOH to yield a yellow solid (497 mg, 1.71 mmol, 93.1 %).

¹H-NMR (400 MHz, CDCl₃) δ / ppm = 8.83 (d, *J* = 15.7 Hz, 1H, 1), 8.48 (d, *J* = 9.3 Hz, 1H, 16), 8.31 - 7.99 (m, 8H, 2-15,17), 6.72 (d, *J* = 15.7 Hz, 1H, 18), 4.31 (t, *J* = 6.7 Hz, 2H, 20), 1.84 - 1.70 (m, 2H, 21), 1.57 - 1.43 (m, 2H, 22), 1.02 (t, *J* = 7.4 Hz, 3H, 23).

¹³C NMR (101 MHz, CDCl₃): δ (ppm) = 167.70, 143.61 – 117.58 (m), 65.04, 31.34, 19.75, 14.28.

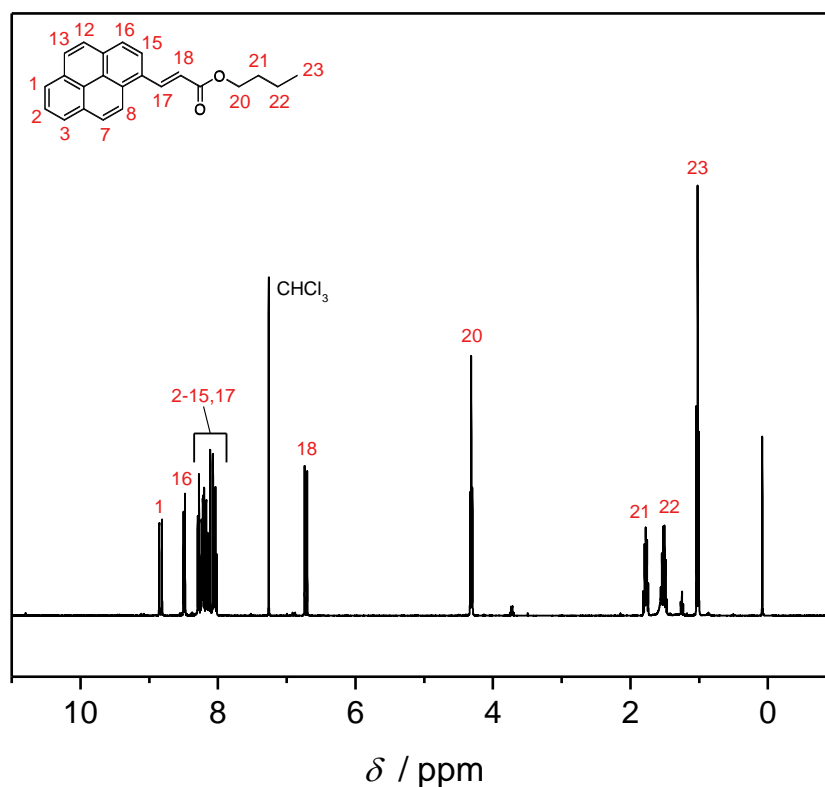
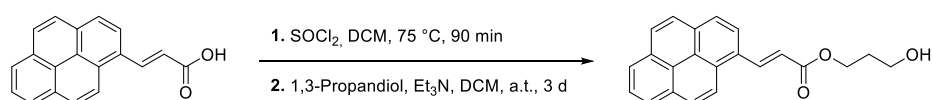


Figure 86. $^1\text{H-NMR}$ (400 MHz, deuterated chloroform) of **9**.

8.3.9 3-Hydroxypropyl (*E*)-3-(pyren-1-yl)acrylate via SOCl_2 -mediated chlorination

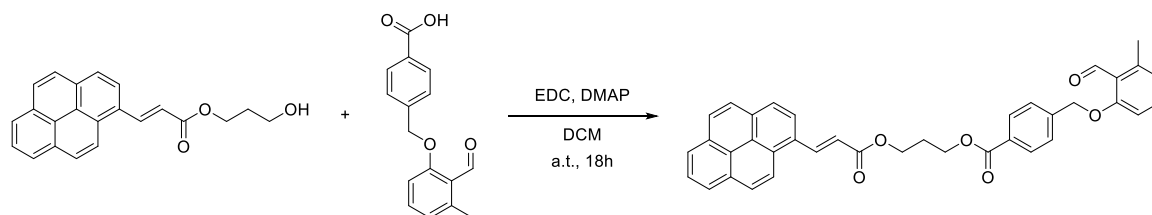


1.00 g (*E*)-3-(pyren-1-yl)acrylic acid (3.67 mmol, 1.00 eq.) were suspended in anhydrous DCM (30 mL). 2.66 mL SOCl_2 (4.37 g, 36.7 mmol, 10.0 eq.) were added and the mixture was heated to 75 °C for 90 min. The solvent and excess SOCl_2 were removed under reduced pressure and the remains were dissolved in dry DCM (30 mL) and added dropwise to a solution of 1.33 mL 1,3-propanediol (1.40 g, 18.4 mmol, 5.00 eq.) as well as 510 μL NEt_3 (372 mg, 3.68 mmol, 1.00 eq.) in 15 mL dry DCM. The mixture was stirred for three days at ambient temperature. The reaction was quenched by adding water (50 mL) and was diluted with DCM (100 mL). The aqueous phase was extracted with DCM (3×50 mL). The combined organic phases were dried over Na_2SO_4 and all volatiles were evaporated under reduced pressure. The pure product was received as orange solid (1.21 g, 3.66 mmol, 99.5 %).

¹H-NMR (400 MHz, DMSO-*d*₆): δ / ppm = 8.74 (d, *J* = 15.7 Hz, 1H), 8.54 (dd, *J* = 8.8, 2.9 Hz, 2H), 8.40 - 8.07 (m, 7H), 6.92 (d, *J* = 15.7 Hz, 1H), 4.61 (t, *J* = 5.2 Hz, 1H), 4.31 (t, *J* = 6.6 Hz, 2H), 3.58 (td, *J* = 6.2, 5.0 Hz, 2H), 1.88 (q, *J* = 6.4 Hz, 2H).

¹³C-NMR (101 MHz, DMSO-*d*₆): δ / ppm = 166.32, 142.14 - 118.29 (m), 61.66, 57.33, 31.66.

8.3.10 (*E*)-3-((3-(pyren-1-yl)acryloyloxy)propyl 4-((2-formyl-3-methylphenoxy)methyl)benzoate (7)

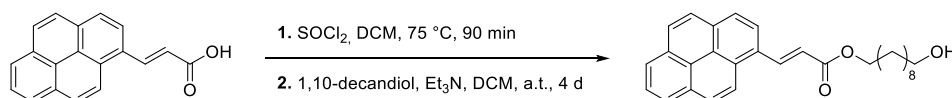


491 mg 4-((2-formyl-3-methylphenoxy)methyl)benzoic acid (1.82 mmol, 1.20 eq.), 868 mg EDC·HCl (4.54 mmol, 3.00 eq.) and 92.0 mg DMAP (0.75 mmol, 0.50 eq.) were dissolved in anhydrous DCM (30 mL) under argon atmosphere and cooled to 0 °C. A solution of 500 mg 3-hydroxypropyl (*E*)-3-(pyren-1-yl)acrylate (1.51 mmol, 1.00 eq.) in anhydrous DCM (30 mL) was added dropwise and the reaction mixture was allowed to reach ambient temperature. After stirring for 18 h, the reaction was quenched by adding water (50 mL) and diluted with DCM (50 mL). The phases were separated, and the organic phase was washed twice with saturated sodium bicarbonate solution (50 mL), 1 M HCl (50 mL) and water (100 mL). The organic phase was dried over Na₂SO₄ and all volatiles were evaporated under reduced pressure. The crude product was purified by column chromatography using a mixture of cyclohexane/DCM as eluent (1:1, *R*_f = 0.19). The product **7** was received as yellow solid (451 mg, 0.77 mmol, 51 %).

¹H-NMR (400 MHz, DMF-*d*₇): δ / ppm = 10.64 (d, *J* = 0.6 Hz, 1H), 8.82 (d, *J* = 15.7 Hz, 1H), 8.60 - 8.03 (m, 11H), 7.66 (d, *J* = 8.3 Hz, 2H), 7.45 (t, 1H), 7.06 (d, *J* = 8.4 Hz, 1H), 6.92 - 6.86 (m, 2H), 5.24 (s, 2H), 4.59 (t, *J* = 6.2 Hz, 2H), 4.53 (t, *J* = 6.3 Hz, 2H), 2.51 (s, 3H), 2.37 - 2.26 (m, 2H).

¹³C-NMR (101 MHz, DMF-*d*₇): δ / ppm = 191.68, 166.80, 166.10, 144.61 - 119.02 (m), 111.40, 69.83, 62.52, 61.99, 28.48, 20.87.

8.3.11 10-hydroxydecyl (*E*)-3-(pyren-1-yl)acrylate

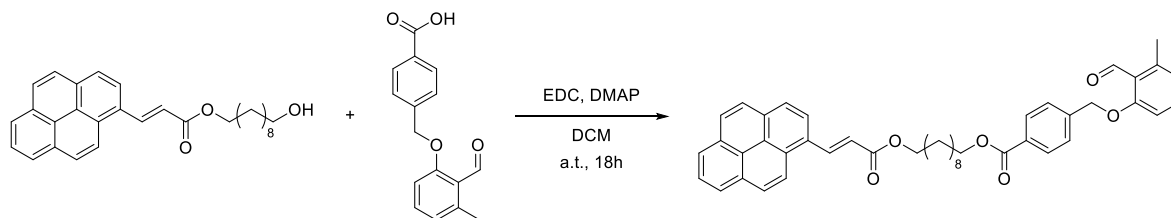


500 mg (*E*)-3-(pyren-1-yl)acrylic acid (1.84 mmol, 1.00 eq.) were suspended in anhydrous DCM (15 mL). 1.33 mL SOCl₂ (2.19 g, 18.4 mmol, 10.0 eq.) were added and the mixture was heated to 75 °C for 90 min. The solvent and excess SOCl₂ were removed under reduced pressure and the remains were dissolved in dry THF (25 mL) and added dropwise to a solution of 1.60 g 1,10-decandiol (9.18 mmol, 5.00 eq.) as well as 205 μL NEt₃ (185 mg, 3.68 mmol, 1.00 eq.) in 30 mL dry THF. The reaction mixture was stirred at ambient temperature for four days. The reaction mixture was filtered and quenched by adding water. The aqueous phase was extracted with DCM (3 × 100 mL). The organic phase was dried over Na₂SO₄ and all volatiles were evaporated subsequently. The residue was purified by column chromatography (cyclohexane/ethyl acetate, 2:1, *R*_f = 0.41). The product was received as yellow solid (508 mg, 1.19 mmol, 64.6 %).

¹H-NMR (400 MHz, CDCl₃) δ / ppm = 8.83 (d, *J* = 15.7 Hz, 1H), 8.48 (d, *J* = 9.3 Hz, 1H), 8.33 - 7.98 (m, 8H), 6.71 (d, *J* = 15.8 Hz, 1H), 4.30 (t, *J* = 6.7 Hz, 2H), 3.63 (t, *J* = 6.6 Hz, 2H), 1.78 (qu, *J* = 8.0, 6.5 Hz, 2H), 1.57 (qu, *J* = 6.8 Hz, 2H), 1.50 - 1.24 (m, 12H).

¹³C-NMR (101 MHz, CDCl₃) δ / ppm = 167.70, 141.76, 134.01 - 119.58 (m), 65.32, 63.52, 33.26, 30.04 - 29.70 (m), 29.26, 26.49, 26.19.

8.3.12 *E*-10-((3-(pyren-1-yl)acryloyl)oxy)decyl 4-((2-formyl-3-methylphenoxy)methyl)benzoate (8)



227 mg 4-((2-formyl-3-methylphenoxy)methyl)benzoic acid (0.84 mmol, 1.20 eq.), 410 mg EDC·HCl (2.10 mmol, 3.00 eq.) and 43.0 mg DMAP (0.75 mmol, 0.50 eq.) were dissolved in anhydrous DCM (20 mL) under argon atmosphere and cooled to 0 °C. A solution of 300 mg 10-hydroxydecyl (*E*)-3-(pyren-1-yl)acrylate (0.70 mmol, 1.00 eq.) in anhydrous DCM (150 mL) was added dropwise and the reaction mixture was allowed to reach ambient temperature. After stirring for 18 h, the reaction was quenched by adding water (50 mL) and diluted with DCM (50 mL). The mixture was diluted with DCM (100 mL) and the phases were separated. The organic phase was washed with a saturated sodium bicarbonate solution as well as brine and all solvents were evaporated under reduced pressure. The residue was purified by column

chromatography (cyclohexane/ethyl acetate, 3:1, $R_f = 0.55$). The product was obtained as yellow solid (325 mg, 0.48 mmol, 68.2 %).

$^1\text{H-NMR}$ (400 MHz, CDCl_3) $\delta = \text{ppm} = 10.74$ (s, 1H,44), 8.83 (d, $J = 15.7$ Hz, 1H, 1), 8.48 (d, $J = 9.3$ Hz, 1H,16), 8.29 - 7.99 (m, 11H, 2-15,17,38,40), 7.49 - 7.45 (m, 2H, 32,34), 7.33 (t, $J = 8.0$ Hz, 1H, 39), 6.83 - 6.80 (m, 2H, 31,35), 6.71 (d, $J = 15.8$ Hz, 1H, 18), 5.18 (s, 2H, 36), 4.31 (dt, $J = 9.8, 6.7$ Hz, 4H, 20,29), 2.58 (s, 3H, 43), 1.77 (ddd, $J = 8.4, 6.5, 1.9$ Hz, 4H, 21,28), 1.50 - 1.30 (m, 12H, 22-27).

$^{13}\text{C-NMR}$ (101 MHz, CDCl_3) $\delta / \text{ppm} = 192.12, 167.36, 166.40, 162.03, 142.42, 141.43, 136.29 - 109.28$ (m), 70.05, 65.38, 65.00, 29.74 - 29.32 (m), 28.91 (d, $J = 9.2$ Hz), 26.18, 21.62.

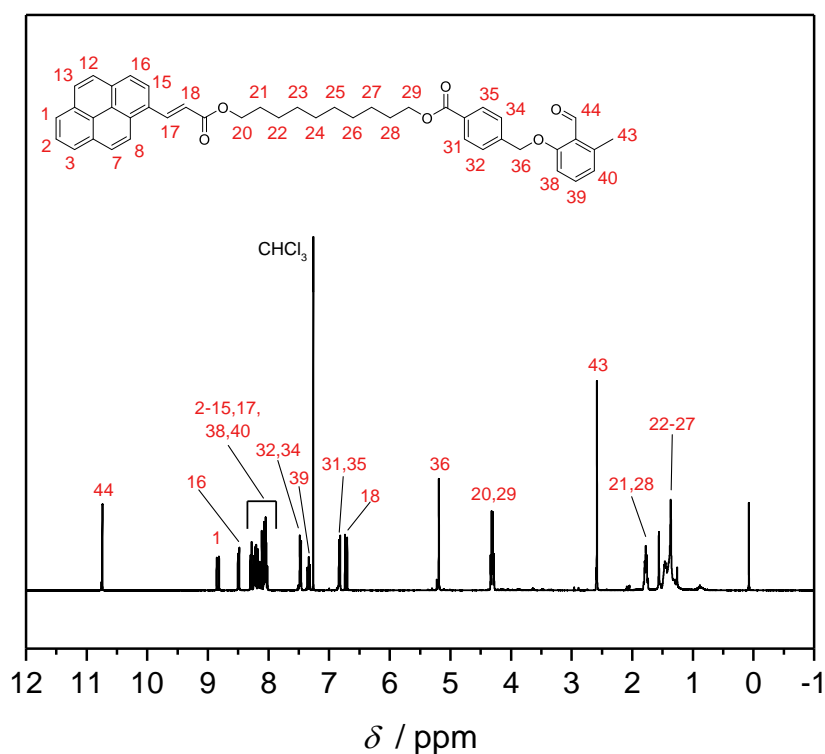
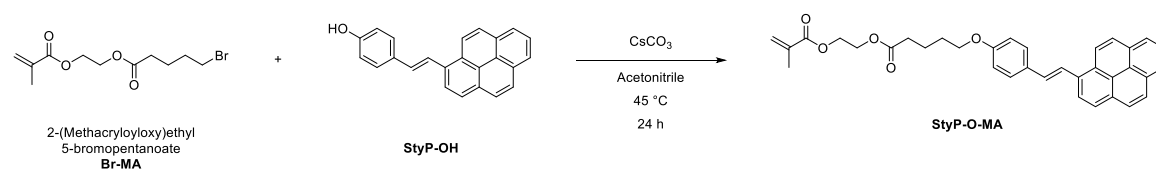


Figure 87. $^1\text{H-NMR}$ (400 MHz, deuterated chloroform) of 8.

8.3.13 Styrylpyrene Monomer (StyP-O-MA, 10)



Styrylpyrene (0.65 g, 2.04 mmol, 1.00 eq.), 2-(methacryloyloxy)ethyl 5-bromopentanoate (1.07 g, 3.66 mmol, 1.8 eq.) and Cs_2CO_3 (1.19 g, 3.66 mmol, 1.8 eq.) were suspended in acetonitrile and degassed with nitrogen for 20 min. The reaction mixture was heated to 45° C for 24h until full conversion of styrylpyrene was reached according to $^1\text{H-NMR}$ (solvent: CDCl_3). The reaction mixture was filtered over cotton (in a pipette) and directly precipitated out of cold methanol (ca. 150 mL). After leaving it in the fridge for 1 h, the precipitate was collected *via* filtration (Millipore) followed by washing with cold methanol and dried under reduced pressure to obtain the pure product (0.46 g, yield: 42 %).

$^1\text{H-NMR}$ (400 MHz, Chloroform-*d*) δ = 8.50 (d, J = 9.3 Hz, 1H, 8), 8.31 (d, J = 8.1 Hz, 1H, 15), 8.20 – 7.97 (m, 8H, 1,3,16,7,18,12,13,2), 7.62 (d, J = 8.8 Hz, 2H, 20,24), 7.31 (d, J = 16.0 Hz, 1H, 17), 6.98 – 6.93 (m, 2H, 21,23), 6.16 – 6.13 (m, 1H, 34), 5.62 – 5.58 (m, 1H, 34), 4.40 – 4.34 (m, 4H, 30,31), 4.06 – 4.01 (m, 2H, 25), 2.50 – 2.42 (m, 2H, 28), 1.96 (dd, J = 1.6, 1.0 Hz, 3H, 33), 1.90 – 1.85 (m, 4H, 26,27).

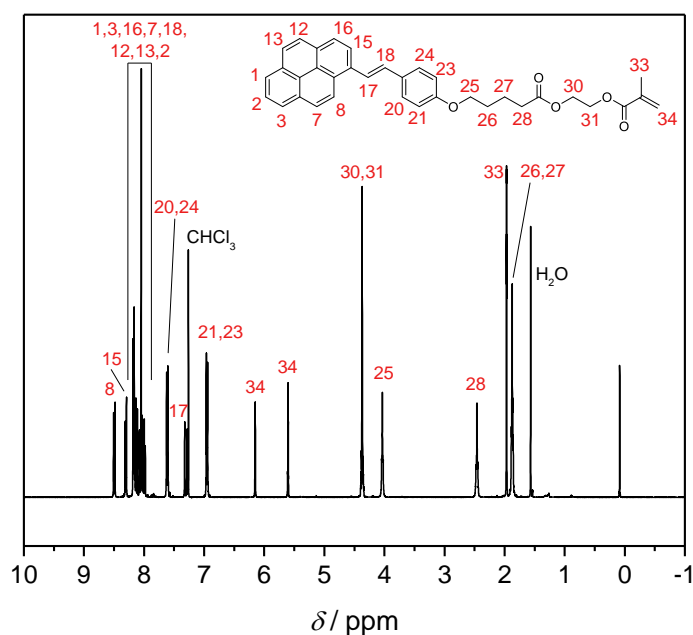
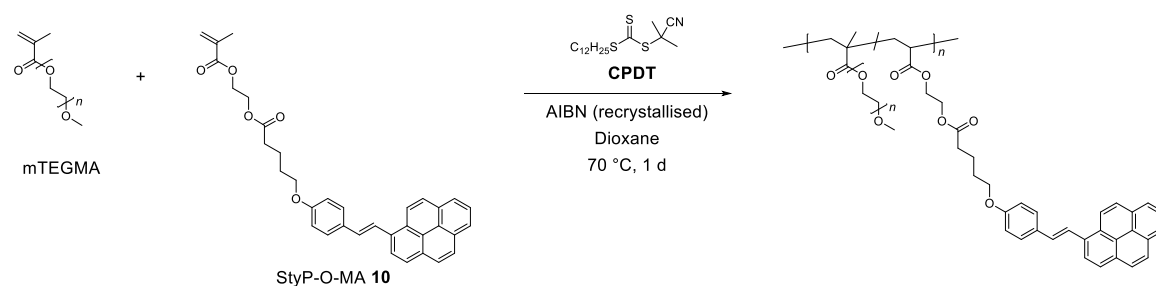


Figure 88. $^1\text{H-NMR}$ (400 MHz, deuterated chloroform) of StyP-O-MA 10.

8.3.14 Styrylpyrene-mTEGMA Copolymers



8.3.14.1 P3

mTEGMA (2.98 g, 12.8 mmol, 68,3 eq.), StyP-O-MA (0.50 g, 939 μ mol, 5.00 eq.), 2-cyano-2-propyl dodecyl trithiocarbonate (CPDT, 64.9 mg, 188 μ mol, 1.00 eq.) and azobisisobutyronitrile (AIBN, 3.08 mg, 18.8 μ mol, 0.10 eq.) were dissolved in toluene. After degassing with nitrogen for 10 min while in an ice bath, the polymerisation was conducted for 24 h at 70 °C and subsequently precipitated in cold diethyl ether. After centrifuging (10 min, 5000 RPM) the solvent was removed, the precipitate dissolved in little THF and precipitated again in cold diethyl ether. The whole process was repeated twice to obtain the final polymer that was analysed via NMR and SEC measurements.

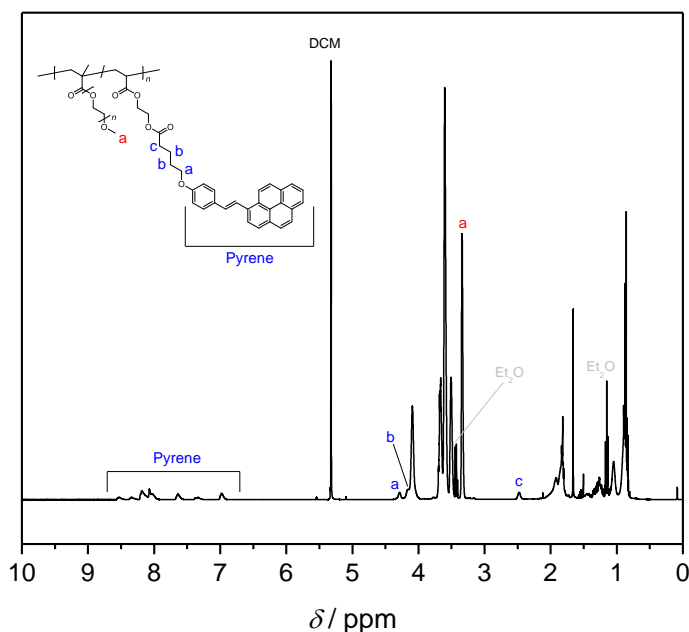


Figure 89. ¹H-NMR (400 MHz, deuterated dichloromethane) of the polymer P3.

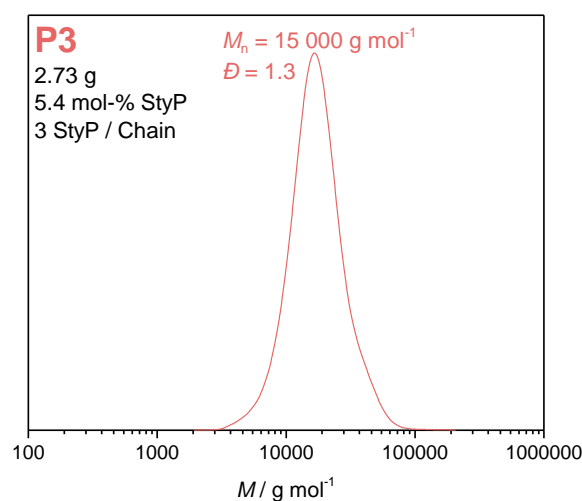


Figure 90. THF SEC (RI detector) chromatogram of the polymer P3.

8.3.14.2 P4

mTEGMA (2.98 g, 12.8 mmol, 136.6 eq.), StyP-O-MA (1.00 g, 1.88 mmol, 20.00 eq.), 2-cyano-2-propyl dodecyl trithiocarbonate (CPDT, 93.9 mg, 188 μmol , 1.00 eq.) and azobisisobutyronitrile (AIBN, 1.54 mg, 9.39 μmol , 0.10 eq.) were dissolved in toluene. After degassing with nitrogen for 10 min while in an ice bath, the polymerisation was conducted for 24 h at 70 °C and subsequently precipitated in cold diethyl ether. After centrifuging (10 min, 5000 RPM) the solvent was removed, the precipitate dissolved in little THF and precipitated again in cold diethyl ether. The whole process was repeated twice to obtain the final polymer that was analysed via NMR and SEC measurements.

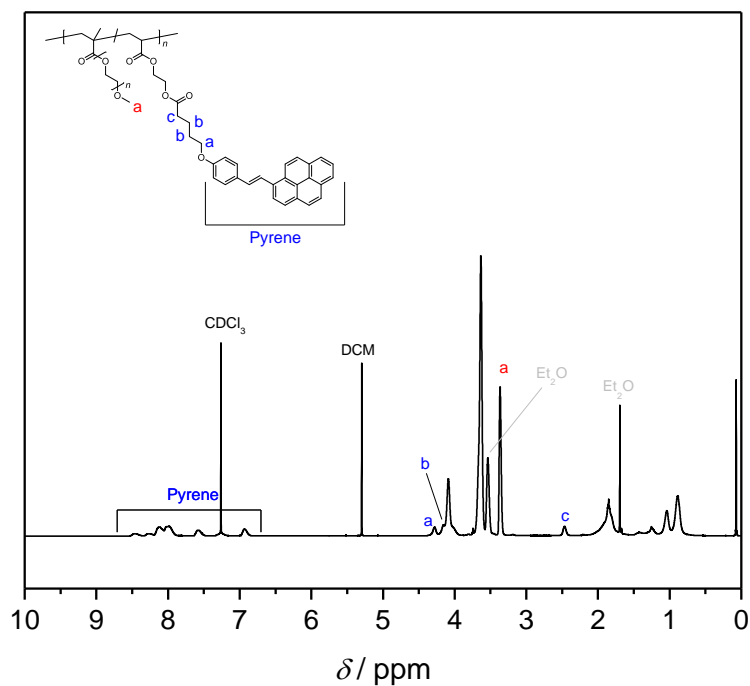


Figure 91. $^1\text{H-NMR}$ (400 MHz, deuterated chloroform) of the polymer **P4**.

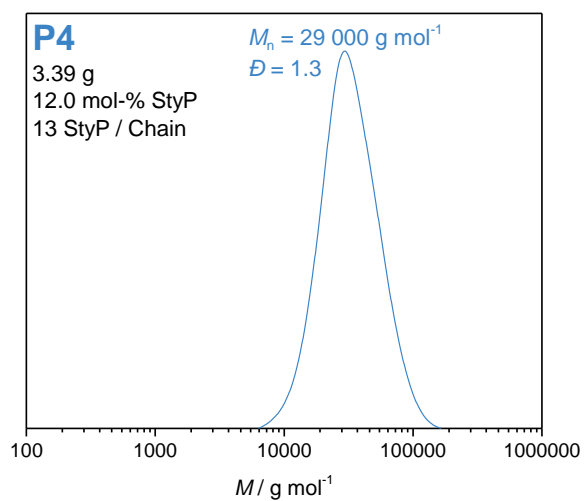
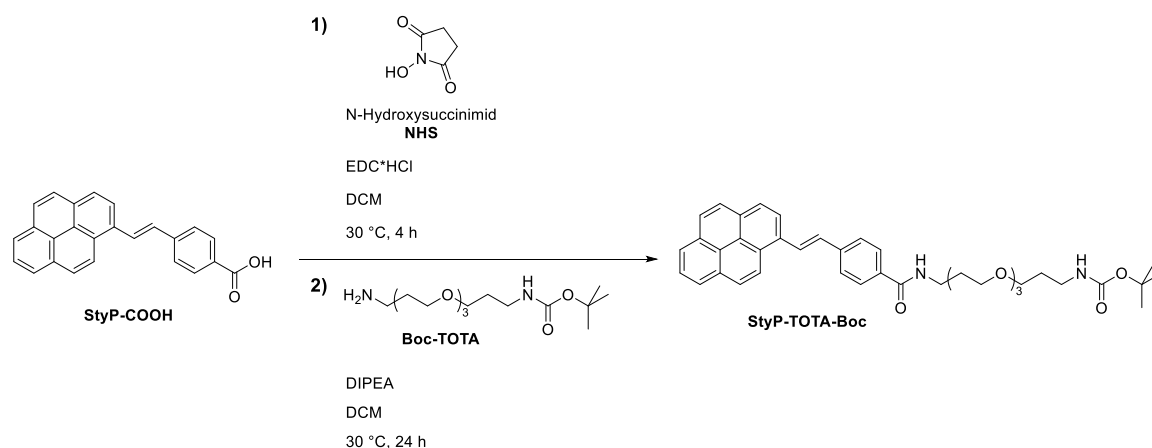


Figure 92. THF SEC (RI detector) chromatogram of the polymer **P4**.

8.3.15 Boc Protected Styrylpyrene-amine (StyP-TOTA-Boc)



StyP-COOH (1.00 g, 2.87 mmol, 1.00 eq.), N-hydroxysuccinimid (NHS, 0.73 g, 6.31 mmol, 2.20 eq.) and *N*-(3-Dimethylaminopropyl)-*N'*-ethylcarbodiimide hydrochloride (EDC·HCl, 1.21 g, 6.13 mmol, 2.20 eq.) were stirred in DCM (30 mL) at 30 °C for 4 h. The NHS activated ester was obtained via filtration (1.03 g, yield: 80.5 %).

In a second step, the NHS ester (1.03 g, 2.31 mmol, 1.00 eq.) was dispersed in DCM (13 mL) before addition of *N,N'*-diisopropylamine (DIPEA, 29.8 mg, 231 μmol, 0.10 eq.) and *N*-Boc-4,7,10-trioxa-1,13-tridecanediamine (Boc-TOTA, 1.01 g, 3.46 mmol, 1.50 eq.). The reaction mixture was stirred at 30 °C for 24 h and turned clear over time. After washing with water (4 x 50 mL), brine (50 mL), drying over MgSO₄ and removing the solvents under reduced pressure, the pure product was obtained (1.43 g, yield: 99.6 %).

¹H-NMR (400 MHz, DMSO-*d*₆) δ = 8.86 – 7.55 (m, 16H, Pyrene,1), 6.75 (t, *J* = 4.9 Hz, 1H, 7), 3.59 – 3.30 (m, 14H, 2,4), 2.97 (q, *J* = 6.6 Hz, 2H, 6), 1.80 (p, *J* = 6.6 Hz, 2H, 3), 1.60 (p, *J* = 6.6 Hz, 2H, 5), 1.36 (s, 9H, 8).

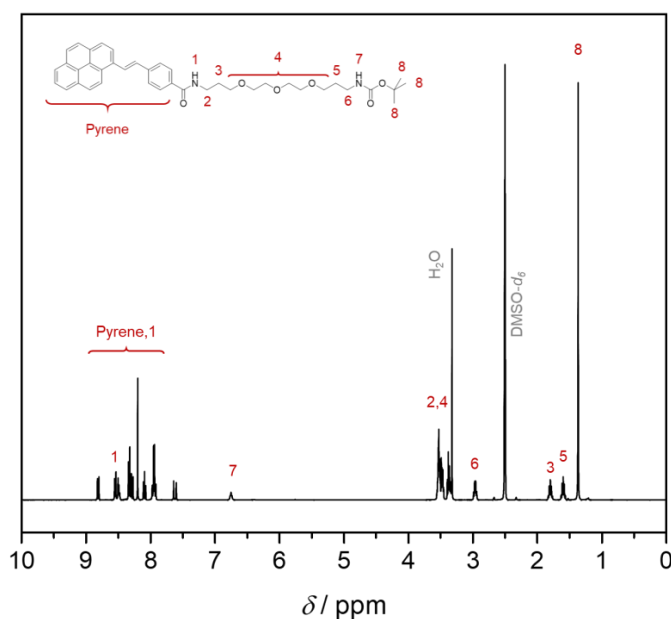


Figure 93. ¹H-NMR (400 MHz, deuterated DMSO) of the boc protected styrylpyrene amine.

8.3.16 Decoration of TEMPO-oxidized cellulose nanofibrils (CNF) with tetrazole-NH₂ in dispersion

The following procedure was performed by Daniel Hönders at the University of Freiburg:

The oxidation of bleached Kraft pulp by TEMPO/NaOCl/NaClO₂ system under neutral conditions was performed according to literature by PTS Hagenau (Dresden, Germany).¹⁸⁵ The resulting content of carboxyl groups is 0.94 mmol g⁻¹ and the degree of polymerization (*DP*_v) is 650. A 1.3 wt-% suspension of TEMPO oxidized Kraft pulp was set to pH = 9 with NaOH and fibrillated by repeated shear cycles in a microfluidizer (Microfluidics corp. MRT CR5, 4 x 1000 bar). For decoration of CNF in dispersion, the gel-like CNF (1 wt-% in water) was diluted to 0.1 wt% in a solvent mixture of water and DMSO (800 mL, final w/w was 1/4) and vigorously stirred to obtain a clear homogeneous dispersion. Styrylpyrene-NH₂ (0.85 g, 2.26 mmol, 3 eq.) was dissolved in DMSO and added to the dispersion and next DMTMM (0.74 g, 2.26 mmol, 3 eq.) dissolved in water was added dropwise. The reaction mixture was stirred at ambient conditions for 24 h. Afterwards the dispersion was washed multiple times with DMSO and water by centrifugation to remove unreacted and adsorbed reactants. The final concentrated CNF-StyP was stored as aqueous dispersion in the fridge and under light protection until used.

Bibliography

- 1 G. Kaur, P. Johnston, K. Saito, *Polym. Chem.*, 2014, **5**, 2171–2186.
- 2 J. K. Sugden, *Biotech. Histochem.*, 2004, **79**, 71–90.
- 3 R. J. Kilian, in *Biomedical and Dental Applications of Polymers*, Springer, 1981, pp. 411–417.
- 4 Z. Liu, M. A. Meyers, Z. Zhang, R. O. Ritchie, *Prog. Mater. Sci.*, 2017, **88**, 467–498.
- 5 K. U. Claussen, T. Scheibel, H.-W. Schmidt, R. Giesa, *Macromol. Mater. Eng.*, 2012, **297**, 938–957.
- 6 L. Ionov, *Mater. Today*, 2014, **17**, 494–503.
- 7 V. Balzani, P. Ceroni, A. Juris, *Photochemistry and Photophysics: Concepts, Research, Applications*, Wiley-VCH, Weinheim, 2014.
- 8 A. Miserez, T. Schneberk, C. Sun, F. W. Zok, J. H. Waite, *Science*, 2008, **319**, 1816–1819.
- 9 J. H. Waite, H. C. Lichtenegger, G. D. Stucky, P. Hansma, *Biochemistry*, 2004, **43**, 7653–7662.
- 10 S. Suresh, *Science*, 2001, **292**, 2447–2451.
- 11 R. Merindol, A. Walther, *Chem. Soc. Rev.*, 2017, **46**, 5588–5619.
- 12 R. Libanori, R. M. Erb, A. Reiser, H. Le Ferrand, M. J. Süess, R. Spolenak, A. R. Studart, *Nat. Commun.*, 2012, **3**, 1265.
- 13 K. U. Claussen, E. S. Lintz, R. Giesa, H. Schmidt, T. Scheibel, *Macromol. Biosci.*, 2013, **13**, 1396–1403.
- 14 K. U. Claussen, R. Giesa, H. W. Schmidt, *Polymer*, 2014, **55**, 29–38.
- 15 D. Kokkinis, F. Bouville, A. R. Studart, *Adv. Mater.*, 2018, **30**, 1705808.
- 16 Y. Zhang, M. C. Tan, *Adv. Mater. Interfaces*, 2018, **5**, 1701374.
- 17 H. Staudinger, *Ber. dtsh. Chem. Ges. A/B*, 1920, **53**, 1073–1085.
- 18 H. Staudinger, J. Fritsch, *Helv. Chim. Acta*, 1922, **5**, 785–806.
- 19 I. Eisenbach, in *English for Materials Science and Engineering*, Vieweg+Teubner, Wiesbaden, 2011, pp. 51–62.
- 20 B. Ellis, R. Smith, *Polymers: a property database*, CRC Press, 2008.
- 21 J. Murphy, *Additives for Plastics Handbook*, Elsevier, 2001.
- 22 M. Wensing, E. Uhde, T. Salthammer, *Sci. Total Environ.*, 2005, **339**, 19–40.
- 23 E. W. Flick, *Plastics Additives, Volume 1: An Industry Guide*, Elsevier, 2019.
- 24 M. P. Stevens, *Polymer Chemistry*, Oxford University Press, 1999.
- 25 G. Odian, *Principles of polymerization*, John Wiley & Sons, Hoboken, NJ, USA, 4th edn.
- 26 C. Barner-Kowollik, *Handbook of RAFT Polymerization*, 2008.
- 27 K. Miki, Y. Washitake, K. Ohe, S. Uemura, *Angew. Chem. Int. Ed.*, 2004, **43**, 1857–1860.
- 28 K. Matyjaszewski, A. H. E. Müller, *Controlled and Living Polymerizations*, Wiley-VCH, Weinheim, 2009.

- 29 K. Matyjaszewski, T. P. Davis, *Handbook of Radical Polymerisation*, Wiley, 2003.
- 30 H. F. Gruber, *Prog. Polym. Sci.*, 1992, **17**, 953–1044.
- 31 C. J. Hawker, *J. Am. Chem. Soc.*, 1994, **116**, 11185–11186.
- 32 S. W. Benson, A. M. North, *J. Am. Chem. Soc.*, 1962, **84**, 935–940.
- 33 P. E. M. Allen, C. R. Patrick, *Die Makromol. Chemie*, 1961, **47**, 154–167.
- 34 J. Krstina, G. Moad, E. Rizzardo, C. L. Winzor, C. T. Berge, M. Fryd, *Macromolecules*, 1995, **28**, 5381–5385.
- 35 F. R. Mayo, *J. Am. Chem. Soc.*, 1943, **65**, 2324–2329.
- 36 K. G. Suddaby, D. R. Maloney, D. M. Haddleton, *Macromolecules*, 1997, **30**, 702–713.
- 37 N. M. Ahmad, F. Heatley, P. A. Lovell, *Macromolecules*, 1998, **31**, 2822–2827.
- 38 J.-S. Wang, K. Matyjaszewski, *J. Am. Chem. Soc.*, 1995, **117**, 5614–5615.
- 39 T. Iwasaki, J. Yoshida, *Macromolecules*, 2005, **38**, 1159–1163.
- 40 P. Vana, R. Storey, Y. Yagci, *Fundamentals of controlled/living radical polymerization*, Royal Society of Chemistry, 2012.
- 41 W. A. Braunecker, K. Matyjaszewski, *Prog. Polym. Sci.*, 2007, **32**, 93–146.
- 42 J. Nicolas, Y. Guilleaume, C. Lefay, D. Bertin, D. Gimes, B. Charleux, *Prog. Polym. Sci.*, 2013, **38**, 63–235.
- 43 M. H. Stenzel, C. Barner-Kowollik, *Mater. Horizons*, 2016, **3**, 471–477.
- 44 J. Chiefari, Y. K. (Bill) Chong, F. Ercole, J. Krstina, J. Jeffery, T. P. T. Le, R. T. A. Mayadunne, G. F. Meijs, C. L. Moad, G. Moad, E. Rizzardo, S. H. Thang, *Macromolecules*, 1998, **31**, 5559–5562.
- 45 S. Perrier, P. Takolpuckdee, *J. Polym. Sci. Part A Polym. Chem.*, 2005, **43**, 5347–5393.
- 46 G. Moad, E. Rizzardo, S. H. Thang, *Aust. J. Chem.*, 2005, **58**, 379–410.
- 47 H. Trommsdorff, *Ann. der Pharm.*, 1834, **11**, 190–207.
- 48 Fritzsche, *J. für Prakt. Chemie*, 1867, **101**, 333–343.
- 49 C. N. Riiber, *Ber. dtsch. Chem. Ges.*, 1902, **35**, 2908–2909.
- 50 G. Ciamician, P. Silber, *Ber. dtsch. Chem. Ges.*, 1902, **35**, 4128–4131.
- 51 M. Planck, *Ann. Phys.*, 1901, **4**, 90.
- 52 A. Einstein, *Ann. Phys.*, 1905, **322**, 132–148.
- 53 P. Atkins, J. De Paula, in *Climate Change 2013 - The Physical Science Basis*, Cambridge University Press, Cambridge, 2006, pp. 1–30.
- 54 H. Frisch, D. E. Marschner, A. S. Goldmann, C. Barner-Kowollik, *Angew. Chem. Int. Ed.*, 2018, **57**, 2036–2045.
- 55 C. M. Marian, *Wiley Interdiscip. Rev. Comput. Mol. Sci.*, 2012, **2**, 187–203.
- 56 K. A. Franz, W. G. Kehr, A. Siggel, J. Wieczorek, W. Adam, *Ullmann's Encyclopedia of Industrial Chemistry*, Wiley-VCH, 2000.
- 57 K. Fujimoto, A. Yamada, Y. Yoshimura, T. Tsukaguchi, T. Sakamoto, *J. Am. Chem. Soc.*, 2013, **135**, 16161–16167.
- 58 Beer, *Ann. Phys.*, 1852, **162**, 78–88.
- 59 J. Franck, E. G. Dymond, *Trans. Faraday Soc.*, 1926, **21**, 536–542.
- 60 E. Condon, *Phys. Rev.*, 1926, **28**, 1182–1201.
- 61 R. Brückner, Springer Verlag, Heidelberg, 2004.
- 62 F. A. Carey, R. J. Sundberg, *Advanced Organic Chemistry: Part A: Structure and Mechanisms*, Springer US, Boston, MA, 2007.
- 63 R. B. Woodward, R. Hoffmann, *J. Am. Chem. Soc.*, 1965, **87**, 395–397.

-
- 64 S. Sankararaman, *Pericyclic Reactions - A Textbook*, Wiley-VCH, Weinheim, 2005.
- 65 R. Anet, *Can. J. Chem.*, 1962, **40**, 1249–1257.
- 66 G. S. Hammond, C. A. Stout, A. A. Lamola, *J. Am. Chem. Soc.*, 1964, **86**, 3103–3106.
- 67 C. H. Krauch, S. Farid, G. O. Schenck, *Chem. Ber.*, 1966, **99**, 625–633.
- 68 H. Morrison, H. Curtis, T. McDowell, *J. Am. Chem. Soc.*, 1966, **88**, 5415–5419.
- 69 R. Hoffman, P. Wells, H. Morrison, *J. Org. Chem.*, 1971, **36**, 102–108.
- 70 F. D. Lewis, S. V. Barancyk, *J. Am. Chem. Soc.*, 1989, **111**, 8653–8661.
- 71 T. Wolff, H. Görner, *Phys. Chem. Chem. Phys.*, 2004, **6**, 368–376.
- 72 F. D. Lewis, D. K. Howard, J. D. Oxman, *J. Am. Chem. Soc.*, 1983, **105**, 3344–3345.
- 73 H. Görner, T. Wolff, *Photochem. Photobiol.*, 2008, **84**, 1224–1230.
- 74 R. Beukers, W. Berends, *Biochim. Biophys. Acta*, 1960, **41**, 550–551.
- 75 G. M. Blackburn, R. J. H. Davies, *Chem. Commun.*, 1965, 215–216.
- 76 Y.-F. Han, G.-X. Jin, C. G. Daniliuc, F. E. Hahn, *Angew. Chem. Int. Ed.*, 2015, **54**, 4958–4962.
- 77 H. He, M. Feng, Q. Chen, X. Zhang, H. Zhan, *Angew. Chem. Int. Ed.*, 2016, **55**, 936–940.
- 78 I.-H. Park, A. Chanthapally, Z. Zhang, S. S. Lee, M. J. Zaworotko, J. J. Vittal, *Angew. Chem. Int. Ed.*, 2014, **53**, 414–419.
- 79 J. Motoyanagi, T. Fukushima, N. Ishii, T. Aida, *J. Am. Chem. Soc.*, 2006, **128**, 4220–4221.
- 80 B. C. Pemberton, N. Baroah, D. K. Srivatsava, J. Sivaguru, *Chem. Commun.*, 2010, **46**, 225–227.
- 81 N. K. Mal, M. Fujiwara, Y. Tanaka, *Nature*, 2003, **421**, 350–353.
- 82 D. Kehroesser, R.-P. Baumann, H.-C. Kim, N. Hampp, *Langmuir*, 2011, **27**, 4149–4155.
- 83 K. Hesse, S. Hünig, *Liebigs Ann. der Chemie*, 1985, **1985**, 715–739.
- 84 Y. Yoshimura, K. Fujimoto, *Org. Lett.*, 2008, **10**, 3227–3230.
- 85 T. K. Claus, S. Telitel, A. Welle, M. Bastmeyer, A. P. Vogt, G. Delaittre, C. Barner-Kowollik, *Chem. Commun.*, 2017, **53**, 1599–1602.
- 86 T. Doi, H. Kawai, K. Murayama, H. Kashida, H. Asanuma, *Chem. Eur. J.*, 2016, **22**, 10533–10538.
- 87 C. de las H. Alarcón, S. Pennadam, C. Alexander, *Chem. Soc. Rev.*, 2005, **34**, 276–285.
- 88 I. Y. Galaev, B. Mattiasson, *Trends Biotechnol.*, 1999, **17**, 335–340.
- 89 S. Ganta, H. Devalapally, A. Shahiwala, M. Amiji, *J. Control. Release*, 2008, **126**, 187–204.
- 90 B. Jeong, A. Gutowska, *Trends Biotechnol.*, 2002, **20**, 305–311.
- 91 M. A. C. Stuart, W. T. S. Huck, J. Genzer, M. Müller, C. Ober, M. Stamm, G. B. Sukhorukov, I. Szleifer, V. V. Tsukruk, M. Urban, F. Winnik, S. Zauscher, I. Luzinov, S. Minko, *Nat. Mater.*, 2010, **9**, 101–113.
- 92 V. P. Torchilin, *Pharm. Res.*, 2006, **24**, 1–16.
- 93 H. Dai, X. Li, Y. Long, J. Wu, S. Liang, X. Zhang, N. Zhao, J. Xu, *Soft Matter*, 2009, **5**, 1987–1989.
- 94 Y. Inaki, H. Hiratsuka, *J. Photopolym. Sci. Technol.*, 2000, **13**, 739–744.
- 95 Y. Kita, T. Uno, Y. Inaki, K. Takemoto, *J. Polym. Sci. Polym. Chem. Ed.*, 1981, **19**, 477–485.
- 96 Y. Kita, T. Uno, Y. Inaki, K. Takemoto, *J. Polym. Sci. Polym. Chem. Ed.*, 1981, **19**, 1733–1744.
- 97 M. J. Moghaddam, Y. Inaki, K. Takemoto, *Polym. J.*, 1990, **22**, 468–476.
- 98 D. M. Martino, D. Reyna, D. A. Estenoz, S. Trakhtenberg, J. C. Warner, *J. Phys. Chem. A*, 2008, **112**, 4786–4792.
- 99 S. Trakhtenberg, J. C. Warner, R. Nagarajan, F. F. Bruno, L. A. Samuelson, J. Kumar, *Chem. Mater.*, 2006, **18**,
-

- 2873–2878.
- 100 M. V. S. N. Maddipatla, D. Wehrung, C. Tang, W. Fan, M. O. Oyewumi, T. Miyoshi, A. Joy, *Macromolecules*, 2013, **46**, 5133–5140.
- 101 Y. Chujo, K. Sada, R. Nomura, A. Naka, T. Saegusa, *Macromolecules*, 1993, **26**, 5611–5614.
- 102 K. Yang, M. Zeng, *New J. Chem.*, 2013, **37**, 920–926.
- 103 K. Saito, L. R. Ingalls, J. Lee, J. C. Warner, *Chem. Commun.*, 2007, 2503–2505.
- 104 D. Habault, H. Zhang, Y. Zhao, *Chem. Soc. Rev.*, 2013, **42**, 7244–7256.
- 105 J. Ling, M. Z. Rong, M. Q. Zhang, *J. Mater. Chem.*, 2011, **21**, 18373–18380.
- 106 G. Kaur, S. L. Y. Chang, T. D. M. Bell, M. T. W. Hearn, K. Saito, *J. Polym. Sci. Part A Polym. Chem.*, 2011, **49**, 4121–4128.
- 107 J. K. Oh, D. I. Lee, J. M. Park, *Prog. Polym. Sci.*, 2009, **34**, 1261–1282.
- 108 J. Khandare, M. Calderón, N. M. Dagia, R. Haag, *Chem. Soc. Rev.*, 2012, **41**, 2824–2848.
- 109 A. L. Sisson, R. Haag, *Soft Matter*, 2010, **6**, 4968.
- 110 A. V. Kabanov, S. V. Vinogradov, *Angew. Chem. Int. Ed.*, 2009, **48**, 5418–5429.
- 111 Q. Jin, X. Liu, G. Liu, J. Ji, *Polymer*, 2010, **51**, 1311–1319.
- 112 Q. Jin, G. Liu, J. Ji, *Eur. Polym. J.*, 2010, **46**, 2120–2128.
- 113 M. J. Moghaddam, K. Kanbara, S. Hozumi, Y. Inaki, K. Takemoto, *Polym. J.*, 1990, **22**, 369.
- 114 S. R. Trenor, T. E. Long, B. J. Love, *Macromol. Chem. Phys.*, 2004, **205**, 715–723.
- 115 H.-A. Wagenknecht, *ChemPhysChem*, 2013, **14**, 3197–3198.
- 116 J. T. Offenloch, M. Gernhardt, J. P. Blinco, H. Frisch, H. Mutlu, C. Barner-Kowollik, *Chem. – A Eur. J.*, 2019, **25**, 3700–3709.
- 117 X. Wang, K. Maeda, A. Thomas, K. Takanabe, G. Xin, J. M. Carlsson, K. Domen, M. Antonietti, *Nat. Mater.*, 2009, **8**, 76–80.
- 118 A. Kojima, K. Teshima, Y. Shirai, T. Miyasaka, *J. Am. Chem. Soc.*, 2009, **131**, 6050–6051.
- 119 C. K. Prier, D. A. Rankic, D. W. C. MacMillan, *Chem. Rev.*, 2013, **113**, 5322–5363.
- 120 X. Liu, Y. Ni, J. Wu, H. Jiang, Z. Zhang, L. Zhang, Z. Cheng, X. Zhu, *Polym. Chem.*, 2018, **9**, 584–592.
- 121 D. Matsukuma, K. Yamamoto, T. Aoyagi, *Langmuir*, 2006, **22**, 5911–5915.
- 122 M. Doycheva, E. Petrova, R. Stamenova, C. Tsvetanov, G. Riess, *Macromol. Mater. Eng.*, 2004, **289**, 676–680.
- 123 C. Barner-Kowollik, M. Bastmeyer, E. Blasco, G. Delaittre, P. Müller, B. Richter, M. Wegener, *Angew. Chem. Int. Ed.*, 2017, **56**, 15828–15845.
- 124 W. Kaiser, C. G. B. Garrett, *Phys. Rev. Lett.*, 1961, **7**, 229.
- 125 G. S. He, L.-S. Tan, Q. Zheng, P. N. Prasad, *Chem. Rev.*, 2008, **108**, 1245–1330.
- 126 W. R. Zipfel, R. M. Williams, W. W. Webb, *Nat. Biotechnol.*, 2003, **21**, 1369–1377.
- 127 M. Pawlicki, H. A. Collins, R. G. Denning, H. L. Anderson, *Angew. Chem. Int. Ed.*, 2009, **48**, 3244–3266.
- 128 Y. Wang, W. J. Hu, W. Song, R. K. V Lim, Q. Lin, *Org. Lett.*, 2008, **10**, 3725–3728.
- 129 J. O. Mueller, F. G. Schmidt, J. P. Blinco, C. Barner-Kowollik, *Angew. Chem. Int. Ed.*, 2015, **54**, 10284–10288.
- 130 J. M. Casas-Solvas, J. D. Howgego, A. P. Davis, *Org. Biomol. Chem.*, 2014, **12**, 212–232.
- 131 M. V. George, C. S. Angadiyavar, *J. Org. Chem.*, 1971, **36**, 1589–1594.
- 132 P. Lederhose, K. N. R. Wüst, C. Barner-Kowollik, J. P. Blinco, *Chem. Commun.*, 2016, **52**, 5928–5931.
- 133 P. An, Z. Yu, Q. Lin, *Chem. Commun.*, 2013, **49**, 9920–9922.

-
- 134 B. T. Tuten, J. P. Menzel, K. Pahnke, J. P. Blinco, C. Barner-Kowollik, *Chem. Commun.*, 2017, **53**, 4501–4504.
- 135 V. X. Truong, F. Li, J. S. Forsythe, *ACS Macro Lett.*, 2017, **6**, 657–662.
- 136 J. P. Menzel, B. B. Noble, A. Lauer, M. L. Coote, J. P. Blinco, C. Barner-Kowollik, *J. Am. Chem. Soc.*, 2017, **139**, 15812–15820.
- 137 D. E. Fast, A. Lauer, J. P. Menzel, A.-M. Kelterer, G. Gescheidt, C. Barner-Kowollik, *Macromolecules*, 2017, **50**, 1815–1823.
- 138 R. B. T. Price, *Dent. Clin. North Am.*, 2017, **61**, 751–778.
- 139 L. Wu, J. Baghdachi, *Functional Polymer Coatings*, John Wiley & Sons, Hoboken, NJ, 2015.
- 140 M. Bechthold, J. C. Weaver, *Nat. Rev. Mater.*, 2017, **2**, 17082.
- 141 K. Hildebrandt, T. Pauloehrl, J. P. Blinco, K. Linkert, H. G. Börner, C. Barner-Kowollik, *Angew. Chem. Int. Ed.*, 2015, **54**, 2838–2843.
- 142 J. P. Olson, M. R. Banghart, B. L. Sabatini, G. C. R. Ellis-Davies, *J. Am. Chem. Soc.*, 2013, **135**, 15948–15954.
- 143 J. R. Hemmer, S. O. Poelma, N. Treat, Z. A. Page, N. D. Dolinski, Y. J. Diaz, W. Tomlinson, K. D. Clark, J. P. Hooper, C. Hawker, J. Read de Alaniz, *J. Am. Chem. Soc.*, 2016, **138**, 13960–13966.
- 144 M. M. Lerch, M. J. Hansen, W. A. Velema, W. Szymanski, B. L. Feringa, *Nat. Commun.*, 2016, **7**, 12054.
- 145 H. Frisch, F. R. Bloesser, C. Barner-Kowollik, *Angew. Chem. Int. Ed.*, 2019, **58**, 3604–3609.
- 146 M. J. Hansen, W. A. Velema, M. M. Lerch, W. Szymanski, B. L. Feringa, *Chem. Soc. Rev.*, 2015, **44**, 3358–3377.
- 147 M. A. H. Fichte, X. M. M. Weyel, S. Junek, F. Schäfer, C. Herbivo, M. Goeldner, A. Specht, J. Wachtveitl, A. Heckel, *Angew. Chem. Int. Ed.*, 2016, **55**, 8948–8952.
- 148 C. Brieke, F. Rohrbach, A. Gottschalk, G. Mayer, A. Heckel, *Angew. Chem. Int. Ed.*, 2012, **51**, 8446–8476.
- 149 O. Diels, K. Alder, *Justus Liebigs Ann. Chem.*, 1928, **460**, 98–122.
- 150 G. Porter, M. F. Tchir, *J. Chem. Soc. D Chem. Commun.*, 1970, 1372.
- 151 G. Porter, M. F. Tchir, *J. Chem. Soc. A Inorganic, Phys. Theor.*, 1971, 3772.
- 152 T. Gegenhuber, L. De Keer, A. S. Goldmann, P. H. M Van Steenberge, J. O. Mueller, O. Reyniers, J. P. Menzel, D. R. D, C. Barner-Kowollik, *Macromolecules*, 2017, **50**, 6451–6467.
- 153 T. Krappitz, F. Feist, I. Lamparth, N. Moszner, H. John, J. P. Blinco, T. R. Dargaville, C. Barner-Kowollik, *Mater. Horizons*, 2019, **6**, 81–89.
- 154 J. Melorose, R. Perroy, S. Careas, in *Climate Change 2013 - The Physical Science Basis*, ed. Intergovernmental Panel on Climate Change, Cambridge University Press, Cambridge, 1955, vol. 99, pp. 1–30.
- 155 T. H. Mamain, *Nature*, 1960, **4736**, 493.
- 156 H. J. Eichler, J. Eichler, *Laser - Bauformen, Strahlführung, Anwendungen*, Springer Berlin Heidelberg, Berlin, Heidelberg, 2015.
- 157 P. F. Duarte, Frank J and Kelley, Paul and Hillman, Lloyd W and Liao, *Dye Laser Principles*, 1990.
- 158 S. E. Harris, *Proc. IEEE*, 1969, **57**, 2096–2113.
- 159 N. P. Kovalenko, A. Abdukadirov, V. I. Gerko, M. V. Alfimov, *J. Appl. Spectrosc.*, 1980, **32**, 607–612.
- 160 N. P. Kovalenko, A. T. Abdukadyrov, V. I. Gerko, M. V Alfimov, *J. Photochem.*, 1980, **12**, 59–65.
- 161 V. X. Truong, F. Li, F. Ercole, J. S. Forsythe, *ACS Macro Lett.*, 2018, **7**, 464–469.
- 162 F. B. Mallory, C. W. Mallory, in *Organic Reactions*, John Wiley & Sons, Inc., Hoboken, NJ, USA, 1984, vol. 30, pp. 1–456.
- 163 H. Frisch, J. P. Menzel, F. R. Bloesser, D. E. Marschner, K. Mundsinger, C. Barner-Kowollik, *J. Am. Chem. Soc.*, 2018, **140**, 9551–9557.
- 164 H. Frisch, F. R. Bloesser, C. Barner-Kowollik, *Angew. Chem. Int. Ed.*, 2019, **58**, 3604–3609.
-

- 165 K. B. Kockler, H. Frisch, C. Barner-Kowollik, *Macromol. Rapid Commun.*, 2018, **39**, 1800516.
- 166 N. Corrigan, J. Xu, C. Boyer, *Macromolecules*, 2016, **49**, 3274–3285.
- 167 S. Hurrele, A. S. Goldmann, H. Gliemann, H. Mutlu, C. Barner-Kowollik, *ACS Macro Lett.*, 2018, **7**, 201–207.
- 168 E. Blasco, M. Wegener, C. Barner-Kowollik, *Adv. Mater.*, 2017, **29**, 1604005.
- 169 C. Girardeaux, J.-J. Pireaux, *Surf. Sci. Spectra*, 1996, **4**, 138–141.
- 170 K. Hildebrandt, M. Kaupp, E. Molle, J. P. Menzel, J. P. Blinco, C. Barner-Kowollik, *Chem. Commun.*, 2016, **52**, 9426–9429.
- 171 K. Murayama, Y. Yamano, H. Asanuma, *J. Am. Chem. Soc.*, DOI:10.1021/jacs.9b03267.
- 172 T. Gruending, K. K. Oehlenschlaeger, E. Frick, M. Glassner, C. Schmid, C. Barner-Kowollik, *Macromol. Rapid Commun.*, 2011, **32**, 807–812.
- 173 A. Blanc, C. G. Bochet, *J. Org. Chem.*, 2002, **67**, 5567–5577.
- 174 T. Förster, *Ann. Phys.*, 1948, **437**, 55–75.
- 175 D. L. Dexter, *J. Chem. Phys.*, 1953, **21**, 836–850.
- 176 A. Isogai, T. Saito, H. Fukuzumi, *Nanoscale*, 2011, **3**, 71–85.
- 177 S. Ehni, B. Luy, *J. Magn. Reson.*, 2013, **232**, 7–17.
- 178 K. Kobzar, B. Luy, *J. Magn. Reson.*, 2007, **186**, 131–141.
- 179 P. Mongondry, C. Bonnans-Plaisance, M. Jean, J. F. Tassin, *Macromol. Rapid Commun.*, 2003, **24**, 681–685.
- 180 O. Mitsunobu, M. Wada, T. Sano, *J. Am. Chem. Soc.*, 1972, **94**, 679–680.
- 181 M. Schlosser, P. Maccaroni, E. Marzi, *Tetrahedron*, 1998, **54**, 2763–2770.
- 182 A. Senthilmurugan, I. S. Aidhen, *European J. Org. Chem.*, 2010, **2010**, 555–564.
- 183 T. Pauloehrl, G. Delaittre, V. Winkler, A. Welle, M. Bruns, H. G. Börner, A. M. Greiner, M. Bastmeyer, C. Barner-Kowollik, *Angew. Chemie - Int. Ed.*, 2012, **51**, 1071–1074.
- 184 J. Oh, J.-I. Hong, *Org. Lett.*, 2013, **15**, 1210–1213.
- 185 R. Tanaka, T. Saito, A. Isogai, *Int. J. Biol. Macromol.*, 2012, **51**, 228–234.

Appendix

Styrylpyrene

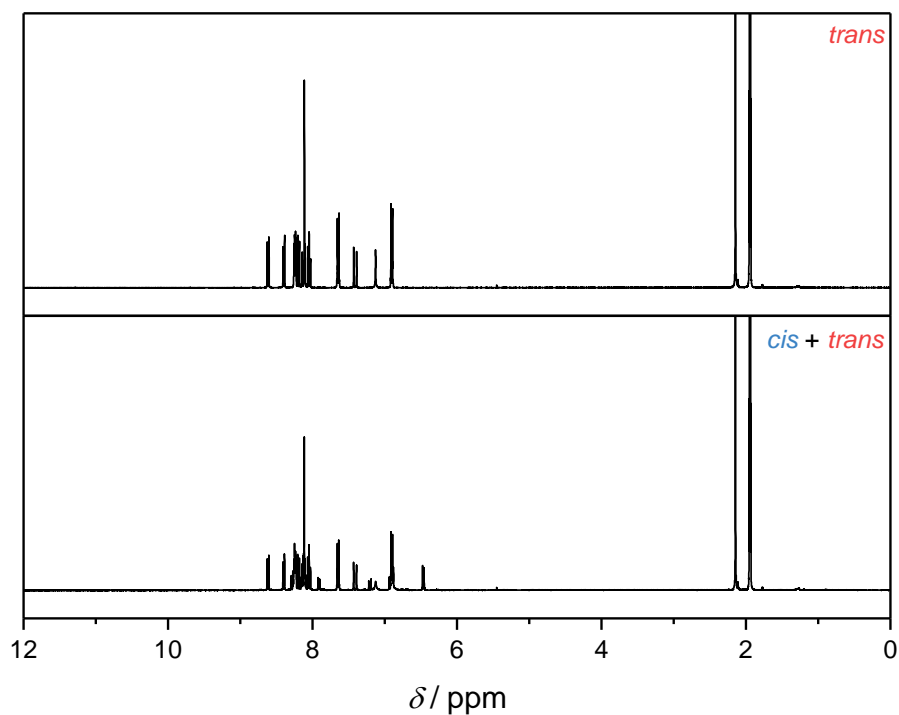
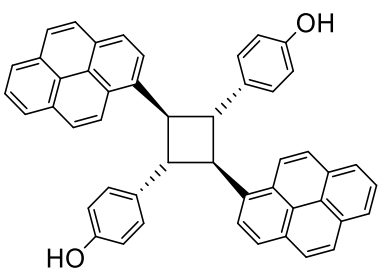
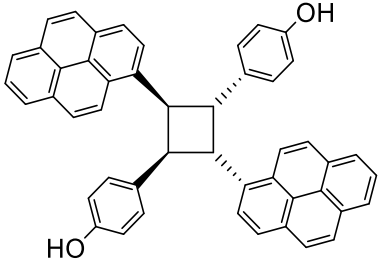
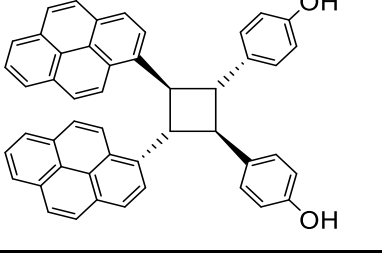
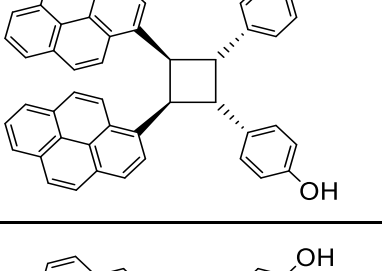
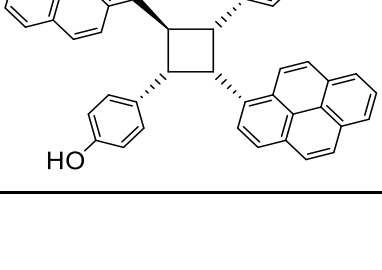


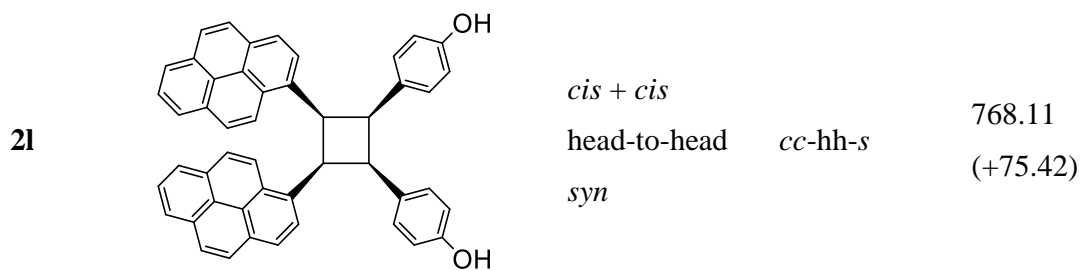
Figure 94. $^1\text{H-NMR}$ (400 MHz, CD_3CN) spectra showing the isomerisation of StyP **1** under irradiation with UV-C light ($\lambda_{\text{max}} = 254$ nm; solvent: deuterated acetonitrile) showing distinct new resonances for the cis-isomer of **1** including one representing a proton of the double bond (peak 17, 7.20 ppm, $J = 12.1$ Hz).

Structures of Possible Photoproducts

Table 7. Structures of possible photoproducts including their molecule number (**2a** – **2l**), the characteristics determining their nomenclature, abbreviations and energies obtained after geometry optimization with MMFF94 force field. The difference in the energy with respect to the lowest energy structure is given in brackets.

Label	Molecule	Characteristics	Abbreviation	Energy* [kJ mol ⁻¹]
2a		<i>trans + trans</i> head-to-tail <i>anti</i>	<i>tt-ht-a</i>	692.69 (0)
2b*		<i>trans + trans</i> head-to-tail <i>syn</i>	<i>tt-ht-s</i>	748.17 (+55.48)
2c		<i>trans + trans</i> head-to-head <i>anti</i>	<i>tt-hh-a</i>	712.28 (+19.60)
2d		<i>trans + trans</i> head-to-head <i>syn</i>	<i>tt-hh-s</i>	695.17 (+2.48)
2e		<i>trans + cis</i> head-to-tail <i>anti</i>	<i>tc-ht-a</i>	973.36 (+280.67)

2f		<i>trans + cis</i> head-to-tail <i>syn</i>	<i>tc-ht-s</i>	718.97 (+26.28)
2g		<i>trans + cis</i> head-to-head <i>anti</i>	<i>tc-hh-a</i>	782.83 (+90.14)
2h		<i>trans + cis</i> head-to-head <i>syn</i>	<i>tc-hh-s</i>	741.90 (+49.21)
2i*		<i>cis + cis</i> head-to-tail <i>anti</i>	<i>cc-ht-a</i>	748.17 (+55.48)
2j		<i>cis + cis</i> head-to-tail <i>syn</i>	<i>cc-ht-s</i>	871.63 (+178.94)
2k		<i>cis + cis</i> head-to-head <i>anti</i>	<i>cc-hh-a</i>	755.17 (+62.48)



* identical from a stereochemistry point of view, formally product of different cycloaddition approaches.

Detailed NMR Analysis of the Photoproducts PP I – III

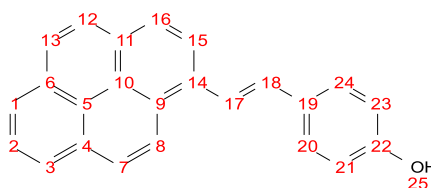


Figure 95. Labelling of the hydroxy-styrylpyrene **I** molecule for detailed NMR assignments.

Table 8. $^1\text{H-NMR}$ chemical shifts for starting material StyP **I** as well as the three photoproducts **PP I–III**, generated upon irradiation with visible light. The scalar couplings are given in Hz in brackets. The asterisk marks overlapping signals where multiplicity and/or scalar couplings could not be evaluated.

Assignment	Starting Structure	PP I	PP II	PP III
	<i>trans</i> -StyP 1	<i>tt</i> -ht- <i>s</i> 2d	<i>tt</i> -ht- <i>a</i> 2a	<i>tt</i> -ht- <i>s</i> 2b
1	8.25 *	8.12 dd (7.2, 0.99)	8.21 d (7.1)	8.03 d*
2	8.05 t (7.6)	7.87 t (7.4)	8.03 t (7.6)	7.86 t (7.6)
3	8.25 *	7.9 dd (7.7, 1.2)	8.24 d (7.3)	8.02 d*
7	8.20 d (9.2)	7.49 d (9.4)	8.17 d (9.3)	7.94 d (9.3)
8	8.62 d (9.3)	7.86 d (9.5)	8.57 d (9.2)	8.61 d (9.3)
12	8.12 *	8.11 d (8.9)	8.08 d (8.9)	7.83 d (8.9)
13	8.12 *	8.05 d (9.0)	8.06 d (9.0)	7.87 d (8.9)
15	8.40 d (8.1)	8.72 d (8.1)	8.42 d (7.9)	8.15 d (8.1)
16	8.24 *	8.39 d (8.1)	8.24 d (7.9)	7.92 d (8.1)
17	7.40 d (16.1)	4.87 -	5.51 dd (10.2, 7.5)	5.85 -
18	8.13 d (16.2)	4.24 -	5.32 dd (10.2, 7.5)	4.96 -

20 / 24	7.64 d (8.6)	7.38 d (8.6)	7.18 d (8.7)	7.29 d (8.6)
21 / 23	6.60 d (8.6)	6.76 d (8.6)	6.27 d (8.7)	6.69 d (8.6)
25	7.21 s	6.82 s	6.39 s	6.73 s

Table 9. ^{13}C -NMR chemical shifts for starting material StyP I as well as the three photoproducts PP I – III, generated upon irradiation with visible light. The shifts marked with an asterisk are interchangeable, while the ones indicated with a hash where observed in HMBC spectra only and could be assigned ambiguously.

Assignment	Starting Structure	Product I (PP I)	Product II (PP II)	Product III (PP III)
	<i>trans</i> -StyP 1	<i>tt</i> -ht-s 2d	<i>tt</i> -ht-a 2a	<i>tt</i> -ht-s 2b
1	126.00 *	126.35	126.38	126.23
2	127.32	127.41	127.52	127.34
3	126.26 *	125.9	126.27	126.03
4	125.69	125.69	131.86 #	125.51
5	132.04	132.75	132.96 #	131.89
6	132.61	125.85	132.72	132.48
7	128.39	127.9	128.12	128.02
8	124.3	124.6	125.78	125.35
9	129.03	131.87	132.22	130.32
10	12k5.86	130.64	130.66 #	125.51
11	131.53	131.35	131.30 #	130.82
12	128.05 *	128.81	128.83	128.53
13	128.50 *	128.28	128.11	128.00
14	133.57	137.42	136.34	136.72
15	124.44	126.26	126.45	126.48
16	126.34	126.86	126.01	125.69
17	132.80	51.84	47.01	46.01
18	123.44	52.92	48.00	48.94

19	130.84	134.95	133.40	133.55
20 / 24	129.33	129.97	130.85	131.01
21 / 23	116.62	116.68	115.57	116.16
22	158.11	157.25	156.32	156.58

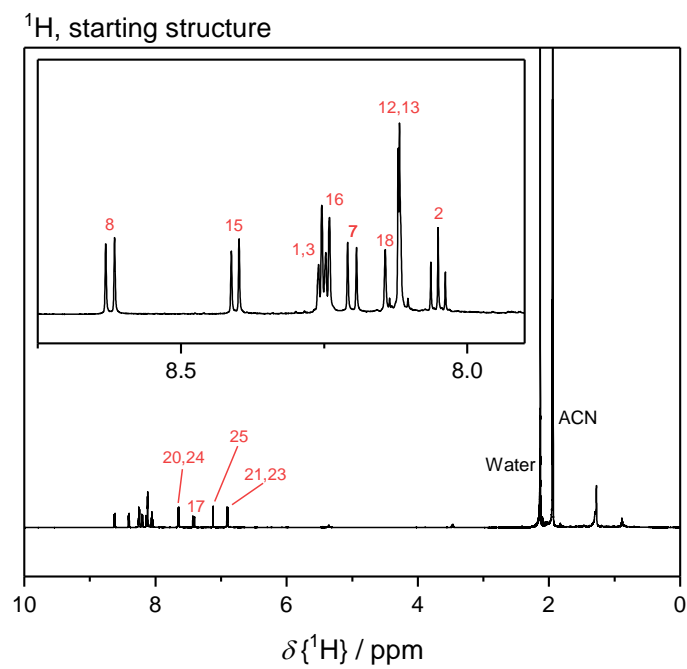


Figure 96. ¹H spectrum of the starting material *trans*-hydroxy-styrylpyrene **1**.

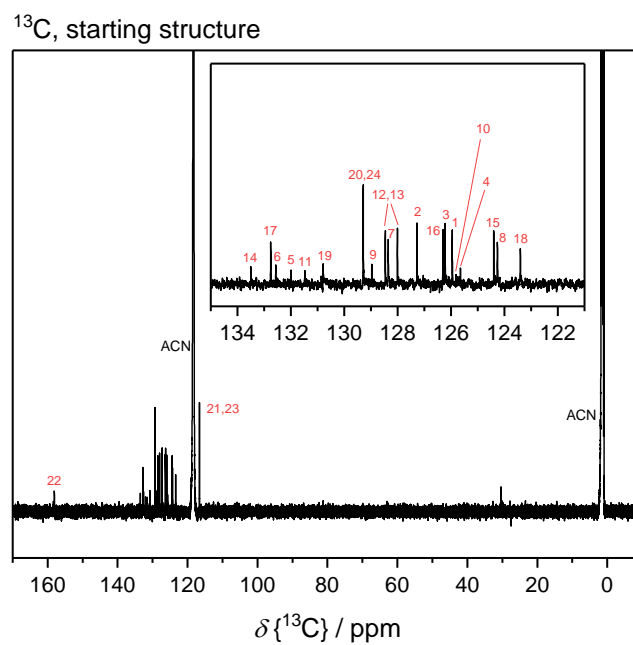


Figure 97. ¹³C spectrum of the starting material *trans*-hydroxy-styrylpyrene **1**.

NOESY, starting structure

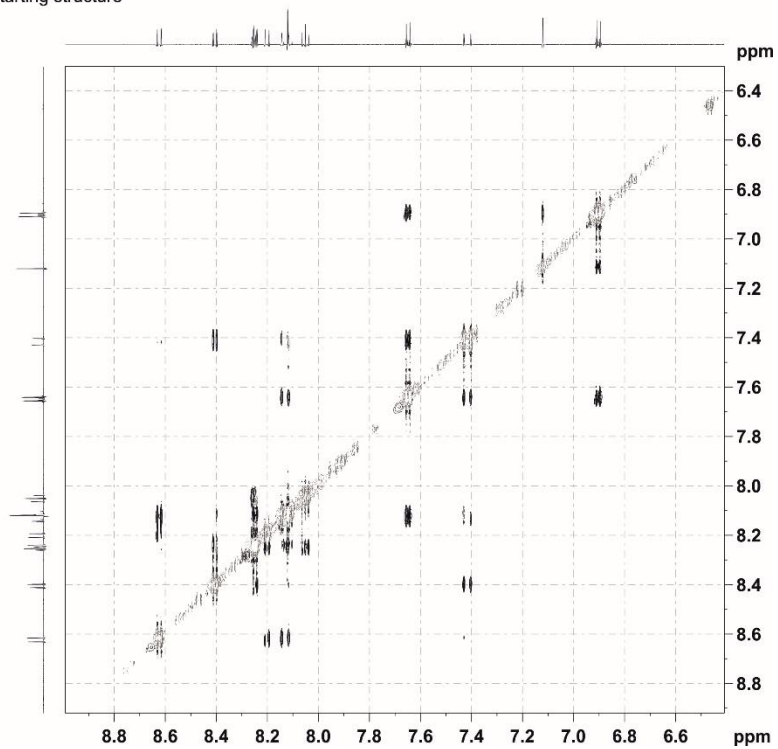


Figure 98. NOESY measurement of the starting material trans-hydroxy-styrylpyrene **1**.

COSY, starting structure

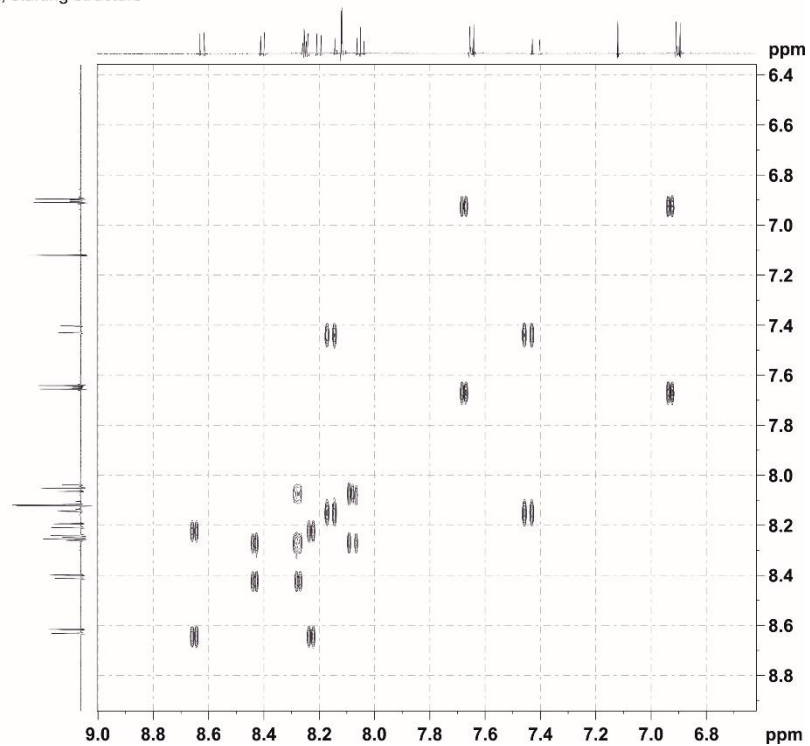


Figure 99. COSY measurement of the starting material trans-hydroxy-styrylpyrene **1**.

HSQC-TOCSY, starting structure, Aromatics

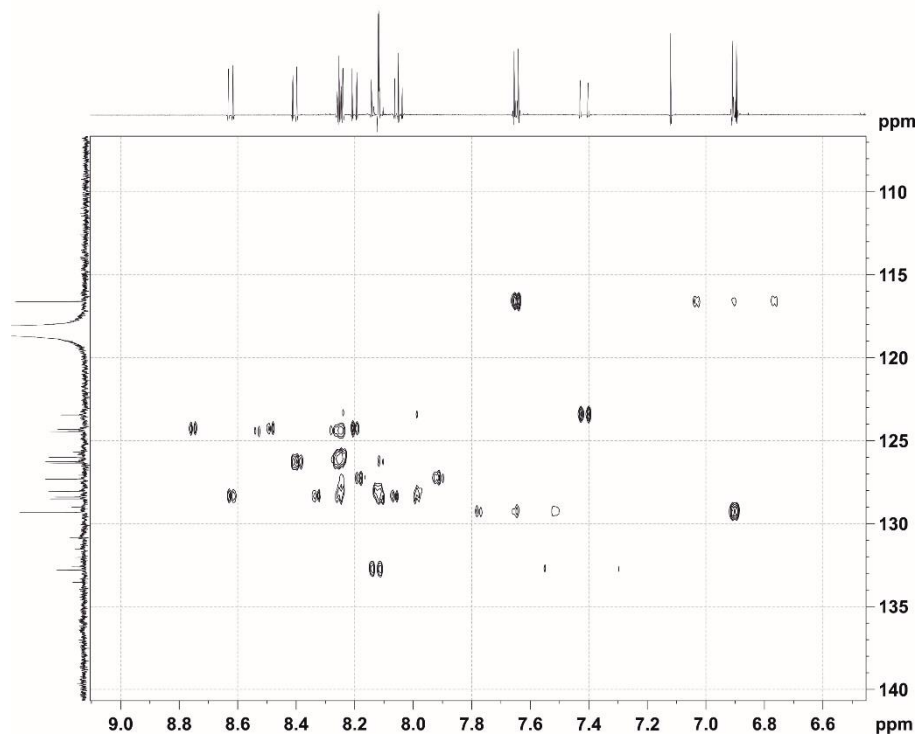


Figure 100. HSQC-TOCSY measurement of the starting material trans-hydroxy-styrylpyrene 1.

dec HSQC, starting structure

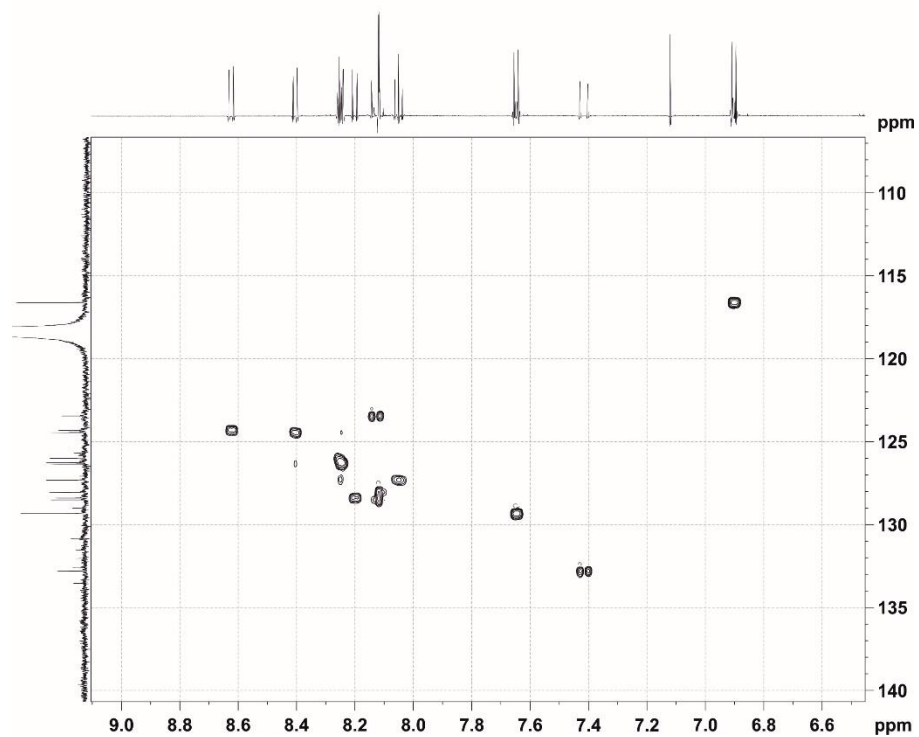


Figure 101. Decoupled HSQC measurement of the starting material trans-hydroxy-styrylpyrene 1.

HMBC, starting structure

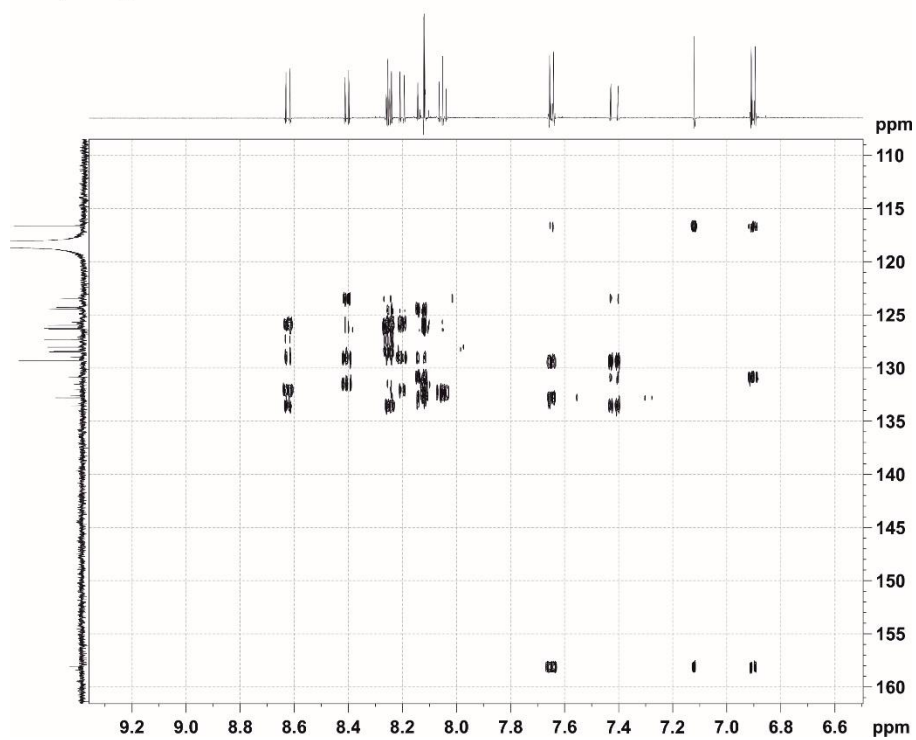


Figure 102. HMBC measurement of the starting material trans-hydroxy-styrylpyrene 1.

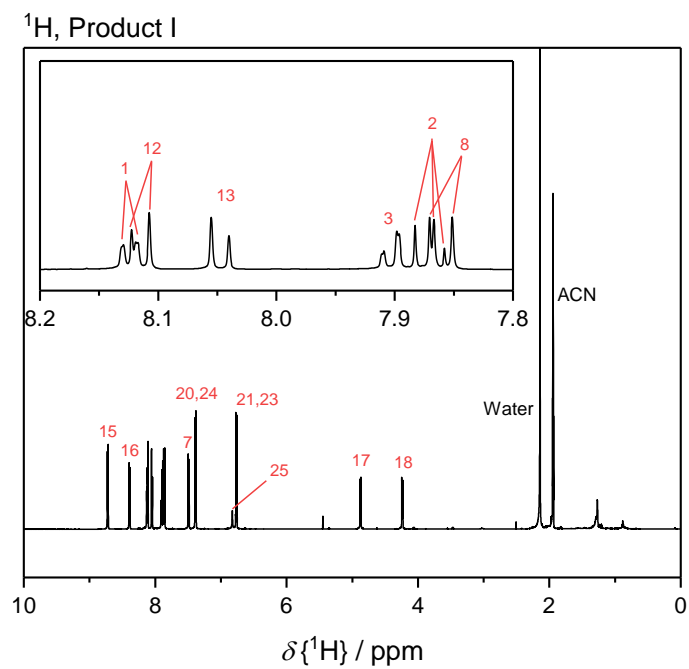


Figure 103. ¹H Spectrum of Product I (tt-ht-s 2d).

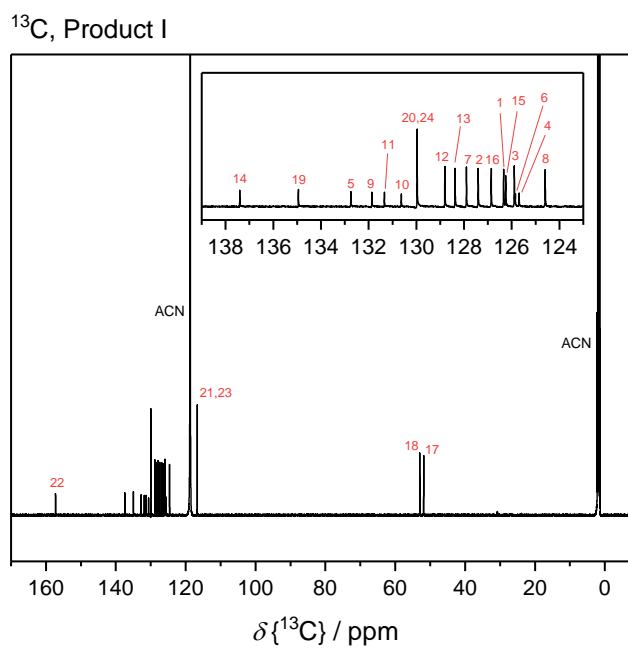


Figure 104. ¹³C Spectrum of Product I (tt-ht-s 2d).

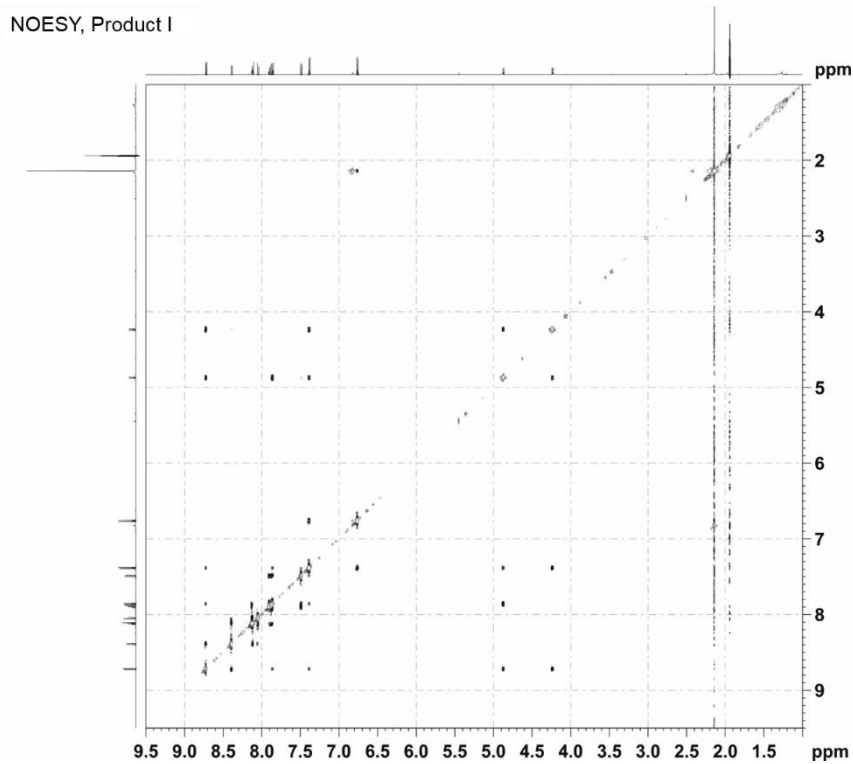


Figure 105. NOESY measurement of Product I (tt-ht-s 2d).

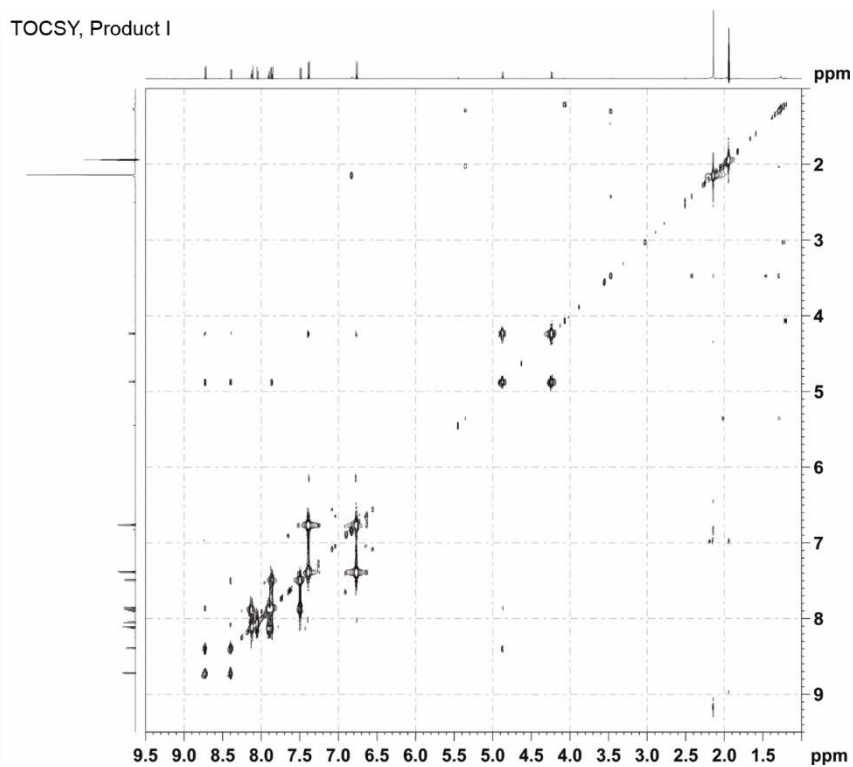
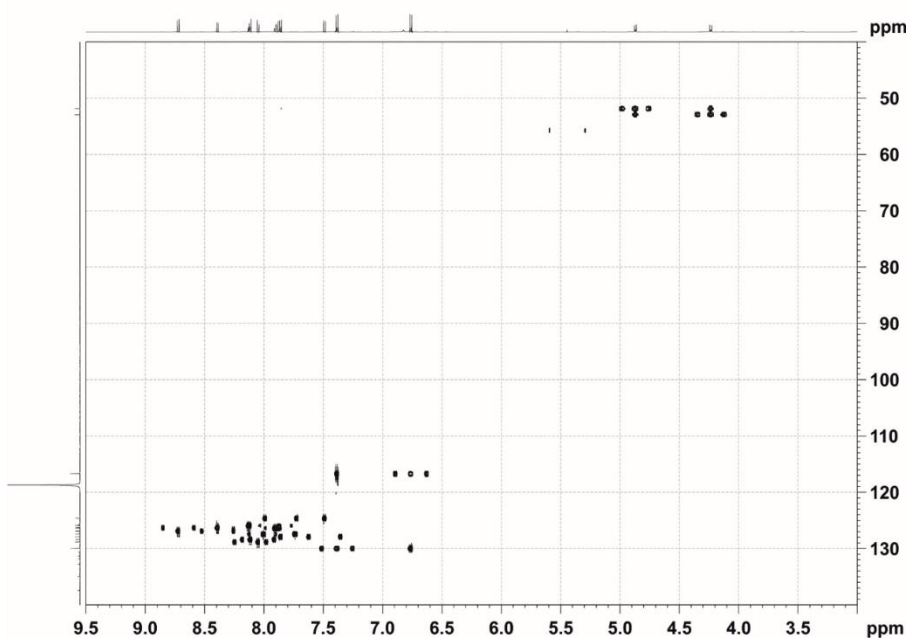
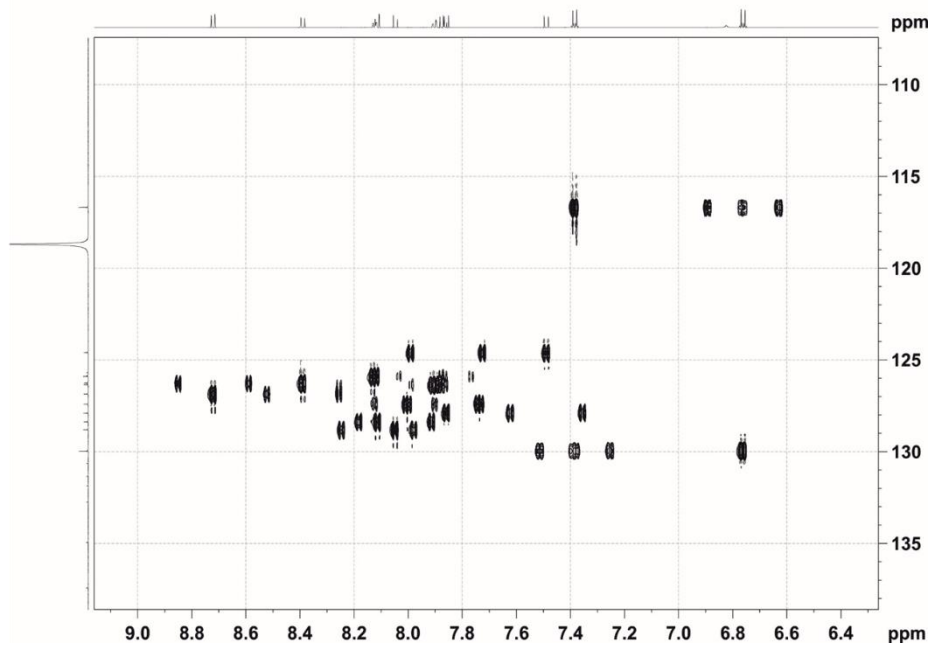


Figure 106. TOCSY measurement of Product I (tt-ht-s 2d).

HSQC-TOCSY, Product I

*Figure 107. HSQC-TOCSY measurement of Product I (tt-ht-s 2d).*

HSQC-TOCSY, Product I, Aromatics

*Figure 108. Enlarged view of the HSQC-TOCSY measurement of Product I (tt-ht-s 2d).*

dec HSQC, Product I

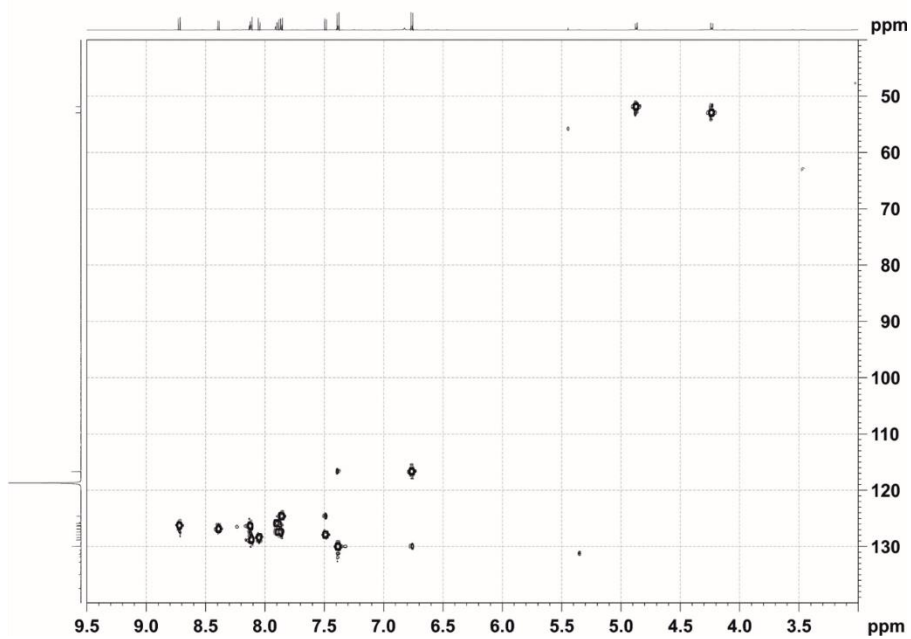


Figure 109. Decoupled HSQC measurement of Product I (tt-ht-s 2d).

HMBC, Product I

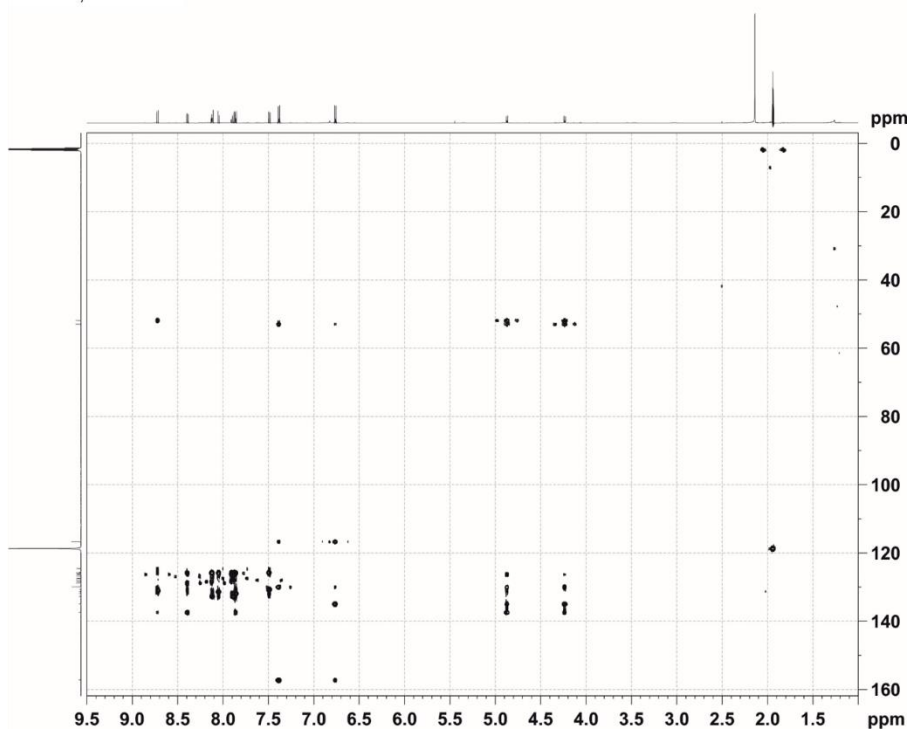


Figure 110. HMBC measurement of Product I (tt-ht-s 2d).

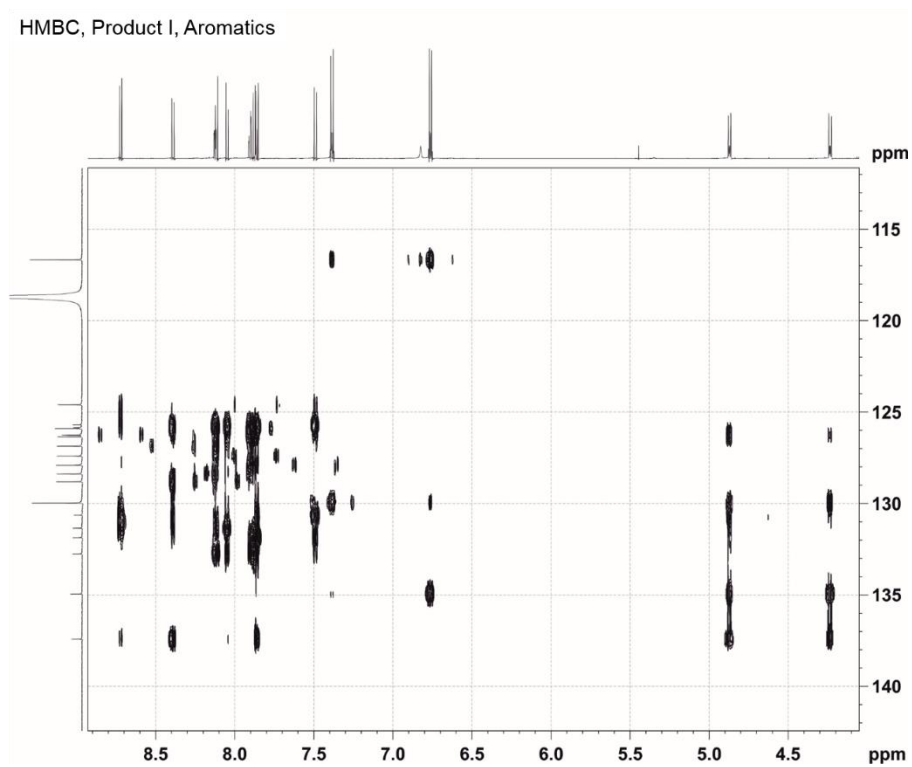


Figure 111. Enlarged view of the HMBC measurement of Product I (tt-ht-s 2d).

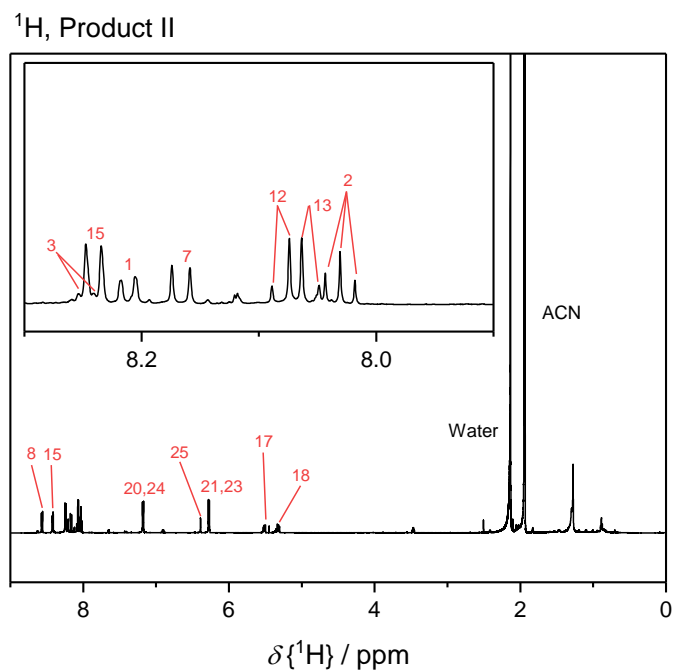


Figure 112. ^1H spectrum of Product II (tt-ht-a 2a).

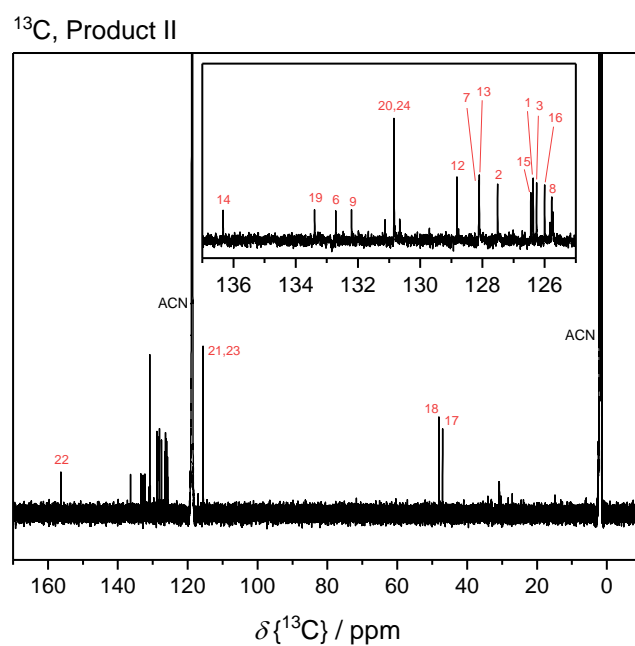


Figure 113. ^{13}C spectrum of Product II (tt-ht-a 2a).

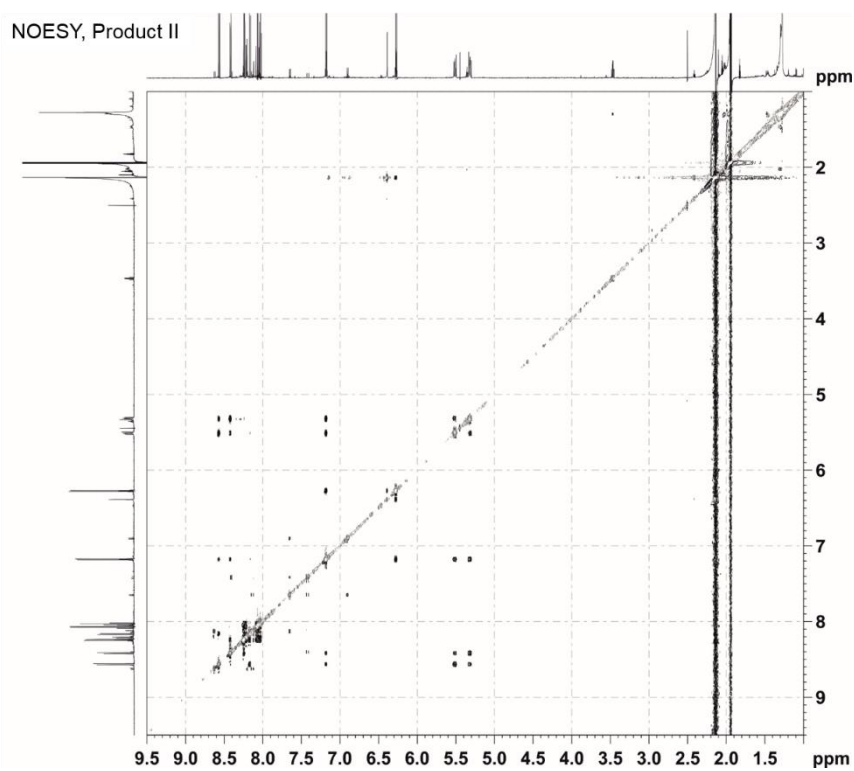


Figure 114. NOESY measurement of Product II (tt-ht-a 2a).

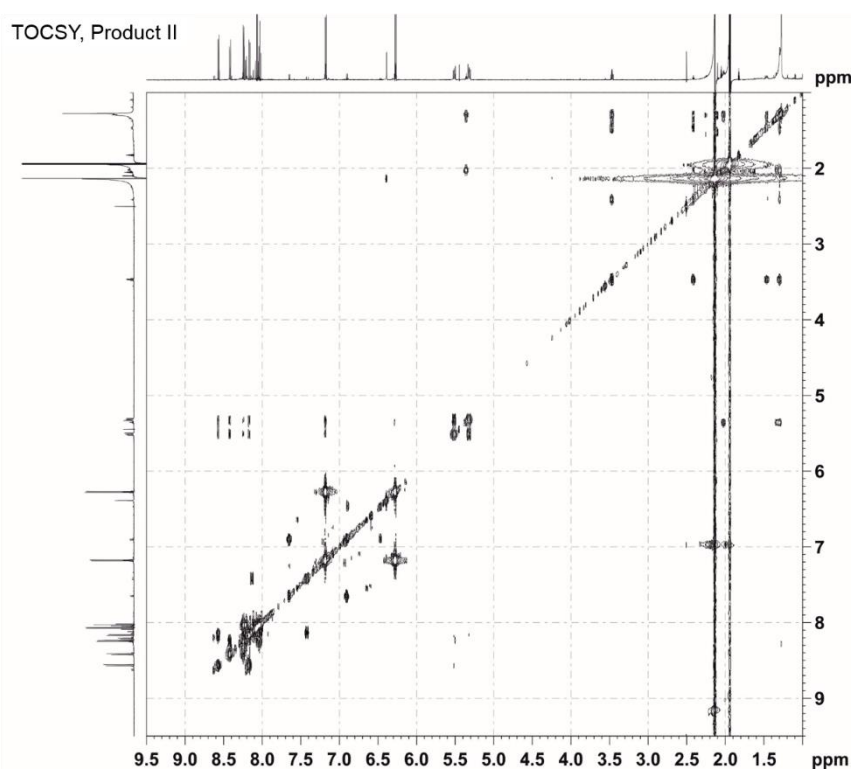
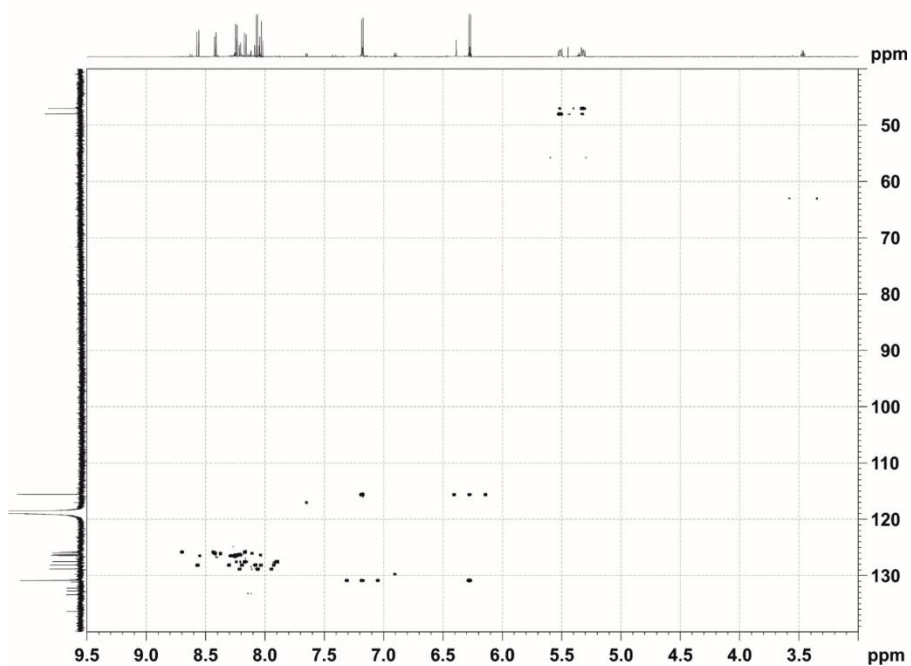
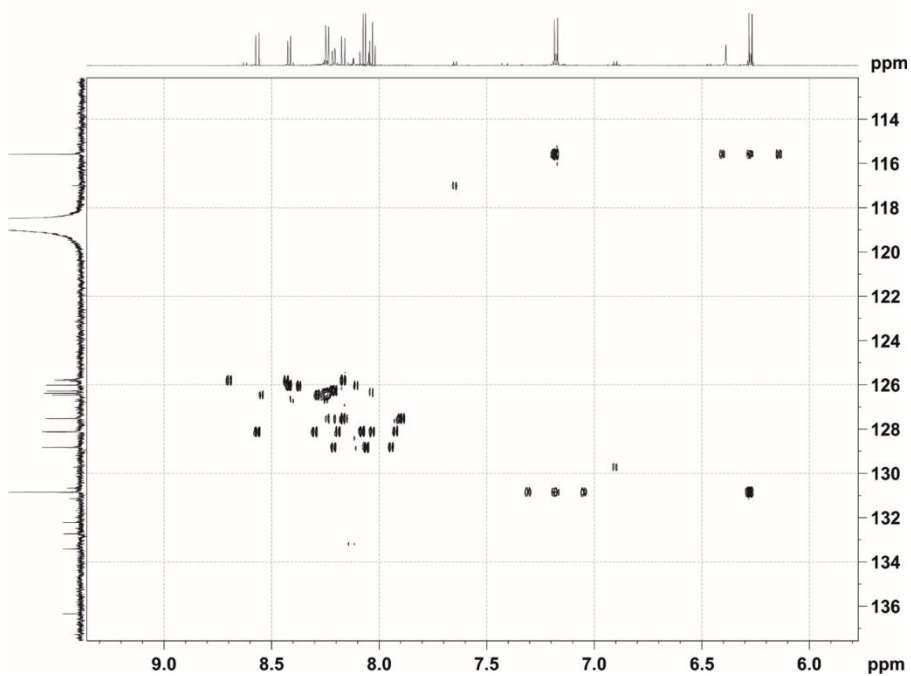


Figure 115. TOCSY measurement of Product II (tt-ht-a 2a).

HSQC-TOCSY, Product II

*Figure 116. HSQC-TOCSY measurement of Product II (tt-ht-a 2a).*

HSQC-TOCSY, Product II, Aromatics

*Figure 117. Enlarged view of the HSQC-TOCSY measurement of Product II (tt-ht-a 2a).*

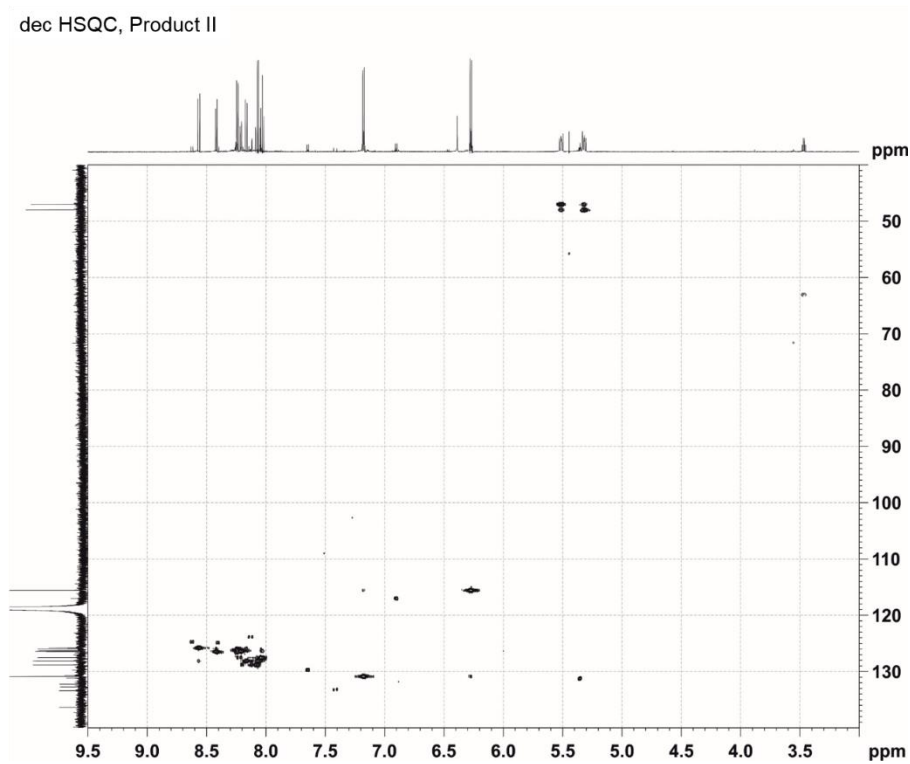


Figure 118. Decoupled HSQC measurement of Product II (tt-ht-a 2a).

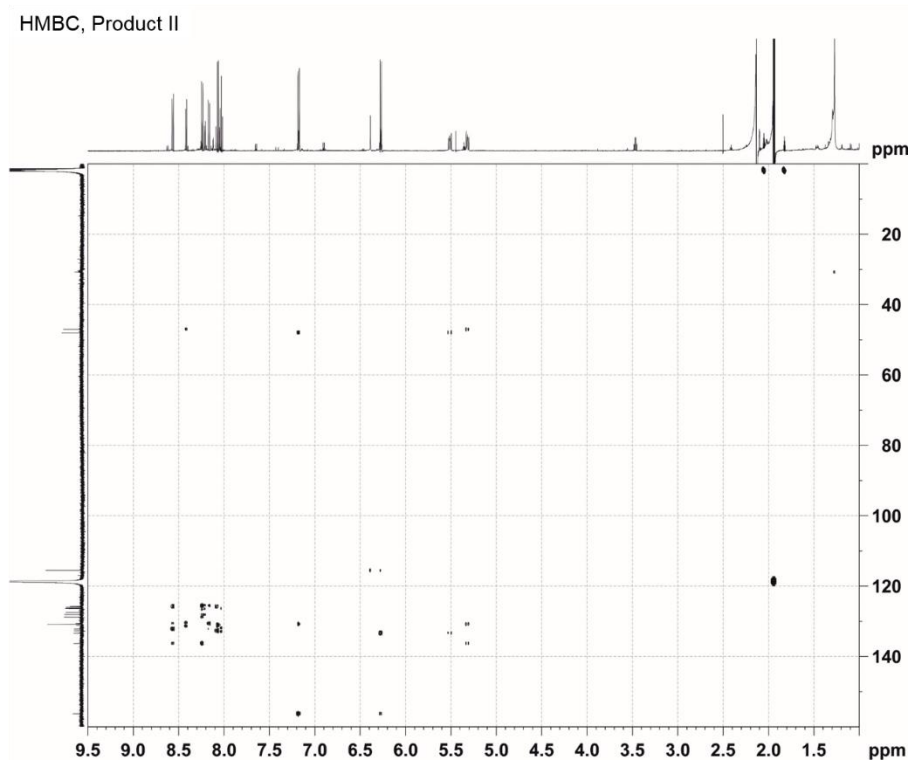


Figure 119. HMBC measurement of Product II (tt-ht-a 2a).

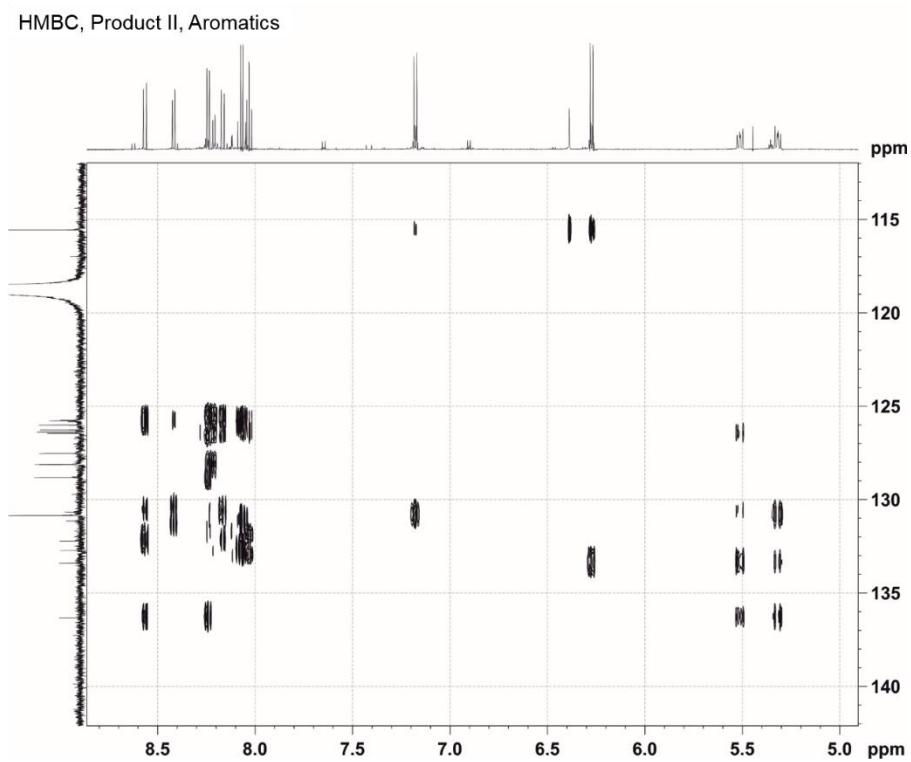


Figure 120. Enlarged view of the HMBC measurement of Product II (tt-ht-a 2a).

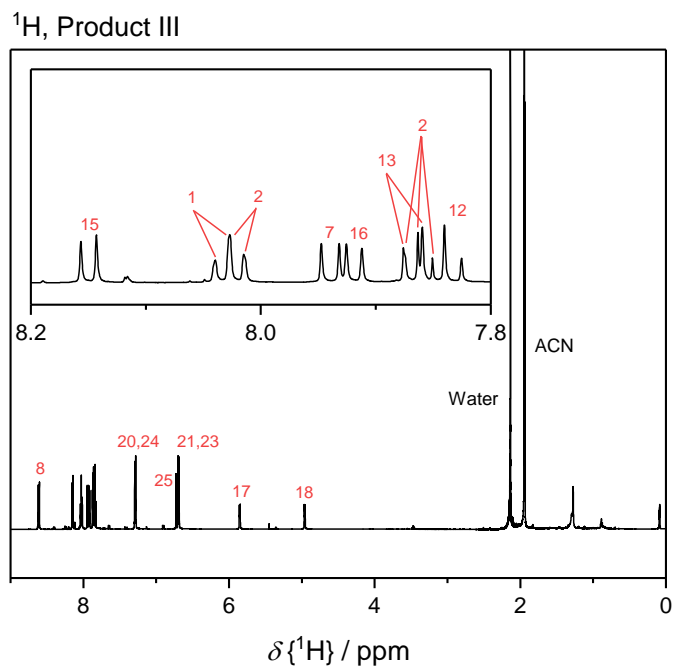


Figure 121. ^1H spectrum of Product III (tt-ht-s **2b**).

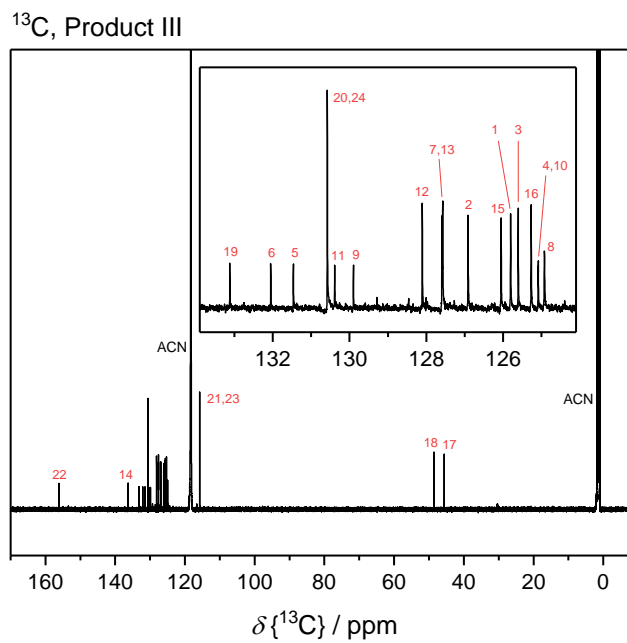


Figure 122. ^{13}C spectrum of Product III (tt-ht-s **2b**).

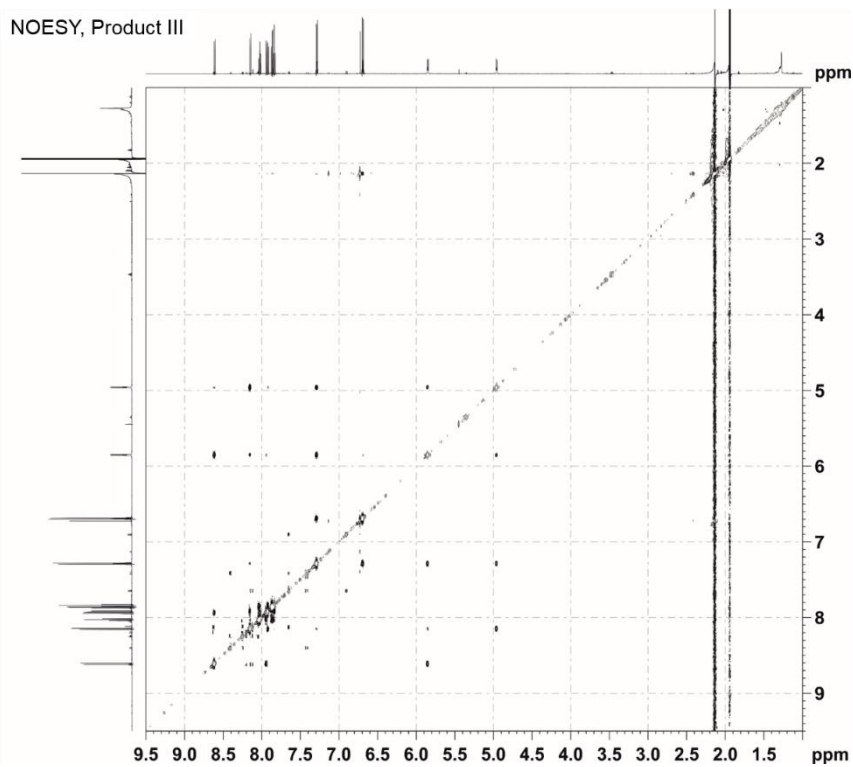


Figure 123. NOESY measurement of Product III (tt-ht-s 2b).

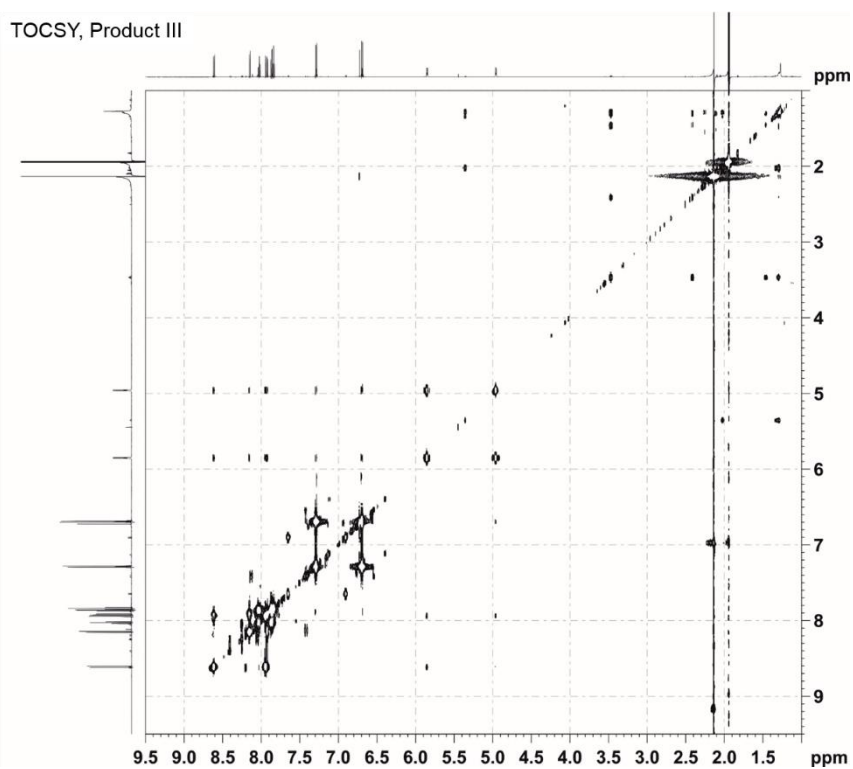


Figure 124. TOCSY measurement of Product III (tt-ht-s 2b).

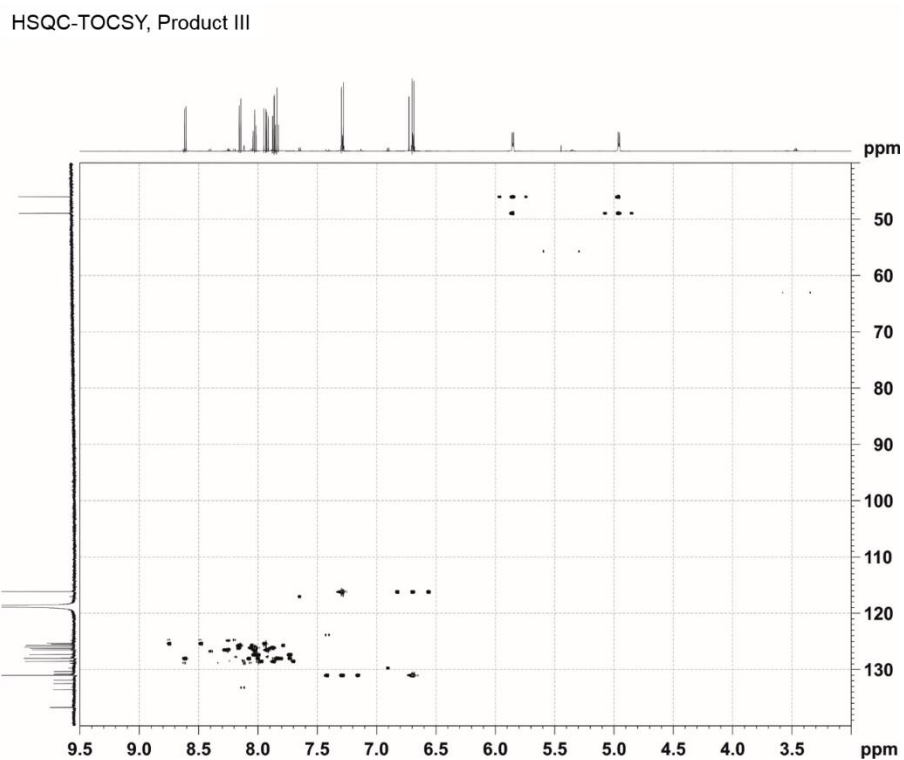


Figure 125. HSQC-TOCSY measurement of Product III (tt-ht-s 2b).

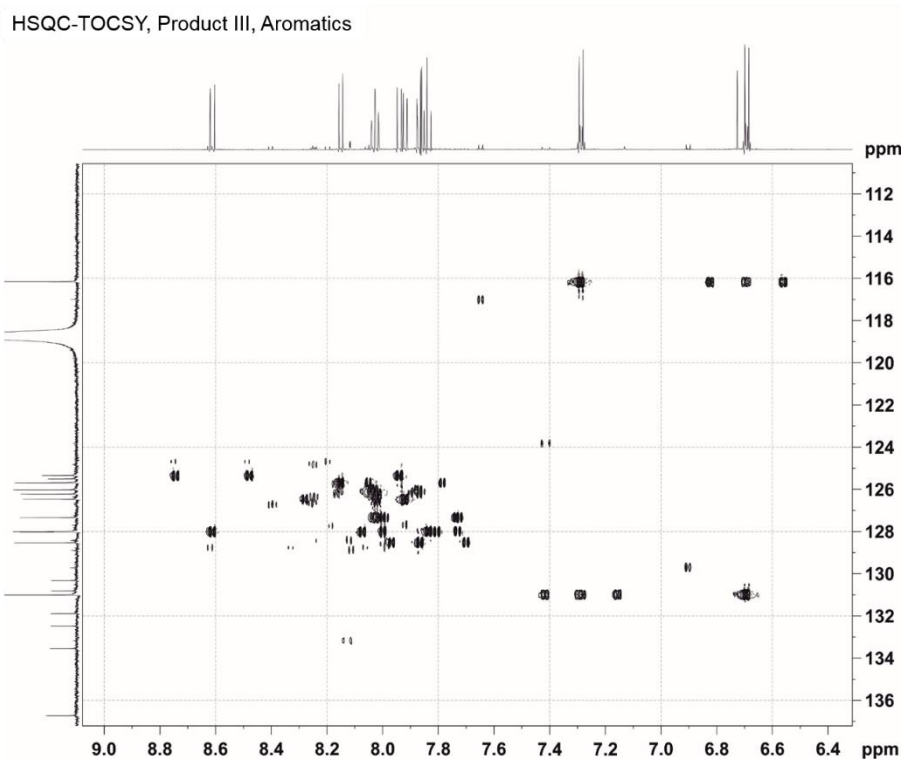


Figure 126. Zoomed version of the HSQC-TOCSY measurement of Product III (tt-ht-s 2b).

dec HSQC, Product III

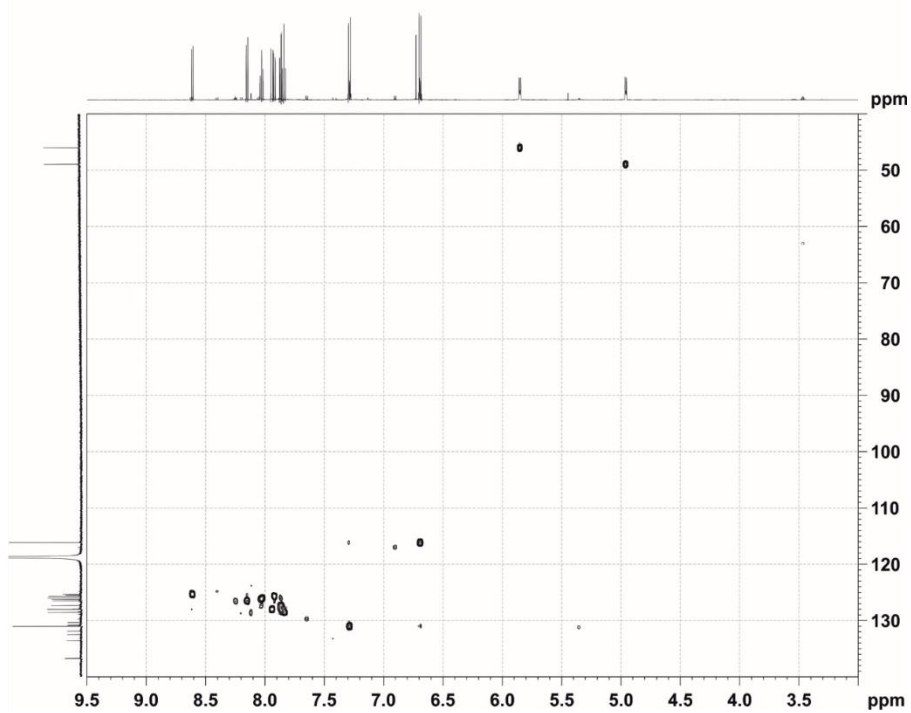


Figure 127. Decoupled HSQC measurement of Product III (tt-ht-s 2b).

HMBC, Product III

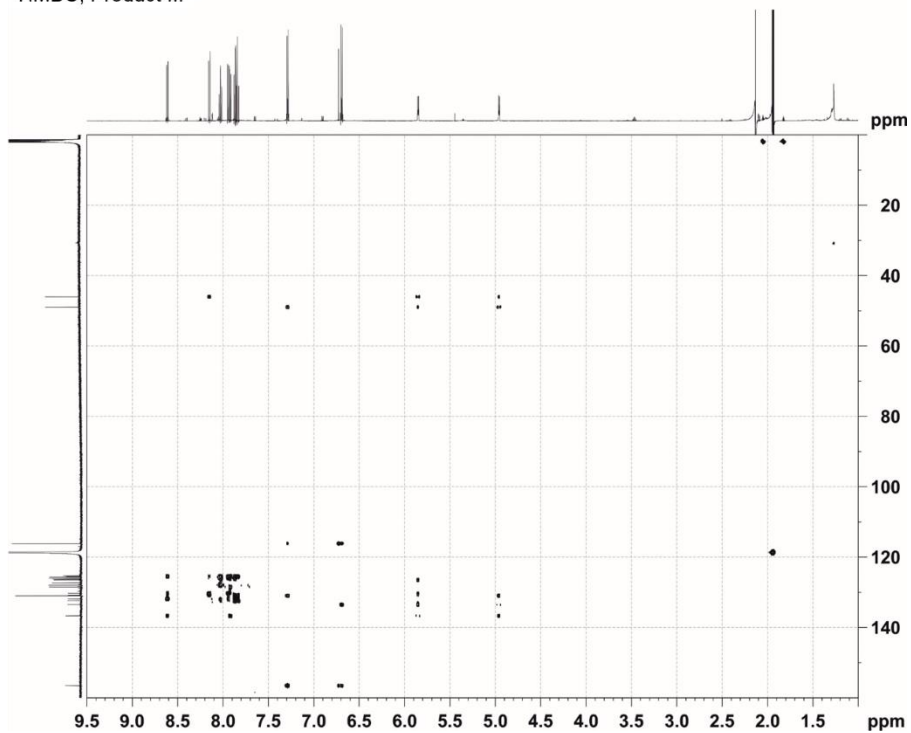


Figure 128. HMBC measurement of Product III (tt-ht-s 2b).

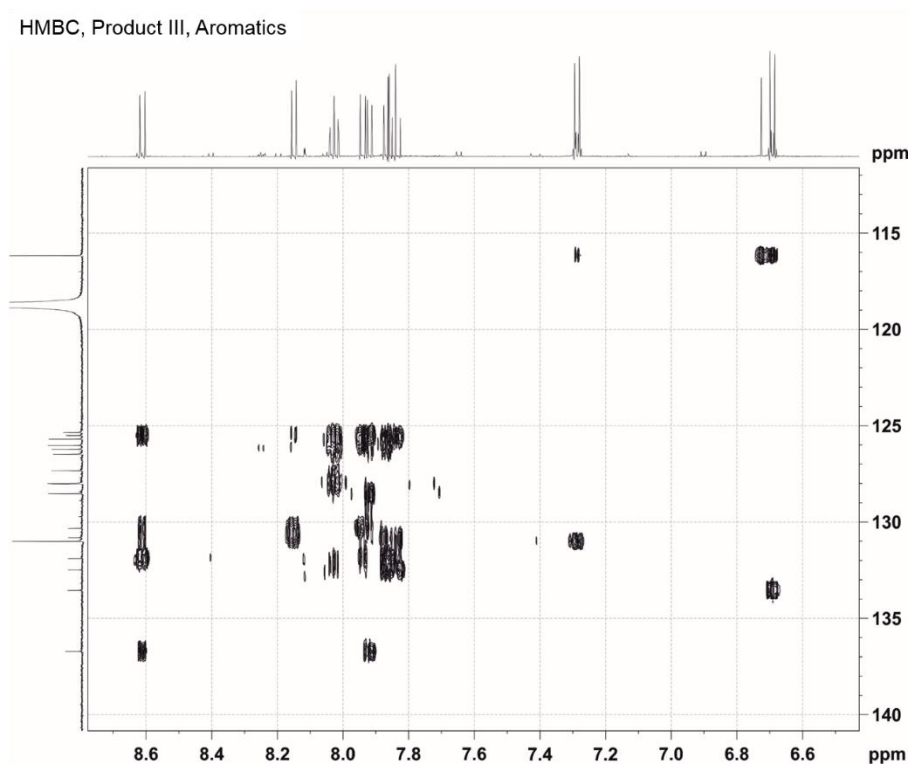


Figure 129. Enlarged view of the HMBC measurement of Product III (tt-ht-s 2b).

NOE data:

- Product I (*tt*-*ht-s* **2d**): H-18 with H-17, H-20/24 and H-15, H-17 with H-18, H-20/24, H-8 and H-15, H-21/23 with H-25 and H-20/24, H-20/24 with H-18, H-17, H-21/23, weak H-8 and weak H-15, H-7 with H-8, H-8 with H-17, weak H-20/24, H-7 and weak H-15, H-2 with H-1 and H-2, H-3 with H-2, H-13 with H-12, H-12 with H-13 and H-16, H-1 with H-13 and H-2, H-16 with H-12 and H-15, H-15 with H-18, H-17, H-20/24, H-16 and H-8.
- Product II (*tt*-*ht-a* **2a**): H-18 with H-17, H-20/24, H-15 and H-8, H-17 with H-18, H-20/24, H-15 and H-8, H-21/23 with –H-20/24, H-25 with H-21/23, H-20/24 with H-17, H-18, weak H-7, weak H-16 or H-3, H-15 and H-8, H-2 with H-1 and H-3, H-13 with H-1, H-12 with H-16, H-7 with H-3 and H-8, H-3 and H-16 (as overlapping resonance) with H-2, H-12, H-13, H-7 and H-15.
- Product III (*tt*-*ht-s* **2b**): H-18 with H-17, H-20/24, H-15 and weak with H-8, H-17 with H-18, H-20/24, weak H-15, strong H-8, H-21/23 with H-20/24, H-20/24 with H-18, H-17, H-21/23 and weak H-15, H-12 with H-16, H-2 with H-1 and H-3, H-13 with H-1, H-16 with H-15 and H-12, H-7 with H-3 and H-8, H-3 with H-7 and H-2, H-1 with H-13 and H-2, H-15 with H-18, weak H-17, H-16 and weak H-20/24, H-8 with H-17, weak H-18, weak H-20/24 and H-7.
- *trans*-Hydroxy-styrylpyrene (*trans*-StyP-OH **1**): H-21/23 with H-25 and H-20/24, H-17 with H-20/24 and H-15, H-20/24 with H-21/23, H-17 and H-18, H-2 with H-1 or H-3, H-12 or H-13 with H-16, H-18 with H-20/24, H-8 and very weak with H-15, H-7 with H-1 or H-3 and H-8, H-16 with H-12 or H-13 and H-15, H-1 or H-3 with H-2 and H-12 or H-13, H-15 with H-16 and H-17, H-8 with H-18 and H-7.

Table 10. Differences of the ^1H chemical shifts in ppm between the starting hydroxy-styrylpyrene **I**, indicated with start and each of the three photoproducts, marked as Product I (**PP I**, *tt-ht-a 2a*), Product II (**PP II**, *tt-ht-a 2a*) and Product III (**PP III**, *tt-ht-s 2b*).

Assignment	$\Delta_{\text{start-PP I}}$	$\Delta_{\text{PP I-PP II}}$	$\Delta_{\text{PP I-PP III}}$	$\Delta_{\text{start-PP II}}$	$\Delta_{\text{PP III-PP II}}$	$\Delta_{\text{start-PP III}}$
1	0.13	-0.09	0.09	0.04	-0.18	0.22
2	0.18	-0.16	0.01	0.02	-0.17	0.19
3	0.35	-0.34	-0.12	0.01	-0.22	0.23
7	0.71	-0.68	-0.45	0.03	-0.23	0.26
8	0.94	-0.89	-0.93	0.05	0.04	0.01
12	0.01	0.03	0.28	0.04	-0.25	0.29
13	0.07	-0.01	0.18	0.06	-0.19	0.25
15	-0.32	0.30	0.57	-0.02	-0.27	0.25
16	-0.15	0.15	0.47	0.00	-0.32	0.32
17	2.53	-0.64	-0.98	1.89	0.34	1.55
18	3.89	-1.08	-0.72	2.81	-0.36	3.17
20 / 24	0.26	0.20	0.09	0.46	0.11	0.35
21 / 23	-0.16	0.49	0.07	0.33	0.42	-0.09
25	0.39	0.43	0.09	0.82	0.34	0.48

Table 11. Differences of the ^{13}C chemical shifts in ppm between the starting hydroxy-styrylpyrene **I**, indicated with start and each of the three photoproducts, marked as Product I (**PP I**, *tt-ht-a 2a*), Product II (**PP II**, *tt-ht-a 2a*) and Product III (**PP III**, *tt-ht-s 2b*).

Assignment	$\Delta_{\text{start-PP I}}$	$\Delta_{\text{PP I-PP II}}$	$\Delta_{\text{PP I-PP III}}$	$\Delta_{\text{start-PP II}}$	$\Delta_{\text{PP III-PP II}}$	$\Delta_{\text{start-PP III}}$
1	-0.35	-0.03	0.12	-0.38	-0.15	-0.23
2	-1.14	-0.11	0.07	-1.25	-0.18	-1.07
3	1.42	-0.37	-0.13	1.05	-0.24	1.29
4	0.00	-6.17	0.18	-6.17	-6.35	0.18
5	-0.71	-0.21	0.86	-0.92	-1.07	0.15
6	6.76	-6.87	-6.63	-0.11	-0.24	0.13
7	0.49	-0.22	-0.12	0.27	-0.1	0.37
8	-0.30	-1.18	-0.75	-1.48	-0.43	-1.05
9	-2.84	-0.35	1.55	-3.19	-1.9	-1.29
10	-4.78	-0.02	5.13	-4.80	-5.15	0.35
11	0.18	0.05	0.53	0.23	-0.48	0.71
12	-3.76	-0.02	0.28	-3.78	-0.3	-3.48
13	0.22	0.17	0.28	0.39	-0.11	0.50
14	-3.85	1.08	0.70	-2.77	0.38	-3.15
15	-1.82	-0.19	-0.22	-2.01	0.03	-2.04
16	-0.52	0.85	1.17	0.33	-0.32	0.65
17	80.96	4.83	5.83	85.79	-1.00	86.79
18	70.52	4.92	3.98	75.44	0.94	74.5
19	-4.11	1.55	1.40	-2.56	0.15	-2.71
20 / 24	-0.64	-0.88	-1.04	-1.52	0.16	-1.68
21 / 23	-0.06	1.11	0.52	1.05	0.59	0.46
22	0.86	0.93	0.67	1.79	0.26	1.53

Styrylpyrene meets *o*-Methyl Benzaldehyde

Detailed NMR Analysis

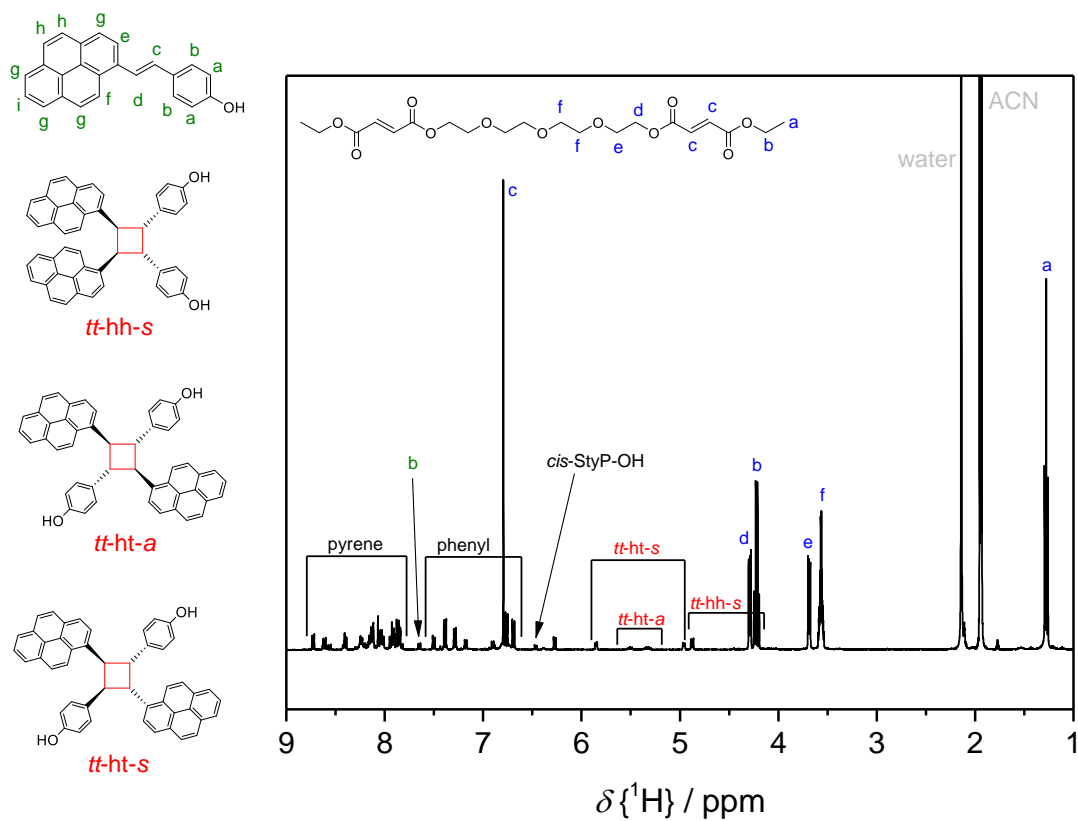


Figure 130. ^1H -NMR spectrum after irradiation of StyP **1** (5.00 mM) in presence of TGD **5** (2.50 mM, solvent: CD_3CN) at a wavelength of 435 nm (483 μmol photons). As expected, **1** underwent dimerisation – proven by the formation of the respective cyclobutane-photoproducts (red) – as well as isomerisation while **5** remained inactive.

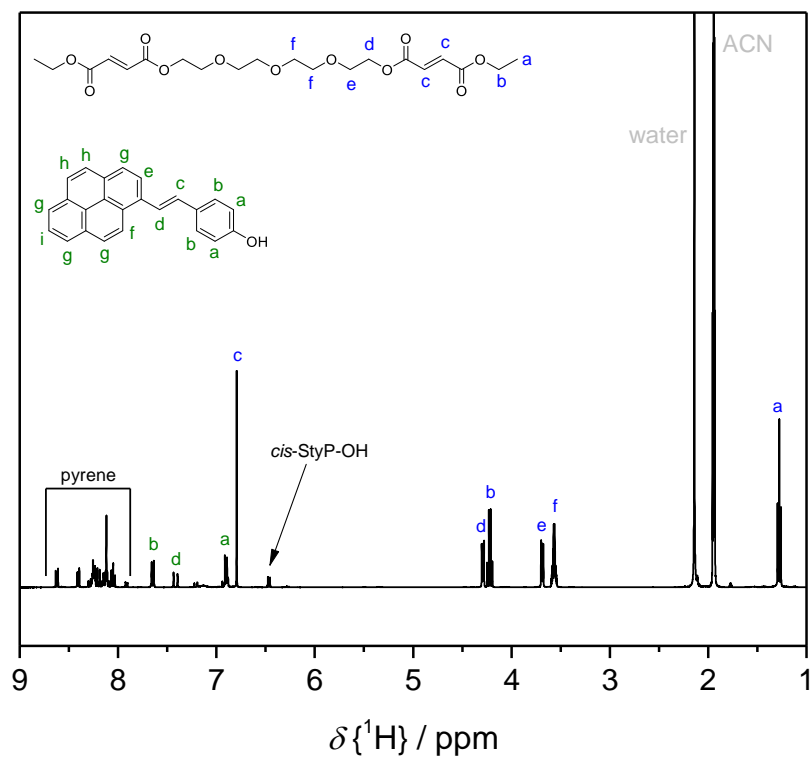


Figure 131. $^1\text{H-NMR}$ spectrum after irradiation of StyP 1 (5.00 mM) in presence of TGD 5 (2.50 mM, solvent: CD_3CN) at a wavelength of 330 nm (483 μmol of photons). As expected, the only reaction taking place was the photochemically triggered isomerisation of **1**.

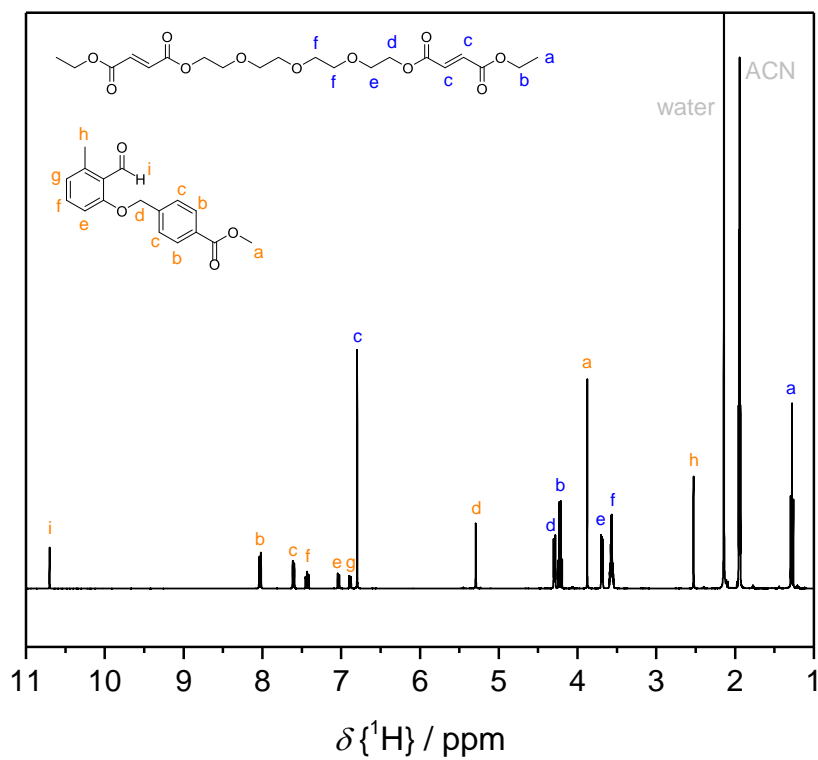


Figure 132. $^1\text{H-NMR}$ spectrum after irradiation of *o*-MBA **4** (5.00 mM) in presence of TGD **5** (2.50 mM, solvent: CD_3CN) at a wavelength of 435 nm (483 μmol of photons). As expected, no photochemical reaction took place, proving the inactivity of both chromophores in the visible light range.

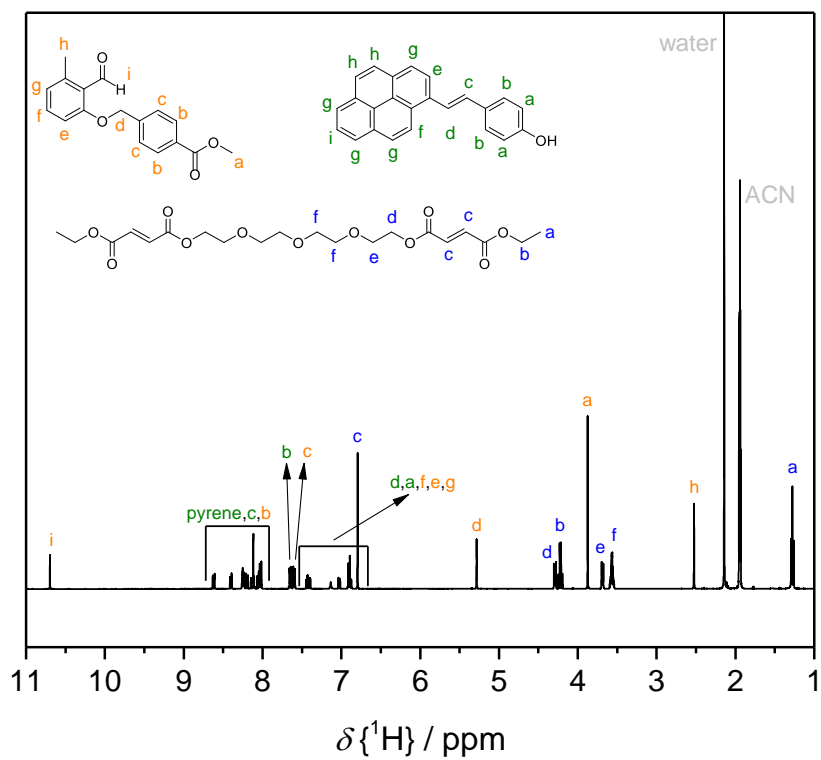


Figure 133. $^1\text{H-NMR}$ spectra of a mixture of StyP 1 (5.00 mM), *o*-MBA 4 (5.00 mM), and TGD 5 (2.50 mM), solvent: CD_3CN before irradiation.

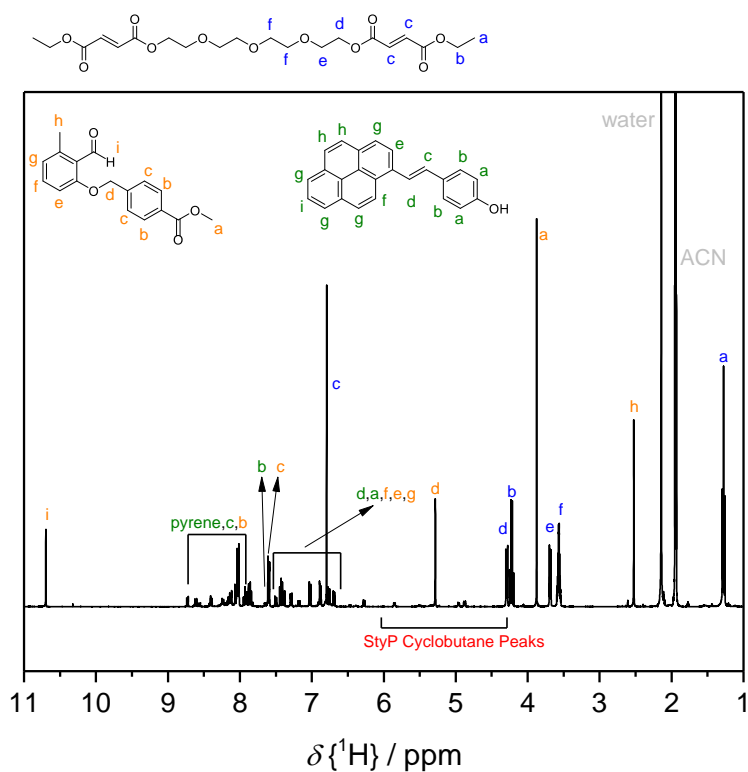


Figure 134. $^1\text{H-NMR}$ spectrum after irradiation of a mixture of StyP **1** (5.00 mM), o-MBA **4** (5.00 mM), and TGD **5** (2.50 mM), solvent: CD_3CN) with visible light (435 nm, 483 μmol photons). As expected, three styrylpyrene photoproducts were formed (marked in red). In addition, o-MBA **4** (compare magnetic resonance **i** close to 11 ppm) and TGD **5** (compare magnetic resonance **a** close to 1.00 ppm) remained intact.

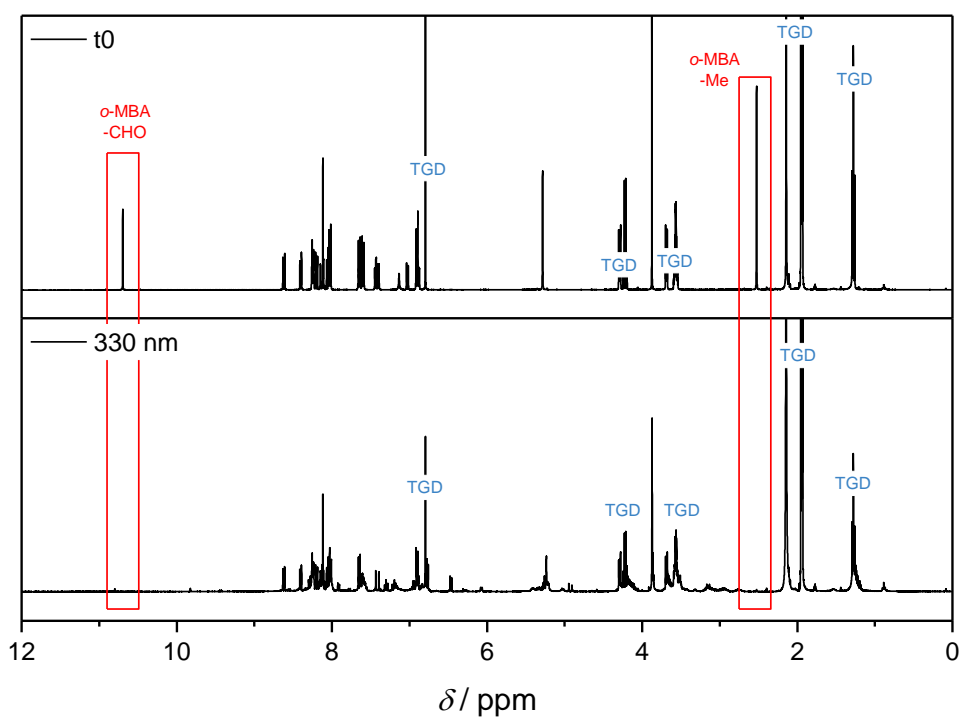


Figure 135. ^1H -NMR spectra before and after irradiation of a mixture of StyP **1**, *o*-MBA **4**, and TGD **5** with UV light (330 nm, 483 μmol photons). While the magnetic resonances for the methyl and aldehyde group of *o*-MBA disappeared (red boxes), TGD stayed intact (blue labelled magnetic resonances). In conclusion, *o*-MBA dimerised with itself instead of reacting with TGD.

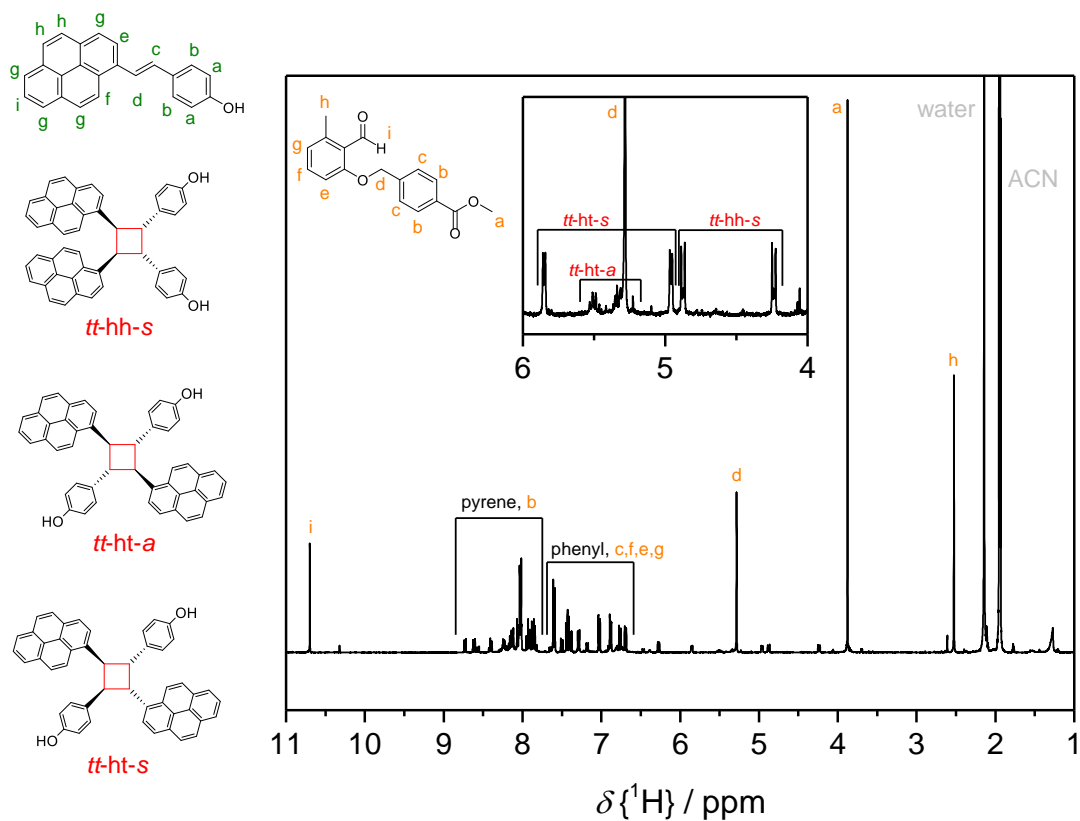


Figure 136. $^1\text{H-NMR}$ spectrum after irradiation of StyP **1** (5.00 mM) and *o*-MBA **4** (5.00 mM, solvent: CD_3CN) at a wavelength of 435 nm (483 μmol photons). As expected, **1** underwent dimerisation – proven by the formation of the respective cyclobutane-photoproducts (red) – as well as isomerisation while **4** remained inactive.

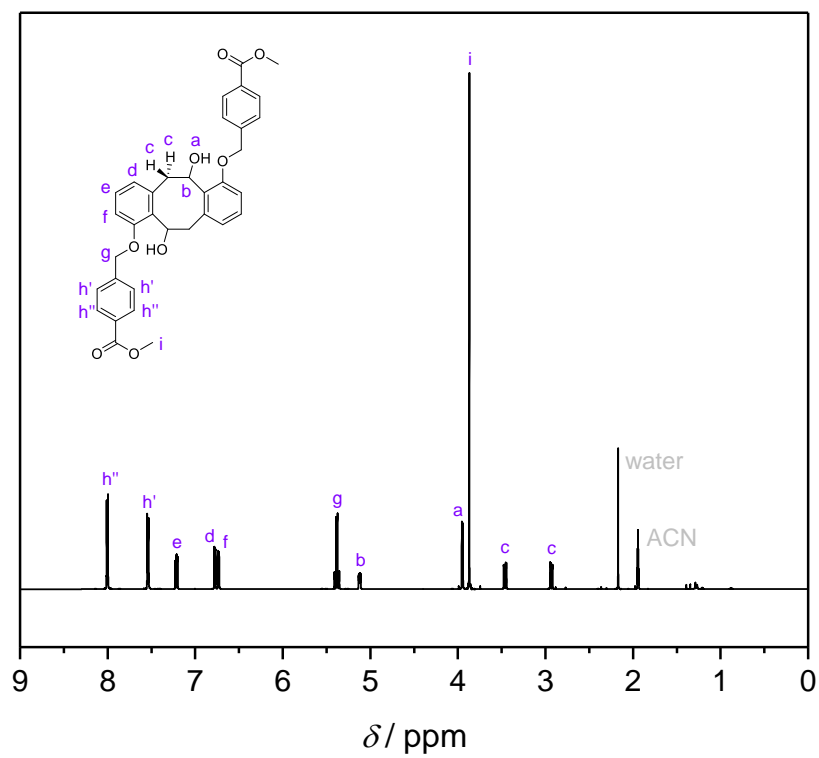


Figure 137. Main product formed via a [4+4] cycloaddition during irradiation of *o*-MBA **4** with UV-A light (330 nm).

Liquid Chromatography Mass Spectroscopy (LC-MS) Measurements

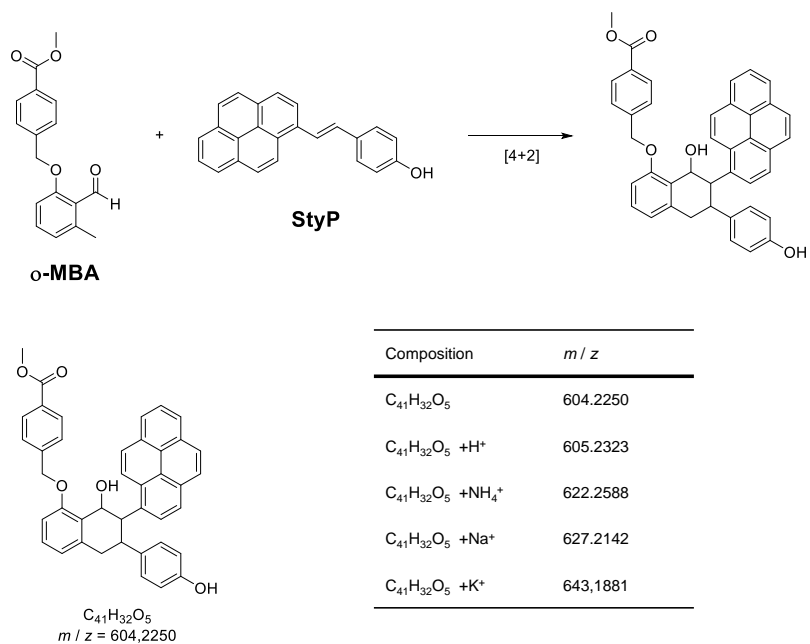
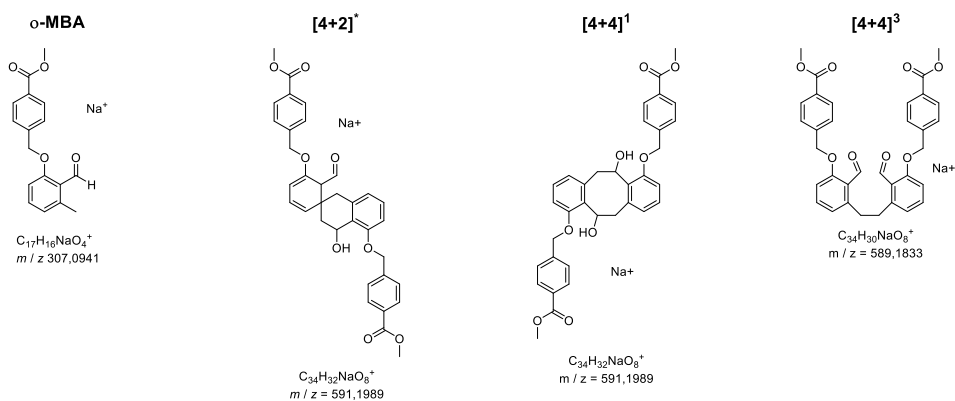


Figure 138. Theoretical *m/z* values that should be observed if a cross product of *o*-MBA with StyP is formed.

Possible Main Peaks



*all [4+2] structures feature the same mass therefore only one is shown as an example

Exemplary Selection of possible Fragments - [4+4]¹

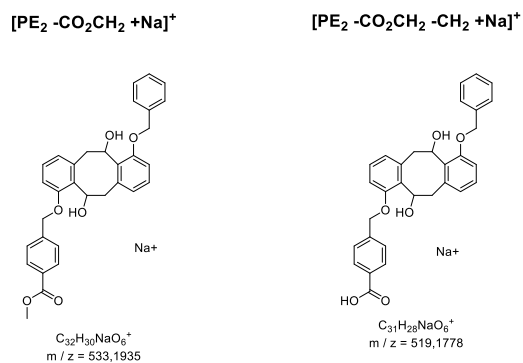


Figure 139. Overview over the possible mass fragments for *o*-MBA dimers.

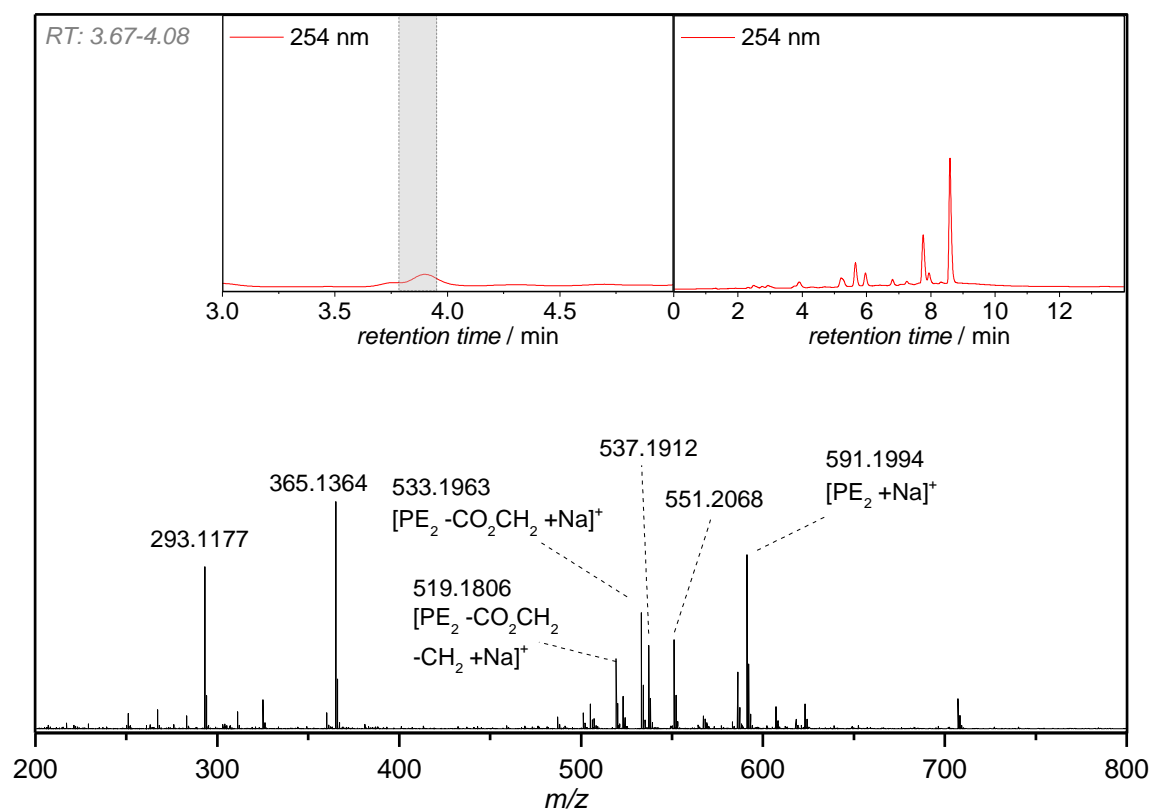


Figure 140. LC-trace (254 nm detector wavelength) and accumulated mass-spectra of the *o*-MBA and StyP mixture irradiated with 330 nm.

Table 12. Fragments found in **Figure 140**.

Symbol	m/z_{exp}	m/z_{theo}	Δ
$[\text{PE}_2\text{-CO}_2\text{CH}_2\text{-CH}_2\text{+Na}]^+$	519.1806	519.1778	0.0028
$[\text{PE}_2\text{-CO}_2\text{CH}_2\text{+Na}]^+$	533.1963	533.1935	0.0028
$[\text{PE}_2\text{+Na}]^+$	591.1994	591.1989	0.0005

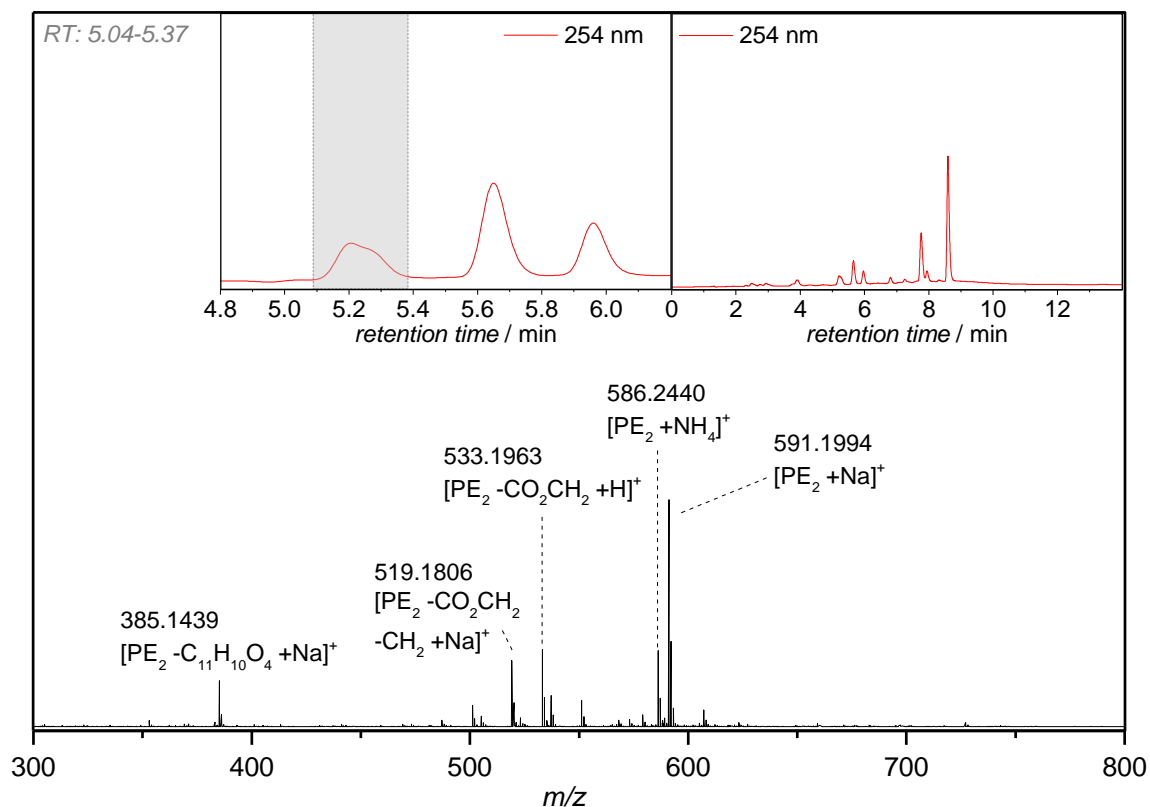


Figure 141. LC-trace (254 nm detector wavelength) and accumulated mass-spectra of the *o*-MBA and StyP mixture irradiated with 330 nm.

Table 13. Fragments found in Figure 141.

Symbol	m/z_{exp}	m/z_{theo}	Δ
$[\text{PE}_2 - \text{C}_{11}\text{H}_{10}\text{O}_4 + \text{Na}]^+$	385.1439	385.1413	0.0026
$[\text{PE}_2 - \text{CO}_2\text{CH}_2 - \text{CH}_2 + \text{Na}]^+$	519.1806	519.1778	0.0028
$[\text{PE}_2 - \text{CO}_2\text{CH}_2 + \text{Na}]^+$	533.1963	533.1935	0.0028
$[\text{PE}_2 + \text{NH}_4]^+$	586.2440	586.2435	0.0005
$[\text{PE}_2 + \text{Na}]^+$	591.1994	591.1989	0.0005

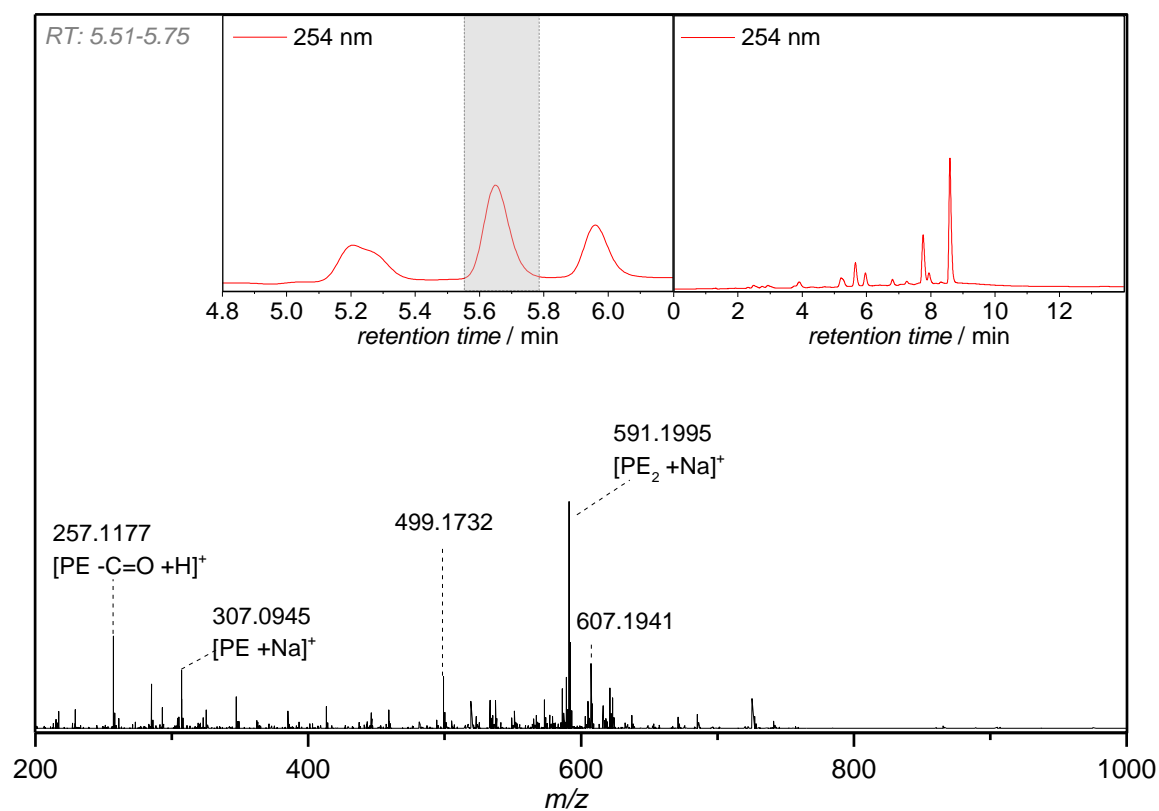


Figure 142. LC-trace (254 nm detector wavelength) and accumulated mass-spectra of the *o*-MBA and StyP mixture irradiated with 330 nm.

Table 14. Fragments found in **Figure 142**.

Symbol	m/z_{exp}	m/z_{theo}	Δ
[PE -C=O +H] ⁺	257.1177	257.1172	0.0005
[PE +Na] ⁺	307.0945	307.0941	0.0004
[PE ₂ +Na] ⁺	591.1995	591.1989	0.0006

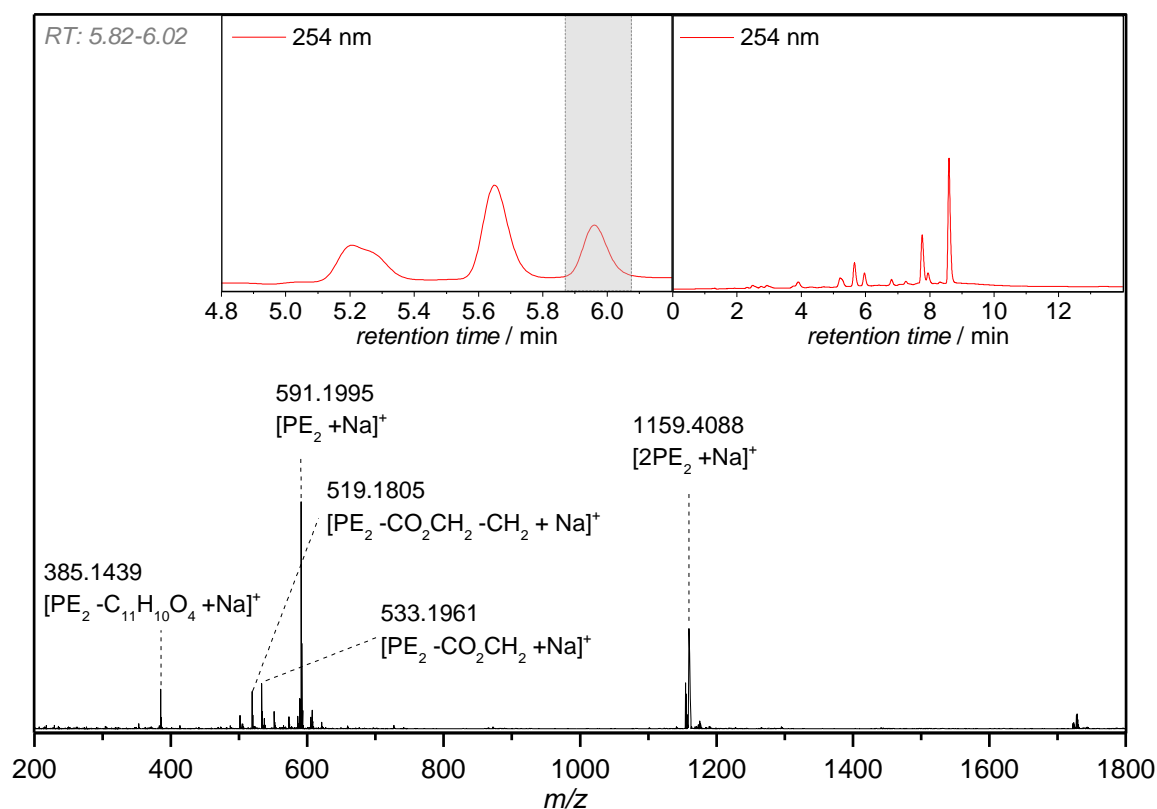


Figure 143. LC-trace (254 nm detector wavelength) and accumulated mass-spectra of the *o*-MBA and StyP mixture irradiated with 330 nm.

Table 15. Fragments found in **Figure 143**.

Symbol	m/z_{exp}	m/z_{theo}	Δ
[PE ₂ - C ₁₁ H ₁₀ O ₄ + Na] ⁺	385.1439	385.1413	0.0026
[PE ₂ - CO ₂ CH ₂ - CH ₂ + Na] ⁺	519.1805	519.1778	0.0027
[PE ₂ - CO ₂ CH ₂ + Na] ⁺	533.1961	533.1935	0.0026
[PE ₂ + Na] ⁺	591.1995	591.1989	0.0006
[2PE ₂ + Na] ⁺	1159.4088	1159.4086	0.0002

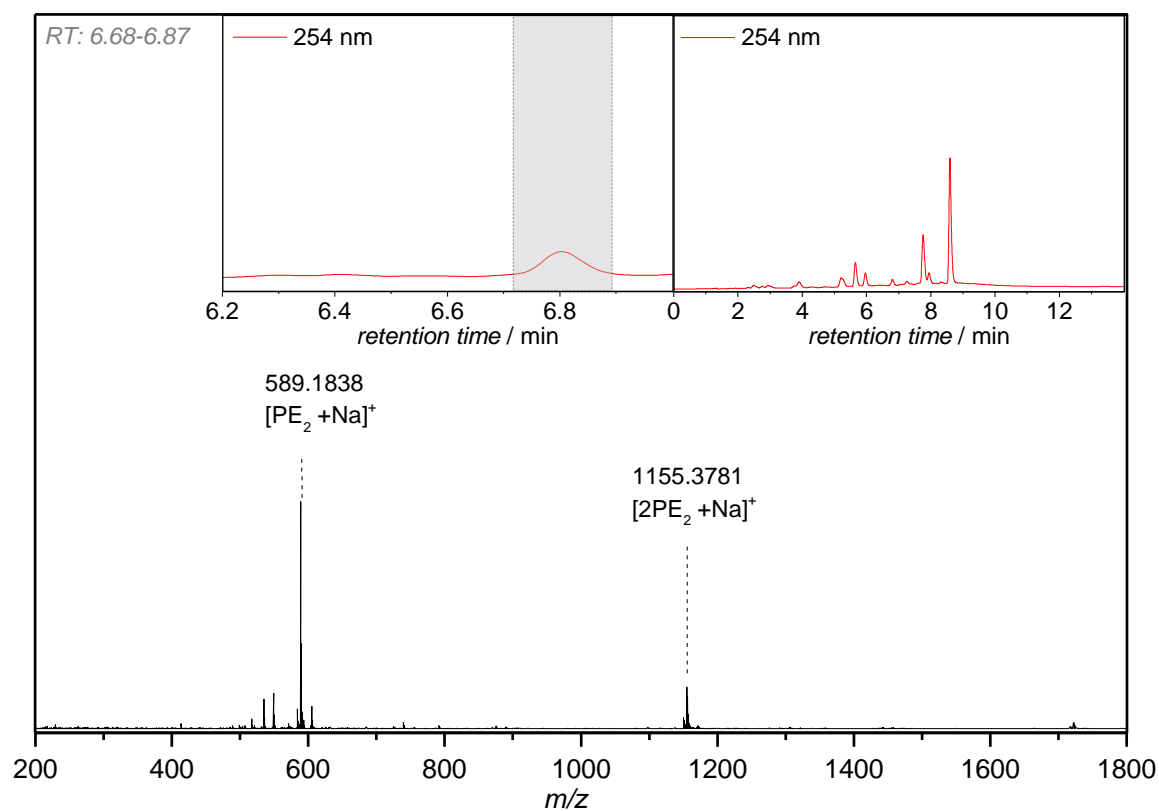


Figure 144. LC-trace (254 nm detector wavelength) and accumulated mass-spectra of the *o*-MBA and StyP mixture irradiated with 330 nm.

Table 16. Fragments found in **Figure 144**.

Symbol	m/z_{exp}	m/z_{theo}	Δ
[PE ₂ + Na] ⁺	589.1838	589.1833	0.0005
[2PE ₂ + Na] ⁺	1155.3781	1155.3720	0.0061

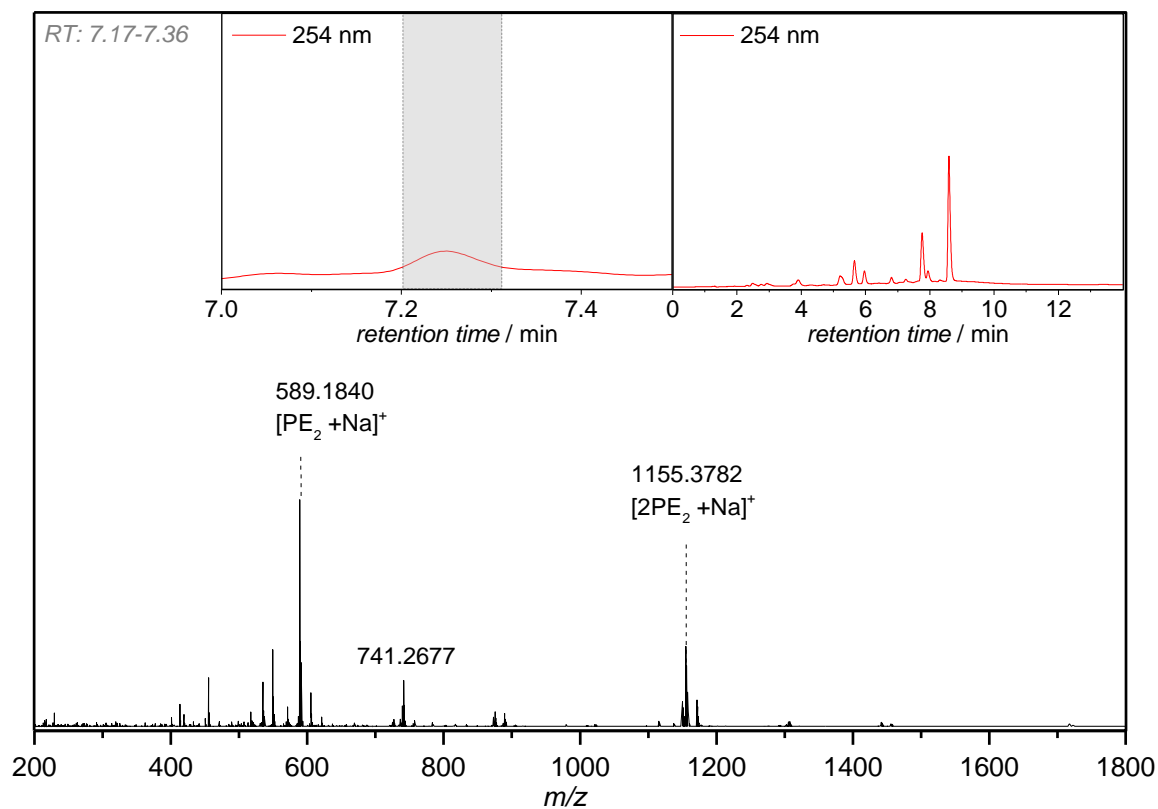


Figure 145. LC-trace (254 nm detector wavelength) and accumulated mass-spectra of the *o*-MBA and StyP mixture irradiated with 330 nm.

Table 17. Fragments found in Figure 145.

Symbol	m/z_{exp}	m/z_{theo}	Δ
$[\text{PE}_2 + \text{Na}]^+$	589.184	589.1833	0.0007
$[2\text{PE}_2 + \text{Na}]^+$	1155.3782	1155.3720	0.0062

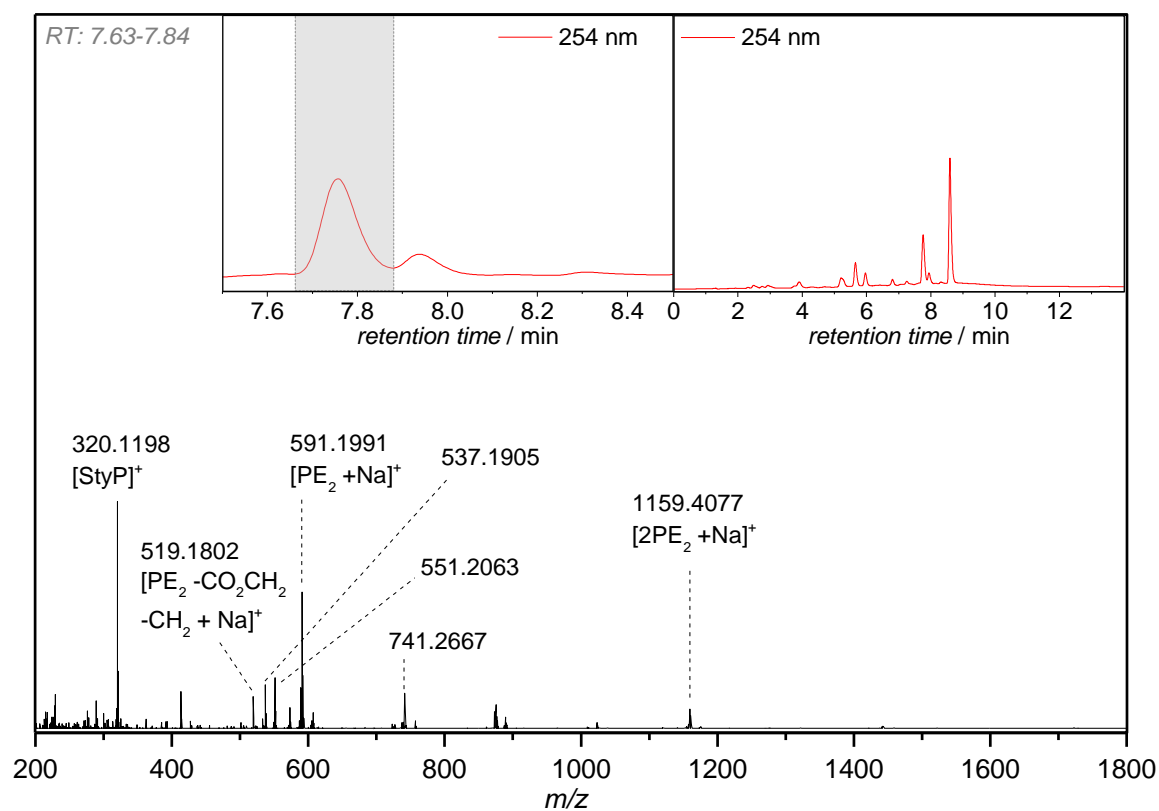


Figure 146. LC-trace (254 nm detector wavelength) and accumulated mass-spectra of the *o*-MBA and StyP mixture irradiated with 330 nm.

Table 18. Fragments found in **Figure 146**.

Symbol	m/z_{exp}	m/z_{theo}	Δ
StyP	320.1198	320.1201	0.0003
$[\text{PE}_2 - \text{CO}_2\text{CH}_2 - \text{CH}_2 + \text{Na}]^+$	519.1802	519.1778	0.0024
$[\text{PE}_2 + \text{Na}]^+$	591.1991	591.1989	0.0002
$[2\text{PE}_2 + \text{Na}]^+$	1159.4077	1159.4086	0.0009

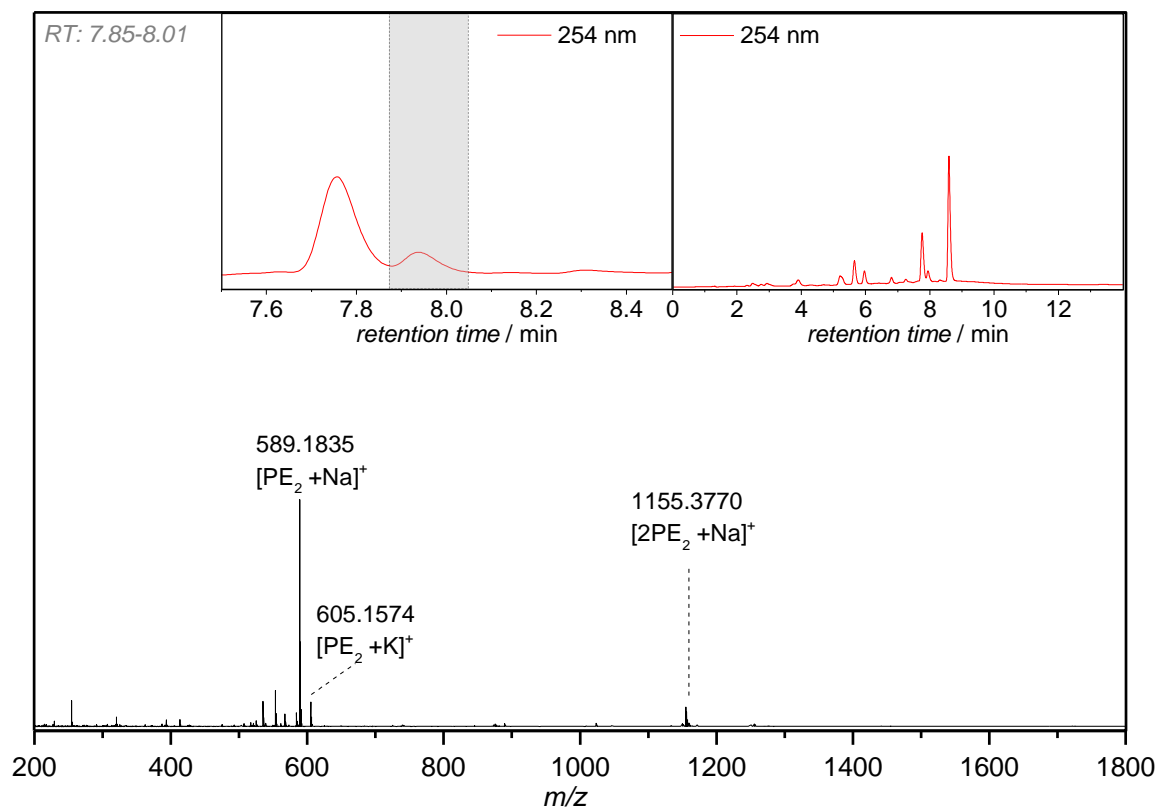


Figure 147. LC-trace (254 nm detector wavelength) and accumulated mass-spectra of the *o*-MBA and StyP mixture irradiated with 330 nm.

Table 19. Fragments found in **Figure 147**.

Symbol	m/z_{exp}	m/z_{theo}	Δ
$[\text{PE}_2 + \text{Na}]^+$	589.1835	589.1833	0.0002
$[\text{PE}_2 + \text{K}]^+$	605.1574	605.1573	0.0001
$[2\text{PE}_2 + \text{Na}]^+$	1155.377	1155.3720	0.0050

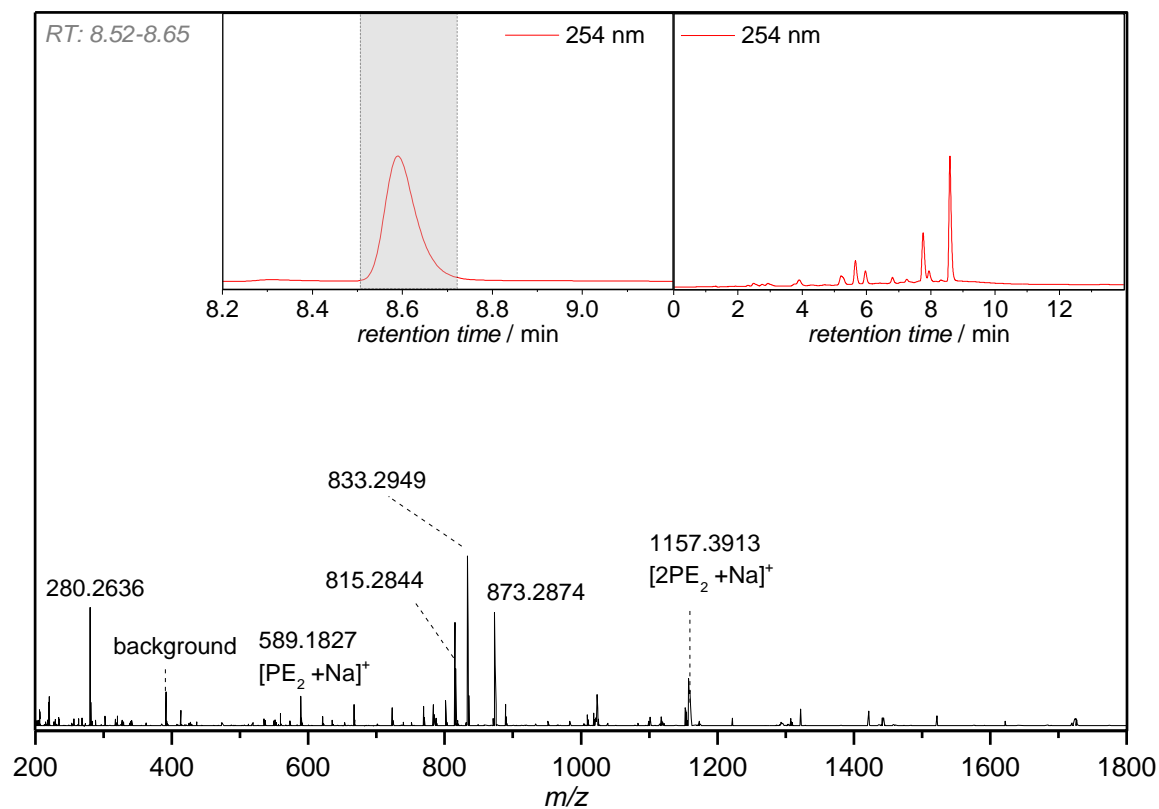


Figure 148. LC-trace (254 nm detector wavelength) and accumulated mass-spectra of the *o*-MBA and StyP mixture irradiated with 330 nm.

Table 20. Fragments found in **Figure 148**.

Symbol	m/z_{exp}	m/z_{theo}	Δ
$[\text{PE}_2 + \text{Na}]^+$	589.1827	589.1833	0.0006
$[2\text{PE}_2 + \text{Na}]^+$	1157.3913	1155.372	2.0193

Polychromophores

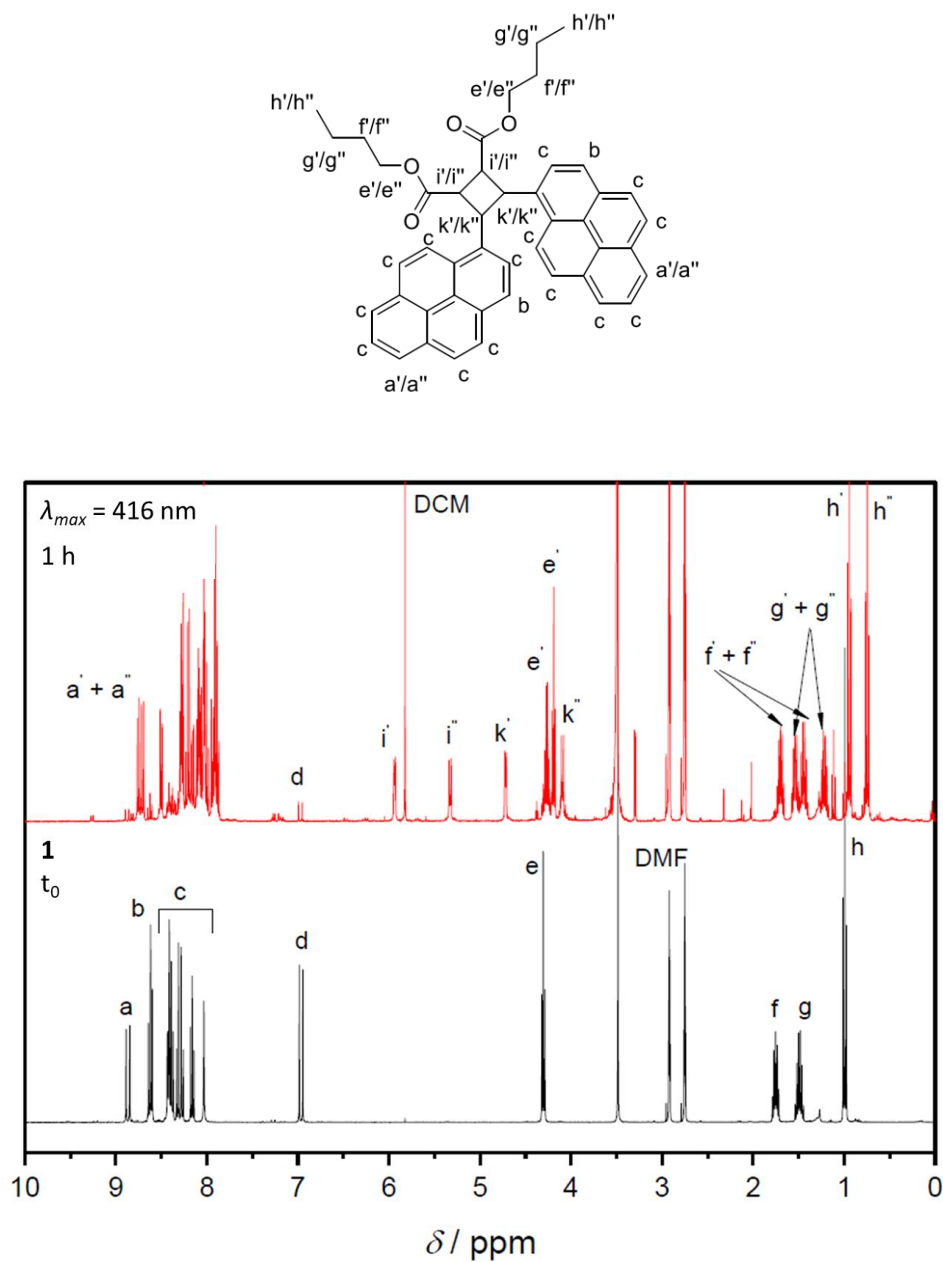


Figure 149. Comparison of proton NMR spectra of **1** (black) and **1** after irradiation for 1 h (red), both in DMF-d₇. The red curve indicates visible light-induced formation of two different cyclobutane-dimers of **9**.

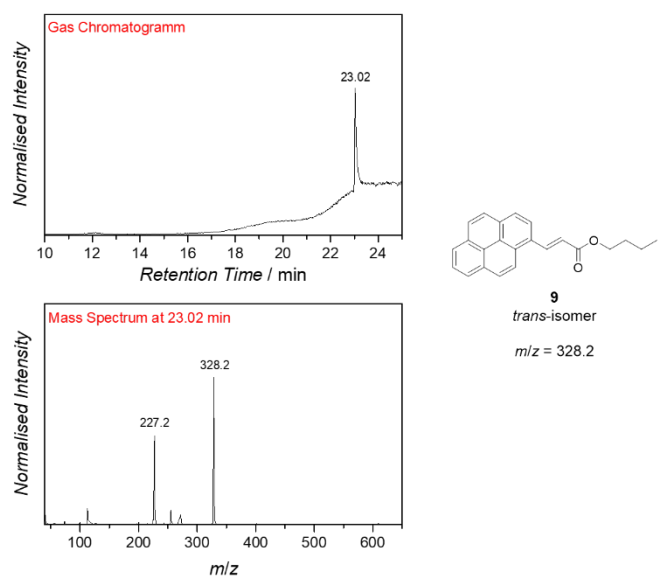


Figure 150. GC-MS measurement of **9** before irradiation.

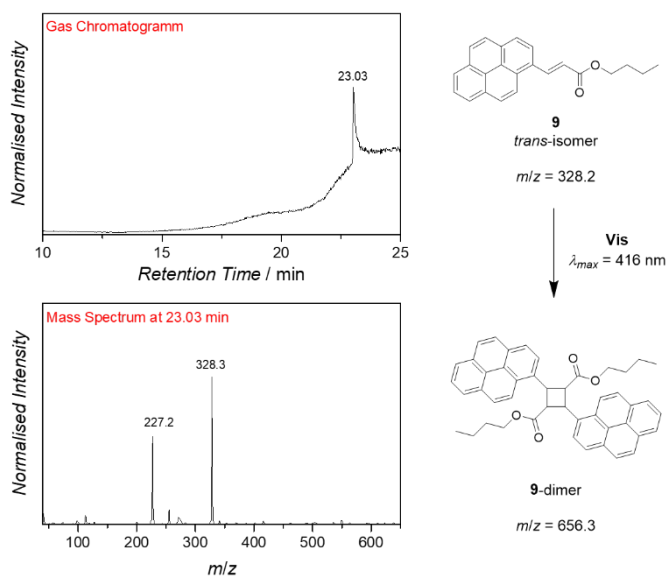


Figure 151. GC-MS of **9** after irradiation with visible light ($\lambda_{\text{max}} = 416 \text{ nm}$). No photodamage is observed during this reaction since no new peaks are arising in the gas chromatogram or the mass spectrum in comparison with **Figure 150**.

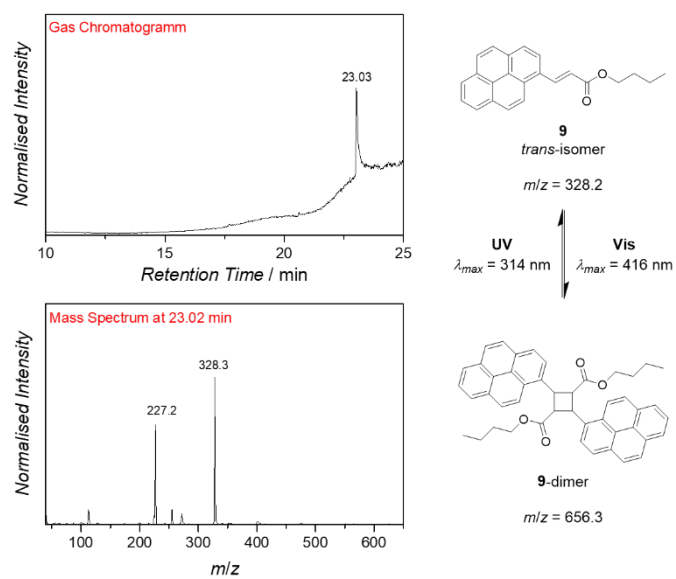


Figure 152. GC-MS of **9** after irradiation with visible light ($\lambda_{\text{max}} = 416 \text{ nm}$) and subsequent irradiation with UV light ($\lambda_{\text{max}} = 314 \text{ nm}$). No photodamage is observed during this reaction, since no new peaks are arising in the gas chromatogram or the mass spectrum in comparison with **Figure 150** and **Figure 151**.

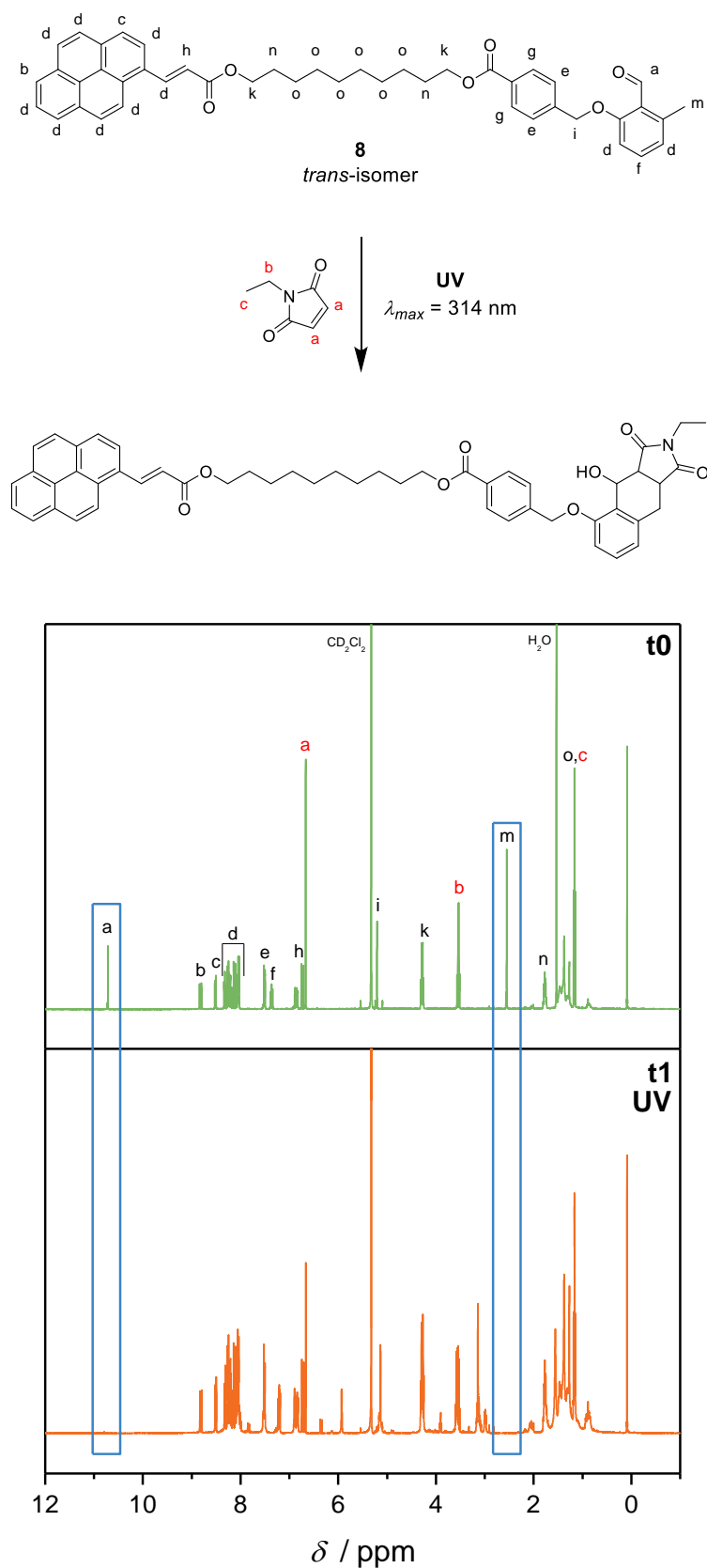


Figure 153. Proton NMR (recorded in deuterated dichloromethane, 400 MHz) of **8** before irradiation (*t0*) and after irradiation with UV light ($\lambda_{max} = 314 \text{ nm}$, *t1*). The disappearance of the magnetic resonances **a** and **m** proves the complete consumption of the *o*-MBA group

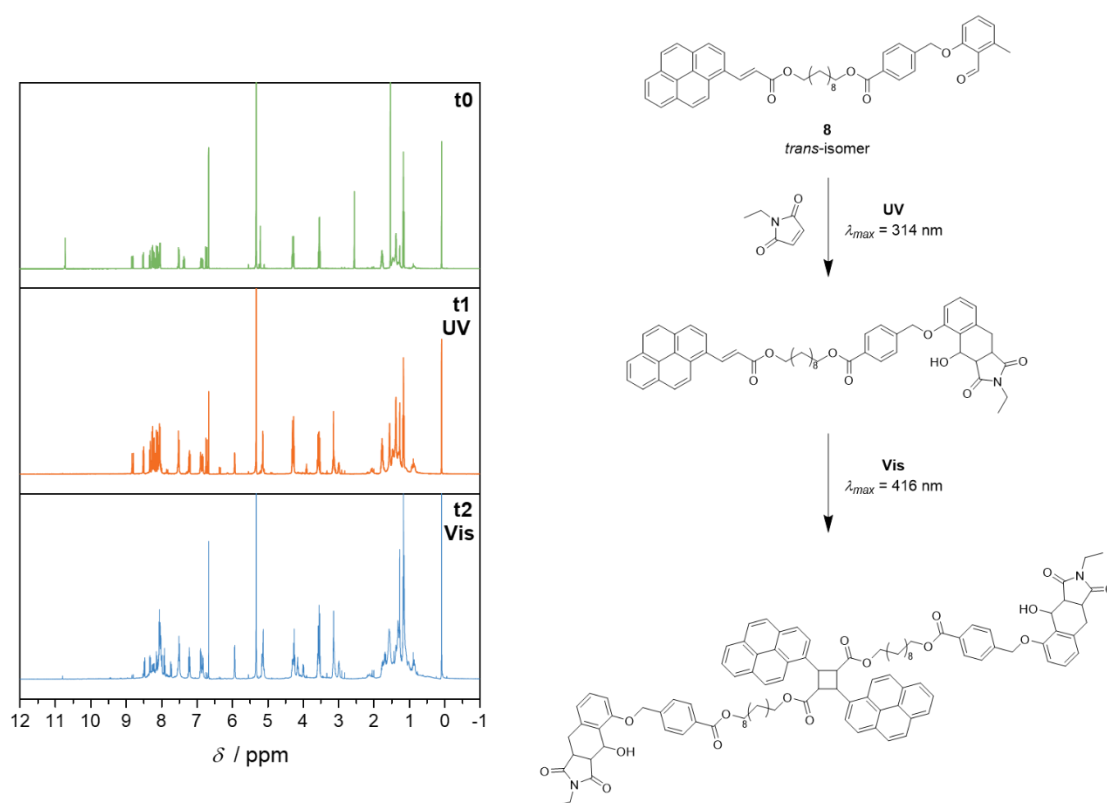


Figure 154. $^1\text{H-NMR}$ (recorded in deuterated dichloromethane, 400 MHz) of **8** before irradiation (t_0), after irradiation with UV light ($\lambda_{\text{max}} = 314 \text{ nm}$, t_1), and subsequent visible light irradiation ($\lambda_{\text{max}} = 614 \text{ nm}$, t_2).

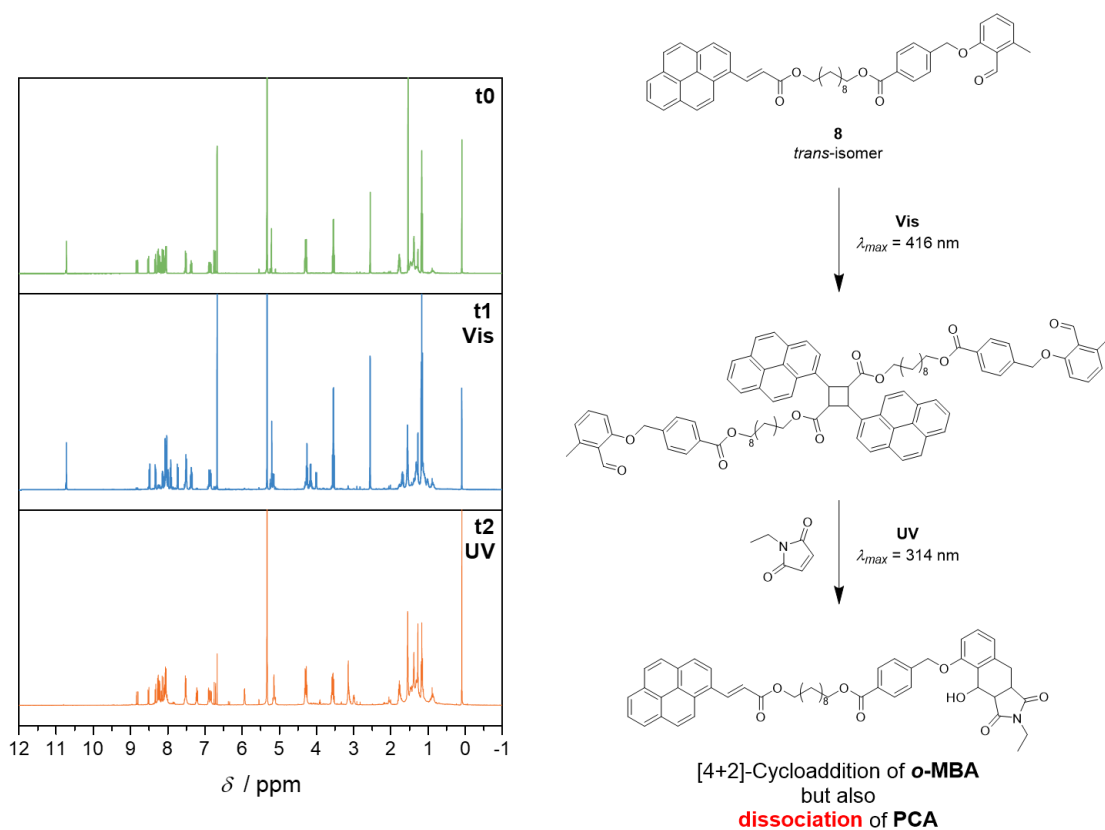


Figure 155. $^1\text{H-NMR}$ (recorded in deuterated dichloromethane) of **8** before irradiation (*t0*), after irradiation with visible light ($\lambda_{\text{max}} = 416 \text{ nm}$, *t1*), and subsequent UV light irradiation ($\lambda_{\text{max}} = 314 \text{ nm}$, *t2*). Upon irradiation not only the [4+2] cycloaddition of *o*-MBA occurs but the unexpectedly the in the first step formed cyclobutane structure also dissociated back to the double bond of PCA.

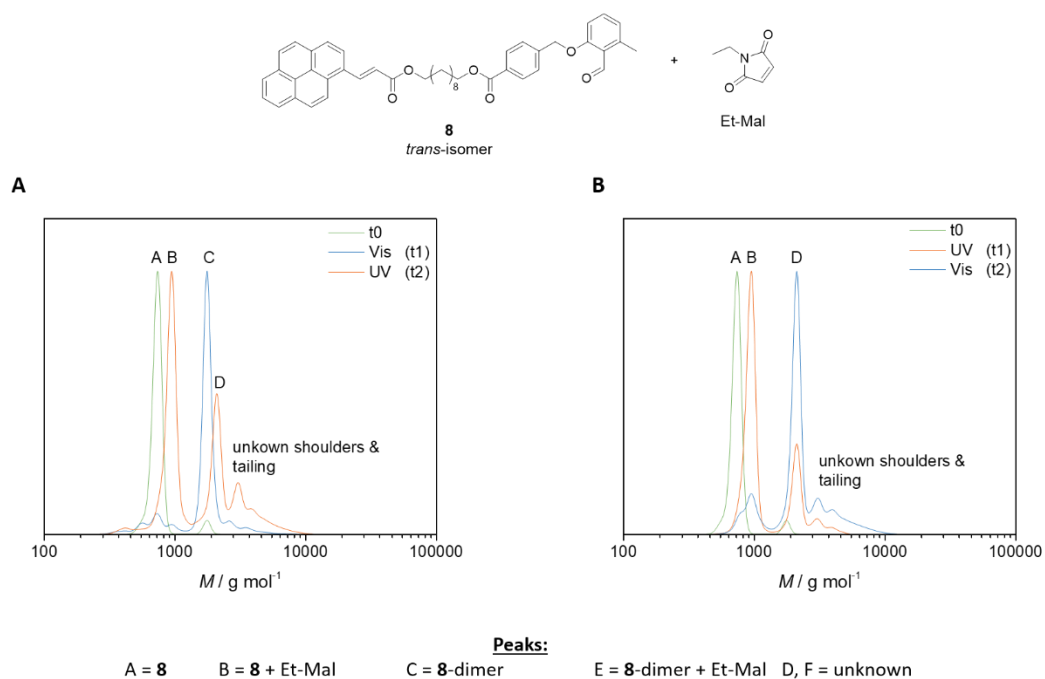


Figure 156. SEC traces (RI detector, with THF as the eluent) of **8** with Et-Mal: A) before irradiation (t_0), after irradiation with visible light (t_1), and subsequent UV light irradiation (t_2). B) before irradiation (t_0), after irradiation with UV light (t_1) and subsequent visible light irradiation (t_2).

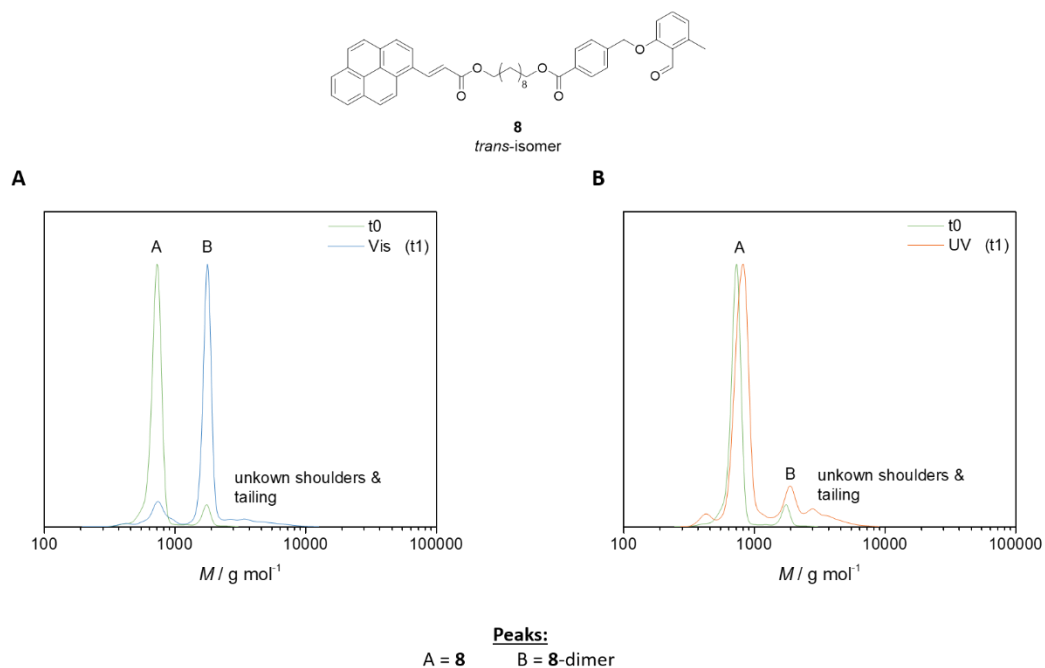


Figure 157. SEC traces (RI detector, with THF as the eluent) of **8**: before irradiation and after irradiation with visible light (A) or UV light (B).

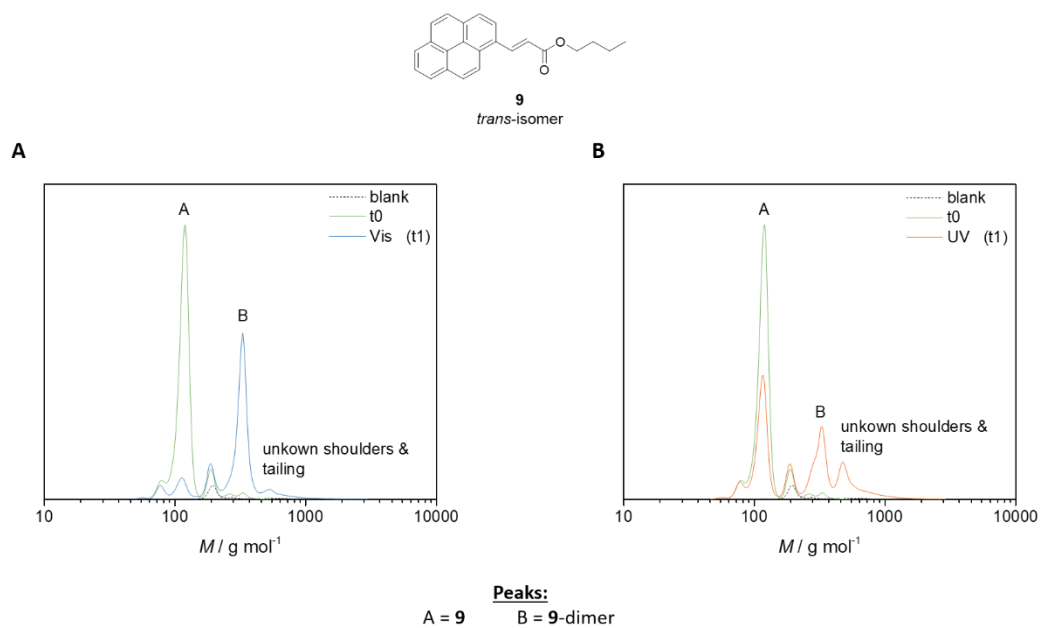


Figure 158. SEC traces (RI detector, with THF as the eluent) of **9**: before irradiation and after irradiation with visible light (A) or UV light (B). Measured on a Tosoh SEC system.

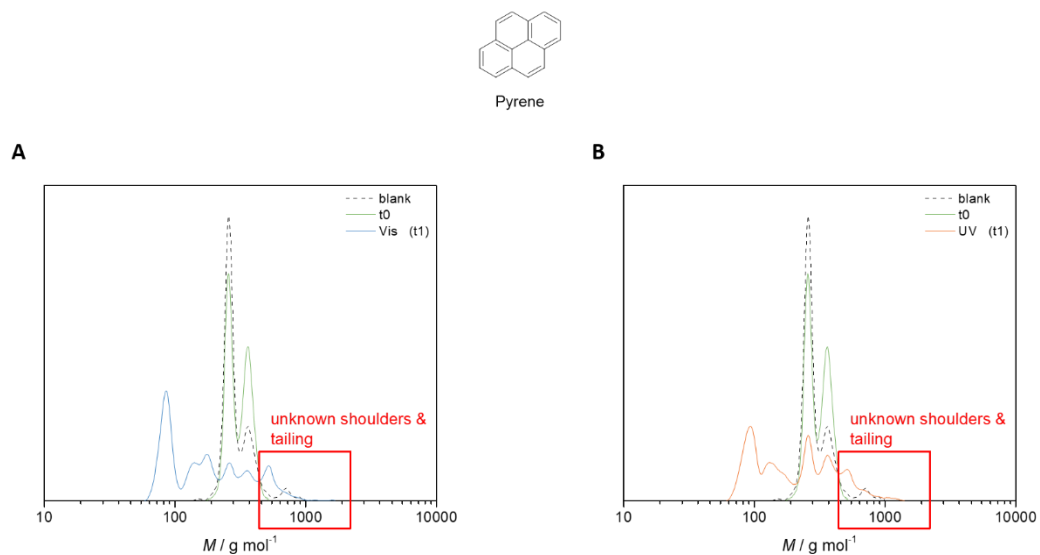


Figure 159. SEC traces (RI detector, with THF as the eluent) of pyrene: before irradiation and after irradiation with visible light (A) or UV light (B). Measured on a Tosoh SEC system.

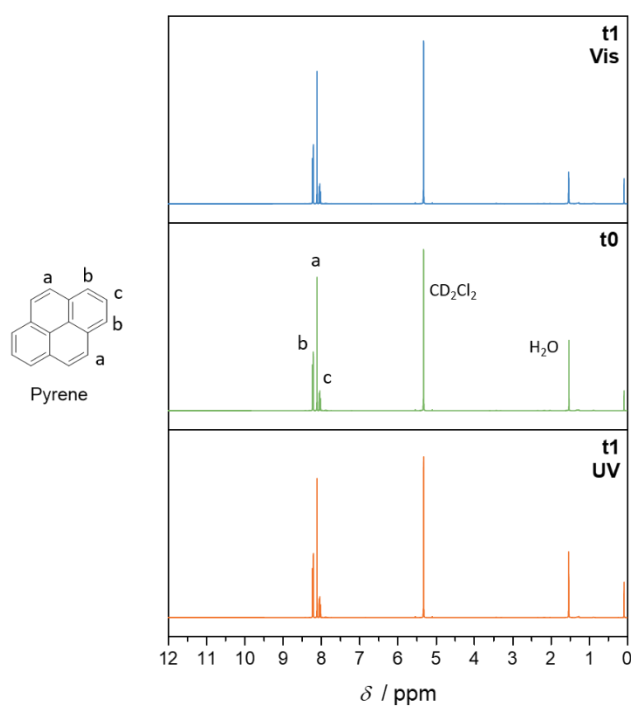


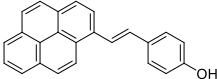
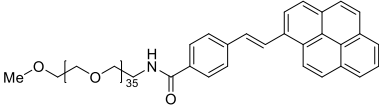
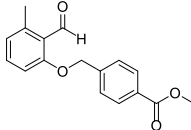
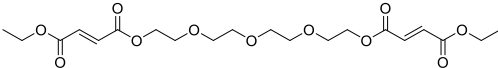
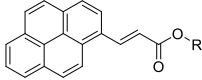
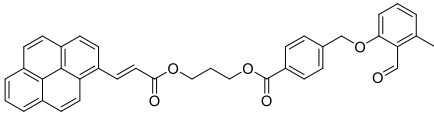
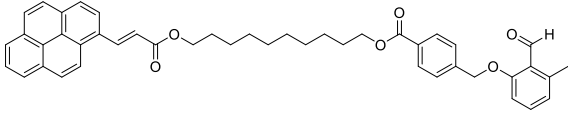
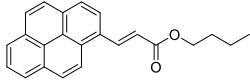
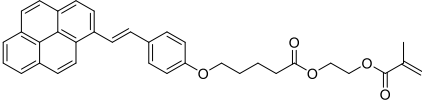
Figure 160. Proton NMR (recorded in deuterated dichloromethane, 400 MHz) of pyrene before irradiation (middle) and after irradiation with visible light (top) or UV light (bottom).

Towards Reversible Nanocellulose Materials

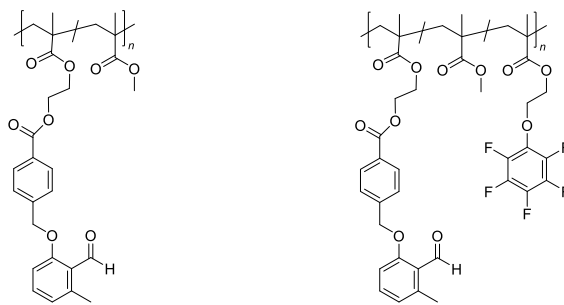


Figure 161. (1) Non-irradiated reference. (2) Irradiation styrylpyrene-polymer (P3) film at 410 – 420 nm for 4 h. Subsequent addition of water dissolved the reference 1 while 2 remained solid, successfully proving the cross-linking upon irradiation.

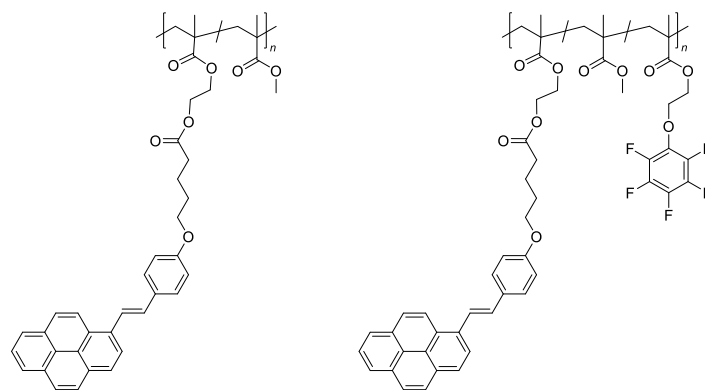
List of Investigated Chemical Compounds

Number	Name (Abbreviation)	Structure
1	<i>trans</i> -(<i>p</i> -Hydroxystyryl)pyrene (StyP)	
2	Styrylpyrene Dimers	refer to Table 7 on page 146
3	mPEG-StyP	
4	<i>ortho</i> -Methyl Benzaldehyde (<i>o</i> -MBA)	
5	Tetraethylene Glycol Difumarate (TGD)	
6	Pyrenyl Cinnamic Acid Derivate (PCA)	
7		
8		
9		
10	StyP-O-MA	

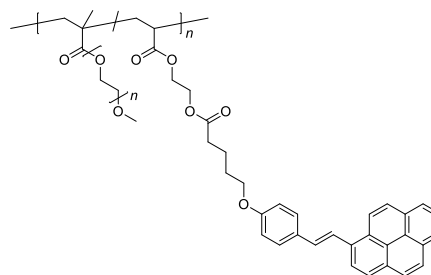
P1 / P1F



P2 / P2F



P3 / P4



List of Figures

Figure 1. Schematic overview over the topics investigated in the present thesis: In-depth investigations of the reversible and visible light cycloaddition of (A) styrylpyrene (Chapter 3) for further utilisation alongside the chromophores (B) o-methyl benzaldehyde (Chapter 4 and 5) and a pyrenyl cinnamic acid derivate (Chapter 5). Polymer Ligations to form (C) block-copolymers (Chapter 3) as well as networks via (D) side chain functional polymer strands (Chapter 4) or (E) by employing cross-linking molecules (Chapter 5). (F) Wavelength-orthogonal network formations enabled by the incorporation of two different chromophores into one material (styrylpyrene and o-methyl benzaldehyde, Chapter 5).....	2
Figure 2. Gradually changing irradiation (intensity or time) of styrylpyrene-functional polymer strands (depicted as blue lines) and styrylpyrene-functional nanocellulose fibrils (depicted as black lines) with visible light, leads to different amounts of cross-linking and thus properties like toughness and stiffness. Irradiation with UV light reverts that process, resulting in a reprogrammable gradient material.....	4
Figure 3. Overview of the FRP mechanism.	9
Figure 4. Overview of the RAFT mechanism.	12
Figure 5. Jablonski diagram showing the possible deactivation pathways after a molecule is irradiated with light.	14
Figure 6. When light of the intensity I_0 passes through a material or solution with the path length l , concentration c , and molar absorption ϵ_λ , it is absorbed according to the Beer-Lambert law and thus reduced to the intensity I	16
Figure 7. Franck Condon principle: Electronic transitions are more likely to occur in between vibrational states with high overlap.....	17
Figure 8. Schematic overview of cycloadditions and their nomenclature.	18
Figure 9. Pathways in which the orbitals of two molecules can partake in a cycloaddition.	19
Figure 10. A Change in orbital symmetry after irradiation with light. B Orbital difference of thermal and photochemical cycloaddition.	19
Figure 11. Overview over the different known reversible cycloadditions including their trigger wavelengths.	21
Figure 12. Reaction Pathways after irradiation of asymmetric alkenes with light. Depending on the symmetry when the reverse reaction is triggered, the cyclobutane is either transferred back to its asymmetric starting material or symmetric analogues that can limit the reversibility of the reaction. λ_2 is higher than λ_3 , λ_1 can be higher, lower or the same than λ_2 and λ_3	22
Figure 13. Examples for red-shifted [2+2] cycloadditions: trans-3-cyanovinylcarbazole, anthracene and styrylpyrene. All of these examples use templating techniques (e.g. DNA, Surface Chemistry).	23
Figure 14. Schematic representation for the preparation of polymeric photo-resist via selective photo-cross-linking and thus immobilisation for semiconductor technologies. Reprinted and adapted with permission of Royal Society of Chemistry, from: G. Kaur, P. Johnston, K. Saito, Polym. Chem., 2014, 5, 2171–2186. Copyright 2019, permission conveyed through Copyright Clearance Center, Inc.	24
Figure 15. Upon irradiation with light, self-healable material through the usage of coumarin-functionalised polymer chain. Reprinted and adapted with permission of Royal Society of Chemistry, from: G. Kaur, P. Johnston, K. Saito, Polym. Chem., 2014, 5, 2171–2186. Copyright 2019, permission conveyed through Copyright Clearance Center, Inc.	25
Figure 16. Photo-reversible linear polymers: A Photopolymerisation of difunctionalised monomers. B Photopolymerisation of difunctionalised macromonomers. C Polymerisation of monomer units containing already dimerised chromophores. Reprinted and adapted with permission of Royal Society of Chemistry, from: G. Kaur, P. Johnston, K. Saito, Polym. Chem., 2014, 5, 2171–2186. Copyright 2019, permission conveyed through Copyright Clearance Center, Inc.....	26

Figure 17. Examples for chromophores that were red-shifted via extension of the conjugated system.	29
Figure 18. Different pathways and strategies to λ -orthogonality: A Minimal spectral overlap allows for independent triggering of two different photoreactive moieties. B Due to spectral overlap, the two reactions only feature sequence dependent orthogonality. C Reversible photochemical reactions allow for complete orthogonality since the cycloreversion of reaction 2 renders the photochemical group inactive when light of the wavelength λ_1 is used. Reprinted and adapted with permission of John Wiley and Sons, from: H. Frisch, D. E. Marschner, A. S. Goldmann, C. Barner-Kowollik, <i>Angew. Chem. Int. Ed.</i> , 2018, 57 , 2036–2045. Copyright 2019, permission conveyed through Copyright Clearance Center, Inc.	31
Figure 19. Mechanism of the photoenol cycloaddition. ¹⁵¹	33
Figure 20. Possible Pathways for the photoenol self-dimerisation. The reaction can proceed either via [4+4] or [4+2] cycloaddition. The former can only yield in two different isomers, either head-to-head or head-to-tail, while the latter can form eight different structure depending on which double bond in the unactivated photoenol is taking the reaction part of the dienophile (refer to Figure 19). ¹⁵³	34
Figure 21. Isomers formed during the light induced [4+2] self-dimerisation of photoenol. ¹⁵³	35
Figure 22. Schematic diagram of a laser device.	36
Figure 23. Schematic setup of the employed tuneable laser device.	37
Figure 24. Dimerisation ($\lambda = 405$ nm) and dissociation ($\lambda \leq 366$ nm) of styrylpyrene as described by Kovalenko et al. in 1980.	41
Figure 25. Enlarged ¹ H-NMR (400 MHz, CD ₃ CN) spectra showing the isomerisation of StyP 1 under irradiation with UV-C light ($\lambda_{\text{max}} = 254$ nm; solvent: deuterated acetonitrile) showing distinct new resonances for the cis-isomer of 1 including one representing a proton of the double bond (resonance 17, 7.20 ppm, $J = 12.1$ Hz). For a complete spectrum refer to Appendix Figure 94 . Copyright 2018 American Chemical Society.	42
Figure 26. Enlarged ¹ H-NMR (600 MHz, CD ₃ CN) spectra showing the three different and separated photoproducts (PP I - III) that are obtained under irradiation of 1 ($\lambda_{\text{max}} = 444$ nm, in deuterated acetonitrile), including enlarged spectra showing the distinct peak pattern for the cyclobutane resonances (red boxes). For complete spectra refer to Appendix Section Styrylpyrene . Copyright 2018 American Chemical Society.	43
Figure 27. Theoretically possible products obtained via the cycloaddition of styrylpyrene 1 (a more detailed description can be found in Table 7 on page 144, *stereochemically identical but possible via different dimerisation approaches). Copyright 2018 American Chemical Society.	44
Figure 28. Enlarged ¹ H-NMR spectrum (600 MHz, CD ₃ CN) of the cyclobutane resonances for the photoproducts PP I , PP II , and PP III as well as their assigned structures. Copyright 2018 American Chemical Society.	46
Figure 29. Investigation of the dimerisation of styrylpyrene 1 (10 mM, deuterated acetonitrile, 242 μmol photons) in relation to (A) the energy per pulse (purple: 120 000 pulses, green: 360 000 pulses) and (B) the impact of oxygen in the reaction mixture (purple: argon, green: oxygen) as determined via ¹ H-NMR analysis. Copyright 2018 American Chemical Society.	48
Figure 30. Wavelength screening for the conversion of 1 (10 mM, deuterated acetonitrile) into the three different photoproducts (2a , 2b , 2d) upon irradiation with 242 μmol as determined via ¹ H-NMR analysis. Copyright 2018 American Chemical Society.	49
Figure 31. WPEA for the photochemical reaction of styrylpyrene 1 (1 mM, deuterated acetonitrile) consisting of (A) the wavelength screening of the dimerisation yield (squares) at a constant number of photons (242 μmol) in comparison with the absorbance of 1 (solid line) and (B) photon kinetics at the most efficient wavelength of $\lambda = 435$ nm. Yields are resulting from ¹ H-NMR analysis subsequent to irradiation. Copyright 2018 American Chemical Society.	50
Figure 32. WPEA for the dimerisation (blue) and dissociation (red) of styrylpyrene 1 (1 mM, deuterated acetonitrile) consisting of (A) the wavelength screening of the dimerisation/dissociation yield (squares) at a constant number of photons (242 μmol) in comparison with the absorbance of 1 (blue solid line) and the photoproduct mixture (red solid	

line), and (B) photon kinetics at the most efficient wavelengths of $\lambda = 435$ nm (blue squares) and $\lambda = 330$ nm (red squares). Yields are resulting from $^1\text{H-NMR}$ analysis subsequent to irradiation. Copyright 2018 American Chemical Society.....	51
Figure 33. Concept of block-copolymer formation via reversible photochemical ligation.	53
Figure 34. Reversible polymer ligation via alternating irradiation of styrylpyrene-functional PEG (10 mM) with visible light ($\lambda = 435$ nm, 483 μmol photons) and UV light ($\lambda = 330$ nm, 483 μmol photons) as well as subsequent analysis via PSS THF SEC (RI detector). Copyright 2018 American Chemical Society.	53
Figure 35. Irradiation of styrylpyrene-functional PEG (11.3 mg in 0.5 mL DMAc) with common light sources: The dimerisation was conducted at $\lambda_{\text{max}} = 441$ nm (11 h) and the dissociation at $\lambda_{\text{max}} = 313$ nm (11 h), as evidenced via DMAc SEC (RI detector). Copyright 2018 American Chemical Society.	54
Figure 36. Reaction cycles conducted for the reversible photochemical polymer ligation of 3 . Copyright 2018 American Chemical Society.	54
Figure 37. Overview over the two approaches that allow for reversible network formation.	57
Figure 38. Action plots for o-MBA 4 and StyP 1 showing their normalised conversion for their dimerisation vs. the irradiation wavelength (squares) as well as their UV/Vis spectra (solid lines). The most efficient wavelength to trigger the UV light reaction of 4 is 330 nm, while the dimerisation of 1 proceeds best under irradiation with visible light at 435 nm. Copyright 2019 John Wiley and Sons.	61
Figure 39. Photochemical reaction of o-MBA 4 with TGD 5 when irradiated with light in the UV-A range.	62
Figure 40. Reaction of o-MBA with TGD when irradiated in deuterated acetonitrile with a wavelength at 330 nm with 483 μmol of photons. Analysis via $^1\text{H-NMR}$ (400 MHz, CD_3CN). The disappearance of the resonances 1 (aldehyde) and 2 (methyl) of the o-MBA species 4 proved its complete conversion.	63
Figure 41. Irradiation of a mixture of StyP 1 and o-MBA 4 with visible light (435 nm, 1.93 mmol of photons). The magnetic resonances in the $^1\text{H-NMR}$ spectra (400 MHz, CD_3CN) were integrated in comparison to sulfolane as a reference. Since the peaks 20/24 of cis-StyP are overlaying with other resonances, protons 21/23 were chosen since they feature the same value than cis-20/24. For fully assigned spectra referred to Appendix Figure 136 . Copyright 2019 John Wiley and Sons.	64
Figure 42. Irradiation of a mixture of StyP 1 and o-MBA 4 with UV light (330 nm, 0.97 mmol of photons). The magnetic resonances in the $^1\text{H-NMR}$ spectra (400 MHz, CD_3CN) were integrated in comparison to sulfolane as a reference. Since the peaks 20/24 of cis-StyP are overlaying with other resonances, protons 21/23 were chosen since they feature the same value than cis-20/24. Copyright 2019 John Wiley and Sons.	65
Figure 43. Comparison of the LC traces (detector wavelength 254 nm) for StyP 1 , the mixture of StyP 1 and its photoproducts after irradiation with 435 nm, the mixture of o-MBA and StyP after irradiation with 330 nm, the main o-MBA dimer formed after irradiation with 330 nm, and o-MBA. Copyright 2019 John Wiley and Sons.	66
Figure 44. Concept of a wavelength-orthogonal system by implementing to different chromophores that can be cured under irradiation with disparate colours of light and result in two different materials. Below, the structures of the investigated polymer strands are shown. Copyright 2019 John Wiley and Sons.	68
Figure 45. XPS F 1s measurements of P1 + P2F irradiated with (A) 330 nm or (B) 435 nm and P1F + P2 irradiated at (C) 330 nm or (D) 435 nm. The blue dashed line represents a fitted function corresponding to the fluorine signals from the tagged-polymer present in the sample (P1F or P2F). The red dashed line matches the fluorine signal of the vial caps used during the irradiation experiments (PTFE). Copyright 2019 John Wiley and Sons.	69
Figure 46. Schematic representation of the spatially resolved photocuring process resulting in two different distinct areas. Half of the photomask was blocked for each irradiation procedure (illustrated by the grey areas in the photomask). Subsequently, the film was postcured via washing with CHCl_3 . Below, light microscopy images are showing the spin-coated film before and after irradiation as well as post-curing, clearly highlighting the differences between the irradiated areas (wrinkled areas: o-MBA 4 , smooth areas: StyP 1). Copyright 2019 John Wiley and Sons.	70

- Figure 47.** AFM topographical images of the step profile and border in between the substrate and photoresists, including a microscopy image of the developed photoresist to highlight the location where the respective AFM measurements were conducted. Copyright 2019 John Wiley and Sons..... 71
- Figure 48.** Reaction overview for the wavelength-orthogonal reaction cycle of a dichromophore (**7** or **8**) featuring two different light-responsive moieties (o-MBA **4** and PCA **6**), which can take part in site specific cycloaddition reactions. 75
- Figure 49.** UV/Vis spectrum of **9** (in DCM). 76
- Figure 50.** Proton NMR (400 MHz, DCM-d₂) of **9** before irradiation (t₀, green line), after irradiation with visible light ($\lambda_{\text{max}} = 416$ nm, t₁, blue line), and subsequent UV light irradiation ($\lambda_{\text{max}} = 314$ nm, t₂, orange line) including an enlarged version which is highlighting the crucial magnetic resonances representing the cycloproducts. 77
- Figure 51.** UV/Vis spectrum (DCM-d₂) of **9** before irradiation (t₀, green line), after irradiation with visible light ($\lambda_{\text{max}} = 416$ nm, t₁, blue line), and subsequent UV light irradiation ($\lambda_{\text{max}} = 314$ nm, t₂, orange line). 78
- Figure 52.** UV/Vis spectra of **9** (dotted line) and light treatment of **9** with different irradiation times: (A) irradiation with visible light (416 nm) as well as (B) irradiation with visible light (416 nm) for 60 min (dashed line) and subsequent treatment with UV light (314 nm). 79
- Figure 53.** ¹H-NMR (400 MHz, deuterated DCM) spectra of **8** (10 mM) in the presence of Et-Mal (10 mM) before and after irradiation (in DCM-d₂) with UV light ($\lambda_{\text{max}} = 314$ nm, 3 h). Disappearance of the methyl (**43**) and aldehyde (**44**) resonances suggests full conversion of o-MBA moiety..... 80
- Figure 54.** ¹H-NMR (400 MHz, deuterated DCM) and UV/Vis spectrum of **8** (10 mM, DCM-d₂) before irradiation (t₀), after irradiation with visible light (t₁, $\lambda_{\text{max}} = 416$ nm, 5 h), and subsequent irradiation with UV light (t₁, $\lambda_{\text{max}} = 314$ nm, 3 h)..... 81
- Figure 55.** UV/Vis spectrum of **8** in the presence of Et-Mal (10 mM each, DCM-d₂) before irradiation (t₀), after irradiation with UV light (t₁, $\lambda_{\text{max}} = 314$ nm, 3 h), and subsequent irradiation with visible light (t₁, $\lambda_{\text{max}} = 416$ nm, 5 h)..... 82
- Figure 56.** UV/Vis spectrum of **8** in the presence of Et-Mal (10 mM each, DCM-d₂) before irradiation (t₀), after irradiation with visible light (t₁, $\lambda_{\text{max}} = 416$ nm, 5 h), and subsequent irradiation with UV light (t₁, $\lambda_{\text{max}} = 314$ nm, 3 h). Upon irradiation with UV light, not only the [4+2] cycloaddition of the o-MBA moiety took place, but also the previously via the double bond of PCA formed photodimers. 83
- Figure 57.** Complete reaction cycle of **8** when irradiated with two disparate wavelengths, visible and UV light, in a subsequent fashion. The reaction pathways were proven via ¹H-NMR as well as UV/Vis spectroscopy. The fact, that UV irradiation did trigger both, the cycloaddition of one functionality (yellow) as well as the dissociation of the other moiety (red) does not introduce a disadvantage for the proposed system, since – due to the reversibility of the visible light system (red) – an additional step results can again trigger the dimerisation to obtain the final product. 84
- Figure 58.** UV/Vis spectra of **8** in presence of mPEG-Mal: (A) before irradiation (t₀), after irradiation with visible light (t₁, $\lambda_{\text{max}} = 416$ nm, 5 h), and subsequent irradiation with UV light (t₁, $\lambda_{\text{max}} = 314$ nm, 3 h). (B) before irradiation (t₀), after irradiation with UV light (t₁, $\lambda_{\text{max}} = 314$ nm, 3 h), and subsequent irradiation with visible light (t₁, $\lambda_{\text{max}} = 416$ nm, 5 h)..... 85
- Figure 59.** THF-SEC measurements of **8** in the presence of mPEG-Mal: (A) before irradiation (t₀), after irradiation with visible light (t₁, $\lambda_{\text{max}} = 416$ nm, 5 h), and subsequent irradiation with UV light (t₁, $\lambda_{\text{max}} = 314$ nm, 3 h). (B) before irradiation (t₀), after irradiation with UV light (t₁, $\lambda_{\text{max}} = 314$ nm, 3 h), and subsequent irradiation with visible light (t₁, $\lambda_{\text{max}} = 416$ nm, 5 h)..... 86
- Figure 60.** After casting CNF and a water-soluble polymer, both functionalised with styrylpyrene **1**, into a film, the latter can be employed in a reversible 2D patterning step to obtain a material with a lateral gradient. The cross-link density, and therefore stiffness of the material, is dependent on the light intensity and time the film is irradiated with..... 90

Figure 61. Synthesis of the styrylpyrene monomer StyP-O-MA 10 , and its copolymerisation with mTEGMA to yield the polymers P3 and P4	91
Figure 62. THF-SEC measurements (RI detector) of the polymers P3 and P4	92
Figure 63. Synthesis and ¹ H-NMR spectrum (DMSO-d ₆) of the styrylpyrene-functional amine.....	93
Figure 64.: (A) Mechanical testing and (B) macroscopically observed fluorescence of films containing CNF and styrylpyrene-functional polymers (P3 , P4) before and after irradiation with $\lambda_{\text{max}} = 430$ nm for 30 min.	95
Figure 65. Emission spectrum of the Avonec actinic blue 3 W LED setup for irradiation with $\lambda_{\text{max}} = 444$ nm.....	106
Figure 66. Emission spectrum of the Luzchem LZC-LBL LED for irradiation with $\lambda_{\text{max}} = 441$ nm.....	106
Figure 67. Emission spectrum of the Luzchem LZC-UVB lamp for irradiation with $\lambda_{\text{max}} = 313$ nm.	107
Figure 68. Photoreactor used for irradiation with broad band UV lights. The setup can be equipped with up to five lamps and features a rotating support for the vial holder.	107
Figure 69. Emission spectrum for the Cosmedico Arimed B6 that can be used with the UV photoreactor for irradiation with $\lambda_{\text{max}} = 314$ nm.	108
Figure 70. Photoreactor used for irradiation with LEDs in the visible light range.	108
Figure 71. Emission spectrum of the Avonec actinic blue 3 W LED used with the visible light photoreactor for irradiation with $\lambda_{\text{max}} = 416$ nm.	109
Figure 72. Experimental setup for the tuneable laser experiments. The energy output is regulated with the attenuator and controlled with the energy meter (setup without sample). Measurement of energy and irradiation of samples cannot be carried out simultaneously. An individual setting of the attenuator is necessary before each irradiation experiment.	110
Figure 73. Left: uncrimped vial; right: vial after removal of the headspace section.	111
Figure 74. Calibration of the glass vial transmittance including a fit to obtain the values that were not determined experimentally. This calibration was done for the laser setup and Glass vials at KIT.	113
Figure 75. Calibration of the glass vial transmittance including a fit to obtain the values that were not determined experimentally. This calibration was done for the laser setup and Glass vials at QUT.....	114
Figure 76. ¹ H-NMR (400 MHz, deuterated acetonitrile) of hydroxy-styrylpyrene (StyP 1).	117
Figure 77. ¹ H-NMR (600 MHz, deuterated DMSO) of carboxy-styrylpyrene (StyP-COOH).	118
Figure 78. ¹ H-NMR (600 MHz, deuterated DMSO) of mPEG-NH ₂	120
Figure 79. DMAc SEC (RI detector) measurement of mPEG-NH ₂	120
Figure 80. ESI-MS measurement of mPEG-NH ₂	121
Figure 81. ¹ H-NMR (600 MHz, deuterated DMSO) of mPEG-StyP 3	123
Figure 82. DMAc SEC (RI detector) measurement of mPEG-StyP.....	123
Figure 83. ESI-MS measurement of mPEG-StyP.	124
Figure 84. ¹ H-NMR (400 MHz, deuterated acetonitrile) of o-MBA 4	125
Figure 85. ¹ H-NMR (400 MHz, deuterated acetonitrile) spectrum of TGD, 5).....	126
Figure 86. ¹ H-NMR (400 MHz, deuterated chloroform) of 9	128
Figure 87. ¹ H-NMR (400 MHz, deuterated chloroform) of 8	131
Figure 88. ¹ H-NMR (400 MHz, deuterated chloroform) of StyP-O-MA 10	132
Figure 89. ¹ H-NMR (400 MHz, deuterated dichloromethane) of the polymer P3	133
Figure 90. THF SEC (RI detector) chromatogram of the polymer P3	134
Figure 91. ¹ H-NMR (400 MHz, deuterated chloroform) of the polymer P4	135
Figure 92. THF SEC (RI detector) chromatogram of the polymer P4	135
Figure 93. ¹ H-NMR (400 MHz, deuterated DMSO) of the boc protected styrylpyrene amine.	137

Figure 94. Enlarged ¹ H-NMR (400 MHz, CD ₃ CN) spectra showing the isomerisation of StyP 1 under irradiation with UV-C light ($\lambda_{\text{max}} = 254$ nm; solvent: deuterated acetonitrile) showing distinct new resonances for the cis-isomer of 1 including one representing a proton of the double bond (peak 17, 7.20 ppm, J = 12.1 Hz).....	145
Figure 95. Labelling of the hydroxy-styrylpyrene 1 molecule for detailed NMR assignments.....	149
Figure 96. ¹ H spectrum of the starting material trans-hydroxy-styrylpyrene 1	152
Figure 97. ¹³ C spectrum of the starting material trans-hydroxy-styrylpyrene 1	152
Figure 98. NOESY measurement of the starting material trans-hydroxy-styrylpyrene 1	153
Figure 99. COSY measurement of the starting material trans-hydroxy-styrylpyrene 1	153
Figure 100. HSQC-TOCSY measurement of the starting material trans-hydroxy-styrylpyrene 1	154
Figure 101. Decoupled HSQC measurement of the starting material trans-hydroxy-styrylpyrene 1	154
Figure 102. HMBC measurement of the starting material trans-hydroxy-styrylpyrene 1	155
Figure 103. ¹ H Spectrum of Product I (tt-ht-s 2d).....	156
Figure 104. ¹³ C Spectrum of Product I (tt-ht-s 2d).	156
Figure 105. NOESY measurement of Product I (tt-ht-s 2d).....	157
Figure 106. TOCSY measurement of Product I (tt-ht-s 2d).....	157
Figure 107. HSQC-TOCSY measurement of Product I (tt-ht-s 2d).....	158
Figure 108. Enlarged view of the HSQC-TOCSY measurement of Product I (tt-ht-s 2d).	158
Figure 109. Decoupled HSQC measurement of Product I (tt-ht-s 2d).	159
Figure 110. HMBC measurement of Product I (tt-ht-s 2d).	159
Figure 111. Enlarged view of the HMBC measurement of Product I (tt-ht-s 2d).	160
Figure 112. ¹ H spectrum of Product II (tt-ht-a 2a).....	161
Figure 113. ¹³ C spectrum of Product II (tt-ht-a 2a).....	161
Figure 114. NOESY measurement of Product II (tt-ht-a 2a).	162
Figure 115. TOCSY measurement of Product II (tt-ht-a 2a).....	162
Figure 116. HSQC-TOCSY measurement of Product II (tt-ht-a 2a).....	163
Figure 117. Enlarged view of the HSQC-TOCSY measurement of Product II (tt-ht-a 2a).....	163
Figure 118. Decoupled HSQC measurement of Product II (tt-ht-a 2a).....	164
Figure 119. HMBC measurement of Product II (tt-ht-a 2a).....	164
Figure 120. Enlarged view of the HMBC measurement of Product II (tt-ht-a 2a).....	165
Figure 121. ¹ H spectrum of Product III (tt-ht-s 2b).....	166
Figure 122. ¹³ C spectrum of Product III (tt-ht-s 2b).	166
Figure 123. NOESY measurement of Product III (tt-ht-s 2b).....	167
Figure 124. TOCSY measurement of Product III (tt-ht-s 2b).	167
Figure 125. HSQC-TOCSY measurement of Product III (tt-ht-s 2b).	168
Figure 126. Zoomed version of the HSQC-TOCSY measurement of Product III (tt-ht-s 2b).....	168
Figure 127. Decoupled HSQC measurement of Product III (tt-ht-s 2b).....	169
Figure 128. HMBC measurement of Product III (tt-ht-s 2b).....	169
Figure 129. Enlarged view of the HMBC measurement of Product III (tt-ht-s 2b).....	170
Figure 130. ¹ H-NMR spectrum after irradiation of StyP 1 (5.00 mM) in presence of TGD 5 (2.50 mM, solvent: CD ₃ CN) at a wavelength of 435 nm (483 μ mol photons). As expected, 1 underwent dimerisation – proven by the formation of the respective cyclobutane-photoproducts (red) – as well as isomerisation while 5 remained inactive.	174
Figure 131. ¹ H-NMR spectrum after irradiation of StyP 1 (5.00 mM) in presence of TGD 5 (2.50 mM, solvent: CD ₃ CN) at a wavelength of 330 nm (483 μ mol of photons). As expected, the only reaction taking place was the photochemically triggered isomerisation of 1	175

Figure 132. ¹ H-NMR spectrum after irradiation of o-MBA 4 (5.00 mM) in presence of TGD 5 (2.50 mM, solvent: CD ₃ CN) at a wavelength of 435 nm (483 μmol of photons). As expected, no photochemical reaction took place, proving the inactivity of both chromophores in the visible light range.....	176
Figure 133. ¹ H-NMR spectra of a mixture of StyP 1 (5.00 mM), o-MBA 4 (5.00 mM), and TGD 5 (2.50 mM, solvent: CD ₃ CN) before irradiation.....	177
Figure 134. ¹ H-NMR spectrum after irradiation of a mixture of StyP 1 (5.00 mM), o-MBA 4 (5.00 mM), and TGD 5 (2.50 mM, solvent: CD ₃ CN) with visible light (435 nm, 483 μmol photons). As expected, three styrylpyrene photoproducts were formed (marked in red). In addition, o-MBA 4 (compare magnetic resonance i close to 11 ppm) and TGD 5 (compare magnetic resonance a close to 1.00 ppm) remained intact.	178
Figure 135. ¹ H-NMR spectra before and after irradiation of a mixture of StyP 1 , o-MBA 4 , and TGD 5 with UV light (330 nm, 483 μmol photons). While the magnetic resonances for the methyl and aldehyde group of o-MBA disappeared (red boxes), TGD stayed intact (blue labelled magnetic resonances). In conclusion, o-MBA dimerised with itself instead of reacting with TGD.....	179
Figure 136. ¹ H-NMR spectrum after irradiation of StyP 1 (5.00 mM) and o-MBA 4 (5.00 mM, solvent: CD ₃ CN) at a wavelength of 435 nm (483 μmol photons). As expected, 1 underwent dimerisation – proven by the formation of the respective cyclobutane-photoproducts (red) – as well as isomerisation while 4 remained inactive.....	180
Figure 137. Main product formed via a [4+4] cycloaddition during irradiation of o-MBA 4 with UV-A light (330 nm).	181
Figure 138. Theoretical m / z values that should be observed if a cross product of o-MBA with StyP is formed.	182
Figure 139. Overview over the possible mass fragments for o-MBA dimers.	183
Figure 140. LC-trace (254 nm detector wavelength) and accumulated mass-spectra of the o-MBA and StyP mixture irradiated with 330 nm.....	184
Figure 141. LC-trace (254 nm detector wavelength) and accumulated mass-spectra of the o-MBA and StyP mixture irradiated with 330 nm.....	185
Figure 142. LC-trace (254 nm detector wavelength) and accumulated mass-spectra of the o-MBA and StyP mixture irradiated with 330 nm.....	186
Figure 143. LC-trace (254 nm detector wavelength) and accumulated mass-spectra of the o-MBA and StyP mixture irradiated with 330 nm.....	187
Figure 144. LC-trace (254 nm detector wavelength) and accumulated mass-spectra of the o-MBA and StyP mixture irradiated with 330 nm.....	188
Figure 145. LC-trace (254 nm detector wavelength) and accumulated mass-spectra of the o-MBA and StyP mixture irradiated with 330 nm.....	189
Figure 146. LC-trace (254 nm detector wavelength) and accumulated mass-spectra of the o-MBA and StyP mixture irradiated with 330 nm.....	190
Figure 147. LC-trace (254 nm detector wavelength) and accumulated mass-spectra of the o-MBA and StyP mixture irradiated with 330 nm.....	191
Figure 148. LC-trace (254 nm detector wavelength) and accumulated mass-spectra of the o-MBA and StyP mixture irradiated with 330 nm.....	192
Figure 149. Comparison of proton NMR spectra of 1 (black) and 1 after irradiation for 1 h (red), both in DMF-d ₇ . The red curve indicates visible light-induced formation of two different cyclobutane-dimers of 9	193
Figure 150. GC-MS measurement of 9 before irradiation.....	194
Figure 151. GC-MS of 9 after irradiation with visible light (λ _{max} = 416 nm). No photodamage is observed during this reaction since no new peaks are arising in the gas chromatogram or the mass spectrum in comparison with Figure 150	194

Figure 152. GC-MS of 9 after irradiation with visible light ($\lambda_{\text{max}} = 416 \text{ nm}$) and subsequent irradiation with UV light ($\lambda_{\text{max}} = 314 \text{ nm}$). No photodamage is observed during this reaction, since no new peaks are arising in the gas chromatogram or the mass spectrum in comparison with Figure 150 and Figure 151	195
Figure 153. Proton NMR (recorded in deuterated dichloromethane, 400 MHz) of 8 before irradiation (t_0) and after irradiation with UV light ($\lambda_{\text{max}} = 314 \text{ nm}$, t_1). The disappearance of the magnetic resonances a and m proves the complete consumption of the o-MBA group	196
Figure 154. ^1H -NMR (recorded in deuterated dichloromethane, 400 MHz) of 8 before irradiation (t_0), after irradiation with UV light ($\lambda_{\text{max}} = 314 \text{ nm}$, t_1), and subsequent visible light irradiation ($\lambda_{\text{max}} = 614 \text{ nm}$, t_2).....	197
Figure 155. ^1H -NMR (recorded in deuterated dichloromethane) of 8 before irradiation (t_0), after irradiation with visible light ($\lambda_{\text{max}} = 416 \text{ nm}$, t_1), and subsequent UV light irradiation ($\lambda_{\text{max}} = 314 \text{ nm}$, t_2). Upon irradiation not only the [4+2] cycloaddition of o-MBA occurs but the unexpectedly the in the first step formed cyclobutane structure also dissociated back to the double bond of PCA.	198
Figure 156. SEC traces (RI detector, with THF as the eluent) of 8 with Et-Mal: A) before irradiation (t_0), after irradiation with visible light (t_1), and subsequent UV light irradiation (t_2). B) before irradiation (t_0), after irradiation with UV light (t_1) and subsequent visible light irradiation (t_2).....	199
Figure 157. SEC traces (RI detector, with THF as the eluent) of 8 : before irradiation and after irradiation with visible light (A) or UV light (B).....	199
Figure 158. SEC traces (RI detector, with THF as the eluent) of 9 : before irradiation and after irradiation with visible light (A) or UV light (B). Measured on a Tosoh SEC system.	200
Figure 159. SEC traces (RI detector, with THF as the eluent) of pyrene: before irradiation and after irradiation with visible light (A) or UV light (B). Measured on a Tosoh SEC system.	200
Figure 160. Proton NMR (recorded in deuterated dichloromethane, 400 MHz) of pyrene before irradiation (middle) and after irradiation with visible light (top) or UV light (bottom).....	201
Figure 161. (1) Non-irradiated reference. (2) Irradiation styrylpyrene-polymer (P3) film at 410 – 420 nm for 4 h. Subsequent addition of water dissolved the reference 1 while 2 remained solid, successfully proving the cross-linking upon irradiation.	202

List of Tables

Table 1. Classes and sub-classes of light suitable for photochemical reactions including their wavelength ranges.	13
Table 2. Woodward-Hoffmann rules for thermal cycloadditions ⁶³	18
Table 3. Transmittance of the glass vials used for the laser experiments. These values were measured with the tuneable laser setup and vials at KIT.....	112
Table 4. Transmittance of the glass vials used for the laser experiments. These values were measured with the tuneable laser setup and vials at QUT.....	113
Table 5. Peak assignment of the ESI-MS data of the synthesized mPEG-NH ₂ showing the structures assigned in Figure 80 , the experimental as well as theoretical m / z values and the resolution.	121
Table 6. Peak assignment of the ESI-MS data of the synthesized mPEG-NH ₂ showing the structures assigned in Figure 83 , the experimental as well as theoretical m / z values and the resolution.	124
Table 7. Structures of possible photoproducts including their molecule number (2a – 2l), the characteristics determining their nomenclature, abbreviations and energies obtained after geometry optimization with MMFF94 force field. The difference in the energy with respect to the lowest energy structure is given in brackets.	146
Table 8. ¹ H-NMR chemical shifts for starting material StyP 1 as well as the three photoproducts PP I – III , generated upon irradiation with visible light. The scalar couplings are given in Hz in brackets. The asterisk marks overlapping signals where multiplicity and/or scalar couplings could not be evaluated.....	149
Table 9. ¹³ C-NMR chemical shifts for starting material StyP 1 as well as the three photoproducts PP I – III , generated upon irradiation with visible light. The shifts marked with an asterisk are interchangeable, while the ones indicated with a hash where observed in HMBC spectra only and could be assigned ambiguously.	150
Table 10. Differences of the ¹ H chemical shifts in ppm between the starting hydroxy-styrylpyrene 1 , indicated with start and each of the three photoproducts, marked as Product I (PP I , tt-ht-a 2a), Product II (PP II , tt-ht-a 2a) and Product III (PP III , tt-ht-s 2b).	172
Table 11. Differences of the ¹³ C chemical shifts in ppm between the starting hydroxy-styrylpyrene 1 , indicated with start and each of the three photoproducts, marked as Product I (PP I , tt-ht-a 2a), Product II (PP II , tt-ht-a 2a) and Product III (PP III , tt-ht-s 2b).	173
Table 12. Fragments found in Figure 140	184
Table 13. Fragments found in Figure 141	185
Table 14. Fragments found in Figure 142	186
Table 15. Fragments found in Figure 143	187
Table 16. Fragments found in Figure 144	188
Table 17. Fragments found in Figure 145	189
Table 18. Fragments found in Figure 146	190
Table 19. Fragments found in Figure 147	191
Table 20. Fragments found in Figure 148	192

Publications and Conferences

Publications Arising from this Thesis

- (1) Visible Light [2+2] Cycloadditions for Reversible Polymer Ligation
D. E. Marschner, H. Frisch, J. T. Offenloch, B. T. Tuten, C. R. Becer, A. Walther, A. S. Goldmann, P. Tzvetkova, C. Barner-Kowollik, *Macromolecules* **2018**, *51*, 3802.
- (2) Access to Disparate Soft Matter Materials by Curing with Two Colors of Light
D. E. Marschner,[#] S. Bialas,[#] L. Michalek,[#] T. Krappitz, M. Wegener, J. Blinco, E. Blasco, H. Frisch, C. Barner-Kowollik, *Adv. Mater.* **2019**, *31*, 1807288.
Highlighted on the Frontispiece in *Advanced Materials* (8/2019).
- (3) Fully Independent Photochemical Reactivity in One Molecule
D. E. Marschner,[#] C. O. Franck,[#] D. Abt, H. Mutlu, C. Barner-Kowollik, *Chem. Commun.* **2019**, *55*, 9877.

Additional Publications

- (4_a) Wavelength-Gated Dynamic Covalent Chemistry
H. Frisch, D. E. Marschner, A. S. Goldmann, C. Barner-Kowollik, *Angew. Chem. Int. Ed.* **2018**, *57*, 2036.
- (4_b) Wellenlängengesteuerte dynamische kovalente Chemie
H. Frisch, D. E. Marschner, A. S. Goldmann, C. Barner-Kowollik, *Angew. Chem.* **2018**, *130*, 2054.
- (5) Photochemistry in Confined Environments for Single-Chain Nanoparticle Design
H. Frisch, J. P. Menzel, F. R. Bloesser, D. E. Marschner, K. Mundsinger, C. Barner-Kowollik, *J. Am. Chem. Soc.* **2018**, *140*, 9551.

Conferences

- (1) Visible Light Activated Photoreversible Polymer Ligation as a Technology Platform for Light Reprogrammable Materials
D. E. Marschner, H. Frisch, J. T. Offenloch, B. T. Tuten, C. R. Becer, A. Walther, A. S. Goldmann, P. Tzvetkova, C. Barner-Kowollik, *Macromolecular Colloquium Freiburg February 2018*, poster presentation.
- (2) Visible Light Activated Photoreversible Polymer Ligation as a Technology Platform for Light Reprogrammable Materials
D. E. Marschner, H. Frisch, J. T. Offenloch, B. T. Tuten, C. R. Becer, A. Walther, A. S. Goldmann, P. Tzvetkova, C. Barner-Kowollik, *27th PhotoIUPAC Dublin July 2018*, poster presentation.

These authors contributed equally.

Acknowledgements

Last but not least, I'd like to thank a few people who supported me throughout the three years of my thesis and shared many great experiences with me.

First of all, I would like to thank my supervisor Christopher Barner-Kowollik for his continuous support and mentorship throughout this thesis, for his enthusiasm for research and his motivating discussions. Thank you very much for making it possible to present my work on international conferences as well as my stay abroad at the QUT in Brisbane, Australia.

In addition, I want to acknowledge the Deutsche Forschungsgemeinschaft (DFG) for funding my research as well as my cooperation partners Andreas Walther and Daniel Hönders, for – together with Christopher Barner-Kowollik and Anja Goldmann – applying for the respective grant and discussing our projects in the cooperation meetings.

I would also like to thank the people who supported me during my research in my own projects as well as during collaborative projects. In specific I'd like to thank Bryan Tuten, Janin Offenloch and especially Pavleta Tzvetkova, for her expertise in NMR studies. I'd like to thank Hendrik Frisch for many constructive discussions during my stay in Brisbane as well as Sabrina Bialas for our idea and work on our shared project. Many thanks to Christoph Franck to approach me with his project to establish a cooperation and Hatice Mutlu for her supervision.

Many thanks to the people who always kept the macroarc group running, especially to Maria Schneider, Evelyn Stühling, Katharina Elies, Vincent Schüler, Anja Goldmann and Eva Blasco.

Bryan Tuten, Eva Blasco, Anja Goldmann and especially Hatice Mutlu and Christopher Barner-Kowollik is thanked for proof-reading my thesis and their helpful comments and discussions.

I am very grateful to all my friends and colleagues from both, in- and outside of work, as well as in both countries, Germany and Australia. Thank you for the great moments and good times I had during my PhD but also for your support during the less nice times. I will never forget all

the amazing things we have done together, starting with shared dinners, coffee breaks, awesome trips, Squash, Beach Volleyball and Tuesdays!

Many thanks go to my friends from studying (Lenz, Samantha, Waldemar, Wolfram, and Dennis) who stuck with me throughout my PhD as well. Special thanks to Bryan the best Aussie flatmate, Sabrina for all our shared breaks, Matze, Dyvia and last but not least Federica, my pineapple and coffee friend, as well as Hendrik, without you my time in Australia wouldn't have been the same. Thank you very much for your motivating ways and all we've experienced together.

I would like to thank my long-term friends from Speyer, especially Felix for always having my back, as well as my family for their continuous support, no matter what.

Thank you very much!